

**UNIVERSIDADE FEDERAL DE SANTA CATARINA  
DEPARTAMENTO DE ENGENHARIA ELÉTRICA**

**Tiago Staudt**

**BRUSHLESS DOUBLY-FED RELUCTANCE  
MACHINE MODELING, DESIGN AND  
OPTIMIZATION**

**FLORIANÓPOLIS  
2015**





**Tiago Staudt**

**BRUSHLESS DOUBLY-FED RELUCTANCE  
MACHINE MODELING, DESIGN AND  
OPTIMIZATION**

Tese submetida à Universidade Federal de Santa Catarina como parte dos requisitos para a obtenção do Grau de Doutor em Engenharia Elétrica.

Orientadores (em cotutela):  
Prof. Dr. Nelson J. Batistela  
Prof. Dr. Frédéric Wurtz  
Coorientador:  
Prof. Dr. Patrick Kuo-Peng

Florianópolis, Junho de 2015.



Ficha de identificação da obra elaborada pelo autor,  
através do Programa de Geração Automática da Biblioteca Universitária da UFSC.

Staudt, Tiago  
Brushless Doubly-Fed Reluctance Machine Modeling,  
Design and Optimization / Tiago Staudt ; orientador,  
Nelson Jhoe Batistela ; coorientador, Frédéric Wurtz. -  
Florianópolis, SC, 2015.  
439 p.

Tese (doutorado) - Universidade Federal de Santa  
Catarina, Centro Tecnológico. Programa de Pós-Graduação em  
Engenharia Elétrica.

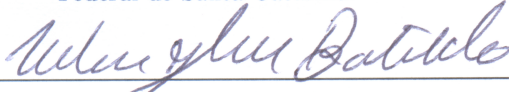
Inclui referências

1. Engenharia Elétrica. 2. Modelagem eletromagnética.  
3. Máquinas de relutância. 4. Otimização de projetos. 5.  
Energia eólica. I. Batistela, Nelson Jhoe . II. Wurtz,  
Frédéric . III. Universidade Federal de Santa Catarina.  
Programa de Pós-Graduação em Engenharia Elétrica. IV. Título.

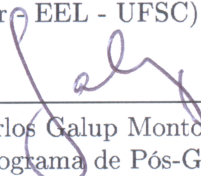


Tiago Staudt  
**BRUSHLESS DOUBLY-FED RELUCTANCE  
MACHINE MODELING, DESIGN AND  
OPTIMIZATION**

Esta Tese foi julgada adequada para a obtenção do título de Doutor em Engenharia Elétrica, Área de Concentração em *Eletromagnetismo e Dispositivos Eletromagnéticos*, e aprovada em sua forma final pelo Programa de Pós-Graduação em Engenharia Elétrica da Universidade Federal de Santa Catarina.



Prof. Dr. Nelson Jhoe Batistela  
(Orientador - EEL - UFSC)



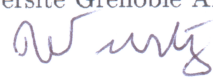
Prof. Dr. Carlos Galup Montoro  
(Coordenador do Programa de Pós-Graduação  
em Engenharia Elétrica)

Banca Examinadora:



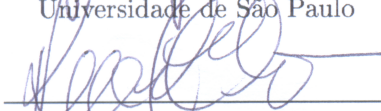
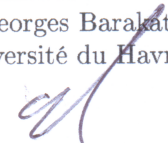
Prof. Nelson Jhoe Batistela, Dr.  
Orientador  
UFSC

Prof. Frédéric Wurtz, Dr.  
Orientador (cotutela)  
Université Grenoble Alpes



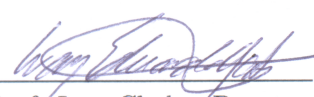
Prof. Silvio Ikuyo Nabeta, Dr.  
Universidade de São Paulo

Prof. Georges Barakat, Dr.  
Université du Havre

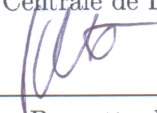


Prof. Renato Carlson, Dr.  
UFSC

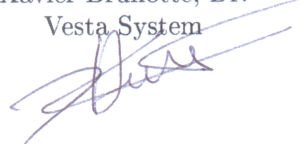
Prof. Laurent Krähenbühl, Dr.  
École Centrale de Lyon



Prof. Ivan Chabu, Dr.  
Universidade de São Paulo



Xavier Brunotte, Dr.  
Vesta System





To my beloved family...

## Acknowledgements

I would like to sincerely thank...

my lovely wife Fran, who shared with me some outstanding experiences during this doctoral period. This time has been amazing, unforgettable and probably the best so far in my life and I am specially thankful for sharing it with you. Thank you for supporting me in the hard times and, most importantly, for being at my side at the great moments.

my family, since this experience as doctoral student would not have been the same without the unconditional support from them. I am specially grateful to my parents Darcisio and Sirlei, my “stepparents” Rolf and Karin, Tati, Luanitts,... thank you for your love, patience and support.

my thesis committee including Professor Silvio Nabeta, Professor Georges Barakat, Professor Renato Carlson, Professor Ivan Chabu, Professor Laurent Krähenbühl, Dr. Xavier Brunotte.

my advisors Professor Frédéric Wurtz, Professor Nelson Jhoe Batis-tela and Professor Patrick Kuo-Peng, for their enthusiasm, competence and technical and personal support during this period.

Professor Laurent Gerbaud, for his motivation, technical knowledge and availability for technically guiding me during my stay in Grenoble. It has been a pleasure to work with you.

all my friends in Grenoble that have contribute to make my doctoral period an unforgettable experience. I have truly enjoyed this time and a great part was because of you. I specially thank Rodrigo, Dyenny, William, Douglas, Angelica, Diego, Lucas, Guilherme, Paula, Vinicius, Juliana, Marcelo, Thiago, Poliana, Lyes, Vincent F., Jonathan, Savana, Vincent R., Lisa, Adrien, Hussein, Laura, Pauline, Yohann, and all my colleagues at G2ELAB.

all my friends in Florianopolis, who have made the path easier to track. My very special thanks to Mauricio, Lidi, Marconi, Fabio, Simone, Ricardo, Helton, Conrado, Leo, Furlan and to all my colleagues, staff and professors from GRUCAD.

and finally, for the international cooperation established in this thesis, I would like to thank the LIA-MAXWELL partnership. For the financial support, I would like to thank CNPq, CAPES and the Region Rhône Alpes.



Resumo da Tese apresentada à UFSC como parte dos requisitos necessários para obtenção do grau de Doutor em Engenharia Elétrica.

## **MODELAGEM, PROJETO E OTIMIZAÇÃO DE MÁQUINAS DE RELUTÂNCIA DUPLAMENTE ALIMENTADAS SEM ESCOVAS**

**Tiago Staudt**

Junho/2015

Orientador: Prof. Dr. Nelson Jhoe Batistela

Orientador: Prof. Dr. Frédéric Wurtz

Coorientador: Patrick Kuo-Peng, Dr.

Área de Concentração: Eletromagnetismo e Dispositivos Eletromagnéticos

Palavras-chave: Modelagem eletromagnética, máquinas sem escovas, máquinas de relutância, modelagem analítica, otimização de projetos, energia eólica.

Número de Páginas: 439

Esta tese aborda a modelagem, o projeto e a otimização, com validação experimental, de máquinas de relutância duplamente alimentadas sem escovas (BDFRM) para sistemas de geração de energia eólica. O objetivo principal dela é de contribuir para o domínio de técnicas de projeto otimizado para a BDFRM através da proposição de uma metodologia baseada em diferentes níveis de modelagem e em otimização. Discute-se como técnicas de otimização podem ser aplicadas em todas as fases de desenvolvimento com objetivos distintos. Especificamente, a metodologia proposta se concentra na definição e na solução iterativa de problemas de otimização com restrições nas saídas utilizando um algoritmo determinístico acoplado a modelos semi-analíticos de diferentes níveis. Como conclusão geral, pode-se afirmar que a BDFRM é potencialmente uma boa candidata para ser utilizada em sistemas de geração de energia eólica. Contudo, aspectos técnicos e econômicos sobre essa escolha devem ainda ser avaliados, comparando-se as diferentes topologias existentes sob o mesmo enfoque metodológico.

Abstract of Thesis presented to UFSC as a partial fulfillment of the requirements for the degree of Doctor in Electrical Engineering.

## **BRUSHLESS DOUBLY-FED RELUCTANCE MACHINE MODELING, DESIGN AND OPTIMIZATION**

**Tiago Staudt**

Junho/2015

Advisor: Nelson Jhoe Batistela, Dr.

Advisor: Frédéric Wurtz, Dr.

Co-advisor: Patrick Kuo-Peng, Dr.

Area of Concentration: Electromagnetism and Electromagnetic Devices

Key words: Electromagnetic modeling; brushless machines; reluctance machines; analytical modeling; design optimization; wind energy.

Number of Pages: 439

This thesis addresses the modeling, design and optimization with experimental validation of the Brushless Doubly-Fed Reluctance Machine (BDFRM) for wind power systems. Its main goal is to contribute on mastering the BDFRM optimized design by proposing a methodological approach based on different modeling levels and on optimization. More precisely, it draws its attention on setting the optimization problem and on the iterative solution of a constrained inputs/outputs problem by using a deterministic algorithm. As a general conclusion, the results show that the BDFRM is potentially a good candidate to be used in wind power systems. However, the technical and economic aspects on this choice must be still assessed, analyzing and comparing the overall system solution of distinct topologies within the same framework.

# Contents

<b>Front page</b>	<b>ii</b>
<b>Table of Contents</b>	<b>xxii</b>
<b>List of Symbols</b>	<b>xxiii</b>
<b>General Introduction</b>	<b>1</b>
<b>1 State of the Art, Electrical Generator Choice &amp; Thesis Proposal</b>	<b>5</b>
1.1 A literature review on wind power systems: market trends, technologies and the choice of a reluctance generator . . .	6
1.1.1 Origins of wind power generation . . . . .	6
1.1.2 Economical aspects on wind power generation: onshore and offshore parks . . . . .	6
1.1.3 Wind power market potentials . . . . .	7
1.1.4 Wind power technological trends discussion . . .	11
1.1.5 Grid code technical requirements for large wind farms . . . . .	12
1.1.6 Overview of existing topologies and electrical machines for wind energy generation and the choice of a reluctance type . . . . .	14
1.1.7 The different reluctance machine concepts for wind power application and the choice of the Brushless Doubly Fed Reluctance Machine . . . . .	19
1.2 The Brushless Doubly Fed Reluctance Machine (BDFRM)	25
1.2.1 Historical Background . . . . .	25
1.2.2 Electromagnetic operating principles . . . . .	28
1.2.3 The advantageous characteristics of the BDFRM	36

1.2.4	The difficulties on the modeling and design of the BDFRM . . . . .	39
1.3	The bottlenecks on the definition of the BDFRM as a viable solution for wind power . . . . .	42
1.3.1	Bottleneck 1: to master BDFRM optimized design	43
1.3.2	Bottleneck 2: to assess the advantages and drawbacks of the BDFRM with respect to other solutions in wind power comparing the system solution as a whole . . . . .	43
1.3.3	Definition of the thesis objective: contributions to develop a design procedure to overcome bottleneck 1 . . . . .	43
1.4	The need of models and optimization approaches . . . . .	44
1.4.1	The design process . . . . .	44
1.4.2	The need of different modeling levels: analytical, semi-analytical and numerical models . . . . .	44
1.4.3	The need of optimization . . . . .	47
1.5	Thesis Proposal: BDFRM modeling for sizing by using optimization to address the bottleneck 1 . . . . .	52
1.5.1	Definition of the proposed BDFRM design procedure . . . . .	52
1.5.2	Specific objectives and main contributions of this thesis . . . . .	56
1.6	Final considerations . . . . .	58
<b>2</b>	<b>Definition of the structural topology of the BDFRM to be investigated</b>	<b>59</b>
2.1	Rotor topology . . . . .	59
2.1.1	The choice of the radially laminated ducted rotor (RLDR) to be used in the BDFRM . . . . .	59
2.1.2	The use of iron bridges (ribs) for mechanical robustness . . . . .	60
2.2	Pre-design definitions . . . . .	61
2.2.1	Discussion on the criteria for choosing the number of poles of grid and control windings and consequently the rotor number of poles . . . . .	61
2.2.2	The choice of the number of stator and rotor slots	65
2.3	Stator topology . . . . .	67
2.3.1	Stator laminations . . . . .	67
2.3.2	Criteria to select the grid as the winding with the highest number of poles . . . . .	68

2.3.3	Grid winding (8 poles) definition . . . . .	68
2.3.4	Control winding (4 poles) definition . . . . .	69
2.4	Topological structure of the machine to be investigated .	71
2.4.1	Resume of the fixed parameters for the investigated machine . . . . .	71
2.4.2	The chosen topology . . . . .	71
2.4.3	The chosen power level . . . . .	72
2.5	Final considerations . . . . .	72
<b>3</b>	<b>BDFRM Semi-Analytical Model (SAM)</b>	<b>73</b>
3.1	Basic principles and requirements to obtain an Equivalent Electric Circuit (EEC) . . . . .	73
3.1.1	Electromagnetic principles . . . . .	73
3.1.2	Hypothesis . . . . .	74
3.1.3	Outputs definition . . . . .	74
3.1.4	Model Structure: definition of the three sub-models	76
3.2	Sub-model 1: equivalent electric circuit to determine phase voltages . . . . .	76
3.2.1	General voltage equations describing the electromagnetic behavior of the BDFRM . . . . .	77
3.2.2	Self and mutual flux linkages and inductances calculation . . . . .	78
3.2.3	Instantaneous flux linkage per phase . . . . .	85
3.2.4	Instantaneous voltage equations per phase . . . . .	86
3.2.5	Equivalent steady-state voltage equations in phasor form . . . . .	87
3.2.6	Definition of the BDFRM equivalent electrical circuit . . . . .	87
3.3	Sub-model 2: power and torque calculation by using the EEC results . . . . .	88
3.3.1	Real power . . . . .	88
3.3.2	Electromagnetic Torque in steady-state . . . . .	89
3.4	Sub-model 3: air-gap flux density calculation to estimate induction levels in stator teeth, stator yoke and rotor flux paths . . . . .	89
3.4.1	Hypotheses to estimate flux densities . . . . .	90
3.4.2	Air-gap flux density calculation considering all the six phases excited . . . . .	91
3.4.3	Nomenclature definition for the calculation of flux densities in several parts around the machine . . . . .	92
3.4.4	Flux density in stator teeth . . . . .	93

3.4.5	Flux density in stator yokes . . . . .	94
3.4.6	Flux density in rotor flux paths . . . . .	94
3.5	Final Considerations . . . . .	95
<b>4</b>	<b>BDFRM Multi-Static Reluctance Network Model (MSRN)</b>	<b>97</b>
4.1	Basic principles and requirements to obtain a multi-static reluctance network (MSRN) model . . . . .	98
4.1.1	General characteristics of the MSRN model . . . . .	98
4.1.2	Electromagnetic principles on modeling by using reluctance networks . . . . .	98
4.1.3	Hypothesis . . . . .	101
4.1.4	Outputs definition . . . . .	102
4.1.5	The need of the voltages as a function of time . . . . .	103
4.1.6	Other performance parameters as a function of time . . . . .	104
4.1.7	MSRN model structure: static and multi-static reluctance networks for taking into account rotor movement and MMF variation in terms of time . . . . .	104
4.2	Sub-model 1: Static Reluctance Network (SRN) . . . . .	105
4.2.1	Reluctance network for one stator tooth . . . . .	106
4.2.2	Reluctance network for one rotor pole . . . . .	108
4.2.3	Air-gap modeling: the choice of the Fourier series to parametrize the reluctances as a function of rotor position . . . . .	110
4.3	Sub-model 2: Air-gap/Source Rotation Model (AGSRM)	117
4.3.1	Different approaches to take into account multi-static calculations and the proposed method used in this thesis . . . . .	117
4.3.2	AGSRM model - Part 1: magnetomotive sources modeling: assessing the equivalent one for each stator tooth to take into account rotor movement	122
4.3.3	AGSRM model - Part 2: reluctance network topology of the air-gap . . . . .	133
4.4	The resulting static reluctance network . . . . .	135
4.5	Outputs calculation . . . . .	137
4.5.1	MSRN model: flowchart of the outputs . . . . .	137
4.5.2	Electromagnetic torque . . . . .	139
4.5.3	Phase Flux linkage . . . . .	140
4.5.4	Induced phase voltage $E$ . . . . .	144
4.5.5	Terminal phase voltage $V$ . . . . .	145
4.5.6	Real power . . . . .	146

4.5.7	Maximum flux density levels in the steel . . . . .	146
4.6	Final Considerations . . . . .	148
<b>5</b>	<b>BDFRM Additional Sizing Equations (ASE)</b>	<b>149</b>
5.1	Definition of the Additional Sizing Equation (ASE) and their role on the global sizing and optimization models .	149
5.2	Preprocessing ASE . . . . .	151
5.2.1	Geometrical parameters defining machine structural topology . . . . .	151
5.2.2	Electrical parameters . . . . .	152
5.2.3	Specific electric loading and current density . . .	153
5.2.4	Duct ratio . . . . .	154
5.2.5	Carter's factor . . . . .	154
5.2.6	Leakage inductances . . . . .	155
5.2.7	Total active mass and volume . . . . .	155
5.3	Post-processing ASE . . . . .	155
5.3.1	Losses calculation . . . . .	155
5.3.2	Apparent Power . . . . .	157
5.3.3	Efficiency . . . . .	158
5.4	Final Considerations . . . . .	159
<b>6</b>	<b>Implementation of the optimization-oriented models</b>	<b>161</b>
6.1	Objectives and requirements for coupling the models with the SQP optimization algorithm . . . . .	161
6.2	Dedicated optimization software tools . . . . .	162
6.2.1	CADES Framework . . . . .	163
6.2.2	Reluctool - a Computer Aid Design software for building semi-analytical models based on the reluctance network approach . . . . .	165
6.3	SAM-based Global Sizing and Optimization Model (GSOM-SAM) implementation in CADES . . . . .	166
6.4	MSRN-based Global Sizing and Optimization Model (GSOM-MSRN) implementation in CADES . . . . .	168
6.4.1	GSOM-MSRN overview . . . . .	168
6.4.2	Static Reluctance Network (SRN) topology implementation . . . . .	169
6.4.3	Limitations of the software tools: the need of manual derivation of the gradient . . . . .	170
6.4.4	Proposed solution . . . . .	170
6.4.5	The MSRN software component implemented in the external Java function (EJF) . . . . .	170

6.4.6	Coupling the MSRN software component to CADES to form the GSOM-MSRN . . . . .	173
6.5	Final considerations . . . . .	174
<b>7</b>	<b>Simulation results</b>	<b>175</b>
7.1	Reference machine definition to verify the models . . . .	175
7.1.1	Geometrical and rated performance parameters .	175
7.1.2	Nomenclature definition . . . . .	177
7.1.3	Impact of the iron ribs on machine performance .	179
7.2	Verifying the GSOM-SAM by comparing its results to the reference FEA model . . . . .	180
7.2.1	Considered performance parameters . . . . .	180
7.2.2	Air-gap flux density versus $\theta_{ag}$ at rated conditions	180
7.2.3	Inductances . . . . .	181
7.2.4	Induced voltages $e_{ga}$ and $e_{ca}$ . . . . .	182
7.2.5	Induced average electromagnetic torque . . . . .	184
7.2.6	Conclusions about the GSOM-SAM . . . . .	185
7.3	Verifying the GSOM-MSRN by comparing its results to the reference FEA model . . . . .	185
7.3.1	Considered performance parameters . . . . .	185
7.3.2	Air-gap flux density versus $\theta_{ag}$ at rated conditions	186
7.3.3	Mutual inductance between grid and control windings . . . . .	186
7.3.4	Induced voltages $e_{ga}$ and $e_{ca}$ . . . . .	187
7.3.5	Electromagnetic torque . . . . .	188
7.3.6	Conclusions about the GSOM-MSRN . . . . .	189
7.4	Simulation time comparison . . . . .	190
7.4.1	Considerations . . . . .	190
7.4.2	Computation time results . . . . .	190
7.5	Final Considerations . . . . .	191
<b>8</b>	<b>BDFRM prototype: design, realization and experimental results used to verify the models</b>	<b>193</b>
8.1	BDFRM prototype design and realization by using an optimization approach . . . . .	194
8.1.1	Prototype specification by using the GSOM-SAM	194
8.1.2	Characteristics of the GSOM-SAM used to specify the prototype: objective function and constraints . . . . .	194
8.1.3	Variable inputs . . . . .	195
8.1.4	Constrained outputs . . . . .	196



8.1.5	Objective function and the resulting machine used on the validations . . . . .	198
8.1.6	Prototype specification . . . . .	198
8.2	Experimental results obtained from the prototype . . . . .	200
8.2.1	Preliminary considerations to present the experimental results . . . . .	200
8.2.2	Mutual inductance test setup . . . . .	201
8.2.3	Voltage measured at control side, 500 rpm, $I_{ga_{DC}}$ excitation . . . . .	202
8.2.4	Mutual inductance between the winding sets . . . . .	203
8.2.5	Open-circuit induced RMS voltage in grid and control sides due to a DC excitation at the respective opposite side at 500 rpm . . . . .	207
8.3	Confronting the experimental and simulation results . . . . .	209
8.3.1	Nomenclature . . . . .	209
8.3.2	Mutual inductances . . . . .	209
8.3.3	Open-circuit induced RMS voltage due to a single phase DC excitation . . . . .	210
8.3.4	Instantaneous open-circuit induced voltages at control and grid windings due to a 3-phase excitation . . . . .	211
8.3.5	Open-circuit induced RMS voltages at control and grid windings as a function of the excitation currents . . . . .	213
8.4	Discussions on the experimental and simulation results . . . . .	214
8.4.1	Preliminary conclusions . . . . .	214
8.4.2	Hypothesis investigation for the differences found between the models and the prototype results . . . . .	215
8.5	Final considerations . . . . .	228
<b>9</b>	<b>BDFRM design by using the proposed optimization procedure: a case study</b> . . . . .	<b>229</b>
9.1	Wind energy system overview: system topology . . . . .	230
9.2	Wind turbine . . . . .	230
9.2.1	Turbine power coefficient ( $C_p$ ) and tip-speed ratio ( $\lambda$ ) . . . . .	230
9.2.2	The choice of the wind turbine: main characteristics . . . . .	231
9.2.3	Maximum Power Point Tracking (MPPT) curve for the chosen turbine . . . . .	233

9.3	The BDFRM design procedure: constraints and operating points definition . . . . .	234
9.3.1	Three modeling levels: GSOM-SAM, GSOM-MSRN and FEA . . . . .	234
9.3.2	Pre-design . . . . .	234
9.3.3	General optimization constraints . . . . .	238
9.3.4	The use of the Pareto front strategy to assess contradictory objectives . . . . .	239
9.4	The use of GSOM-SAM in early design stages to define a “first-cut” design . . . . .	240
9.4.1	GSOM-SAM optimization results: Pareto front to identify the best trade-off between total active mass and efficiency at rated conditions . . . . .	240
9.4.2	The chosen “first-cut” machine design using the GSOM-SAM to be further explored . . . . .	242
9.5	Refining the design: GSOM-MSRN to obtain accurate results whereas using deterministic optimization . . . . .	243
9.5.1	GSOM-MSRN optimization results: Pareto front to identify the best trade-off between total active mass and efficiency at rated conditions . . . . .	243
9.5.2	GSOM-MSRN optimization results: Pareto front to identify the best trade-off between total active mass and efficiency for the three operating points solved simultaneously . . . . .	245
9.6	Verifying optimization results with the reference model: finite element analysis (FEA) . . . . .	248
9.6.1	Air-gap flux density . . . . .	249
9.6.2	Phase voltages at rated conditions . . . . .	249
9.6.3	Instantaneous torque at rated conditions . . . . .	250
9.7	Simulation time comparisons among the three modeling levels . . . . .	250
9.8	Final Considerations . . . . .	252

<b>General Conclusion and Perspectives</b>	<b>255</b>
General Conclusions . . . . .	255
Perspectives . . . . .	259

<b>Bibliography</b>	<b>279</b>
---------------------	------------

<b>Appendixes</b>	<b>279</b>
-------------------	------------

<b>A Winding Function Theory</b>	<b>281</b>
----------------------------------	------------

A.1 Introduction . . . . .	281
A.2 Distributed windings . . . . .	282
A.3 Winding Function . . . . .	284
A.4 Magnetomotive force . . . . .	284
A.5 Flux linkage and inductances . . . . .	284

<b>B Implementation of a gradient-based reluctance network</b>	<b>287</b>
--	------------

B.1 Gradient-Based Reluctance Network: optimization by deterministic algorithms . . . . .	287
B.1.1 Introduction . . . . .	287
B.1.2 Gradient-based reluctance network implementation: the use of the implicit equation theorem . . . . .	288
B.2 Implementation of the Fourier series used to calculate the air-gap reluctance widths . . . . .	289
B.3 MSRN Jacobian matrix calculation . . . . .	290
B.3.1 Updating the SRN Jacobian matrix obtained from Reluctool . . . . .	292
B.3.2 Calculation of the MSRN output partial derivatives	296
B.4 Graph theory definitions . . . . .	304
B.5 Definition of the coil vectors to calculate the phase flux linkage in the MSRN model . . . . .	305

<b>C Analytical calculation of the flux density in air-gap, leakage inductances and effective air-gap</b>	<b>309</b>
---	------------

C.1 Air-gap flux density calculation for a radially laminated ducted rotor . . . . .	309
C.2 Strategy to evaluate coupling effectiveness among different number of poles possibilities . . . . .	311
C.3 Leakage inductances . . . . .	314
C.3.1 Estimation of the leakage inductances per phase for the SAM . . . . .	314
C.3.2 Equivalent reluctance to take into account the stator slot leakage flux for the MSRN model . . . . .	316
C.4 Carter's Factor . . . . .	319

<b>D</b>	<b>BDFRM prototype characteristics: reference machine used for model comparisons</b>	<b>321</b>
D.1	Main characteristics and rated parameters . . . . .	321
<b>E</b>	<b>Optimization constraints for the case study</b>	<b>323</b>
E.1	GSOM-SAM constraints for the case study . . . . .	323
E.1.1	Variable inputs . . . . .	323
E.1.2	Constrained outputs . . . . .	326
E.1.3	The chosen “first-cut” machine design using the GSOM-SAM to be further explored . . . . .	328
E.2	GSOM-MSRN machine for the case study: the chosen one at rated conditions at 750 rpm . . . . .	329
E.3	GSOM-MSRN optimization results at the 3 OP: the chosen final design . . . . .	331
<b>F</b>	<b>Different approaches and comparison for modeling the MMF sources</b>	<b>333</b>
F.1	Analysis of different methods to calculate the MMF sources	333
F.1.1	Parameters used in the simulation . . . . .	334
F.1.2	Modeling the magnetomotive force . . . . .	334
F.1.3	Comparisons of the MMF source modeling . . .	335
F.1.4	Definition of the MMF sources modeling approach to be implemented in the MSRN . . . . .	340
F.2	Analytical solution of equation (4.27) to calculate the winding functions for each phase using the “harm” method introduced in Section 4.3.2.3 . . . . .	341
F.3	Analytical solution of the magnetomotive forces for grid and control windings using the “harm” method introduced in Section 4.3.2.3 . . . . .	344
<b>G</b>	<b>Semi-Analytical Model Spreadsheet in Mathcad ®</b>	<b>349</b>
G.1	Global Sizing and Optimization Model by using the Semi-Analytical Model . . . . .	349

# List of Symbols

## Acronyms

AGSRM	Air-gap Source Rotation Model
ALR	Axially Laminated Rotor
ASE	Additional Sizing Equations
BDFIM	Brushless Doubly-Fed Induction Machine
BDFM	Brushless Doubly-Fed Machines
BDFRM	Brushless Doubly-Fed Reluctance Machine
CADES	Component Architecture for the Design of Engineering Systems
DEBRM	Doubly Excited Brushless Reluctance Machine
DFIG	Doubly-Fed Induction Generator
DRI	Ideal Ducted Rotor
DRNI	Not Ideal Ducted Rotor
DWRG	Dual Winding Reluctance Generator
ECC	Equivalent Electric Circuit
EJF	External Java Function
FEA	Finite Element Analysis
fob	Objective function
FRT	Fault-Ride Through

FSM	Fourier Series Method
GEMM	Global Electromagnetic Model
GSOM	Global Sizing and Optimization Model
GWEO	Global Wind Energy Outlook
LI	Linear
LVRT	Low Voltage Ride Through
MMF	Magnetomotive force
MPPT	Maximum Power Point Tracking
MSRN	Multi-Static Reluctance Network
NL	Nonlinear
PMSG	Permanent Magnet Synchronous Generator
PM	Permanent Magnets
PROT	Prototype
RLDR	Radially Laminated Ducted Rotor
RN	Reluctance Network
SAM	Semi-Analytical Model
SCIG	Squirrel Cage Induction Generator
SPR	Salient Pole Rotor
SQP	Sequential Quadratic Programming
SRM	Straight Teeth Method
SRM	Switched Reluctance Machine
SRN	Static Reluctance Network
SyncRM	Synchronous Reluctance Machine
TSO	Transmission System Operators

## **Symbols**

$\alpha$	Hysteresis coefficient (expoent)
$\alpha_c$	Phase difference between the two windings sets [rad]
$\alpha_{rho}$	coefficient representing the evolution of the resistivity in terms of the temperature [1/°C]
$\beta$	Normalized air-gap function
$\epsilon$	Electrical Permittivity [F/m]
$\epsilon_0$	Electrical Permittivity of free space: $8,854 \cdot 10^{-12}$ [F/m]
$\eta$	Efficiency
$\gamma_1$	Electrical angle related to the rotor initial position $\gamma_1 = P_r \theta_{rm0}$ [rad]
$\gamma_{rc}$	$\gamma_{rc} = \gamma_1$ [rad]
$\gamma_{rg}$	Equivalent electric circuit angle $\gamma_{rg} = 2\alpha_c + \gamma_{rc}$ [rad]
$\lambda$	Flux linkage [Wb]
$\lambda$	Tip-speed ratio
$\lambda_{c,abc}$	Phase flux linkage from control winding [Wb]
$\lambda_{coils_x}$	Flux linkage of a coil from phase $x$ [Wb]
$\lambda_{g,abc}$	Phase flux linkage from grid winding [Wb]

$\mathbb{F}_c$	Three-phase magnetomotive force contribution from control winding [A – turns]
$\mathbb{F}_g$	Three-phase magnetomotive force contribution from grid winding [A – turns]
$\mathbb{F}_t$	Three-phase total magnetomotive force [A – turns]
$\mathbb{F}_{3\phi c}$	Three-phase magnetomotive force of control winding [A – turns]
$\mathbb{F}_{3\phi g}$	Three-phase magnetomotive force of grid winding [A – turns]
$\mathbb{F}_{3\phi total}$	Total three-phase magnetomotive force [A – turns]
$\mu$	Magnetic permeability [H/m]
$\mu_0$	Vacuum magnetic permeability: $4 \pi 10^{-7}$ [H/m]
$\omega_c$	Angular frequency of control winding [rad/s]
$\omega_{gen}$	Generator angular speed [rad/s]
$\omega_g$	Angular frequency of grid winding [rad/s]
$\omega_{rm}$	rotor angular mechanical speed [rad/s]
$\omega_{sync}$	Synchronous angular speed [rad/s]
$\omega_{turb}$	Wind turbine angular speed [rad/s]
$\bar{E}_{ca}$	Voltage phasor of ca [V]



$\bar{E}_{ga}$	Voltage phasor of ga [V]
$\bar{I}_{ca}$	current phasor of ca [A]
$\bar{I}_{ga}$	current phasor of ga [A]
$\bar{V}_{ga}$	Voltage phasor of ca [V]
$\bar{V}_{ga}$	Voltage phasor of ga [V]
$\phi$	magnetic flux [Wb]
$\phi_{ca}$	reference position of control winding [rad]
$\phi_{ga}$	reference position of grid winding [rad]
$\phi_{th}$	Magnetic flux circulating through a stator tooth [Wb]
$\phi_{Torque}$	Torque angle [rad]
$\phi_x$	Magnetic flux passing through phase $x$ [Wb]
$\phi_{ys,1}$	Center of the stator slot number 1 [rad]
$\phi_{ys,i}$	Center of the $i$ 'th stator slot (angle) [rad]
$\psi_{st}$	arc between any two adjacent stator teeth [rad]
$\mathfrak{R}_{air}$	Air reluctances [A - turns/Wb]
$\mathfrak{R}_{gap_n}$	Aig-gap reluctance [A - turns/Wb]

$\rho_{air}$	air density [ $kg/m^3$ ]
$\rho_{copper}$	copper resistivity [ $\Omega m$ ]
$\sigma$	Electrical conductivity [ $S/m$ ]
$\theta_{ag}$	mechanical angle around the air-gap [ $rad$ ]
$\theta_{ag}^{DR}$	angle around the machine air-gap periphery corresponding to the other extremity of the flux path starting at position $\theta_{ag}$ [ $rad$ ]
$\theta_{mmf}$	Angle used to rotate the MMF sources $rad$
$\theta_{rm0}$	Rotor initial position at $t = 0s$ [ $rad$ ]
$\theta_{rm_{mod}}$	Angle derived from $\theta_{rm}$ using the modulo function with period $\psi_{st}$ $rad$
$\theta_{rm}$	rotor mechanical angle [ $rad$ ]
$\vec{B}$	Magnetic Induction [ $T$ ]
$\vec{D}$	Electric Induction [ $C/m^2$ ]
$\vec{E}$	Electric Field [ $V/m$ ]
$\vec{H}$	Magnetic Field [ $A/m$ ]
$\vec{J}$	Current density [ $A/m^2$ ]
$\xi$	Parameter used to control the pulse wave width (Fourier series method)

$A$	Swept area of the wind turbine blades [ $m^2$ ]
$A_{sel_x}$	Specific electrical loading (linear current density) [ $A/m$ ]
$B_{gap}$	Air-gap flux density [ $T$ ]
$B_{round}^{pk}$	amplitude of the air-gap flux density function that one would obtain if a solid (round) rotor were used [ $T$ ]
$B_{rt}$ or $B_{fb}$	Induction levels in rotor teeth (flux paths) [ $T$ ]
$B_{th}$	Induction levels in stator teeth [ $T$ ]
$B_{yk}$	Induction levels in stator yoke [ $T$ ]
$C_p$	Wind turbine power coefficient
$ca$	Phase $A$ of control winding
$cb$	Phase $B$ of control winding
$cc$	Phase $C$ of control winding
$Der$	Rotor external diameter [ $mm$ ]
$Des$	Stator external diameter [ $mm$ ]
$Dir$	Rotor internal diameter [ $mm$ ]
$Dis$	Stator internal diameter [ $mm$ ]

$DR$	Duct Ratio
$DutyC_r$	duty cycle of the rotor waveform
$DutyC_s$	duty cycle of the stator waveform
$E_{ca_{rms}}$	Internal induced rms phase voltage ( $ca$ ) [V]
$E_{ga_{rms}}$	Internal induced rms phase voltage ( $ga$ ) [V]
$E_{x_{rms}}$	Internal induced rms phase voltage [V]
$EqWidth_n$	Equivalent air-gap reluctance width [mm]
$f_c$	Control winding frequency [Hz]
$f_g$	Grid winding frequency [Hz]
$f_{op}$	Operating frequency [Hz]
$f_{test}$	Test frequency [Hz]
$g^{-1}$	Inverse air-gap function
$ga$	Phase A of grid winding
$gap$	Air-gap length [mm]
$gap_{ef}$	effective air-gap length, compensated by using the Carter's coefficient [mm]

$gb$	Phase $B$ of grid winding
$gc$	Phase $C$ of grid winding
$i_{c,abc}$	Instantaneous phase currents from control winding [A]
$I_c$	Current peak value in control winding [A]
$i_{g,abc}$	Instantaneous phase currents from grid winding [A]
$I_g$	Current peak value in grid winding [A]
$I_{x_{rms}}$	RMS value of the phase currents [A]
$J_x$	Current density [A/mm <sup>2</sup> ]
$K$	The number of multi-static calculation that are performed
$k$	Index used to refer to each one of the $K$ multi-static calculations
$k_e$	Excess losses coefficient
$k_f$	Eddy currents coefficient
$k_h$	Hysteresis coefficient (multiplying factor)
$k_{d_x}$	Distribution factor of phase $x$
$K_{p_x}$	Short-pitching factor of phase $x$
$K_{w_x}$	Winding factor of phase $x$

$K_{wc}$	Winding factor of control winding
$K_{wg}$	Winding factor of grid winding
$L_{c,abc}$	Self and mutual inductance matrix of control winding [H]
$L_{cm}$	Control winding self inductance [H]
$L_c$	Three phase self inductance of control winding (obtained when all 6-phases are excited) [H]
$L_{g,abc}$	Self and mutual inductance matrix of grid winding [H]
$L_{gc,abc}$	Matrix of the mutual inductance between the windings [H]
$L_{gcm\max}$	Mutual inductance between the winding sets [H]
$L_{gc}$	Mutual inductance between the winding sets ( $= 3/2 \times L_{gcm\max}$ ) [H]
$L_{gm}$	Grid winding self inductance [H]
$L_g$	Three phase self inductance of grid winding (obtained when all 6-phases are excited) [H]
$L_{lc}$	Phase leakage inductance of control winding [H]
$L_{lg}$	Phase leakage inductance of grid winding [H]
$L_{stkef}$	Effective machine axial length [mm]
$Loss_{Rx}$	Copper losses in phase $x$ [W]

$m$	Number of phases
$M_{3c}$	amplitude of the fundamental magnetomotive force from control winding [A – turns]
$M_{3g}$	amplitude of the fundamental magnetomotive force from grid winding [A – turns]
$Mass$	Active mass [Kg]
$N_{fourier}$	number of Fourier terms used to truncate the series
$N_{mmf}$	Integer number that indicates how many times the sources must be rotated of an angle $\psi_{st}$
$N_{slc}$	number of turns per slot (control)
$N_{slg}$	number of turns per slot (grid)
$N_{str}$	
$N_{sl}$	Number of slots
$N_{tp_x}$	Number of turns per pole
$N_{phc}$	Total number of turns per phase of control winding
$N_{phg}$	Total number of turns per phase of grid winding
$P$	Real power [W]
$P_{3\phi_{cint}}$	Three-phase real power from control winding [W]

$P_{3\phi g_{int}}$	Three-phase real power from grid winding [W]
$P_{act_x_{int}}$	Internal active power per phase (calculated from $E_x$ ) [W]
$P_{act_x_{ter}}$	Terminal active power per phase (calculated from $V_x$ ) [W]
$P_{ca_{int}}$	Internal real power per phase (calculated from $E_{ca}$ ) [W]
$P_{ca_{ter}}$	Terminal real power per phase (calculated from $V_{ca}$ ) [W]
$P_c$	Number of poles of control winding
$P_{ga_{int}}$	Internal real power per phase (calculated from $E_{ga}$ ) [W]
$P_{ga_{ter}}$	Terminal real power per phase (calculated from $V_{ga}$ ) [W]
$P_g$	Number of poles of grid winding
$P_r$	Rotor number of poles
$P_{turbine}$	Wind turbine power output [W]
$PF$	Power factor
$Q$	Reactive power [Var]
$q$	number of slots per pole per phase
$R$	Radius to tip of wind turbine rotor [m]
$R_c$	Control winding phase resistance [ $\Omega$ ]



$r_{gap}$	Air-gap radius
$r_{gap}$	air-gap radius [mm]
$R_g$	Grid winding phase resistance [ $\Omega$ ]
$S$	Apparent power [VA]
$s$	slip
$slop$	Slot opening [mm]
$SlrWidth$	width of rotor duct (slot) [mm]
$Sslot$	available area at each slot [mm <sup>2</sup> ]
$T_r$	“Period” of the rotor waveform for the Fourier series method
$T_s$	“Period” of the stator waveform for the Fourier series method
$T_{em_{ave}}$	Average value of the electromagnetic torque [Nm]
$T_{em}$	Electromagnetic torque [Nm]
$ts$	Simulation time [s]
$v_{c,abc}$	Instantaneous phase voltages from control winding [V]
$V_{ca_{rms}}$	Terminal output rms phase voltage ( <i>ca</i> ) [V]
$v_{g,abc}$	Instantaneous phase voltages from grid winding [V]

$V_{ga_{rms}}$	Terminal output rms phase voltage ( $ga$ ) [V]
$V_{mag}$	magnetic scalar potential [A – turns]
$V_{x_{rms}}$	Terminal output rms phase voltage (considers the voltage drop in the phase resistances) [V]
$w$	winding function
$W_{co}$	Total system coenergy [J]
$wapsl$	Total area occupied by the copper wires inside one stator slot [mm <sup>2</sup> ]
$wff$	Winding filling factor
$x$	Refers to the phases (ga, gb, gc, ca, cb, cc)
$ykw$	Yoke width [mm]
$ytr$	Yoke width to stator width ratio [mm]

# General Introduction

This thesis addresses the modeling, design and optimization with experimental validation of an electrical generator for wind power systems.

In the last decades, the growing demand for electrical energy, specially from renewable sources, has been motivating the scientific community to develop new technologies for producing electricity more efficiently, reliably and economically. Solar and wind energy sources are the greatest examples of this trend and especially wind power generation has grown significantly in recent years.

The ever growing concern on environmental issues is one of the main factors that stimulate this tendency, targeting to considerably reduce the use of fossil fuels to “generate” electrical energy by replacing sources of this kind by renewable ones. In this context, some aspects that make the wind energy to play a dominant role can be highlighted, among them:

- the huge availability of wind power capacity in nature as a whole, many times higher than the global demand for primary energy;
- the technological maturity of wind energy systems, which allowed it to wide spread around the world in recent years and greatly reduced the generation cost considering this source;

Nevertheless, there are still some questions to be answered regarding wind power generation, one of them is: *what is the best generating system topology to be applied?*

To answer this general question, it is necessary to assess multidisciplinary topics such as electrical generator technology and design, manufacturing process, raw material availability, power electronics technologies, maintenance issues, efficiency, and so on. The list is not exhaustive and, for all of these items, a major factor plays a dominant role: the

overall system cost. Only a systematic study, analyzing the generating system as a whole within the same framework would be capable of answering this question appropriately.

For wind power generating systems, basically two generator technologies, applied to distinct system topologies, compete on variable speed application nowadays: the permanent magnet (PMG) and the doubly-fed induction (DFIG) generators. Both have advantages and drawbacks and there is no ultimate best technology that can be inferred for all kind of applications. The future employability of these distinct technologies are related to their ability of complying with both market expectations and the requirements of grid utility companies [1].

In the last decades, the Doubly-Fed Induction Generator (DFIG) emerged as the most used solution in wind power application [2, 3, 1]. This topology has become widely used in applications where the benefits of limited variable speed operation are required, because it allows the use of a fractionally-rated power converter (around 30% of total system capacity). It also permits a decoupled control of active and reactive power and it has become the preferred alternative mainly due to lower cost of power electronics involved.

On the other hand, the DFIG has some drawbacks. The most important one is the use of brushes and slip rings to connect the wound rotor to the frequency converter. Those elements are a known source of reliability issues, which may cause machine failures and electrical losses [1]. Additionally, the costs associated to both generator manufacturing with brushes and the subsequent regular maintenance are quite high. These issues are among the factors of greatest economic impact on the operation of wind farms, especially offshore [4].

Regarding this thesis, the proposed approach is to identify and study a cost-effective and robust solution for wind power applications by using optimization. As the main guideline, it has been established that the solution shall avoid the use of permanent magnets (PM) and preferably use a fractionally-rated power converter. In this context, an alternative to the DFIG solution that keeps the advantageous features of it and at the same time overcomes the maintenance problems related to the brushes and slip rings seems to be an appropriate choice. *Among the possible solutions, the Brushless Doubly-Fed Reluctance Machine (BDFRM) has been chosen as the electrical generator to be investigated.*

The scientific relevance on the BDFRM research is also evidenced by other authors [5, 6, 7, 8, 9]. Although many works have presented advances along last years, there is still a lack of researches to define a procedure on its electromagnetic design mostly due to its complex

electromagnetic field interaction occasioned by rotor modulation. In [10], it is highlighted the need for design methods dedicated to address application specific requirements in order to define a high performance machine design, whereas in [11] it is stated that most of papers analyses existing design rather than focusing on the development of new designs. According to Schulz *et al.* [12], there is no reason why the BDFRM cannot surpass the performance of the induction machine in many applications if well designed. In general, the BDFRM has similar characteristics to the traditional DFIG solution with the advantage of brushless operation and this places the BDFRM as a strong candidate to play an important role in the future of wind power generation systems [4].

Two bottlenecks can be identified in the literature on the consideration of the BDFRM as a viable solution for variable speed wind power application:

1. to master BDFRM optimized design;
2. to assess the advantages and drawbacks of the BDFRM with respect to other solutions in wind power comparing the system solution as a whole.

The main goal of this thesis is to contribute on bottleneck 1: to master BDFRM optimized design. For that purpose, it focus on the development of a methodological approach for the Brushless Doubly-Fed Reluctance Machine modeling and design by using optimization. A *design procedure* is proposed, which in turns allows to take into account effectively application requirements in the optimization process. It discusses how optimization could be applied in all development stages with distinct objectives to be assessed. More precisely, it draws its attention on setting the optimization problem and on the iterative solution of a constrained inputs/outputs problem by using a deterministic algorithm coupled to analytical-based modeling levels. To that end, models have been developed, verified and validated comparing to both Finite Element Analysis (FEA) and experimental results.

The dissertation is divided in the following manner:

Chapter 1 starts by presenting a literature review on wind power application, analyzing the technological and economical aspects of this kind of generation. The reason for choosing the BDFRM to be further investigated are outlined and the thesis proposal is defined.

Chapter 2 introduces the BDFRM pre-design guidelines and the considerations to choose the topological structure of the machine to

be investigated. Chapter 3, Chapter 4 and Chapter 5 present, respectively, the Semi-Analytical Model (SAM), the Multi-Static Reluctance Network Model (MSRN) and the Additional Sizing Equations (ASE) that constitute the modeling basis of the BDFRM by using analytical and semi-analytical approaches.

Chapter 6 shows how the electromagnetic models have been implemented and coupled to the Sequential Quadratic Programming (SQP) optimization algorithm, whereas Chapter 7 presents a verification of the SAM and MSRN models: their simulation results are compared to the reference Finite Element Analysis (FEA) model.

All these developments allowed to specify a BDFRM prototype by using an optimization approach. This experimental machine has then been conceived and used to further validate the models by confronting the experimental and simulation results. A complete discussion on the BDFRM prototype is presented in Chapter 8. Finally, Chapter 9 illustrates with a case study the design procedure that has been proposed in this thesis. The goal is to define a BDFRM optimized design, starting from the application requirements up to the final machine. A multi-objective optimization has been set up for that purpose, having the total active mass and efficiency as the main objective functions. Each development stage (and the associated modeling level) is assessed individually and a Pareto front strategy has been used to define the optimal machine.

# Chapter 1

## State of the Art, Electrical Generator Choice & Thesis Proposal

### Abstract

*The main objective of this chapter is to define the thesis proposal based on a literature review assessing the use of a reluctance generator on variable speed wind power applications. Firstly, a study on some aspects of wind power generation is presented, discussing its historical development, requirements, market trends and technological state of the art. From this review, the Brushless Doubly Fed Reluctance Machine (BDFRM) is chosen as the generator type that will be further investigated on this research. Its basic electromagnetic operating principles are introduced, highlighting the difficulties that may arise on the modeling and design process of this machine. Then, two major bottlenecks on the use of the BDFRM in wind power application are identified. The strategy to address them is presented and the thesis proposal and the objectives are finally stated.*

## 1.1 A literature review on wind power systems: market trends, technologies and the choice of a reluctance generator

### 1.1.1 Origins of wind power generation

The use of wind power in human history dates back at least 3000 years. Its main application was to convert wind energy into mechanical energy being used nearly up to the beginning of 20th century to pump water or to grind grains [13, 2]. By this time at the beginning of modern industrialization, however, the development of the steam engine and other technologies for converting fossil fuels into useful energy significantly reduced the interest in wind power [14, 13].

Manwell *et al.* [14] point out at least five factors that contributed for the great regained interest in this form of energy from the late 1960s. The first one refers to the need of an alternative energy source, since at that time there was already an emerging awareness of the drawbacks on burning fossil fuels. The second reason was the great potential of wind energy: it is available everywhere on earth and at some regions with a particularly high energy density. The development of new technologies, especially related to the power electronics, revolutionized the way wind power could be extracted and it is mentioned as the third main factor. The remaining two factors refers to the new vision on how the wind power could be explored, technically and commercially, and the political will to make it happen. Government subsidies were necessary to finance research, development and testing of wind turbines, as well as to provide regulatory reform to allow them to be interconnected to electrical network.

### 1.1.2 Economical aspects on wind power generation: onshore and offshore parks

Modern wind turbines can operate in a distributed or clustered way, forming generation parks (or farms). A wind farm is defined as concentrated groups of wind turbines that are connected both electrically and commercially [14]. They are usually classified according to their place of construction as onshore or offshore parks.

Onshore parks are installed on the continent and they are usually designed for operation on higher altitudes to take full advantage of high wind speeds with less turbulence. Problems associated to onshore turbines that may negatively influence on their installation are the acoustic



noise and the greater visual impact depending on where they are built [15].

Offshore parks are located at least 5 *km* away of the coast and may take full advantage of higher average wind speeds. The advantages of this type of facility also include reduced visual and acoustic noise impacts. Their drawbacks are related to the higher costs of construction and operation of offshore wind turbines as well as the unwanted effects of parasitic impedances in the cables due to long distances to connect the farms to the power system [15].

From a commercial point of view, wind farms are an important structure, since geographic regions that enable an economically viable wind generation are somewhat limited. With the concentration of turbines in these areas, it increases the produced power and the financial yield. Another advantage of the concentration of turbines at a specific location is the reduced cost with logistical issues for maintenance and repairs for both onshore and offshore parks [14].

### 1.1.3 Wind power market potentials

The available wind power energy around the world is huge. Marvel *et al.* [16] claim that wind turbines installed on the surface of the Earth could produce about 400 *TW* of power and that number could reach 1800 *TW* if wind energy extraction was done at high altitudes. The energy availability is so great that, according to the authors, the extraction of energy in these rates could even cause impacts on Earth's climate. However, comparing these numbers with the global primary power demand (i.e. considering all energy sources) which is approximately 18 *TW* [17], wind turbines distributed along the surface of the planet would not cause risks. Regardless of the wind capacity installed worldwide, these numbers clearly illustrate the growth potential of this form of electrical power generation in the coming years.

Another important aspect that reinforces the need of investments on renewable energy sources is the greenhouse gas emissions. The power sector is the largest single contributor (around 40 %) of the total CO<sub>2</sub> emissions [18]. Increasing the market penetration of wind energy sources would help to significantly reduce the greenhouse gas emissions due to the burning of fossil fuels to produce electrical energy.

#### 1.1.3.1 Worldwide context

The installation rate of wind power turbines worldwide has experienced fast growing rates over the last years, mainly in Europe, United

States and China. In a recent study, the 2014 edition of the Global Wind Energy Outlook report (GWEO) [18], issued by the Global Wind Energy Council and Greenpeace International, gives an overview of the market potential for wind energy. It indicates that the wind power installed capacity worldwide could increase from 318 *GW* in 2013 up to 2000 *GW* in 2030, representing 17-19 % of global electricity. By 2050, wind power could provide 25-30 % of global electricity supply in the best analyzed scenario. The growth rate of wind power at these levels would certainly have economical, technological and environmental impacts in many regions on earth. Fig. 1.1 highlights the tremendous wind power market possibilities for the next upcoming years considering three scenarios presented in the GWEO <sup>1</sup>.

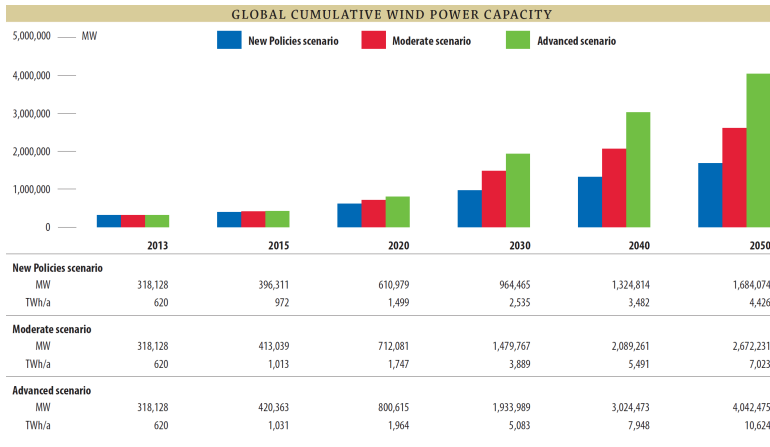


Figure 1.1: Global cumulative wind power capacity. Adapted from the Global Wind Energy Outlook 2014 [18].

<sup>1</sup>The three considered scenarios are: (i) The “New Policies” refers to the “current directions and intentions of both national and international energy and climate policy”, although some of them may not have been transformed already into law. (ii) The “Moderate” one is based on the “New Policies”, but it assumes that “all policy measures to support renewable energy are either already enacted or in the planning stages around the world”. (iii) The “Advanced” considers the most ambitious case and it “outlines the extent to which the wind industry could grow in a best case” assuming an unambiguous political commitment to renewable energy [18].

### 1.1.3.2 Brazilian context

The Brazilian context on wind power generation has particularly motivated this thesis and some insights about it are introduced.

#### 1.1.3.2.1 Latin America Scenario

According to the GWEO [18], Latin America in general is considered as one of the most promising markets for the deployment of wind power, having the Brazil as the leader in wind power installations. This kind of energy could be used as a major factor to supply the growing electricity demand on this region. Fig. 1.2 illustrates the expected scenarios that may occur in the future.

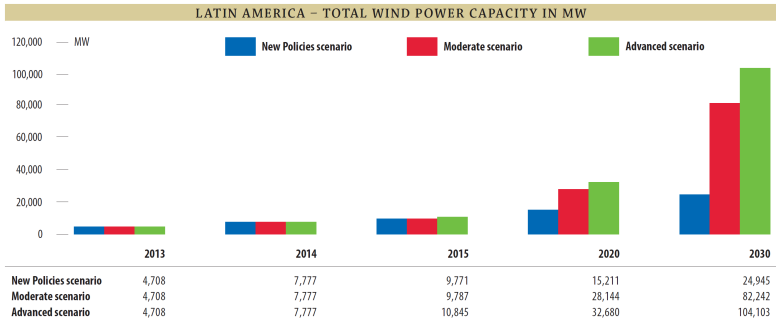


Figure 1.2: Latin America cumulative wind power capacity. Adapted from the Global Wind Energy Outlook 2014 [18].

#### 1.1.3.2.2 Estimated capacity

To illustrate the potentials for wind power generation, Fig. 1.3 depicts the estimated capacity of this kind of renewable energy source in Brazil, which is estimated at around 143.5GW for winds measured at 50m [19]. This capacity corresponds to more than 10 Itaipu power plants (the Itaipu dam <sup>2</sup> is one of the largest operating hydroelectric facilities in the world, with installed capacity of around 14 GW). The available power could be even more significant for winds at 100m [20].

<sup>2</sup><http://www.itaipu.gov.br/>

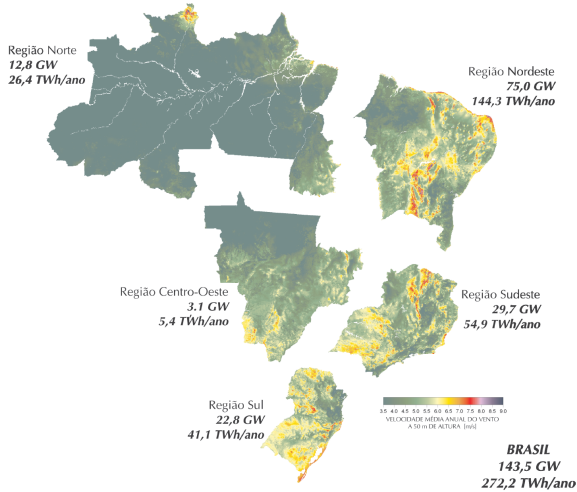


Figure 1.3: Wind Speed at 50m in Brazil. Adapted from [19].

### 1.1.3.2.3 Complementarity between hydropower and wind power

Another relevant factor that could be used as an incentive to further invest in wind power in Brazil is the possibility of complementarity between hydropower and wind power. Most of the electricity in the country is produced by hydropower generation, corresponding to around 80% of its needs [21, 18]. Studies suggest that the largest wind power generation availability in the Northeast (see Fig. 1.3) occurs during periods of low water availability as shown in Fig. 1.4 [22, 20].

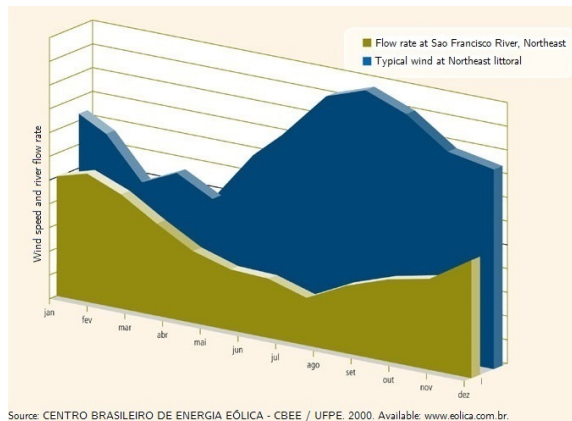


Figure 1.4: Complementarity between wind and water flow of the São Francisco river in Brazilian Northeast region. Adapted from [22].

#### 1.1.3.2.4 Current installed capacity

In August 2014, the wind power installed capacity in Brazil has overcome 5 GW (which is sufficient to supply around 12 millions people, equivalent to the city of São Paulo), representing an increasing of 3 GW in about 2 years [23]. By 2030, the installed capacity is expected to reach around 13500 MW [24]. The Global Wind Energy Outlook report sets the Brazil as the most promising market for wind energy in Latin America for the next years [18].

### 1.1.4 Wind power technological trends discussion

Over the last decades, the wind power technology has experience a remarkable development. They are more reliable, cost effective and quieter. However, there are still interesting possibilities for further development [14].

In their work, Li *et al.* [1] point out that new developments in relation to wind turbines should focus on the gradual improvement of already known technologies and summarize them as follows:

- The generation power capacity on a single turbine will continue to increase, as this reduces the cost of deploying the turbine, especially in offshore parks;
- Offshore generation is more attractive because there are more high speed winds and more space than on onshore parks;

- A growing trend is the reduction of dispersed turbine in favor of concentrated turbines forming wind farms;
- There is a tendency to increase the market share of wind energy on power systems.

In a similar manner, Manwell *et al.* [14] also highlight that there are still many difficulties to be overcome on the implementation of offshore facilities. According to them, “the world of offshore wind energy is just in its infancy” and “improved engineering methods for the analysis, design, and for mass-produced manufacturing will be required”. They mention as well the need to reduce the costs of wind energy at sites with lower wind speeds and to establish a commercially viable solution for remote communities. These key points are still valid nowadays.

In general, it can be inferred from the literature that most of future developments on wind power generation are associated to the variable cost. Technological improvements shall focus on the identification of alternatives to maximize generation efficiency and the financial yield for each application. Consequently, one of the key points is to address the *total* system cost, analyzing distinct turbine technologies, and the costs related to installation, operation and maintenance in order to identify the solution with best overall cost-benefit ratio.

### 1.1.5 Grid code technical requirements for large wind farms

The growth of the wind energy penetration in power systems motivates manufacturers, researchers and regulators to seek solutions to mitigate the potential impacts of high levels of wind power in the electrical system. For example, Hansen *et al.* [3] claim that the biggest challenge for the coming years is the connection and the optimized integration of large wind farms into the power system.

According to [15], there are significant differences among conventional (hydropower, thermal, nuclear) and wind power generation. The latter, for example, often employs frequency converters and the source of mechanical energy, the wind, is not controllable. It floats stochastically and the typical capacity of the wind turbine is usually much smaller than a conventional unit that uses a synchronous generator in thermal or hydroelectric units. Because of these differences, wind generation interacts differently with the network and can have global and local impacts on power system operation. In order to regulate the connection of large wind turbine to the power grid, transmission system

operators (TSO) impose a series of rules known as the grid codes [2], introduced in the sequence.

### 1.1.5.1 General requirements

The grid codes may differ from country to country and a good review of their main aspects is presented in [25]. As a general guideline, the main requirements for connecting a wind turbine to the power system may be summarized by [1, 2, 25, 4]:

- Voltage stability control independently of the input variation (wind speed);
- Frequency control;
- Active power control;
- Reactive power control;
- Voltage flicker minimization;
- Fault-ride through capability.

All of these requirements are associated to the increasing level of wind energy in the power system. Basically, the wind farms are expected to behave as conventional generating units, i.e. they must meet the same requirements as for traditional power plants units with grid support capabilities [1].

### 1.1.5.2 Low Voltage Ride Through (LVRT) capability

The main cause of voltage instability is the inability of the power system to supply the reactive power demand [26]. For this reason, of special concern of TSO is the fault-ride through (FRT) capability of generating units (also known as low voltage ride through - LVRT). The LVRT is defined as the wind turbine capability to withstand and remain connected to the grid to support its recovery in case of faults/disturbances such as a voltage dip. The LVRT capability curve is defined based on the fault voltage levels as a function of the fault duration [1].

The LVRT requirements may vary depending on the TSO [25]. For illustration purpose, Fig. 1.5 depicts an example of a typical fault-ride through capability curve.

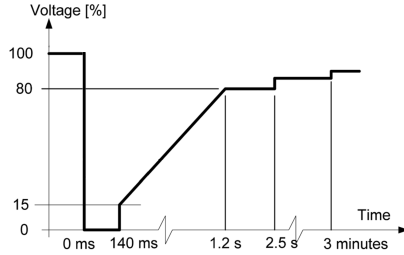


Figure 1.5: Fault-ride through characteristic of a typical wind turbine installation. Adapted from [2].

In the event of a voltage dip, as a general rule, the wind turbine shall remain connected and assist in system recovery if the voltage is above the curve specifying the LVRT capability and may disconnect if the fault leads to an operation below the curve [25, 1, 2].

Next section investigates the existent wind turbine technologies and their constraints to fulfill these TSO requirements.

### 1.1.6 Overview of existing topologies and electrical machines for wind energy generation and the choice of a reluctance type

Along the years, many system topologies for large wind turbines have been proposed. Although some variations indeed exist, the solutions may be generally classified in three types: fixed speed, variable speed with a partial scale converter and variable speed with a full scale power converter [15, 1]. Fig. 1.6 resumes this classification and their main characteristics are pointed out as follows.

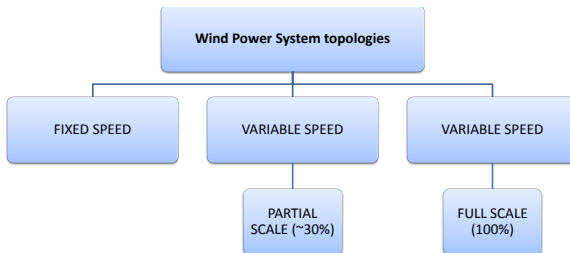


Figure 1.6: Simplified classification wind power systems topologies.



### 1.1.6.1 Fixed speed wind turbines

The fixed speed wind turbines consist of an aerodynamic rotor coupled to a low-speed shaft, a gearbox, a high speed shaft and a generator [15]. The electrical machine typically used in this solution is the Squirrel Cage Induction Generator - (SCIG). This generator has the characteristic of operating in a restricted range of speeds close to the synchronous speed and, therefore, require a multistage gearbox to couple turbine and generator speed [1]. Fig. 1.7 illustrates the fixed speed topology.

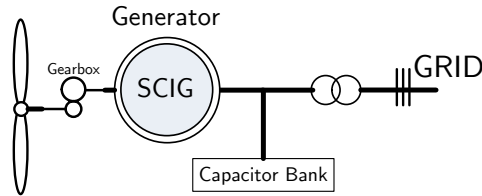


Figure 1.7: Fixed speed, geared-driven wind turbine topology with a squirrel cage induction generator.

An important characteristic of the SCIG is the need to absorb reactive power for excitation. This power is obtained from the network itself or through capacitor banks installed to correct the power factor for each turbine [15]. As this version of the induction generator has no windings on the rotor, and therefore has no brushes or slip rings, it is a robust solution. Moreover, it is relatively easy to control and it has lower production costs.

As negative points, it can be cited the fact that the generator speed is not controllable, which implies that variations in wind speed are translated directly into electromechanical torque fluctuations. This causes high mechanical and fatigue stresses on the system and does not allow to maximize wind energy extraction as a function of wind speed [1].

The main drawbacks of this solution, however, are related to the need to obtain excitation currents from the stator winding terminals. Therefore, it is impossible for this solution to support grid voltage control [1] by compensating reactive power. This kind of technology have been relegated along the years and nowadays the majority of wind turbines installations uses variable speed solutions.

### 1.1.6.2 Variable speed turbines

One of the greatest advantages of variable speed operation is the possibility to maximize wind power extraction. To do so, control algorithms are implemented to regulate generator speed to match the maximum possible power that can be extracted from the wind turbine as a function of wind speed. Such a technique is known as the Maximum Power Point Tracking (MPPT) [27, 28, 29]. Other key advantages of variable speed operation are related to the possibility to effectively control active and reactive power at wind turbine terminals, permitting to meet the TSO requirements for grid connection.

In variable speed operation, two main solutions have emerged depending on the rating of the power converter as presented in the sequence.

#### 1.1.6.2.1 Variable speed, partial-scale converter

The first system topology is the one which uses a partial-scale power converter and the Doubly Fed Induction Generator (DFIG), depicted in Fig. 1.8.

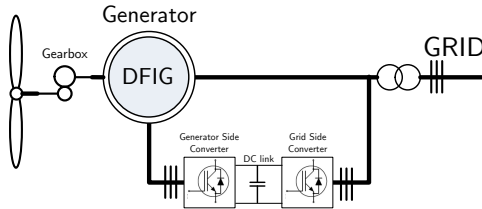


Figure 1.8: Variable speed, geared-driven wind turbine topology with a doubly fed induction generator and a partial-scale power converter.

In the DFIG, the stator is directly connected to the grid while its wound rotor is connected to a converter, which controls the excitation frequency in the rotor and hence its speed. This concept supports a wide range of speeds depending on the drive size, typically varying  $\pm 30\%$  with respect to synchronous speed. The converter nominal power is rated in general at 25–30% of the total system capacity, which makes it a very attractive concept from an economic point of view [1] due to the reduced cost of power electronics, especially for high capacity wind turbines.

On the DFIG solution, the power converter can provide reactive power compensation and smooth grid connection, since the grid-side

power converter can control its reactive power, independently of the generator operation. This allows the voltage support capability towards the grid [1]. The ability of active and reactive power control, together with a lower-rated power converter has made this solution the most used one on wind power application.

The use of the DFIG, however, has a major drawback that is the use of brushes and slip rings to connect the wound rotor to the power converter. These components may incur in reliability problems and require frequent maintenance, which has an impact on operating costs of the generating unit, especially on offshore wind farms [4]. The need of a gearbox to match turbine and generator speed may also be considered a drawback of this solution, since the DFIG speed is greater than turbine speed which is around  $10 - 25 \text{ rpm}$  [1].

#### 1.1.6.2.2 Variable speed, full-scale converter

On this solution, the generator is connected to the power system through a converter that handles all of the generated energy. This isolates the generator dynamics from the power system and allows effective control of active and reactive power and smooth grid connection. A gearbox may or may not be used, depending on generator characteristics and different machines can be used, the most commons being the induction, wound-rotor synchronous or permanent magnet (PMSG) synchronous generators [15]. Fig. 1.9 illustrates the topology without gearbox and with the PMSG.

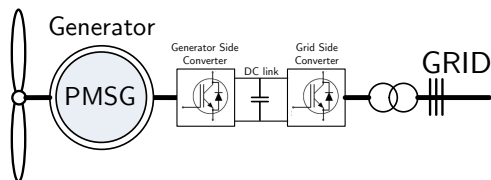


Figure 1.9: Variable speed, gearless wind turbine topology with a permanent-magnet synchronous generator and a full-scale power converter.

One of the advantages of this topology is the possibility to remove the gearbox of the system, resulting in a simplified drive train. On the other hand, this implies in low speed generators and, to obtain the same output power, a high torque machine is necessary. Usually this means a higher number of poles and a significant increase in the generator volume. The PMSG is a good option to this solution because it re-

sults in high torque density generators. However, the use of permanent magnets present the disadvantages of high cost of raw materials, difficulties to handle in manufacture and demagnetization of PM at high temperatures [1]. In general, this solution tends to be more expensive than the one with a partial-scale converter due the fully rated power electronics and the higher generator cost [1].

### 1.1.6.3 Appraisal of the different topologies

From the discussion presented so far, it can be inferred that the use of variable speed systems has become mandatory for high capacity turbines. The DFIG concept with a partial-scale converter still dominates the market due to the interesting characteristic to manage only a fraction of the total generated power. On the other hand, the solution that considers a fully-rated converter has some advantages such as greater overall efficiency, reliability, availability, and the possibility of operation without gearboxes that can make it very attractive for certain applications [1]. Schulz *et al.* [4] affirm that there are many configurations implemented by various manufacturers, but so far, no solution has been (or can be) considered as the ideal one. The definition of one technology over the other should evaluate the best cost-benefit ratio regarding generator efficiency and the costs associated to wind turbine manufacturing, installation and maintenance during operation.

### 1.1.6.4 The choice of a reluctance machine as the electrical generator

In the context of the proposed research, the goal is to identify and study a cost-effective and robust solution for wind power applications by using optimization. As the main guideline, it has been established that the solution shall avoid the use of permanent magnets (PM) and preferably use a partial-scale power converter. Among the electrical machine possibilities to meet system operator requirements and at the same time being in accordance to the identified trends, this work propose the study of a *reluctance generator* for wind turbine application.

One of the main arguments in the use of reluctance machines for wind power applications is their robustness. They have no windings on the rotor and consequently do not require brushes and slip rings, components that depend on constant maintenance and make the system more prone to failure. Furthermore, they do not have copper losses in the rotor due to the absence of conductors and they are potentially more efficient than the traditional induction machines. Additionally,

they have no permanent magnets and therefore are less sensitive to failures (demagnetization of magnets) in case of operation at high temperatures. The high cost of PM materials is another factor that weighs in favor of reluctance machines.

The following section aims to contextualize the use of these devices in wind generation, indicating how the different reluctance machines are classified according to the system topologies.

### **1.1.7 The different reluctance machine concepts for wind power application and the choice of the Brushless Doubly Fed Reluctance Machine**

The reluctance concept is probably the oldest one among the electrical machines and began to be developed between the 1830s and 1850 (Anderson, Chapter 2, [30]). There are different types and configurations of these devices, but, in general, they have similar characteristics such as manufacturing simplicity and robustness.

Most applications use these machines as motors and the researches focus on improvements on their design and performance. Historically, generating operation has received reduced attention because it was believed they had less practical importance. Only from the 1980s researchers related to the use of reluctance machines in wind turbines have arisen [31].

In the literature, three basic reluctance machine types can be identified: the Switched Reluctance Machine (SRM), the Synchronous Reluctance Machine (SyncRM) and the Brushless Doubly-Fed Reluctance Machine (BDFRM).

#### **1.1.7.1 Switched Reluctance Machine**

The Switched Reluctance Machine (SRM) is a simple electrical device regarding its construction and operating principle. Constructively, the stator and the rotor have salient poles and its working principle is based on the tendency of the magnetic flux to maintain a path of minimal reluctance. An important feature of this machine is the need of an electronic drive system and, depending on the excitation firing angles with respect to the rotor position, a positive (motoring) or negative (generating) torque is obtained. Fig. 1.10 illustrates a cross-sectional view of a SRM with 6 stator poles and 4 rotor poles.

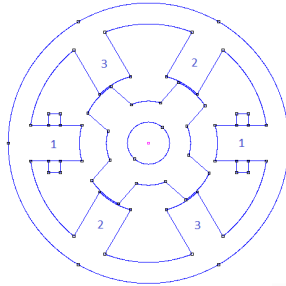


Figure 1.10: Cross-sectional view of a Switched Reluctance Machine.

The SRM topology in wind power would be similar to the one which uses a fully rated power converter presented in Fig. 1.11.

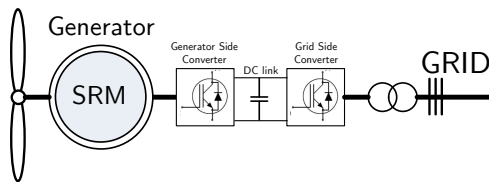


Figure 1.11: Variable speed, gearless wind turbine topology with a Switched Reluctance Machine and a full-scale power converter.

According to Helle *et al.* [32] (Chapter 13), the most common arguments in the use of SRM in wind applications rely on their high efficiency, reduced costs due to its simple structure and no need of a gearbox. However, the size and capacity of the drive tend to limit the use of SRM for low and medium powers, since it must manage all the energy generated.

Most of the studies in the literature considers SRM motor operation, but there are some studies on the use of SRM in wind energy applications. As an example, one can cite the work of Torrey [33, 34] and Cardenas *et al.* [35, 36], among others. Despite the great scientific and academic interest in the use of SRM as a generator, this solution is currently not used on large scale.

### 1.1.7.2 Synchronous Reluctance Machine

The synchronous reluctance machine (SyncRM) is a robust and low-cost one. Its stator is divided into slots to assembly a three phase

winding set, arranged in a way to produce the same number of poles of the rotor. The rotor is made of only iron and it is designed aiming to maximize the saliency ratio between direct and quadrature axes. It has no windings or magnets on it. Fig. 1.12 shows a cross-sectional view of the SyncRM.

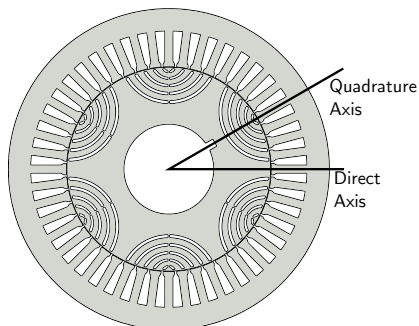


Figure 1.12: Cross-sectional view of a Synchronous Reluctance Machine.

SyncRM operation is based on the difference between the direct and quadrature axes inductances. The greater the direct axis and the smaller the quadrature axis inductances, the greater the power and torque for a given load angle [37]. As mentioned by Kim [38], a major issue for efficient operation of SyncRM is the rotor design. It is on the optimization of this component that one can act to maximize the torque generated by the machine.

To operate as a generator, self-excitation is required for the SyncRM. This process is comparable to the excitation of the squirrel cage induction generator, since it consumes reactive power [39] that can be obtained from a capacitor bank or from the network. This generation system is similar to the one which uses a fixed speed turbine and the squirrel cage induction generator. Fig. 1.13 illustrates the topology where the SyncRM can be used.

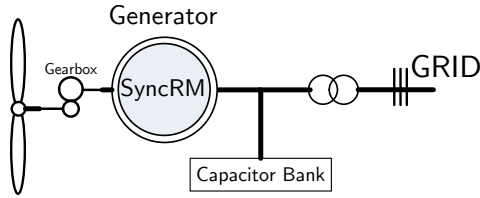


Figure 1.13: Example of wind turbine topology with a Synchronous Reluctance Machine.

### 1.1.7.3 Brushless Doubly-Fed Reluctance Machines

The Brushless Doubly Fed Reluctance Machine (BDFRM) is constructively very similar to SyncRM. The stator is divided into slots, similar to the one of an induction machine. The major difference between the BDFRM and the SyncRM is on the stator windings: the BDFRM has two sets of independent three phase windings, while SyncRM has only one.

Fig. 1.14 shows a simplified cross-sectional view of the BDFRM, including the distinct three phase winding sets with a salient reluctance rotor.

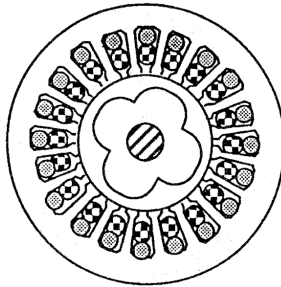


Figure 1.14: Cross-section view of a salient rotor BDFRM. Adapted from [40].

The characteristic of two independent winding sets is very interesting because it allows to control power flow and speed in the BDFRM. As the rotor is constituted of only iron, (there is no windings or permanent magnets) and the windings are located only on the stator, this machine has no brushes and slip rings.

The BDFRM topology in a wind power generation system is very



similar to the one that considers the Doubly Fed Induction generator (DFIG), because it also permits to use a partial-scale power converter if the speed range is limited. An additional advantage of the BDFRM over the DFIG is its brushless structure, resulting in a potentially more robust and reliable solution. Fig. 1.15 shows the wind turbine topology that can be used with the BDFRM.

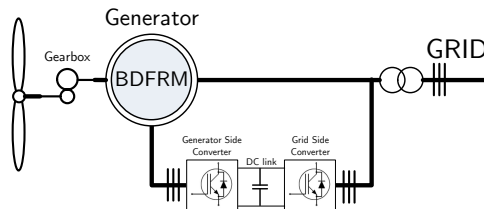


Figure 1.15: Variable speed, wind turbine topology with a Brushless Doubly Fed Reluctance Machine and a partial-scale power converter.

#### 1.1.7.4 The choice of the Brushless Doubly Fed Reluctance Machine

From the literature review, it can be seen that the solution using the DFIG is usually the preferred one mostly due to the reduced cost of power electronics. Considering the proposed context on this thesis, a cost-effective alternative solution that mitigate the drawbacks of the DFIG and keeps roughly its same advantages seems to be an appropriate choice, which leads to the *choice of the Brushless Doubly Fed Reluctance Machine* to be further investigated.

The Brushless Doubly Fed *Reluctance* Machine is a particular case of the family of Brushless Doubly Fed Machines (BDFM) that can be basically classified in two types depending on the rotor structure: the induction (BDFIM) [41, 42, 43] or the reluctance (BDFRM) versions [44, 45, 46, 47, 48]<sup>3</sup>. The BDFM concept can be considered one of the most innovative solutions in wind power generation [1] and, although they are still in research phase, they are considered an interesting alternative for future development on this application [2].

Figure 1.16 shows the topology of wind generation with a BDFM.

---

<sup>3</sup>A BDFRM is also referenced in the literature as Doubly Excited Brushless Reluctance Machine (DEBRM) or as Dual Winding Reluctance Generator (DWRG).

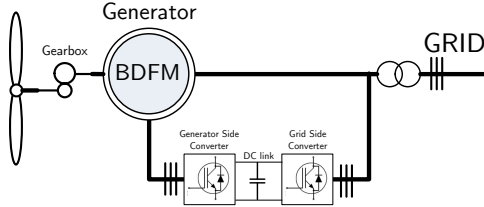


Figure 1.16: Topology of a wind power generation system with a brushless doubly fed machine.

Comparing the induction and reluctance versions, both have features that allow meeting the system operators requirements and mitigate the brushes-related problems of the DFIG solution, which is particularly interesting for offshore operation. As pointed out in [49], the advantages of the reluctance version over the induction one is that it is potentially more efficient (because there is no copper losses in the rotor) and it is easier to achieve decoupled control of active and reactive power. Additionally, as all copper losses concentrates in stator for the BDFRM, more efficient cooling methods could be used in order to extract more power and increase torque density. These reasons reinforce the choice of the reluctance version, although further work shall be done to address which version would be the best alternative to wind power applications.

The scientific relevance of the study of the BDFRM is also evidenced by other authors [5, 6, 7, 8, 9]. Despite many works have presented advances along last years, there is still a lack of researches to define a procedure on its electromagnetic design mostly due to its complex electromagnetic field interaction occasioned by rotor modulation. In [10], it is highlighted the need of design methods dedicated to address application specific requirements in order to define a high performance machine design. According to Schulz *et al.* [12], there is *a priori* no reason why the BDFRM cannot surpass the performance of the DFIG and this places it as a strong candidate to play an important role in the future of wind power generation systems [4].

## 1.2 The Brushless Doubly Fed Reluctance Machine (BDFRM)

### 1.2.1 Historical Background

#### 1.2.1.1 First development stages

The first researches that can be found in the literature about the Brushless Doubly Fed Machines (BDFM) date back the beginning of the 20th century [42] on a patent from Siemens Brothers and Lydall in 1902 [50]. From then on, this kind of machine has gone through three major development stages [10]. In the 10s, Hunt [51, 52] and Creedy [53] researched the concept of self-cascade machines where two wound rotor induction machines share the same shaft. The rotor windings from both machines were directly connected and, since there is no connection to the stator, there were no need for brushes or slip rings [42, 10]. These machine became well known by providing speed regulation and high starting torque. The concepts related to BDFM were subsequently studied by Broadway *et al.* [54, 55, 56] in the 70s, that essentially proposed to collapse the two machine stators into the same core [57]. They investigated two distinct rotors, the nested cage and the salient reluctance rotor, originating the concepts of the induction and reluctance versions of the BDFM. Further work has been presented on the subject in the 80s by [58, 59, 60] but the BDFM had not effectively found its market niche by that time.

#### 1.2.1.2 The regained interests in the 1990s

In the 90s, a regained interest in the BDFM has arisen, mainly motivated by the new possibilities that the fast development of power electronics could offer to vector control this machine and, supposedly, take full advantages of BDFM in variable speed applications [10].

Early in the 90s, the work of Liang *et al.* [47] e Xu *et al.* [46] presented a model for BDFRM analysis using the “dq” reference frame theory. The authors proposed a technique to calculate the inductances of the machine and formulated a transient model for its simulation. A methodology for analyzing steady state performance has been introduced by Liao *et al.* [40] and subsequently Betz *et al.* [44, 45] also investigated the electromagnetic principles of BDFRM.

In [61], Betz and Jovanovic discuss a comparison between the Synchronous Reluctance Machine (SyncRM) and Brushless Doubly Fed Reluctance Machine (BDFRM) addressing some aspects such as torque

capacity, efficiency and inverter ratings. The same authors present some theoretical analysis of control properties of the BDFRM in [49, 57]. Control aspects have also been extensively researched in the last decades, for example in [62, 63, 64, 6, 6, 65, 66, 67, 68, 69, 70, 71, 72, 10, 73, 74].

Regarding the electromagnetic design, the focus has been mostly on the study of existing design, highlighting machine capabilities, rather than on the development of appropriate design guidelines [11]. One of the key issues on BDFRM is the rotor design to improve coupling between windings and the initial research focused on the reluctance rotor topologies. There are at least three basic rotor structures depicted in Fig. 1.17. Fig. 1.17 (a) shows a salient pole rotor, (SPR), Fig. 1.17 (b) a axially laminated rotor (ALR) and Fig. 1.17 (c) a radially laminated with axial flux barriers, also referred as ducted rotor (RLDR) in the literature.

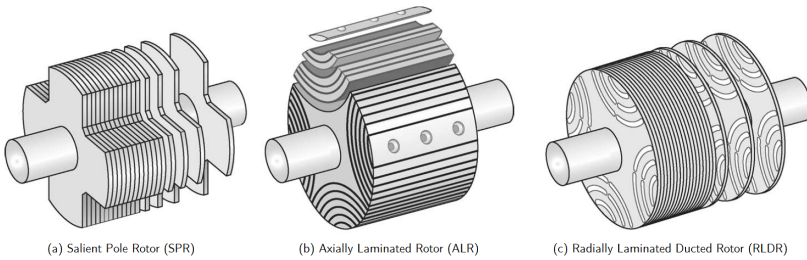


Figure 1.17: Different kinds of reluctance rotors for the BDFRM. Adapted from [75]

### 1.2.1.3 Researches on the salient pole rotor (SPR)

The aforementioned initial researches on the reluctance type of the BDFM focused mostly on the salient pole rotor, similar to the one used in the Switched Reluctance Machine. These early prototypes offered relatively low efficiency, power factor and torque density when compared to more conventional machine [11] and were used basically to better understand the electromagnetic working principles and to highlight the complexity on designing this machine.

#### 1.2.1.4 Researches on the axially laminated rotor (ALR)

The use of an axially laminated rotor (ALR) in the BDFRM has naturally been considered, since it had been previously investigated with some success in its “cousin”, the Synchronous Reluctance Machine. Schulz *et al.* [76] make a comparative study between the ALR and the SPR versions and, in [12], the same researchers addressed the influence of the stacking factor in an ALR. They claimed that an ALR can produce the double of torque when compared to the SPR. However, due to losses and torque ripple remarked when using the ALR rotor, they mentioned that the most appropriate solution for BDFRM is a radially laminated ducted rotor (RLDR), which has radial laminations (to minimize magnetic losses) and axial flux barriers, essentially resulting in an intermediary solution between the ALR and the SPR. Similar phenomenon with the ALR version was observed by Scian *et al.* [77] and Dorrell *et al.* [9].

#### 1.2.1.5 Researches on the radially laminated ducted rotor (RLDR)

Although the ALR presents superior coupling between the windings, the magnetic losses associated to this rotor pointed further researches to the radially laminated rotor. The RLDR offers a good compromise between electromagnetic performance and lower rotor losses due to the laminations.

Targeting BDFRM application in large wind turbines, Dorrell *et al.* [8] presented a study for a 2MW BDFRM by using the RLDR rotor version. They discuss some basic requirements for the BDFRM in such application and also address machine control. Koshinski [48] review the basic BDFRM analytical model and build a 20kW prototype considering a RLDR rotor with 10 poles. It has been reported that this prototype was adapted from an existent stator of an induction machine and low power factor and efficiency have been found.

In [75], it is presented a simplified model for the RLDR to quantify BDFRM performance and the results are investigated experimentally. Liu [7] perform a comparison considering an RLDR rotor with different number of poles. They also proposed a change in the basic analytic modeling to take into account this type of rotor instead of one with salient poles. It is concluded that a rotor number of poles equal to 5 presents the greatest mutual coupling between the windings among the analyzed combinations. However, Dorrell *et al.* [5, 78] show analytically that this combination has a high Unbalance Magnetic Pull - UMP

that can produce vibrations and may cause failures especially at higher power capacity machines. They indicate that the configuration with 4 and 8 poles in the stator will have a good linkage with reduced UMP.

The saturation and ducting effects on the RLDR is investigated in [79] focusing on the machine performance. In [80], it is discussed the influence of design parameters such as flux barrier ending geometry, rotor slot number combination, interpolar air flux barrier, rotor slot arc angle and duct ratio considering their impact on global machine performance through finite element analysis.

Knight *et al.* [81, 82, 11] presented a strategy to quantify the effects of different number of rotor and stator poles combinations by defining coupling factors and they introduce a technique to model the radially laminated ducted rotor (RLDR) considering an idealized rotor. Additionally in [11], some design equations taking into account an ideal rotor are presented, focusing on a qualitative analysis of power factor issues on this machine. It is also discussed good practices to choose the number of stator and rotor slots combination.

Studies addressing the modeling of Brushless Doubly Fed Machines by reluctance networks have been presented in [83, 84, 85, 86]. In [85, 83, 84], the modeling of the *induction* version is analyzed taking into account the effect of induced currents in the rotor. In [83], the reluctance version is also investigated.

This section discussed the historical background on the development of the Brushless Doubly Fed Reluctance Machines and the aforementioned references are used as a basis for this thesis. In the sequence, the basic analytical modeling for BDFRM and the main difficulties associated to its design are presented.

## 1.2.2 Electromagnetic operating principles

The operating principles of the BDFRM are known for a long time and are well established in the literature. This section aims to review the basic requirements so that electromechanical energy conversion takes place on this machine and refers to [47, 46, 40, 44, 45] as the main references.

### 1.2.2.1 Hypothesis for deriving the analytical model

Normally, to be feasible, the deduction of an analytical model implies in mechanical and electromagnetic simplifications. For the following discussion, it is considered that:

- the iron has infinite permeability;
- the two sets of three phase windings in stator are uniformly distributed in space (i.e. they can be modeled adequately by sinusoidal functions);
- the excitation currents are represented by sinusoidal waveforms;
- regarding the system topology, the grid winding is directly connected to the network under normal operating conditions and the control winding is connected to the grid through a power converter.

### 1.2.2.2 Air-gap modeling by using the salient pole rotor

The salient pole (SPR) is normally used in the literature to illustrate the basic operating mechanisms of the BDFRM, since it allows a simplified analytical approach to be used for that purpose. Therefore, it will be considered in this section to describe the BDFRM basic electromagnetic working principles and, where appropriated in the subsequent chapters, the respective considerations to take into account different rotor types will be assessed.

Additionally to the idealized assumptions previously stated, it is considered that the air-gap of a salient reluctance rotor can be represented by a sine function [87]. Taking into account these particularizations, the inverse air-gap function is given by [40, 44]:

$$g^{-1}(\theta_{ag}, \theta_{rm}) = m + n \cos [P_r(\theta_{ag} - \theta_{rm})] \quad (1.1)$$

where the constants  $m$  and  $n$  are real numbers (refer to Fig. 1.18 for details), satisfying  $m \geq n > 0$  and:

- $P_r \triangleq$  rotor number of poles;
- $\theta_{rm} \triangleq$  rotor mechanical angle;
- $\theta_{ag} \triangleq$  mechanical angle around the air-gap.

Fig. 1.18 shows an example of the waveform obtained with (1.1).

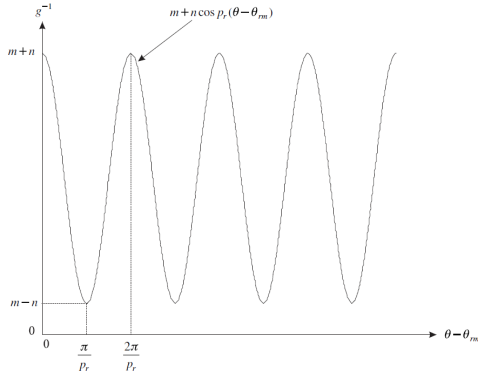


Figure 1.18: Inverse air-gap function. Adapted from [44].

### 1.2.2.3 Calculation of the magnetomotive force

The models consider balanced three-phase currents for their excitation as shown in (1.2) and (1.3):

$$\left. \begin{aligned} i_{ga} &= I_g \cos(\omega_g t) \\ i_{gb} &= I_g \cos\left(\omega_g t - \frac{2\pi}{3}\right) \\ i_{gc} &= I_g \cos\left(\omega_g t + \frac{2\pi}{3}\right) \end{aligned} \right\} \text{Grid} \quad (1.2)$$

$$\left. \begin{aligned} i_{ca} &= I_c \cos(\omega_c t - \alpha_c) \\ i_{cb} &= I_c \cos\left(\omega_c t - \alpha_c - \frac{2\pi}{3}\right) \\ i_{cc} &= I_c \cos\left(\omega_c t - \alpha_c + \frac{2\pi}{3}\right) \end{aligned} \right\} \text{Control} \quad (1.3)$$

where:

- $ga \rightarrow$  Phase  $A$  of grid winding
- $gb \rightarrow$  Phase  $B$  of grid winding
- $gc \rightarrow$  Phase  $C$  of grid winding
- $ca \rightarrow$  Phase  $A$  of control winding
- $cb \rightarrow$  Phase  $B$  of control winding
- $cc \rightarrow$  Phase  $C$  of control winding
- $I_g \rightarrow$  Current peak value in grid winding
- $I_c \rightarrow$  Current peak value in control winding
- $\omega_g \rightarrow$  Angular frequency of grid winding
- $\omega_c \rightarrow$  Angular frequency of control winding
- $\alpha_c \rightarrow$  Phase difference between the two windings sets



The three-phase magnetomotive forces (only the fundamental component is considered at this time) from each winding set can be calculate from traditional machine analysis and are given by:

$$\mathbb{F}_{3\phi g}(\theta_{ag}, t) = M_{3g} \cos \left( \omega_g t - \frac{P_g}{2} \theta_{ag} + \phi_{ga} \right) \quad (1.4)$$

and

$$\mathbb{F}_{3\phi c}(\theta_{ag}, t) = M_{3c} \cos \left( (\omega_c t - \frac{P_c}{2} \theta_{ag} + \phi_{ca} - \alpha_c) \right) \quad (1.5)$$

where:

- $P_g$  → number of poles of grid winding ( $W_g$ )
- $P_c$  → number of poles of control winding ( $W_c$ )
- $M_{3g}$  → amplitude of the fundamental magnetomotive force from grid winding and it is given by (1.6) [88]
- $M_{3c}$  → amplitude of the fundamental magnetomotive force from control winding and it is given by (1.7) [88]
- $\phi_{ga}$  → reference position of grid winding (phase a axis of  $W_g$ )
- $\phi_{ca}$  → reference position of control winding (phase a axis of  $W_c$ )

$$M_{3g} = \frac{3}{2} \cdot M_{1g} = \frac{3}{2} \cdot \underbrace{\frac{4}{\pi} \frac{Nphg \cdot Kwg}{P_g} \cdot I_g}_{M_{1g}} \quad (1.6)$$

$$M_{3c} = \frac{3}{2} \cdot M_{1c} = \frac{3}{2} \cdot \underbrace{\frac{4}{\pi} \frac{Nphc \cdot Kwc}{P_c} \cdot I_c}_{M_{1c}} \quad (1.7)$$

where  $Nphg, c$  are the total number of turns per phase and  $Kwg, c$ <sup>4</sup> are the winding factors.

The total magnetomotive force due to both windings is given by:

$$\mathbb{F}_{3\phi total} = \mathbb{F}_{3\phi g} + \mathbb{F}_{3\phi c} \quad (1.8)$$

#### 1.2.2.4 The air-gap flux density by using the salient pole rotor (SPR)

From Ampère's Law, considering the previously stated assumptions, the air-gap flux density can be calculated by (1.9) [40, 44]:

---

<sup>4</sup>The winding factor  $Kw$  takes into account the distribution  $k_d$  and short pitching  $k_p$  effects. It is calculated by  $Kw = k_d \cdot k_p$  [88].

$$B(\theta_{ag}, \theta_{rm}, t) = \mu_0 \cdot g^{-1}(\theta_{ag}, \theta_{rm}) \cdot \mathbb{F}_{3\phi total}(\theta_{ag}, t) \quad (1.9)$$

To illustrate the electromagnetic working principles, the air-gap function given by (1.1) can be rewritten as (1.10) by considering  $m = n = G/2$ ,  $G = 1/gap$ , where  $gap$  is the minimum air-gap length.

$$g^{-1}(\theta_{ag}, \theta_{rm}) = \frac{G}{2} (1 + \cos P_r(\theta_{ag} - \theta_{rm})) \quad (1.10)$$

Substituting (1.10) and (1.4) into (1.9), the air-gap flux density due to the grid winding is obtained [40, 44]:

$$\begin{aligned} B_g(\theta_{ag}, \theta_{rm}, t) &= \\ &= \mu_0 \left[ \frac{G}{2} [1 + \cos(P_r(\theta_{ag} - \theta_{rm}))] \right] \left[ M_{3g} \cos\left(\omega_g t - \frac{P_g}{2} \theta_{ag}\right) \right] \\ &= \frac{\mu_0 G M_{3g}}{2} \left[ \cos\left(\omega_g t - \frac{P_g}{2} \theta_{ag}\right) + \right. \\ &\quad \left. + \cos\left(\omega_g t - \frac{P_g}{2} \theta_{ag}\right) \cos(P_r(\theta_{ag} - \theta_{rm})) \right] \end{aligned} \quad (1.11)$$

Equation (1.11) can be further developed to result in:

$$\begin{aligned} B_g(\theta_{ag}, \omega_{rm}, t) &= \\ &= \frac{\mu_0 G M_{3g}}{2} \left\{ \cos\left(\omega_g t - \frac{P_g}{2} \theta_{ag}\right) + \frac{1}{2} \left[ \right. \right. \\ &\quad \cos\left((\omega_g - P_r \omega_{rm})t - \left(\frac{P_g}{2} - P_r\right) \theta_{ag}\right) + \\ &\quad \left. \left. \cos\left((\omega_g + P_r \omega_{rm})t - \left(\frac{P_g}{2} + P_r\right) \theta_{ag}\right) \right] \right\} \end{aligned} \quad (1.12)$$

where:

$$\theta_{rm} = \omega_{rm} t$$

$\omega_{rm} \triangleq$  rotor angular mechanical speed, in [rad/s]

Similarly, the air-gap flux density due to the control winding can be calculated and it is given by:

$$\begin{aligned}
B_c(\theta_{ag}, \omega_{rm}, t) = & \\
= \frac{\mu_0 GM_{3c}}{2} & \left\{ \cos \left( \omega_c t - \alpha_c - \frac{P_c}{2} \theta_{ag} \right) + \frac{1}{2} \left[ \right. \right. \\
& \cos \left( (\omega_c - P_r \omega_{rm}) t - \left( \frac{P_c}{2} - P_r \right) \theta_{ag} - \alpha_c \right) + \\
& \left. \left. \cos \left( (\omega_c + P_r \omega_{rm}) t - \left( \frac{P_c}{2} + P_r \right) \theta_{ag} - \alpha_c \right) \right] \right\} \\
& (1.13)
\end{aligned}$$

Equations (1.12) and (1.13) are the flux densities from both grid and control windings resulted from the *rotor flux modulation* action. It can be noticed that these equations have a fundamental component and two sidebands shifted in temporal and spatial domains. Depending on the pole number and frequency combinations, as presented in the sequence, there will be coupling between the windings and this is the basis for electromagnetic energy conversion on this machine [40, 44].

#### 1.2.2.5 Conditions for electromagnetic torque production: the coupling between the two windings sets

Based on (1.12) and (1.13), it can be stated that the coupling between the winding sets in the BDFRM is obtained if one of the sidebands of one winding couples the fundamental component of the complementary winding. To that end, it must exist a rotor pole number  $P_r$  that satisfies this requirement. The possible temporal (“ $t$ ”) and spatial (“ $\theta_{ag}$ ”) coupling conditions are illustrated in Fig. 1.19 (the  $\pm$  signal is used because the cosine is an even function).

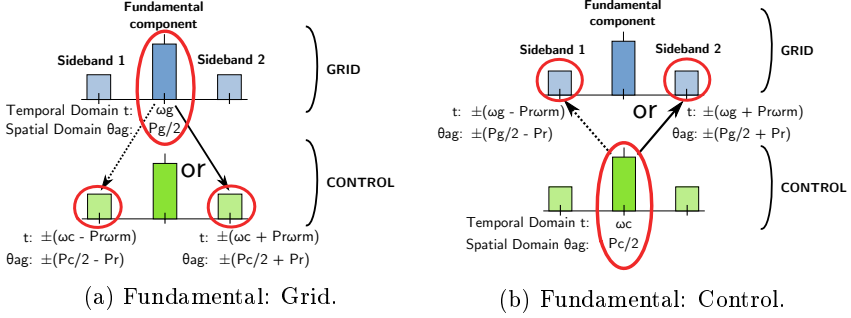


Figure 1.19: Coupling conditions for torque production on the BDFRM in spatial and temporal domains.

As an example, let us analyze the coupling of the fundamental component from control winding with one of the sidebands from grid winding due to rotor modulation. From a mathematical point of view, this means that:

$$\cos \left( (\omega_g - P_r \omega_{rm}) t - \left( \frac{P_g}{2} - P_r \right) \theta_{ag} \right) = \cos \left( \omega_c t - \alpha_c - \frac{P_c}{2} \theta_{ag} \right) \quad (1.14)$$

This results in the following conditions:

$$\begin{aligned} \omega_g - P_r \omega_{rm} = \omega_c &\rightarrow P_r \omega_{rm} = \omega_g - \omega_c \\ \text{or} & \\ -\omega_g + P_r \omega_{rm} = \omega_c &\rightarrow P_r \omega_{rm} = \omega_g + \omega_c \end{aligned} \quad (1.15)$$

and

$$\begin{aligned} \frac{P_g}{2} - P_r = \frac{P_c}{2} &\rightarrow P_r = \frac{P_g}{2} - \frac{P_c}{2} \\ \text{or} & \\ -\frac{P_g}{2} + P_r = \frac{P_c}{2} &\rightarrow P_r = \frac{P_g}{2} + \frac{P_c}{2} \end{aligned} \quad (1.16)$$

Similar analysis can be done for each one of the four combinations between fundamental component of one winding and the two sidebands of the complementary winding as illustrated in Fig 1.19. It can be shown that *only one* of the sidebands can be coupled to the fundamen-

tal component of the complementary winding at any one time. The remaining sideband will result in a leakage flux, since it will have a wrong pole number to provide coupling between the windings [44].

Checking the possible coupling combinations, the following conditions for torque production can be derived for the BDFRM:

$$\left. \begin{aligned} P_r &= \frac{|P_g - P_c|}{2} \\ \omega_{rm} &= \frac{\omega_g - \omega_c}{P_r} \end{aligned} \right\} \text{Negative case} \quad (1.17)$$

or

$$\left. \begin{aligned} P_r &= \frac{P_g + P_c}{2} \\ \omega_{rm} &= \frac{\omega_g + \omega_c}{P_r} \end{aligned} \right\} \text{Positive case} \quad (1.18)$$

Only the positive case stated in (1.18) will be considered in this thesis.

### 1.2.2.6 The fundamental influence of the mutual inductance on machine performance due to rotor design

Previous section has shown the elementary role of the rotor on energy conversion in the BDFRM. As  $P_g$  and  $P_c$  are different, if a smooth rotor is considered, there is no direct coupling between the windings. The rotor is essentially responsible for providing coupling between them by satisfying either (1.17) or (1.18) conditions.

To better quantify the rotor influence on machine performance, let us take a look on the electromagnetic torque expression in *steady state* for the BDFRM. It is given by (1.19) [40]:

$$T_{em} = -\frac{3}{2} \left( \frac{P_g + P_c}{2} \right) L_{gc} I_g I_c \sin(\phi_{Torque}) \quad (1.19)$$

where  $L_{gc} = 3/2 \cdot L_{gcmax}$  is related to the mutual inductance between windings and  $\phi_{Torque}$  is the torque angle, related to the reference angle between the two windings sets and the rotor angle.

From (1.19), we see that the mutual inductance  $L_{gc}$  between the windings is directly proportional to the induced torque in the machine. Not only the rotor pole number is important (a necessary condition), but also a good design shall maximize  $L_{gc}$  in order to provide competitive torque density on this machine. This can potentially be achieved

by optimizing rotor design.

## 1.2.3 The advantageous characteristics of the BDFRM

### 1.2.3.1 General aspects

Regarding its topological structure, the BDFRM has the inherent advantage of the reluctance principle: there is no winding or permanent magnets on the rotor and all the windings are located on the stator. The machine has no brushes and slip rings and therefore it can be considered a robust machine from the mechanical point of view. Compared to the induction version, the BDFIM, the BDFRM is potentially more efficient (since there are no copper losses in the rotor) and simpler to control owing to the cage-less structure [57, 71]. Additionally, the BDFRM allows the possibility of using a fractionally rated power converter due to the slip power recovery property<sup>5</sup> and it potentially offers a superior LVRT capability than the DFIG, as discussed in the sequence.

### 1.2.3.2 Slip power recovery property

#### 1.2.3.2.1 Power Expressions

The slip power recovery property can be deduced from the power expressions for the BDFRM in steady state conditions given by (1.20) and (1.21) [44, 45]. These equations neglect losses of any kind for this qualitative analysis.

$$P_{3\phi g_{int}} = -\frac{3}{2}(\omega_g)L_{gc}I_gI_c \sin(\phi_{torque}) \quad (1.20)$$

$$P_{3\phi c_{int}} = -\frac{3}{2}(\omega_c)L_{gc}I_gI_c \sin(\phi_{torque}) \quad (1.21)$$

where  $P_{3\phi g_{int}}$  and  $P_{3\phi c_{int}}$  are the three phase real power from grid and control windings, respectively.

#### 1.2.3.2.2 Slip definition

Firstly, let us define the “slip” in the BDFRM, represented by “s”. From the induction machine theory, the slip is defined as the relative speed between the electrical synchronous speed and the electrical rotor speed in a per-unit basis given by:

---

<sup>5</sup>The DFIG and the BDFIM also share this characteristic.

$$s = \frac{\omega_{sync} - P_r \omega_{rm}}{\omega_{sync}} \quad (1.22)$$

In the BDFRM, it is assumed that the synchronous rotating field is given by  $\omega_{sync} = \omega_g$  since the grid winding is connected directly to the grid. Recalling from (1.18) that  $P_r \omega_{rm} = (\omega_g + \omega_c)$ , the slip can be defined [45]:

$$s = \frac{\omega_g - P_r \omega_{rm}}{\omega_g} = \frac{\omega_g - (\omega_g + \omega_c)}{\omega_g} = -\frac{\omega_c}{\omega_g} \quad (1.23)$$

By using the slip definition, (1.21) can be written as a function of (1.20):

$$P_{3\phi c_{int}} = -s P_{3\phi g_{int}} \quad (1.24)$$

### 1.2.3.2.3 BDFRM operating modes

From (1.20), (1.21) and (1.24) one can identify three modes of operation in the BDFRM [40, 44, 45]:

- $\omega_c = 0$ : synchronous operation with DC excitation. At this condition, the machine behaves essentially as a conventional synchronous machine, with the control winding playing the role of the field winding. In a qualitative analysis, neglecting losses of all kind,  $s = 0$  and, from (1.24), there is no *real* power flowing through the control winding.
- $\omega_c > 0$ : the BDFRM operates in a supersynchronous condition. In the maximum speed case when  $\omega_c = \omega_g$ , the real power is shared evenly by grid and control windings. If  $\omega_c = 1/2\omega_g$ , the real power flowing through the control winding is equivalent to the half of the real power that is passing through the grid winding at the same time. In this case, the control winding is managing roughly 1/3 of the total real power in the machine.
- $\omega_c < 0$ : the BDFRM is operating in the subsynchronous condition.  $\omega_c < 0$  essentially mean that the phase sequence of the three phase currents has been reversed. For example, let us consider a motoring condition, where  $P_{3\phi g_{int}} > 0$  is assured by proper control of the  $\phi_{torque} < 0$  angle in (1.20). Frequency  $\omega_c < 0$  implies that  $P_{3\phi g_{int}} > 0$  and  $P_{3\phi c_{int}} < 0$ . It means that some of the power flowing into the machine through the grid winding is being re-generated by the control winding. The BDFRM subsynchronous operation is very inefficient, since some of the real power is just

circulating throughout the machine, incurring in losses [57, 45]. Similar conclusions can be inferred for the generating condition.

#### 1.2.3.2.4 Slip power recovery property

From the operating modes, it can be seen that the rotor mechanical speed is directly related to the real power shared between the windings. In this sense, (1.24) implies that, depending on the ratio between the winding frequencies, the control side shall manage only a fraction of the real power of the system if the speed variation is limited. This is usually the case for wind power generation, especially for the large turbines [57, 6].

Equation (1.24) also indicates that the power flow in control winding may be bi-directional. If the power converter is from a bi-directional back-to-back type, energy can be extract from control winding and regenerated into the grid depending on the rotor speed.

#### 1.2.3.3 Superior LVRT capability without a crowbar

In the partial scale converter topology of doubly-fed machines, one of the stator winding sets is directly connected to the grid. A voltage dip on the network will result in a sudden loss of the machine magnetization, producing a current surge in the machine-side converter [89, 90, 91].

There are some solutions for LVRT implementation for the DFIG. Usually, a crowbar circuit is used to protect the converter from over-currents by short-circuiting the rotor connections of the DFIG during the fault, such that the overcurrent flows through the crowbar circuitry [92, 93, 94, 91], as illustrated in Fig. 1.20.

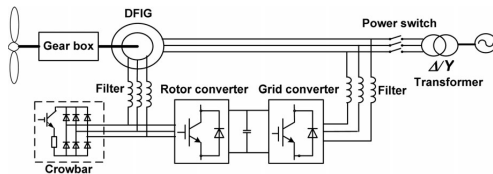


Figure 1.20: DFIG topology with crowbar [95].

The Brushless Doubly Fed Machines have inherently a larger leakage reactance due to the lower coupling between the windings as previously discussed for the BDFRM. In the case of system faults, the larger leakage reactance tends to limit the transient currents, offering a superior LVRT capability for this kind of machines over the DFIG solution



[96, 91, 71]. In [91], it has been investigated that the Brushless Doubly Fed Induction Machine (BDFIM) may potentially achieved LVRT even without the need of a crowbar circuitry [96, 91, 71], reducing control complexity and costs. As the leakage inductance values of the induction and reluctance versions of Brushless Doubly Fed machines are of comparable order, the superior LVRT characteristic identified for the BDFIM could potentially be extended to the BDFRM [68, 71].

## 1.2.4 The difficulties on the modeling and design of the BDFRM

The different number of poles combinations and the rotor flux modulation process makes the BDFRM a quite complex machine design, probably more than the most traditional ones. Schulz *et al.* [12], for example, highlighted the fact that the “design and optimization of the BDFRM requires radically different techniques to other machines”. Some key points on the BDFRM design are discussed in the sequence.

### 1.2.4.1 Lower torque density due to the inefficient coupling between the winding sets

One known possible drawback with the BDFRM is the relatively high leakage flux resulting from the flux modulation process by the rotor. As a consequence, this kind of machine tends to have a lower power factor (PF) and a lower torque density than more traditional ones [49]. Although it is possible to improve the power factor in one winding, it is hard to do it simultaneously in both windings [79, 11]. This potentially increases the converter  $kVA$  rating at the control winding side. Although a higher leakage flux may have some advantages (as discussed in Section 1.2.3.3), it is usually desirable to improve power factor. Regarding this topic, there are some papers in the literature indicating that the BDFRM can operate with high torque density and efficiency if *appropriately* designed, for example in [10, 11, 4].

### 1.2.4.2 Composition of the magnetomotive force from both stator windings

The two three-phase winding sets with different number of poles will produce an equivalent magnetomotive force (MMF) in the air-gap that will be a composition of them.

Fig. 1.21 shows a particular case of the MMF, considering only the fundamental component, taking into account the stator windings

with 4 (control) and 8 (grid) poles at  $t = 0$  s and rated conditions. The criteria used to choose the machine topological structure will be presented in Chapter 2 and, at this point, these values are used just for illustration purpose.

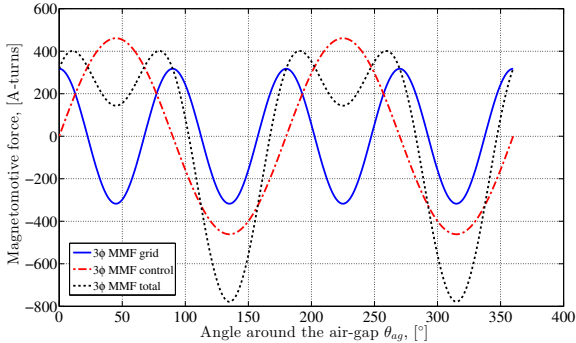


Figure 1.21: Magnetomotive forces for each winding at  $t = 0$  s as a function of the angle around the air-gap.

To better remark the effect on the “total” MMF waveform, Fig. 1.22 illustrates the 3D representation of the MMF as a function of the time and the position around the air-gap at rated conditions.

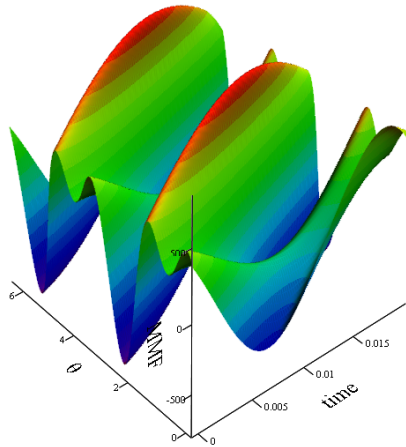


Figure 1.22: 3D representation of the total magnetomotive force  $\mathbb{F}_{total}$ .

Considering only the fundamental component of the magnetomotive

forces, one can already infer some difficulties on designing a BDFRM: the resulting MMF  $F_{total}$  is not sinusoidal and will be further modulated by rotor action as shown in the sequence.

#### 1.2.4.3 Non-sinusoidal air-gap flux density

The accurate determination of the air-gap flux density is directly related to model precision and it is essential on the modeling and analysis of any electrical machine.

In the BDFRM, the flux modulation process by the rotor results in a non-sinusoidal air-gap flux density that looks similar to the one depicted in Fig. 1.23, obtained from 2D Finite Element Analysis (FEA) [97] for the same conditions introduced in the previous section, considering a radially laminated ducted rotor.

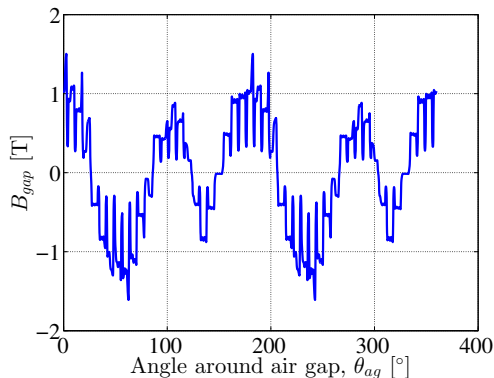


Figure 1.23: FEA result for  $B_{gap}$  at rated conditions.

This non-sinusoidal characteristic shall be taken into account to correctly represent the electromagnetic behavior of the BDFRM when developing the models.

#### 1.2.4.4 Half machine symmetry

From a modeling point of view, the different number of poles nature of the BDFRM restricts some simplifications that are usually done on machine models to reduce the electromagnetic domain to be analyzed and mitigate computational effort.

For example, for the particular case with grid and control windings with respectively 8 and 4 poles and the rotor with 6 poles, only

half machine, at best, can be used, as illustrated in Fig. 1.24. This increases model complexity and computation time. Furthermore, this figure clearly emphasizes the complex electromagnetic field iteration caused by the rotor modulation process on the BDFRM, resulting in fluxes that are not evenly distributed between the poles.

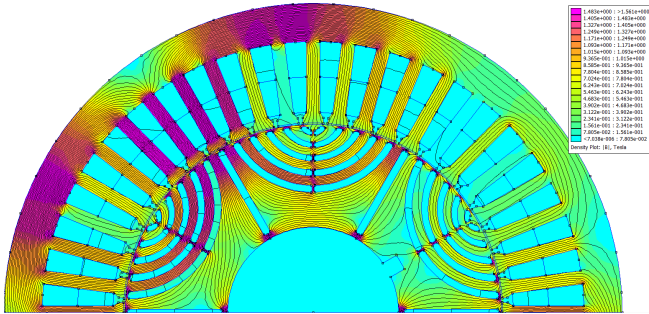


Figure 1.24: FEA simulation with half symmetry considering a 8-4 stator poles, 6 rotor poles BDFRM machine.

### 1.3 The bottlenecks on the definition of the BDFRM as a viable solution for wind power

Based on the discussion presented so far, it can be seen that designing BDFRM electromagnetic structure remains a challenging task and an optimized design aiming to maximize the coupling between stator windings is required for competitive performance.

According to Xu *et al.* [10] the researches about the BDFRM in the recent years have shown “a series of fundamental issues and challenges with respect to the design and control of this machine”, and they cite as examples: (i) what are the rules for optimal design aiming to maximize torque and power densities? (ii) what are the suitable control algorithms? (iii) how to improve energy efficiency? (iv) what are the limits on design and control of this machine?

In the literature, there are many studies addressing the advantages and drawbacks of alternative solutions for wind power generation. Brushless Doubly Fed Machines (induction or reluctance versions) have appeared as promising alternatives to the DFIG in variable speed ap-

plication by using a fractionally rated power converter, whereas others claim that Permanent Magnet machines with fully rated converters are a more adequate solution. It is clear that the best overall system solution will be a compromise between technical and economical aspects, from both manufacturing and operation points of view.

Two bottleneck can be identified on the consideration of the BDFRM as a viable solution for variable speed wind power application:

### **1.3.1 Bottleneck 1: to master BDFRM optimized design**

The first bottleneck refers to master BDFRM optimized design. Before comparing the BDFRM with other solutions, it is required to explore all possibilities to extract maximum performance from the machine.

### **1.3.2 Bottleneck 2: to assess the advantages and drawbacks of the BDFRM with respect to other solutions in wind power comparing the system solution as a whole**

Once the BDFRM optimized design is defined, one will be able to compared this solution to others and conclude if it is effectively a viable solution for wind power. The advantages and drawbacks of distinct solutions shall be assessed considering the generation system as a whole, taking into account efficiency, reliability, machine size, converter rating and manufacturing and operation costs.

### **1.3.3 Definition of the thesis objective: contributions to develop a design procedure to overcome bottleneck 1**

The main objective of this thesis is to address bottleneck 1 and to contribute in the sense to master BDFRM design. To that end, it is proposed a procedure for modeling, design and analysis of the Brushless Doubly-Fed Reluctance Machine (BDFRM) for wind power applications using an optimization approach based on deterministic algorithms.

## 1.4 The need of models and optimization approaches

### 1.4.1 The design process

The goal of a design process is to design a complex system by starting from just a few specifications in order to find a feasible (optimal) solution that satisfy the constraints that have been imposed. In general, this is a rather difficult task that may involve multi-disciplinary topics (electrical, magnetic, thermal, mechanical *etc.*). Many attempts to formalize the design process can be found in the literature [98] and Fig. 1.25 depicts the basic idea in a simplified diagram.

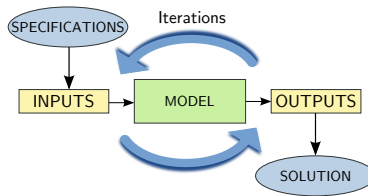


Figure 1.25: Simplified design process schematic.

Most part of the design chain relies on models and it is most likely an iterative process. Depending on the number of uncertainties or unknowns parameters on the starting phases, more or less iterations shall be performed in order to find the best solution. Additionally, different modeling levels and approaches may be used, as introduced in the sequence.

### 1.4.2 The need of different modeling levels: analytical, semi-analytical and numerical models

#### 1.4.2.1 General aspects on modeling

A model may be defined as an entity that is *representative* to describe a system or phenomena. Two distinct modeling approaches can be defined, namely the direct and inverse models. The direct model is implemented in a natural physical way [99]. For example, given the input design parameters such as the device dimensions, number of turns and so on, the output performance parameters (voltages, power *etc.*) can be evaluated. On the contrary, the inverse model uses as inputs the performance parameters (main specifications) and tries to find out

the design parameters that may satisfy the constraints imposed by the specifications [100, 101, 102, 99]. This thesis will focus on direct models. These different approaches are illustrated in Fig. 1.26.

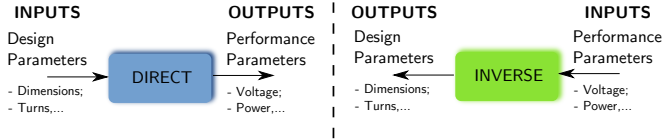


Figure 1.26: Direct and inverse models.

### 1.4.2.2 Analytical models

An analytical model aims to represent the phenomena associated to the system being described through analytical equations. The latter can be related to the physical dimensions, electromagnetic principles, thermal etc. In general, an analytical model is based on empirical assumptions and simplifications due to the fact that it is hard to take into account analytically magnetic material non-linearities, iron losses, frequency influence on system, just to cite a few example. In the case of rotating electrical machines, the task may be even more complicated, since the device topology has most of the time complex geometries and there are always moving parts that varies their position as a function of a rotating magnetic field. Due to their nature, the analytical models are very fast, but usually not very accurate due to the simplifications that are considered. A priori, no specialized tool is required and this kind of model can be implemented in calculation sheets such as Excel <sup>®</sup> or Mathcad <sup>®</sup>, etc.)

### 1.4.2.3 Numerical models: Finite Element Method

The numerical methods are usually associated to high accurate results. Probably the most known type is the Finite Element Method [103, 104]. With this method, the electromagnetic domain is discretized, forming a mesh, and the Maxwell's equations are solved locally by the application of a convenient formulation to each element. It is very precise, since magnetic material non-linearities are taken into account. Regarding the computation time, however, the FEM can be very time consuming depending on how dense the generated mesh is. For the implementation, usually dedicated tools are used.

#### 1.4.2.4 Semi-analytical models

A semi-analytical model is an intermediary approach between the analytical and the numerical model. In general, it is the coupling of analytical equations to numerical methods to solve specific parts of the model. This can include calculations such as the solution of implicit equations and numerical integrals and also include algorithms with programming structures such as tests (if-else) and loops (for, do-while). With this approach it is possible, for example, to take into account magnetic non-linearities. The main advantage of these models is that they present a good trade-off among precision and computation time. Any model that couples analytical equations to numerical approaches to calculate outputs can be considered a semi-analytical model. One example is the reluctance network model that solves nonlinear equations by taking into account magnetic material nonlinearities and, at the same time, may have the reluctances calculation parametrized by analytical equations.

#### 1.4.2.5 The need of different modeling levels in the design process

There are some characteristics that can be associated to a model that are useful to compare them: precision, linear/non-linear, computation time, analytical, numerical etc. Different modeling levels have inherent advantages and drawbacks and there is no ultimately *best solution*. In the design process, what is important is to identify the development stages and associate modeling levels that are compatible to each one of them.

As an example, one may consider a new machine design, where most parameters are unknown and must be deduced from just a few specifications. Many different modeling approaches may be applied. The most traditional is the one based on solving analytically Maxwell's equations. To that end, all the iron non-linearities are neglected and one can obtain a first idea of device performance even if the results are normally not very accurate. The most important advantage of this method is that the results are quickly obtained and they fall within an acceptable precision for a "first-cut" design. Although theoretically possible, it is harder to use Finite Element Analysis (FEA) to find an optimal machine because the number of uncertainties are huge and the computational time prohibitive for that purpose. Depending on the design complexity, it may be useful to use an intermediary semi-analytical model: it will keep the advantages of an analytical model



(notably fast computation) and will produce more accurate results, helping to refine the design and reduce the number of unknowns. In this strategy, FEA may be very useful in final stages, where only a few parameters might be assessed to find the best solution for a specific application.

### 1.4.3 The need of optimization

As presented in previous section, usually the design process implies in many iterations. Depending on the number of uncertainties, it is logical to automatize the calculations. In the context of this work, it is proposed to use optimization to address this issue.

The considered approach defines a *direct* optimization model, where the most of the performance parameters (specifications) are set as outputs and they are calculated as a function of the design parameters and excitation conditions. The idea behind using optimization is to constrain outputs  $C_i$  and to define range intervals for the inputs variables  $P_i$  and let the optimization algorithm iterate and solve the problem whereas minimizing (maximizing) an objective function. Fig. 1.27 illustrates this process.

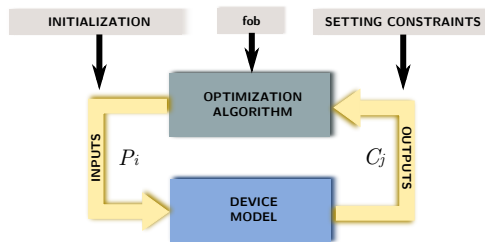


Figure 1.27: General optimization principle.

#### 1.4.3.1 What is optimization

Optimization algorithms are techniques that automatically explore mathematical spaces aiming to solve the following  $\mathbb{P}$  problem [100, 101, 105]:

$$\mathbb{P} \Rightarrow \begin{cases} fob = \text{Min}f(\bar{x}) \in \mathbb{R} \\ g_i(\bar{x}) \leq 0 & i = 1, \dots, l \\ h_j(\bar{x}) = 0 & j = 1, \dots, m \\ x_k^{\text{min}} \leq x_k \leq x_k^{\text{max}} & k = 1, \dots, n \end{cases} \quad (1.25)$$

where

- $fob$  → is the objective function
- $\bar{x}$  → is a vector of size  $n$  containing the search space (unknowns) for the optimization problem
- $g, h$  → are functions that also depends on  $\bar{x}$  that can be submitted to equality and inequality constraints

### 1.4.3.2 Global and local optimum

It is possible that the function  $f(\bar{x})$  have many extreme values where the first derivative is zero, indicating that it has many local optimums. Fig. 1.28 illustrates an example and highlights the minimum values.

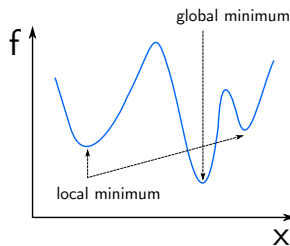


Figure 1.28: Global and local *minimum*.

A local minimum  $x' \in \Omega$  is so defined if there is at least one point  $x$  that satisfies  $f(x) \leq f(x')$ . Similarly, a global minimum  $x' \in \Omega$  must satisfy the following condition:  $\forall x \in \Omega f(x') \leq f(x)$  [106, 105].

It may not be easy to determine if a solution of an optimization problem returns a global or local minimum since usually the knowledge of function being optimized is only local [106]. This is the case, for example, for the non-linear models used to describe electromagnetic devices such as an electrical machine. Although some work-around strategies can be applied to try to find the global solution, in general,

optimization is better suited as tool for aiding the designer to take pertinent decisions. It will never replace the expertise of the latter on the design process.

### 1.4.3.3 Multi-objective optimization: the Pareto front

A multi-objective problem may be defined as the one that has many contradictory objectives [101]. Supposing two contradictory objectives  $f_1$  and  $f_2$ , one of the best ways to compare them is by plotting their Pareto front [105]. In this example, the Pareto front corresponds to the minimization of  $f_1$  and the maximization of  $f_2$ . It represents the best compromise between these objectives and indicates that one can not be improved without degrading the other. If two objectives are considered, it is possible to draw a two dimension curve representing the Pareto front as illustrated in Fig. 1.29.

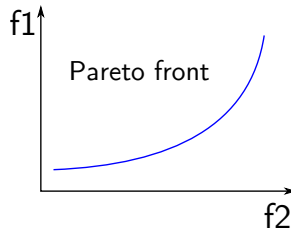


Figure 1.29: The Pareto front.

If three objectives are considered, the Pareto front becomes a surface. If even more contradictory objectives are considered, the graphical representation is no longer possible and this strategy may lose its practical value [105].

### 1.4.3.4 Optimization algorithms

The optimization algorithms may be classified in two main branches as follows.

#### 1.4.3.4.1 Deterministic

A deterministic method is the one that will always produce the same solution for the same input data set. The great advantages of this kind of algorithms are that they have fast computation time and are capable of dealing with many constrained outputs. In this work, we are particularly interested in the Sequential Quadratic Programming (SQP)

optimization algorithm [107, 106]. The SQP requires the Jacobian matrix of the model, which is a matrix containing the partial derivatives of the outputs with respect to the inputs. The drawbacks related to these kind of algorithm is that the initial set of values must not be so far from the desired optimal solution to minimize the risk to find a local minimum. In any case, it is hard to assess if the solution is a global or local minimum [105]. One possible work-around to mitigate the possibilities to fall into a local minimum is to test many combination of the initial values of input parameters for the same optimization problem. It is possible to automatize this process by using an hybridization technique presented in the sequence.

#### **1.4.3.4.2 Stochastic**

The stochastic optimization algorithms introduces a random aspect to the search of the best solution. This is the reason why it is more likely to find the global optimum, but they are much more expensive in terms of computation time. Additionally, it is hard to take into account many constraints on this kind of algorithms and they are usually used in problems with a limited number of constrained outputs [105, 101]. One good example of this branch is the genetic algorithm approach.

#### **1.4.3.4.3 Hybridization**

Hybridization may be one suitable alternative to take full advantage of fast computation time and capacity to deal with many constraints of the deterministic type, whereas introducing an aleatory aspect on the definition of the starting point of the calculation (initial values) by using an stochastic algorithm. The idea behind this technique is that, at each iteration, the genetic algorithm sets the initial values (new population) and a SQP calculation is launched in order to find a solution that respect all constraints. In general, this will increase the optimization time and will difficult convergence when compared to a pure deterministic optimization algorithm. However, it is more likely to find the global minimum/maximum.

#### **1.4.3.5 Why the use of the optimization approach is fundamental to design the BDFRM and answer the bottleneck 1**

According to (1.19), the mutual inductance, closely related to the rotor design, should be maximized to improve electromechanical conversion. However, many other design constraints should also be taken

into consideration simultaneously such as output terminal voltages, total active mass, efficiency, power factor, current densities and eventually torque ripple, voltage harmonics, just to cite a few examples. There are many coupled phenomena that are hard to take them into account separately by using classical machine design techniques, either by using heuristic formulas or by defining distinct components (stator, rotor, windings) independently from the others.

Assuming that it is possible to represent in a model most electromagnetic effects to take them into account simultaneously, the use of an optimization algorithm capable of dealing with several constrained outputs seems to be definitively an appropriated choice to better design this machine. In this context, typically two goals can be identified for using optimization techniques: the first one is to *solve* the problem, i.e. find a machine design that satisfies simultaneously all the constraints through an iterative calculation. The second one is to effectively *optimize* the machine design taking into account application specific requirements.

#### **1.4.3.6 The choice of the SQP as the optimization algorithm: constraints management**

In this work, we are particularly interested in optimization algorithms that are able to deal with *many constraints*. It is assumed that the designer has *a priori* a limited knowledge of the problem in the beginning of the design process and the idea is to use the powerful capabilities of the optimization approach to explore the solution domain in order to find the best device. To that end, it has been chosen the fast, deterministic, Sequential Quadratic Programming - SQP optimization algorithm to be coupled to the models that have been developed. The main reason for that choice is the possibility to manage tens, hundreds or even thousands of unknown parameters in a constrained output problem. This would be simply prohibitive from a computational point of view with, for example, stochastic methods such as the genetic algorithm approach. The coupling of the models to the SQP requires the determination of the Jacobian matrix associated to the model outputs. A schematic of the optimization model using SQP is presented in Fig. 1.30.

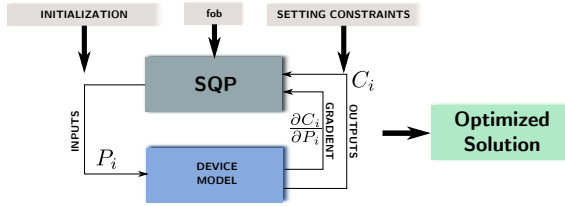


Figure 1.30: Optimization model: coupling to the SQP.

#### 1.4.3.7 The choice of the optimization tool: CADES - a framework for optimizations with a high number of parameters and constraints

The CADES (Component Architecture for the Design of Engineering Systems) [108] is a framework dedicated to simulation and optimization and it has been initially developed at the Grenoble Electrical Engineering Laboratory (G2ELAB) [109, 110, 98, 100]. It has been used, together with the software RelucTOOL [111, 112], as the design tool to implement the models developed in this thesis and to manage the coupling to the optimization algorithm. Details on this are presented in Chapter 6.

## 1.5 Thesis Proposal: BDFRM modeling for sizing by using optimization to address the bottleneck 1

### 1.5.1 Definition of the proposed BDFRM design procedure

The general concept behind the proposed procedure is to use a deterministic optimization algorithm in order to solve a complex electromagnetic design iteratively, whereas maximizing or minimizing an objective function. Roughly, optimization methods might be used in all machine development phases. However, every stage has its constraints and must have a model adapted for its purpose [99, 113] as introduced in the sequence.

### 1.5.1.1 Global Electromagnetic Models

For designing the BDFRM, three modeling levels using different approaches are proposed to calculate the machine electromagnetic performance, as depicted in Fig. 1.31.

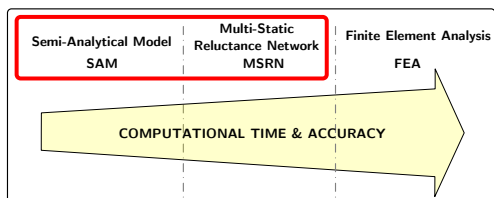


Figure 1.31: Three modeling levels approach.

The Semi-Analytical Model (SAM) relies on the BDFRM equivalent electrical circuit to calculate its outputs. The SAM is very useful for initial designs because it is fast and allows testing many different design variations.

The Multi-Static Reluctance Network Model (MSRN) uses a permeance network approach to discretize the electromagnetic domain and determine the operating conditions of the machine for a given excitation. It considers magnetic non-linearities and provides an interesting compromise between computation time and accuracy.

The Finite Element Analysis (FEA) is a two-dimensional model and it is used as the reference one to verify and validate the SAM and the MSRN. The software FEMM [97] has been used for the simulations shown throughout this work.

Only the SAM and the MSRN are coupled to the deterministic optimization algorithm. They are based on semi-analytical approaches and, therefore, their gradients can be exactly determined. In the context of this thesis, the SAM and the MSRN are Global Electromagnetic Models (GEMM), since they are used to determine exclusively the electromagnetic outputs of the machine.

### 1.5.1.2 Global Sizing and Optimization Models

The Global Electromagnetic Models SAM and MSRN are coupled to the Additional Sizing Equations (ASE) to form the Global Sizing and Optimization Models (GSOM). The ASE refer to analytical equations representing different aspects in the machine design. The ASE are mainly related to the description of the BDFRM physical dimen-

sions, calculating the geometrical relationships to define its topological structure. Additionally, they may also be constituted by many different sub-models to take into account iron losses, material costs, volume, mass, thermal aspects, etc. Fig. 1.32 illustrates the Global Electromagnetic Models and the Additional Sizing Equations in the context of the Global Sizing and Optimization Model.

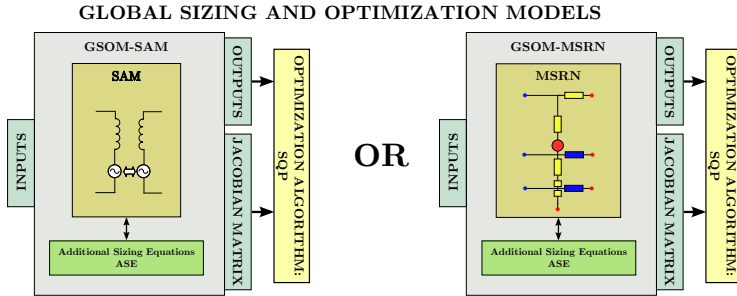


Figure 1.32: Overview of GSOM and GEMM models.

The Global Electromagnetic Models SAM and MSRN, when coupled to the ASE, form distinct GSOM models (GSOM-SAM and GSOM-MSRN). They share roughly the same ASE, but the electromagnetic outputs are calculated by using different approaches, impacting on model accuracy and calculation time. As a basic requirement, the GSOM must provide the outputs in terms of the inputs, as well as the associated partial derivatives, to be able to couple it to SQP optimization algorithm.

### 1.5.1.3 Proposed BDFRM design procedure

Fig. 1.33 depicts the proposed methodology on the design of the Brushless Doubly-Fed Reluctance Machine.



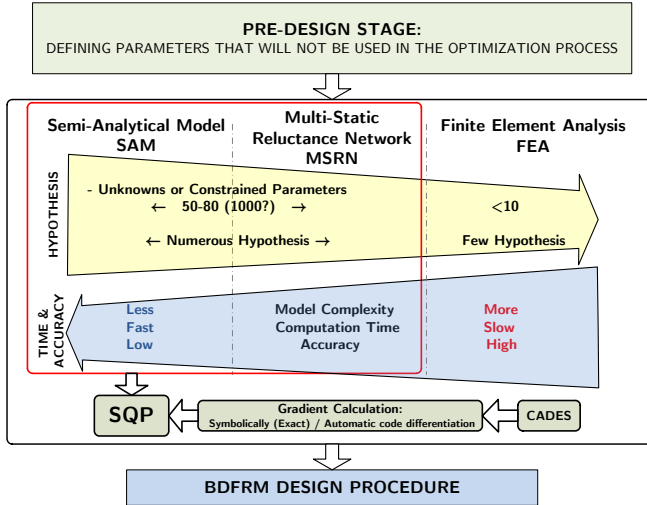


Figure 1.33: Proposed three modeling levels approach.

### 1.5.1.3.1 Pre-design definitions

The first step in the procedure addresses some pre-design definitions. All the parameters that are fixed in the beginning of the design process are defined at this pre-design stage and they are considered constants (fixed) in the optimization process. For example, depending on the application, it is desired to set a speed range within which the machine shall operate, which is directly related to the number of poles combinations of stator windings and rotor and the grid frequency ( $\omega_g$ ). From the definition of the number of poles, usually the number of stator and rotor slots can also be inferred.

### 1.5.1.3.2 Semi-Analytical Model (SAM)

Then, the first model to be used in the design process is the Semi-Analytical Model (SAM). At initial design stages, normally only a few specifications are available (e.g. power, terminal voltage and speed) and there is no information on how the machine will look like in the end. The designer is usually more interested in obtaining quickly the results, taking typically a few seconds, to test many possibilities and design constraints, assuming that the number of unknown parameters is huge. High accuracy in this phase is less important than computation time.

### 1.5.1.3.3 Multi-Static Reluctance Network model (MSRN)

The intermediary step is based on a Multi-Static Reluctance Network model (MSRN). This method uses a discretized domain (coarser than using finite element method) in order to reach a good compromise between precision and computation time. Additionally, it allows taking into account steel nonlinearities and also rotor movement effects (e.g. torque ripple and voltage harmonics) by executing multi-static calculations.

### 1.5.1.3.4 Finite Element Analysis (FEA)

The last stage is the Finite Element Analysis (FEA). This modeling level can be very often the preferred solution for machine analysis because of its accurate calculations. However, FEA is not very well adapted for early design stages due to the high number of unknown parameters (from some hundreds up to some thousands of constraints). If one is interested in testing distinct solutions by checking all possibilities on the constrained search space, using FEA may be impractical. The proposed methodology uses FEA to verify optimization results and, eventually, to optimize further the resulting design with just a few constraints (e.g. less than 10). The very last stage would be the prototype definition based on the model results.

### 1.5.1.3.5 Resulting design procedure characteristics

This procedure allows to design a BDFRM from just a few specifications. One starts with many unknowns parameters in a less complex model and gradually reduces the number of uncertainties whereas increasing calculation accuracy to define an optimized design.

## 1.5.2 Specific objectives and main contributions of this thesis

From the discussion previously presented, the specific objectives of the thesis can finally be stated:

1. Perform a literature review on wind power system, choose the machine to be further investigate (BDFRM) and study its operating principles;
2. Develop the proposed optimization-oriented electromagnetic models (SAM and MSRN) and couple them to the Additional Sizing Equations (ASE);

3. Implement the BDFRM global sizing and optimization models targeting the use of a deterministic optimization approach, considering the different goals in the design process, and verify the models through comparisons with Finite Element Analysis (FEA) simulations;
4. Specify and realize a BDFRM prototype to validate the models through experimental results;
5. Perform optimization studies with the proposed BDFRM design procedure.

In general terms, the activities performed during this thesis can be divided in five main topics. The first refers to the study of the BDFRM and its operating principles in the context of wind power. The second discusses the BDFRM electromagnetic modeling aspects using different approaches and on the definition of additional sizing equations to complement them. The implementation of the models focusing on deterministic optimization and their verification through simulations using FEA are considered the third topic. The fourth aspect refers to the BDFRM prototype: firstly, its specification by using an optimization approach is presented. Then, the experimental data obtained from the prototype have been confronted to the simulation results to validate the models. The fifth aspect explores through a case study the use of the proposed BDFRM design procedure for wind power applications.

The obtained results provide technical and methodological contributions to this research field. The main ones are highlighted in the sequence:

1. *The development of the optimization-oriented BDFRM Semi-Analytical Model (SAM).* The SAM collects and put together from different references many design equations for sizing a BDFRM. The BDFRM equivalent electric circuit (EEC) expressions coupled to the Additional Sizing Equations (ASE) allows to establish important constraints for machine design. Furthermore, this model is transformed into an optimization model where its output/input relationships and the associated Jacobian matrix are calculated. The model is then solved iteratively by using the SQP optimization algorithm in a constrained input/output problem.
2. *The development of the optimization-oriented BDFRM Multi-Static Reluctance Network model (MSRN)* The MSRN implements a BDFRM static reluctance network model and provides means to

effectively take into account multi-static simulations, by considering simultaneously the rotating field and rotor movement. It implements an air-gap model and a source rotation procedure that provides a computationally efficient technique, using the symmetry principle, to perform these tasks. The model presents a very interesting trade-off between computation time and accuracy, comparable to FEA when global performance parameters are assessed. Moreover, the model calculates the Jacobian matrix required for coupling to the SQP algorithm, providing a fast and accurate model that is explored in the context of deterministic optimizations.

3. *The proposition of a BDFRM design procedure.* The methodology considering the three modeling levels coupled to optimization provide the necessary elements to refine step by step the BDFRM design from just a few specifications up to the final optimal machine for a specific application. A case study is presented in Chapter 9.
4. *The realization of the BDFRM prototype.* We were able to specify and realize a reduced scale BDFRM prototype by using an optimization approach as presented in Chapter 8. Since there are just a few experimental machines of this kind around the world up to this date, the initial results and the ones that can be obtained in perspective of this thesis by using this machine are also highlighted as a contribution.

## 1.6 Final considerations

From a review on wind power applications, the first part of this chapter addressed their basis, requirements, market trends and technological issues. In the context of the proposed work, the Brushless Doubly Fed Reluctance Machine (BDFRM) has been chosen to be further investigated as a possible candidate to replace the most used solution nowadays in wind power application, notably the Doubly Fed Induction Generator (DFIG). In the second part of this chapter, a review on the BDFRM historical background has been presented and its basic operating principles has been discussed. Then, considerations regarding the BDFRM design complexity have been highlighted and the thesis proposal has been outlined.

# Chapter 2

## Definition of the structural topology of the BDFRM to be investigated

### Abstract

*This chapter discusses the choice of the BDFRM structural topology that will be investigated in this thesis. The goal is to define the parameters that are fixed and that are not part of the optimization process, such as the number of poles, the rotor type and the number of stator and rotor slots. The arguments and the criteria used for defining the stator and rotor topologies are presented, based on previous works available in the literature.*

### 2.1 Rotor topology

#### 2.1.1 The choice of the radially laminated ducted rotor (RLDR) to be used in the BDFRM

The rotor geometry is a major factor on the BDFRM design. Although very useful to understand the BDFRM electromagnetic operating principles, the Salient Pole Rotor (SPR) is known for its inferior performance when compared to other solutions [11]. Recent researches, introduced in Section 1.2.1, indicate that the axially laminated type (ALR) offers good coupling, but presents higher magnetic losses due to the absence of radial laminations. These studies concluded that

the radially laminated ducted rotor version (RLDR) provides the best compromise between higher performance and lower rotor iron losses and this will be the one considered when developing the models in the subsequent chapters.

### 2.1.2 The use of iron bridges (ribs) for mechanical robustness

Ideally, the ducted rotor should act as a perfect flux guide. In other words, all the flux lines flowing into one flux path should get out at the other extremity without any leakage between adjacent flux paths. This implies in the consideration that the magnetic material is infinitely permeable and that there is no connection between flux paths. Fig. 2.1a illustrates one rotor pole of an idealized rotor.

In a real rotor, however, the magnetic steel has finite permeability and some means for mechanical robustness shall be provided. It is out of the scope of this work to perform a deep investigation in the mechanical structure of the rotor. For this reason, the chosen rotor topology is inspired in previous prototypes presented in the literature. Just to cite some examples, Xu *et al.* [10] highlight the need to minimize any kind of rotor losses and proposes the use of epoxy bonding materials to hold all laminated segments. Knight *et al.* [82] investigates some rotor variation using iron bridges and/or dovetails for assembling rotor poles. Targeting the simplest rotor topology for manufacturing, it has been chosen the solution that has only iron bridges to provide mechanical integrity, as shown in Fig. 2.1b for one rotor pole. This geometry resembles the one used in [82]. The ideal rotor geometry shown in Fig. 2.1a will be designate in this work by “DRI” whereas the practical rotor geometry in Fig. 2.1b will be referred as “DRNI”.

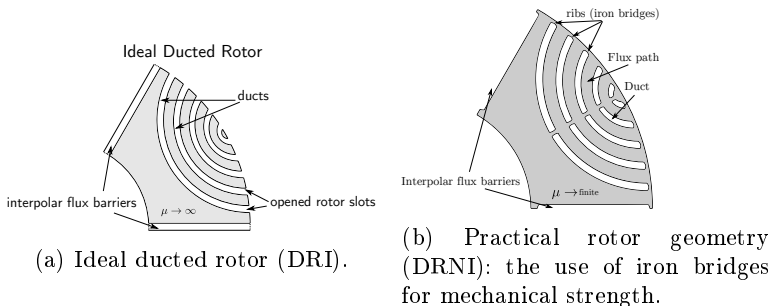


Figure 2.1: An ideal (a) *versus* a practical (b) ducted rotor.

## 2.2 Pre-design definitions

### 2.2.1 Discussion on the criteria for choosing the number of poles of grid and control windings and consequently the rotor number of poles

This section makes a brief literature review on the criteria to choose the number of poles combination in the BDFRM. In this work, the following notation will be used: the grid winding is defined as the one that is connected directly to the power system and the control winding is the one connected to the power system through a back-to-back converter. Fig. 2.2 illustrates these definitions. The combination of the number of poles of grid, control and rotor will be represented in the form Pg-Pc-Pr. For example, 8-4-6 indicates a machine with grid, control and rotor number of poles of, respectively, 8, 4 and 6.

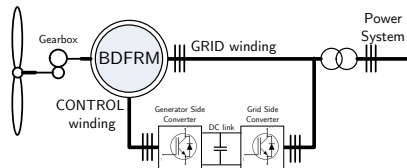


Figure 2.2: Definition of grid and control windings considering the BDFRM topology.

#### 2.2.1.1 Possible combinations based on the requirements for torque production and their respective coupling factors

The choice of the correct combination of the number of poles depends on many aspects. The first and most important one is to respect the coupling conditions for torque production, deduced in Section 1.2.2.5. However, there are good and bad alternatives among them that must be further evaluated.

Knight *et al.* [81, 82, 11] propose a solution to quantitatively determine the coupling factors for different combinations of the number of poles in order to help the designer to choose the most appropriated solution for a specific application. By using an idealized machine, a normalized function  $\beta$  of the air-gap flux density is defined, using as the reference function the maximum value that one can obtain by using the air-gap flux density of a round rotor, without any saliency:

$$\beta(\theta_{ag}) = \frac{B_{gap}}{B_{round}^{pk}} \quad (2.1)$$

where:

- $\theta_{ag} \triangleq$  angle around the air-gap.
- $B_{gap} \triangleq$  air-gap flux density of the radially laminated ducted rotor. This function is calculated for each combination of the number of poles
- $B_{round}^{pk} \triangleq$  amplitude of the air-gap flux density function that one would obtain if a solid (round) rotor were used.

The magnitude of the Fourier series of the normalized function  $\beta$  for each combination of the number of poles is calculate, providing a quantitative mean to asses the coupling capacity of each one of them. Details on this strategy are outlined in Appendix C.2. Table 2.1 shows the resulting coupling factor calculated by using the approach proposed in the aforementioned references for several combinations. In this table, *cc* and *gg* are the self coupling factor of control and grid windings and *gc* is the mutual coupling factor between the windings. Since the speed is a function of the number of poles, the synchronous speed ( $\omega_c = 0$ ) for  $\omega_g = 2\pi 50$  is also shown in Table 2.1.

Table 2.1: Ideal coupling factors [11].

Number of Poles			Coupling Factors			wrmsync
Pg	Pc	Pr	Ccc	Cgc=Ccg	Cgg	[rpm]
8	4	2	0,0000	0,0000	0,0000	1500
6	2	4	0,1817	0,3183	0,6061	750
6	4	5	0,3831	0,4677	0,5780	600
10	2	6	0,0865	0,2067	0,5827	500
8	4	6	0,2933	0,4135	0,6034	500
14	2	8	0,0498	0,1501	0,5643	375
12	4	8	0,1817	0,3183	0,6061	375
10	6	8	0,3499	0,4502	0,5900	375
18	2	10	0,0323	0,1169	0,5520	300
16	4	10	0,1216	0,2523	0,5946	300
14	6	10	0,2477	0,3784	0,6081	300
12	8	10	0,3831	0,4677	0,5780	300
22	18	20	0,4454	0,4918	0,5447	150



### 2.2.1.2 Restrictions with a rotor with 4 poles

It can be seen in Table 2.1 that the combination 8-4-2 provides no coupling when the RLDR is considered and it cannot be used. Regarding the 6-2-4, the 4 rotor poles version, illustrated in Fig. 2.3, it can be noticed that it has a reduced coupling factor when compared to other alternatives. This would be by itself a reason to avoid this choice, but this solution has an additional drawback: if a third harmonic is induced in the 2-poles windings due to, for example, saturation, it will cause an unwanted coupling to the 6-pole winding, degrading even further machine performance [11, 114, 9]. For these reasons, this solution should be avoided.

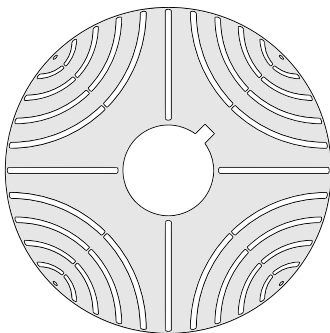


Figure 2.3: Cross-sectional view of the RLDR topology with 4 poles.

### 2.2.1.3 Unbalanced magnetic pull in rotors with an odd number of poles

There are in the literature studies considering BDFRMs with odd number of rotor poles [10, 7], as depicted in Fig. 2.4a for a machine with 5 rotor poles. This may cause some confusion at first sight, however the terminology “number of rotor poles” actually means the number of parts into which the ducted rotor is divided. For example, the rotor shown in Fig. 2.3 has 4, whereas in Fig. 2.4a there is 5 rotor parts (or poles). At any case, there will always be in the air-gap an even number of *magnetic poles*, even if the number of rotor parts (poles) are odd [11].

Table 2.1 indicates that the 6-4-5 machine have an interesting coupling factor. However, an odd number of rotor poles presents an unbalanced magnetic pull - UMP (radial forces) in the shaft [78, 5, 79, 82, 11].

The equivalent UMP on this number of poles combination is illustrated in Fig. 2.4b. As this may reduce the lifetime expectancy of the bearings, a solution with an odd number of rotor poles must also be avoided.

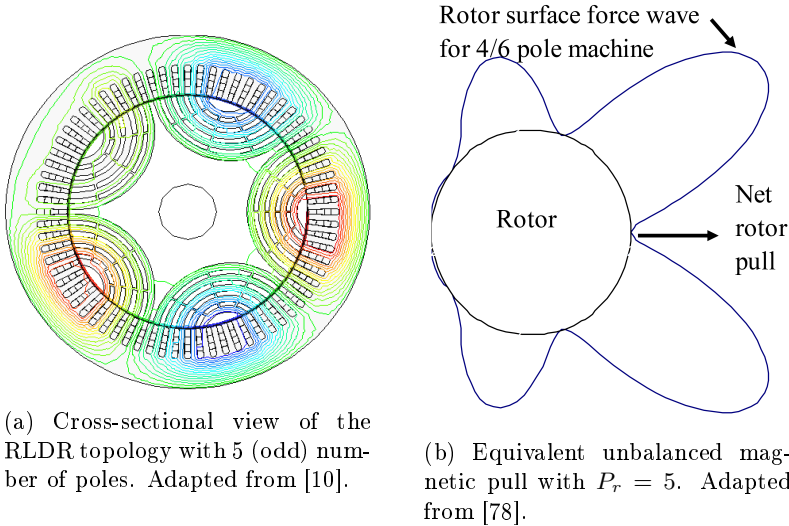


Figure 2.4: (a) BDFRM with 5 rotor poles and (b) the schematic of the unbalanced magnetic pull when an odd number of poles is considered.

#### 2.2.1.4 Number of poles definition for the machine to be investigated

Previous discussion indicates that the minimum number of rotor poles should be 6 to improve machine performance. Additionally, not only the mutual coupling factor is important when choosing the number of poles, since the speed is also a function of this choice as shown in Table 2.1. For this reason, application requirements on this parameter shall also be taken into account. A higher operational speed means more power per unit torque, which is proportional to machine volume. Since the BDFRM has no permanent magnets to improve torque density, it is, a priori, desirable to operate at the highest possible speed to limit generator size.

In this work, it has been chosen the 8-4-6 machine for the following reasons:

- it provides an acceptable high mutual coupling factor;

- there will be no significant unbalanced magnetic pull;
- it has the highest synchronous speed among the most indicated combinations.

## 2.2.2 The choice of the number of stator and rotor slots

### 2.2.2.1 Number of stator slots

The stator windings in the BDFRM are placed into slots. The choice of the number of slots is a decisive step that will impact the final characteristics of the machine. It must be an integer number and it is a function of the number of poles ( $P$ ), the number of phases ( $m$ ) and the desired number of slots per pole per phase ( $q$ ), given by [37]:

$$N_{sl} = 2mq \frac{P}{2} \quad (2.2)$$

As a general rule, the more stator slots there are, the more sinusoidal the magnetomotive force will be in the air-gap. However, this increases the number of coils and the price of the machine [37]. In this work, it has been decided to use a minimum of 2 slots per pole per phase in order to improve the sinusoidal distribution of the three phase windings and, at the same time, to keep the machine as simple as possible to manufacture. Thus, the minimum number of slots required for assembling the three-phase, 8-poles winding (worst case) is:

$$N_{sl} = 2mq_g \frac{P_g}{2} = 2 \cdot 3 \cdot 2 \cdot \frac{8}{2} = 48 \quad (2.3)$$

which is the number of slots chosen for the BDFRM to be investigated in this research.

Consequently, the number of slots per pole per phase of the 4-poles winding will be 4.

$$q_c = \frac{N_{sl}}{2m} \frac{2}{P_c} = \frac{48}{2 \cdot 3} \cdot \frac{2}{4} = 4 \quad (2.4)$$

### 2.2.2.2 Number of rotor slots

The combination of the number of stator and rotor slots may produce undesirable torque and voltage harmonics and their values should

be selected to minimize these effects. As a general guideline, lower-order slotting harmonics “ $h$ ” with the same space order generated by rotor and stator slots shall be avoided [11].

Vagati *et al.* [115] suggests values for  $N_{sl}$  and  $N_{slr}$  aiming the minimization of the torque ripple for the Synchronous Reluctance Machine. For a  $P$ -pole machine, the slotting harmonics can be calculated by [11]:

$$h_s = P \left( 1 \pm m \frac{N_{sl}}{P} \right) \quad (2.5)$$

$$h_r = P \left( 1 \pm n \frac{N_{slr}}{P} \right) \quad (2.6)$$

where:

$P$	is the number of poles
$m, n$	are integers
$N_{sl}$	is the number of stator slots
$N_{slr}$	is the number of rotor slots

Knight *et al.* [11] highlight the additional constraints for the BDFRM due to the two stator winding sets with different number of poles. They proposed the following equations to assess the slotting harmonics on this machine:

$$h_{sg} = P_g \left( 1 \pm m \frac{N_{sl}}{P_g} \right) \quad (2.7)$$

$$h_{sc} = P_c \left( 1 \pm m \frac{N_{sl}}{P_c} \right) \quad (2.8)$$

$$h_{rg} = P_g \left( 1 \pm n \frac{N_{slr}}{P_g} \right) \quad (2.9)$$

$$h_{rc} = P_c \left( 1 \pm n \frac{N_{slr}}{P_c} \right) \quad (2.10)$$

where indexes  $g$  and  $c$  refers, respectively, to grid and control windings.

An additional criterion to be taken into account is that the number of rotor slots ( $N_{slr}$ ) must be an integer multiple of the number of rotor poles  $P_r$ , which is in this case 6. Reasonable practical possibilities for  $N_{slr}$  are 54, 60, 66 and 72. Solution of equations (2.7) to (2.10) allows to identify the lowest matching harmonics for these combinations, assuming  $N_{sl} = 48$ . The calculations are presented in Appendix G and Table 2.2 shows the resulting values.

Table 2.2: Lower matching slotting harmonics considering some combinations for the number of stator and rotor slots.

$N_{sl}$	$N_{slr}$	<b>Lower matching space order</b>	
48	54	104	104
48	60	52	56
48	66	136	140
48	72	136	140

A good design should select the number of stator/rotor slots combination with the highest possible value of the lowest matching space order to minimize harmonics effects. Table 2.2 shows that the  $N_{slr} = 66$  or  $N_{slr} = 72$  are the best ones according to this criterion. In [80], it is presented a study comparing these both rotor designs by using Finite Element Analysis. It has been found that the design with 66 rotor slots has, a priori, a slightly higher mean torque with comparable torque ripple. Since a rotor with 66 slots is potentially easier to manufacture than the one with 72, the  $N_{slr} = 66$  version is selected.

## 2.3 Stator topology

### 2.3.1 Stator laminations

The BDFRM stator laminations are formed by 48 opened slots, as shown in Fig. 2.5. The BDFRM stator looks like the one of an induction machine, the only difference being the required slot area to accommodate both three phase winding sets of the BDFRM.

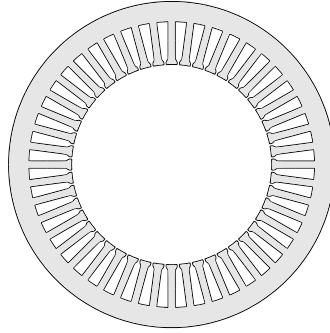


Figure 2.5: Cross-sectional view of the stator laminations.

### 2.3.2 Criteria to select the grid as the winding with the highest number of poles

Although, a priori, both winding sets may be assigned to be either the grid or the control winding, a choice shall usually be made in design phase about which one will have the higher number of poles. In the literature, there are still a limited number of references that investigate this topic.

In [9], a discussion on the selection criteria is introduced, analyzing the differences from the stator and rotor iron losses perspective. Since the iron losses estimation in the BDFRM is a difficult task due to the dual winding - dual frequency configuration (iron losses in the BDFRM will be further discussed in Section 5.3.1.2), they conclude that, although it seems to exist a preference for choosing the grid winding with the higher number of poles, more researches must be pursued to confirm this choice. In [11], it is suggested that the grid winding shall have the higher number of poles to maximize the specific electrical loading.

Since there is still no ultimate consensus on this choice, the machine to be investigate in this work follows the trend identified in the literature. Therefore, the grid windings has been set to be the one with the higher number of poles, with 8 poles, leaving the control winding with 4 poles.

### 2.3.3 Grid winding (8 poles) definition

Once the number of poles of grid winding has been chosen, it is possible to defined the winding's position in the slots. It is considered

a full-pitch winding and Fig. 2.6 presents the position of each one of the three phases around the machine air-gap.

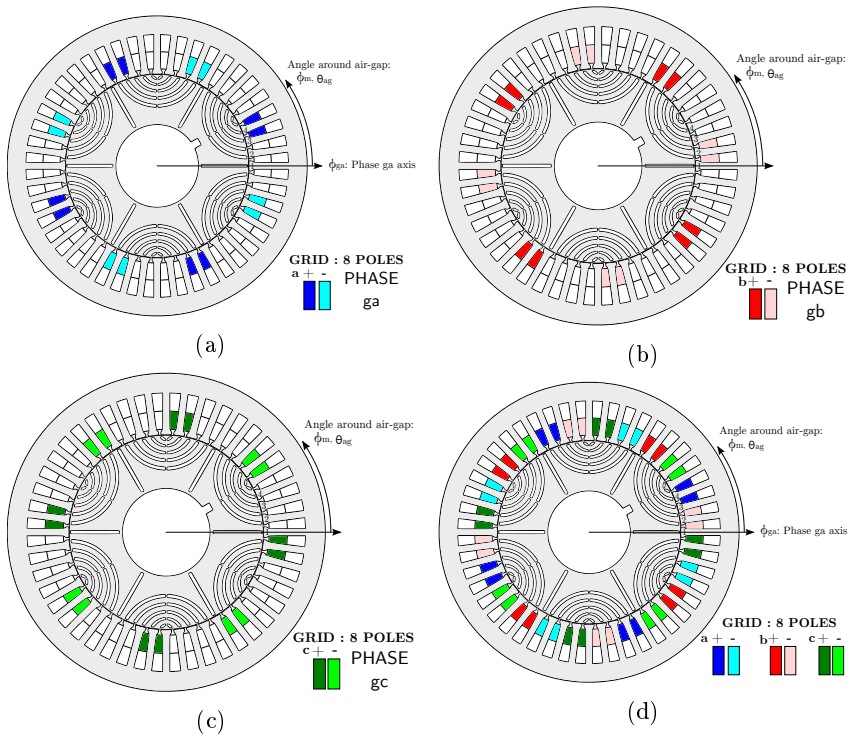


Figure 2.6: Definition of the position of the grid winding phases around the air-gap.

The following definitions are used throughout this thesis to refer to each one of the phases of the grid winding:

- $ga$  → Phase A of grid winding
- $gb$  → Phase B of grid winding
- $gc$  → Phase C of grid winding

### 2.3.4 Control winding (4 poles) definition

Similarly, Fig. 2.7 shows all the three phases for the control winding with 4 poles, with their respective position around the machine air-gap. The control windings is a full-pitch winding as well.

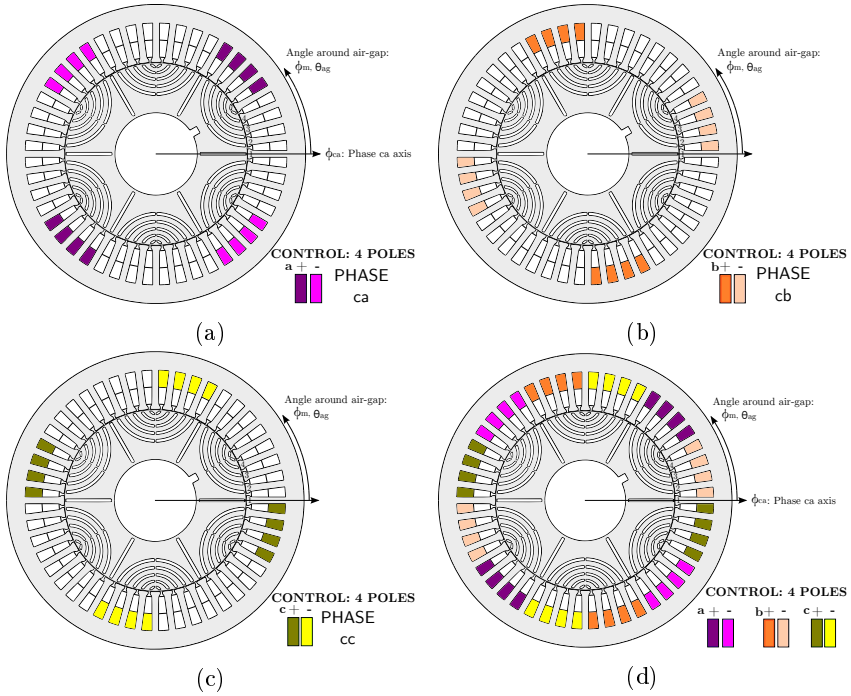


Figure 2.7: Definition of the position of the control winding phases around the air-gap.

The following definitions are used throughout this thesis to refer to each one of the phases of the control winding:

- $ca \rightarrow$  Phase A of control winding
- $cb \rightarrow$  Phase B of control winding
- $cc \rightarrow$  Phase C of control winding



## 2.4 Topological structure of the machine to be investigated

### 2.4.1 Resume of the fixed parameters for the investigated machine

Table 2.3 resumes the parameter choices that have been discussed in the preceding sections. These parameters are fixed and will not be considered as variables to be optimized

Table 2.3: Fixed parameters (not considered in the optimization).

<b>Parameter</b>	<b>Description</b>	<b>Value</b>
$N_{sl}$	Number of stator slots	48
$N_{slr}$	Number of rotor slots	66
$P_g$	Number of poles of the grid winding	8
$P_c$	Number of poles of the control winding	4
$P_r$	Number of poles of the rotor	6

### 2.4.2 The chosen topology

Considering the fixed parameters from Table 2.3, Fig. 2.8 illustrates the machine topology that will be considered in this work with the respective windings.

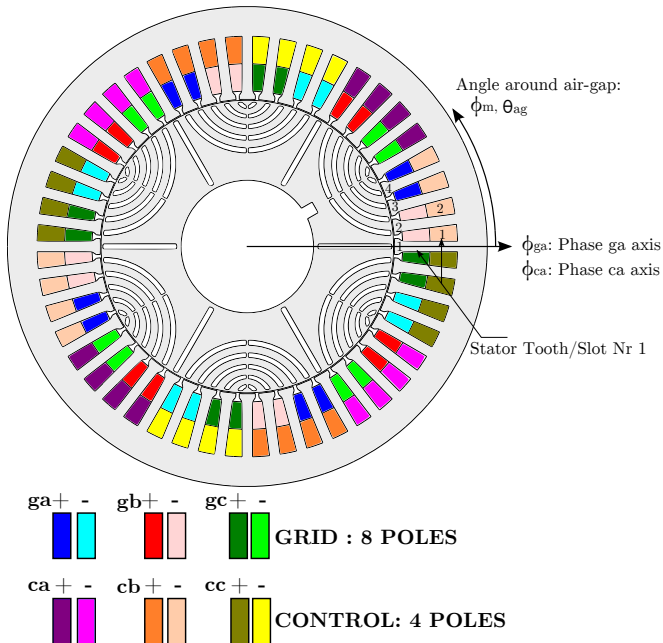


Figure 2.8: Considered BDFRM topology to be investigated.

### 2.4.3 The chosen power level

A prototype is manufactured and tested to validate the models that are developed in this thesis and it was necessary to keep its cost at reduced values. To match the power level of the practical device, the models focus on the design of low power machines ( $\approx 1kW$ ). They could, however, be adapted with minor modifications for designing higher power machines.

## 2.5 Final considerations

Based on the literature, this chapter presented the criteria that have been used to choose design parameters that are fixed in the machine design process. Next chapter presents the Semi-Analytical model of the BDFRM.

# Chapter 3

## BDFRM Semi-Analytical Model (SAM)

### Abstract

*This chapter presents the Semi-Analytical Model (SAM), which is based on the solution of the steady-state equivalent electrical circuit (EEC) of the BDFRM. SAM's goal is to provide a computationally fast model that helps the designer to test many possibilities and constraints at earlier design stages. Fundamentally, it permits to better understand the main phenomena taking place on machine operation. The SAM is a linear model and it relies on the estimation of the air-gap flux density to calculate the electromagnetic output parameters. In the following sections, a procedure to evaluate the phase voltages, power, torque and flux densities in the stator teeth, yoke and in the rotor flux paths is set forth.*

### 3.1 Basic principles and requirements to obtain an Equivalent Electric Circuit (EEC)

#### 3.1.1 Electromagnetic principles

The Semi-Analytical Model (SAM) is a BDFRM optimization-oriented global electromagnetic model (GEMM) based on the performance parameters calculation in steady state by using an equivalent electric circuit (EEC) approach. It is a linear model and, therefore, it does not take into account magnetic saturation.

The SAM relies on the analytical determination of the air-gap flux density ( $B_{gap}$ ). From  $B_{gap}$  results, the winding functions theory [46, 47, 40, 44, 45, 87] is used to calculate the fluxes linkages among the phases. By considering the excitation of one phase (out of 6 total) at a time, one can determine the self and mutual fluxes for each phase individually and the respective inductances. Then, with all the EEC lumped parameters known, it is possible to solve its steady-state equations to obtain the internal and terminal voltages and, consequently, the power and the electromagnetic torque. The estimation of  $B_{gap}$  is also used to assess the flux density levels in the stator teeth, yoke and in the rotor flux paths.

### 3.1.2 Hypothesis

To obtain the SAM's equivalent electric circuit, the following idealized assumptions are considered:

- The magnetic material has infinite permeability;
- The stator windings are uniformly distributed in space (i.e. they can be modeled adequately by sinusoidal functions);
- The excitation currents (inputs) can also be represented by sinusoidal waveforms;
- The stator and rotor surfaces are smooth. Carter's coefficient is used to compensate slotting effects.
- The grid and control three phase windings are balanced so that the calculation of only one phase of each one is required.
- The magnetic material is lossless;
- The radially laminated ducted rotor (RLDR) is considered as an ideal flux guide (all flux lines entering in a flux path will get out at its respective extremity, without any leakage among the adjacent flux paths).

### 3.1.3 Outputs definition

The SAM is responsible for calculating the outputs related to the electromagnetic behavior of the BDFRM as a function of machine structural physical dimensions and excitation conditions. Basically, SAM's output are voltages, power, electromagnetic torque and flux densities

in several parts of the machine (e. g. stator teeth, yoke and rotor flux paths). Since the SAM is a linear model, the latter are important to provide to the designer means to assess the actual iron magnetization levels. Consequently, it is possible to restrict the solution domain so that the induction remains within reasonable practical values (material non-saturated region). When the SAM is coupled to the SQP, the flux density parameters may be constrained ( $0 < B_{actual} < B_{max}$ ) in order to limit the optimization algorithm search space.

Table 3.1 depicts the SAM outputs to be evaluated.

Table 3.1: Outputs definition of the Semi-Analytical Model.

<b>Parameter</b>	<b>Description</b>
$T_{em}$	Mean value of the electromagnetic torque [ $Nm$ ].
$E_{ga_{rms}}$	Internal induced rms phase voltage ( $ga$ ) [ $V$ ]
$E_{ca_{rms}}$	Internal induced rms phase voltage ( $ca$ ) [ $V$ ]
$V_{ga_{rms}}$	Terminal output rms phase voltage ( $ga$ ) [ $V$ ]
$V_{ca_{rms}}$	Terminal output rms phase voltage ( $ca$ ) [ $V$ ]
$P_{ga\_int}$	Internal real power per phase (calculated from $E_{ga}$ ) [ $W$ ]
$P_{ca\_int}$	Internal real power per phase (calculated from $E_{ca}$ ) [ $W$ ]
$P_{ga\_ter}$	Terminal real power per phase (calculated from $V_{ga}$ ) [ $W$ ]
$P_{ca\_ter}$	Terminal real power per phase (calculated from $V_{ca}$ ) [ $W$ ]
$B_{th}$	Induction levels in stator teeth [ $T$ ]
$B_{yk}$	Induction levels in stator yoke [ $T$ ]
$B_{rt}$	Induction levels in rotor teeth (flux paths) [ $T$ ]

### 3.1.4 Model Structure: definition of the three sub-models

The Semi-Analytical Model is divided into three sub-models as illustrated in Fig. 3.1, which depicts the basic flowchart to evaluate model outputs. The following sections will describe in details the procedure to define each one of these sub-models.

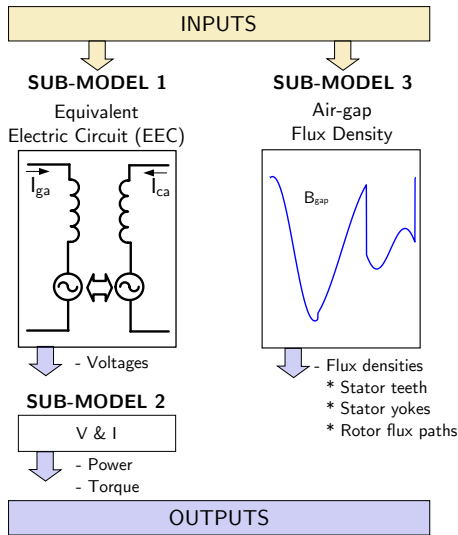


Figure 3.1: Simplified schematic of the SAM model.

## 3.2 Sub-model 1: equivalent electric circuit to determine phase voltages

The definition of the BDFRM equivalent electric circuit presented in this section is based on former works [46, 47, 40, 44, 45] available in the literature. Firstly, the general dynamic voltage equations are stated and, in the sequence, the procedure to calculate the machine inductances by using the winding function is presented.

### 3.2.1 General voltage equations describing the electromagnetic behavior of the BDFRM

In electric machine theory, the deduction of an analytical model usually starts by the determination of the voltage equations for each one of the phase windings. By inspection, six equations are necessary for the BDFRM due to the two sets of three phase windings:

$$v_{g,abc} = R_g i_{g,abc} + \frac{d\lambda_{g,abc}}{dt} \quad (3.1)$$

$$v_{c,abc} = R_c i_{c,abc} + \frac{d\lambda_{c,abc}}{dt} \quad (3.2)$$

where  $R_g$  and  $R_c$  are the phase resistances from grid and control windings, respectively. The phase resistances are calculated by the Additional Sizing Equation (ASE) in terms of the number of turns and machine geometric dimensions. Therefore, from SAM point of view, they are inputs, since SAM evaluates only the *electromagnetic* output parameters.

The following vector nomenclature is used for the three phase voltages and currents:

$$v_{g,abc} = \begin{pmatrix} v_{ga} \\ v_{gb} \\ v_{gc} \end{pmatrix}, v_{c,abc} = \begin{pmatrix} v_{ca} \\ v_{cb} \\ v_{cc} \end{pmatrix}, i_{g,abc} = \begin{pmatrix} i_{ga} \\ i_{gb} \\ i_{gc} \end{pmatrix} \text{ and } i_{c,abc} = \begin{pmatrix} i_{ca} \\ i_{cb} \\ i_{cc} \end{pmatrix}$$

The phase flux linkages  $\lambda_{g,abc} = \begin{pmatrix} \lambda_{ga} \\ \lambda_{gb} \\ \lambda_{gc} \end{pmatrix}$ ,  $\lambda_{c,abc} = \begin{pmatrix} \lambda_{ca} \\ \lambda_{cb} \\ \lambda_{cc} \end{pmatrix}$  can be rewritten in terms of their respective inductances. In a general way [47].

$$\lambda_{g,abc} = L_{g,abc} i_{g,abc} + L_{gc,abc} i_{c,abc} \quad (3.3)$$

$$\lambda_{c,abc} = L_{gc,abc} i_{g,abc} + L_{c,abc} i_{c,abc} \quad (3.4)$$

where:

$$L_{g,abc} = \begin{pmatrix} L_{gaga} & L_{gagb} & L_{gagc} \\ L_{gbga} & L_{gbgb} & L_{gbgc} \\ L_{gcga} & L_{gccb} & L_{gcgc} \end{pmatrix}$$

$$L_{c,abc} = \begin{pmatrix} L_{caca} & L_{cacb} & L_{cacc} \\ L_{cbca} & L_{cbcb} & L_{cbcc} \\ L_{ccca} & L_{cccb} & L_{cccc} \end{pmatrix}$$

$$L_{gc,abc} = \begin{pmatrix} L_{gaca} & L_{gacb} & L_{gacc} \\ L_{gbca} & L_{gbcb} & L_{gbcc} \\ L_{gcc a} & L_{gcc b} & L_{gcc c} \end{pmatrix}$$

In matrix form, the grid and control windings voltage equations can be written as:

$$\begin{bmatrix} v_{ga} \\ v_{gb} \\ v_{gc} \\ v_{ca} \\ v_{cb} \\ v_{cc} \end{bmatrix} = \begin{bmatrix} \left( \begin{matrix} L_{gaga} & L_{gagb} & L_{gagc} \\ L_{gbga} & L_{gbgb} & L_{gbgc} \\ L_{gcga} & L_{gcgb} & L_{gcgc} \end{matrix} \right) \\ \left( \begin{matrix} L_{gaca} & L_{gacb} & L_{gacc} \\ L_{gbca} & L_{gbcb} & L_{gbcc} \\ L_{gcc a} & L_{gcc b} & L_{gcc c} \end{matrix} \right) \end{bmatrix} \begin{bmatrix} i_{ga} \\ i_{gb} \\ i_{gc} \\ i_{ca} \\ i_{cb} \\ i_{cc} \end{bmatrix} \quad (3.5)$$

It can be noticed that, to obtain the phase voltages, it is necessary to determine the phase inductances which are calculated as a function of machine dimensions.

## 3.2.2 Self and mutual flux linkages and inductances calculation

### 3.2.2.1 The use of the winding functions approach to calculate inductances in the BDFRM

The winding function technique has been chosen to calculate the self and mutual inductances in the SAM. The basic principles regarding this technique are introduced in Appendix A.1, based on [87]. Xu *et al.* [46] and Liang *et al.* [47] originally proposed to use this method to evaluate inductances in the BDFRM and this approach has been further used by other authors, for example, in [40, 45, 49, 44]. In [44], it is presented a detailed deduction of the inductance expressions for the BDFRM using this concept for the salient pole rotor version (SPR). As the radially laminated ducted rotor version (RLDR) is considered in this work, the SPR inductance equations cannot be directly used. The procedure to calculate the machine inductances taking into account the RLDR rotor is shown in the sequence.



### 3.2.2.1.1 Flux linkage calculation by using the winding function theory

The winding function theory states that the flux linkage and, consequently, the inductances associated to each winding can be readily evaluated by using the following integral [87, 44]:

$$\lambda_{ij} = r_{gap} L_{stkef} \int_0^{2\pi} B_{i_{gap}}(\theta_{ag}) w_j(\theta_{ag}) d\theta_{ag} \quad (3.6)$$

$$L_{ij} = \frac{\lambda_{ij}}{I_i} \quad (3.7)$$

where:

- $i$  and  $j$  → phase indexes that may assumed  $c$  and  $g$  values, representing the phases of control and grid windings, respectively (self and mutual inductances may be calculated by this approach)
- $B_{i_{gap}}(\theta_{ag})$  → spatial distribution of the magnetic flux density in air-gap due to phase  $i$
- $w_j(\theta_{ag})$  → winding function of winding  $j$
- $L$  → phase inductance
- $I_i$  → DC current used to generate the magnetic flux at phase  $i$
- $r_{gap}$  → air-gap radius
- $L_{stkef}$  → machine effective axial length

The functions  $B_{i_{gap}}(\theta_{ag})$  and  $w_j(\theta_{ag})$  must be determined to evaluate (3.6) and the procedure is shown in the sequence.

### 3.2.2.1.2 Winding function per phase

The winding function may be considered as a normalized (unitless) function of the spatial magnetomotive force (MMF) distribution of a winding. It represents the continuous distribution of the winding turns and the following equation can be used to determine  $w$  if  $\mathbb{F}_{1\phi}$  is known [87, 44]:

$$w_j(\theta_{ag}) = \mathbb{F}_{1\phi}(\theta_{ag})/I \quad (3.8)$$

where  $\mathbb{F}_{1\phi}$  is the single phase MMF and  $I$  the current used to generate it.

Equation (3.8) can be used to calculate all the winding functions by analytically assessing the single phase contribution of the MMF generated by each phase winding. Based on the hypothesis previously

mentioned, only the fundamental component of the MMF will be considered in the SAM and, for each phase, it is given by [88]:

$$\mathbb{F}_{1\phi}(\theta_{ag}) = M_{1\phi} \cos\left(\frac{P_g}{2}\theta_{ag} + \phi\right) I \quad (3.9)$$

where  $\phi$  is an angle representing the phase axis.

$M_{1\phi} = \frac{4}{\pi} \frac{Nph \cdot Kw}{P}$ , where  $Nph$  is the total number of turns per phase,  $Kw$  is the winding factor and  $P$  the number of poles.

Thus, the winding functions of each phase can be shown to be:

For grid winding:

$$\begin{aligned} w_{ga}(\theta_{ag}) &= M_{1\phi g} \cdot \cos\left(\frac{P_g}{2}\theta_{ag} + \phi_{ga}\right) \\ w_{gb}(\theta_{ag}) &= M_{1\phi g} \cdot \cos\left(\frac{P_g}{2}\theta_{ag} + \phi_{ga} - 2\pi/3\right) \\ w_{gc}(\theta_{ag}) &= M_{1\phi g} \cdot \cos\left(\frac{P_g}{2}\theta_{ag} + \phi_{ga} + 2\pi/3\right) \end{aligned} \quad (3.10)$$

where:

$$M_{1\phi g} = \frac{4}{\pi} \frac{Nphg \cdot Kwg}{P_g}$$

For control winding:

$$\begin{aligned} w_{ca}(\theta_{ag}) &= M_{1\phi c} \cos\left(\frac{P_c}{2}\theta_{ag} + \phi_{ca}\right) \\ w_{cb}(\theta_{ac}) &= M_{1\phi c} \cos\left(\frac{P_c}{2}\theta_{ag} + \phi_{ca} - 2\pi/3\right) \\ w_{cc}(\theta_{ac}) &= M_{1\phi c} \cos\left(\frac{P_c}{2}\theta_{ag} + \phi_{ca} + 2\pi/3\right) \end{aligned} \quad (3.11)$$

where:

$$M_{1\phi c} = \frac{4}{\pi} \frac{Nphc \cdot Kwc}{P_c}$$

and  $\phi_{ga}$ ,  $\phi_{ca}$  are the reference position (electrical angles) of each winding (phase a axis of grid and control windings, respectively).  $Nphg, c$  are the total number of turns per phase and  $Kwg, c$  are the winding factors that takes into account distribution and short-pitching effects of the winding physical assembly [88].

### 3.2.2.1.3 Air-gap flux density per phase

Equation (3.6) also requires the calculation of the of the air-gap flux

density  $B_{i_{gap}}(\theta_{ag})$  of phase  $i$  considering the radially laminated ducted rotor (RLDR).  $B_{i_{gap}}(\theta_{ag})$  is obtained by exciting one phase at a time and it is used the procedure presented by Knight *et al.* [81, 82, 11] to determine it in the SAM. General aspects on the determination of  $B_{gap}$  are presented in Appendix C.1 based on the aforementioned references.

The basic idea behind this approach is to consider the (RLDR) as an ideal flux guide. The flux modulation process is represented by assuming that all the flux entering at one rotor flux path  $\phi_{in}$  at angle  $\theta_{gap}$  will get out at the corresponding opposite flux path extremity  $\phi_{out}$  at angle  $\theta_{gap}^{DR}$  without any leakage. Fig. 3.2 represents a linearized rotor and defines angles  $\theta_{gap}$  and  $\theta_{gap}^{DR}$ . The procedure to calculate  $\theta_{gap}^{DR}$  as a function of  $\theta_{gap}$  is outlined in Appendix C.1.

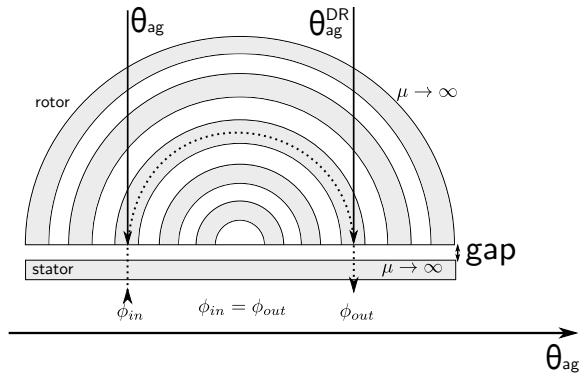


Figure 3.2: Idealized radially laminated ducted rotor and angles definition to calculate the air-gap flux density in SAM. Adapted from [82].

From [81, 82, 11], the air-gap flux density  $B_{i_{gap}}(\theta_{ag})$  can be calculated by:

$$B_{i_{gap}}(\theta_{ag}) = \frac{\mu_0}{2 \cdot gapef} [\mathbb{F}_{i_{gap}}(\theta_{ag}) - \mathbb{F}_{i_{gap}}(\theta_{ag}^{DR})] \quad (3.12)$$

where:

- $\mathbb{F}_{i_{gap}}$  → single phase magnetomotive force of winding  $i$
- $\theta_{ag}$  → mechanical angle around the air-gap
- $\theta_{ag}^{DR}$  → angle around the machine air-gap periphery corresponding to the other extremity of the flux path starting at position  $\theta_{ag}$ .
- $gapef$  → effective air-gap length, compensated by using the Carter's coefficient presented in Appendix C.4.

The MMF  $\mathbb{F}_{i_{gap}}$  can be obtained from (3.9) by setting the angle  $\phi$  for each phase displaced by  $120^\circ$ .

### 3.2.2.2 Analytical calculation of BDFRM inductances by using the winding functions

#### 3.2.2.2.1 Procedure

The procedure to calculate the inductances considers that a DC current (represented in the sequence by  $I_{g\_ind}$  or  $I_{c\_ind}$ ) is applied to one of the phases to generate the respective single phase MMF ( $\mathbb{F}_{i_{gap}}$ ). The modulated air-gap flux density due to the ducted rotor is then calculated by (3.12). The winding functions (3.10) and (3.11) are substituted into (3.6) and the self and mutual inductances can be readily found. As shown in Appendix C.1, the  $\theta_{ag}^{DR}$  is calculated by using the modulo function and, consequently, the integrals in (3.6) are solved numerically.

#### 3.2.2.2.2 Dependence of the inductances on rotor position

It is widely known in the literature [44, 46, 47, 40, 45] that, ideally, the self (e.g. gaga, ggbg...) and the mutual inductances between the windings of the same set (e.g. gagb, gage or cacb, cacc) are constants and do not vary according to rotor position. Only the mutual inductances among the phases of the grid and control windings (e.g. gaca, gacb, gacc,...) do vary sinusoidally as a function of rotor position and effectively participate on electromechanical energy conversion.

Based on this fact and, since SAM's assumes idealized hypothesis, it is possible to calculate the BDFRM inductances by only considering one rotor position, limiting the number of integrals to be solved. By solving (3.6) for one of the phases, the integral result will provide the respective inductance (self or mutual) for the considered rotor position. Since the self and mutual inductances between the phases of the same winding set do not vary according to this parameter, their values are directly determined, since they are independent of the rotor position. To calculate the position dependent mutual inductance among the phases of grid and control windings, one only needs to consider the rotor position where one of them will be at its maximum value and take this as the amplitude of the sinusoidal functions that describe the mutual inductances among the two different winding sets. It is possible to identify this specific position by previously performing some calculations for one of the mutual inductances (let us say, for example,  $L_{gaca}$ )

as a function of the rotor position. For the considered machine topology presented in Chapter 2, the  $L_{gaca}$  is maximum at  $\theta_{rm} = 0^\circ$  and this is the considered rotor position used in all inductance calculations.

### 3.2.2.2.3 Self inductances

The self flux linkage of phase  $gaga$  and its respective inductance are calculated by:

$$L_{gaga} = L'_{gaga} + L_{lg} \quad (3.13)$$

where:

$$L'_{gaga} = \lambda_{gaga}/I_{g\_ind} \quad (3.14)$$

and:

$$\lambda_{gaga} = r_{gap} L_{stkef} \int_0^{2\pi} B_{ga_{gap}}(\theta_{ag}) w_{ga}(\theta_{ag}) d\theta_{ag} \quad (3.15)$$

$B_{ga_{gap}}$  is calculated by assuming a current  $I_{g\_ind}$  flowing in phase  $ga$ :

The self flux linkage of phase  $caca$  and its respective inductance are calculated by:

$$L_{caca} = L'_{caca} + L_{lc} \quad (3.16)$$

where:

$$L'_{caca} = \lambda_{caca}/I_{c\_ind} \quad (3.17)$$

and:

$$\lambda_{caca} = r_{gap} L_{stkef} \int_0^{2\pi} B_{ca_{gap}}(\theta_{ag}) w_{ca}(\theta_{ag}) d\theta_{ag} \quad (3.18)$$

$B_{ca_{gap}}$  is calculated by assuming a current  $I_{c\_ind}$  flowing in phase  $ca$ :

Symbols  $L_{lg}$  e  $L_{lc}$  in (3.13) and (3.16) are the leakage inductances of grid and control windings, respectively. Their calculations are discussed in Appendix C.3. The remaining self inductances of phases  $gbgb$ ,  $gcgc$ ,  $cbcb$  and  $cccc$  use similar procedure and are not be presented here.

It can be shown that the following conditions apply for the self-inductances of grid and control windings, respectively [44]:

$$L_{gm} = L'_{gaga} = L'_{gbgb} = L'_{gcgc} \quad (3.19)$$

and

$$L_{cm} = L'_{caca} = L'_{cbcb} = L'_{cccc} \quad (3.20)$$

### 3.2.2.2.4 Mutual inductances between the phases of the same winding set

The mutual flux linkages and their respective inductances between the phases of the same winding set are [44]:

For grid winding:

$$L_{gab} = \lambda_{gab}/I_{g\_ind} \quad (3.21)$$

where:

$$\lambda_{gab} = r_{gap} L_{stkef} \int_0^{2\pi} B_{gb_{gap}}(\theta_{ag}) w_{ga}(\theta_{ag}) d\theta_{ag} \quad (3.22)$$

$B_{gb_{gap}}$  is calculated by assuming a current  $I_{g\_ind}$  flowing in phase  $gb$ :

And for control winding:

$$L_{cab} = \lambda_{cab}/I_{c\_ind} \quad (3.23)$$

where:

$$\lambda_{cab} = r_{gap} L_{stkef} \int_0^{2\pi} B_{cb_{gap}}(\theta_{ag}) w_{ca}(\theta_{ag}) d\theta_{ag} \quad (3.24)$$

$B_{cb_{gap}}$  is calculated by assuming a current  $I_{c\_ind}$  flowing in phase  $cb$ :

It can be shown that the mutual inductances between the windings of the same set are [44]:

$$L_{gab} = L_{gbgc} = L_{gcga} = -\frac{1}{2}L_{gm} \quad (3.25)$$

and:

$$L_{cab} = L_{cbcc} = L_{ccca} = -\frac{1}{2}L_{cm} \quad (3.26)$$

### 3.2.2.2.5 Mutual inductances between the phases of different winding sets

Finally, the maximum value of the mutual flux linkages and the respective maximum inductances between the two sets of three phase windings are:

For grid winding, considering the excitation on control winding:

$$L_{gaca_{max}} = \frac{\lambda_{gaca_{max}}}{I_{c\_ind}} \Big|_{\theta_{rm}=0^\circ} \quad (3.27)$$

where:

$$\lambda_{gaca_{max}} = r_{gap} L_{stkef} \int_0^{2\pi} B_{ca_{gap}}(\theta_{ag}) w_{ga}(\theta_{ag}) d\theta_{ag} \Big|_{\theta_{rm}=0^\circ} \quad (3.28)$$

And for control winding, considering the excitation on grid winding:

$$L_{caga_{max}} = \frac{\lambda_{caga_{max}}}{I_{g\_ind}} \Big|_{\theta_{rm}=0^\circ} \quad (3.29)$$

where:

$$\lambda_{caga_{max}} = r_{gap} L_{stkef} \int_0^{2\pi} B_{ga_{gap}}(\theta_{ag}) w_{ca}(\theta_{ag}) d\theta_{ag} \Big|_{\theta_{rm}=0^\circ} \quad (3.30)$$

It can be shown that the maximum value of the mutual inductance between the phases of grid and control windings satisfies (3.31) [44]:

$$L_{gcmax} = L_{gaca_{max}} = L_{caga_{max}} \quad (3.31)$$

where  $L_{gaca_{max}}$  is given by (3.27), assuming the rotor position  $\theta_{rm} = 0^\circ$  for the inductance calculations and the considered BDFRM topology.

The procedure described to calculate the inductances can be better illustrated by an example. In Appendix G, a complete spreadsheet in Mathcad <sup>®</sup> calculating all outputs and intermediary equations of the Semi-Analytical Model (SAM) is presented. In this spreadsheet, the inductances are calculated by using the aforementioned procedure and the reader is referred to it for details on the calculations.

### 3.2.3 Instantaneous flux linkage per phase

From the single phase inductances calculation, it is possible to assess the three-phase flux linkage, i.e. the flux linkage seen by one of the phases due to the simultaneous excitation of all the six phases in the BDFRM. The three-phase flux linkages in the BDFRM are given by (3.3) and (3.4).

It can be shown, by following the procedure depicted in [44], that the three-phase flux linkages for the phase  $a$  of grid and control windings

are [47, 40, 44] :

$$\lambda_{ga} = L_g I_g \cos(\omega_g t) + L_{gc} I_c \cos(\omega_g t + \alpha_c + \gamma_1) \quad (3.32)$$

$$\lambda_{ca} = L_c I_c \cos(\omega_c t - \alpha_c) + L_{gc} I_g \cos(\omega_c t + \gamma_1) \quad (3.33)$$

where the inductances  $L_g$ ,  $L_c$  and  $L_{gc}$  are the three-phase inductances obtained by considering the excitation of all the 6 phases simultaneously. They are related to the inductances between individual windings by [44]:

$$L_g = \frac{3}{2} L_{gm} + L_{lg} \quad (3.34)$$

$$L_c = \frac{3}{2} L_{cm} + L_{lc} \quad (3.35)$$

$$L_{gc} = \frac{3}{2} L_{gcm} \quad (3.36)$$

The parameter  $\gamma_1$  in (3.32) and (3.33) arises from the calculation of the flux integrals. Its value is given by  $\gamma_1 = P_r \theta_{rm0}$ , where  $\theta_{rm0}$  is the rotor initial position at  $t = 0s$  [44].

### 3.2.4 Instantaneous voltage equations per phase

By deriving the three-phase flux linkages (3.32) and (3.33), it is possible to calculate the induced phase voltages. Their expressions are given by (3.37) and (3.38)

$$e_{ga} = -\omega_g L_g I_g \sin(\omega_g t) - \omega_g L_{gc} I_c \sin(\omega_g t + \alpha_c + \gamma_1) \quad (3.37)$$

$$e_{ca} = -\omega_c L_c I_c \sin(\omega_c t - \alpha_c) - \omega_c L_{gc} I_g \sin(\omega_c t + \gamma_1) \quad (3.38)$$



### 3.2.5 Equivalent steady-state voltage equations in phasor form

Equations (3.37) and (3.38) can be written in phasor form [44, 40]. The current phasors  $\bar{I}_{ga}$  and  $\bar{I}_{ca}$  are defined by <sup>1</sup>:

$$\bar{I}_{ga} = \frac{I_g}{\sqrt{2}} \angle 0^\circ \quad (3.39)$$

$$\bar{I}_{ca} = \frac{I_c}{\sqrt{2}} \angle -\alpha_c \quad (3.40)$$

The induced phase voltage phasors  $\bar{E}_{ga}$  and  $\bar{E}_{ca}$  are:

$$\bar{E}_{ga} = j\omega_g L_g \bar{I}_{ga} + j\omega_g L_{gc} \bar{I}_{ca} e^{j\gamma_{rg}} \quad (3.41)$$

$$\bar{E}_{ca} = j\omega_c L_c \bar{I}_{ca} + j\omega_c L_{gc} \bar{I}_{ga} e^{j\gamma_{rc}} \quad (3.42)$$

where:

$$\gamma_{rg} = 2\alpha_c + \gamma_{rc} \quad (3.43)$$

$$\gamma_{rc} = \gamma_1$$

Equations (3.41) and (3.42) can be modified to take into account phase resistances. From (3.1) and (3.2):

$$\bar{V}_{ga} = R_g \bar{I}_{ga} + j\omega_g L_g \bar{I}_{ga} + j\omega_g L_{gc} \bar{I}_{ca} e^{j\gamma_{rg}} \quad (3.44)$$

$$\bar{V}_{ca} = R_c \bar{I}_{ca} + j\omega_c L_c \bar{I}_{ca} + j\omega_c L_{gc} \bar{I}_{ga} e^{j\gamma_{rc}} \quad (3.45)$$

### 3.2.6 Definition of the BDFRM equivalent electrical circuit

Fig. 3.3 shows the equivalent electrical circuit for one of the phases of the BDFRM that can be drawn from (3.44) and (3.45). Solution of these equations allows to determine the BDFRM phase voltages.

---

<sup>1</sup>Notice that the effective or root mean square “rms” value is considered as the phasor amplitude ( $I/\sqrt{2}$ ).

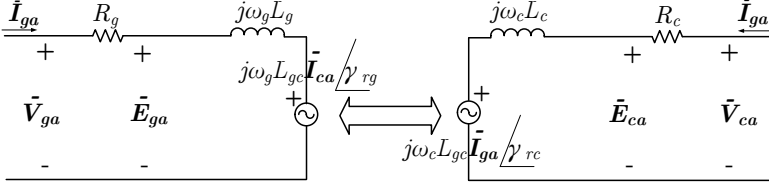


Figure 3.3: BDFRM Equivalent Electric Circuit.

### 3.3 Sub-model 2: power and torque calculation by using the EEC results

Equations (3.41) and (3.42) can be used to calculate power and electromagnetic torque in the BDFRM [40, 44].

#### 3.3.1 Real power

##### 3.3.1.1 Internal real power

From the electrical circuits theory <sup>2</sup>:

$$P_{ga\_int} = \Re \{ \bar{\mathbf{S}}_{ga\_int} \} = \Re \left\{ (\bar{\mathbf{E}}_{ga} \bar{\mathbf{I}}_{ga}^*) \right\} \quad (3.46)$$

$$P_{ca\_int} = \Re \{ \bar{\mathbf{S}}_{ca\_int} \} = \Re \left\{ (\bar{\mathbf{E}}_{ca} \bar{\mathbf{I}}_{ca}^*) \right\} \quad (3.47)$$

$$P_{3\phi g\_int} = \Re \{ \bar{\mathbf{S}}_{3\phi g\_int} \} = 3 \Re \left\{ (\bar{\mathbf{E}}_{ga} \bar{\mathbf{I}}_{ga}^*) \right\} \quad (3.48)$$

$$P_{3\phi c\_int} = \Re \{ \bar{\mathbf{S}}_{3\phi c\_int} \} = 3 \Re \left\{ (\bar{\mathbf{E}}_{ca} \bar{\mathbf{I}}_{ca}^*) \right\} \quad (3.49)$$

where  $P_{ga\_int}$  and  $P_{ca\_int}$  are the internal real power per phase and  $P_{3\phi g\_int}$  and  $P_{3\phi c\_int}$  are the internal three phase real power from grid and control windings sets.

The internal total three phase real power is given by the sum of (3.48) and (3.49):

$$P_{3\phi t\_int} = P_{3\phi g\_int} + P_{3\phi c\_int} \quad (3.50)$$

<sup>2</sup>Symbols  $\Re$  and  $\Im$  mean, respectively, the real and the imaginary parts of the complex number

Substituting (3.39), (3.40), (3.41) and (3.42) into (3.48) and (3.49), the real power from each winding can be shown to be:

$$P_{3\phi g_{int}} = -\frac{3}{2}(\omega_g)L_{gc}I_gI_c \sin(\phi_{torque}) \quad (3.51)$$

$$P_{3\phi c_{int}} = -\frac{3}{2}(\omega_c)L_{gc}I_gI_c \sin(\phi_{torque}) \quad (3.52)$$

$$P_{3\phi t_{int}} = -\frac{3}{2}(\omega_g + \omega_c)L_{gc}I_gI_c \sin(\phi_{torque}) \quad (3.53)$$

where  $\phi_{torque} = \alpha_c + \gamma_1$ .

### 3.3.1.2 Terminal real power

The terminal real power per phase,  $P_{ga\_ter}$  and  $P_{ca\_ter}$ , that include the phase resistances, are:

$$P_{ga\_ter} = \mathbb{R} \{ \bar{\mathbf{S}}_{ga_{ter}} \} = \mathbb{R} \{ (\bar{\mathbf{V}}_{ga} \bar{\mathbf{I}}_{ga}^*) \} \quad (3.54)$$

$$P_{ca\_ter} = \mathbb{R} \{ \bar{\mathbf{S}}_{ca_{ter}} \} = \mathbb{R} \{ (\bar{\mathbf{V}}_{ca} \bar{\mathbf{I}}_{ca}^*) \} \quad (3.55)$$

## 3.3.2 Electromagnetic Torque in steady-state

Equation (3.53) representing the total internal power neglects any kind of losses. Consequently, all the power must be going into electromechanical power. The induced electromagnetic torque (3.56) can be derived recalling that  $P_{3\phi} = T_{em}\omega_{rm}$  and, from (1.18),  $(\omega_g + \omega_c) = P_r\omega_{rm} = \frac{P_g+P_c}{2}\omega_{rm}$  [44]. Therefore:

$$T_{em} = -\frac{3}{2} \left( \frac{P_g + P_c}{2} \right) L_{gc}I_gI_c \sin(\phi_{torque}) \quad (3.56)$$

## 3.4 Sub-model 3: air-gap flux density calculation to estimate induction levels in stator teeth, stator yoke and rotor flux paths

From a practical point of view, it is important to estimate the flux densities around the machine. The SAM is a linear model and, depend-

ing on the excitation conditions, these quantities may reach unpractical values. This is particularly important for the optimization process, in order to constraint the outputs into ranges that are reasonable from an electromagnetic point of view.

### 3.4.1 Hypotheses to estimate flux densities

To calculate flux densities in SAM, some assumptions have been made. Firstly, it is considered that the machine is equivalent to a  $P_r$  pole machine, where the flux in one rotor pole stays confined on it and circulates through the stator teeth and yoke as shown in Fig. 3.4.

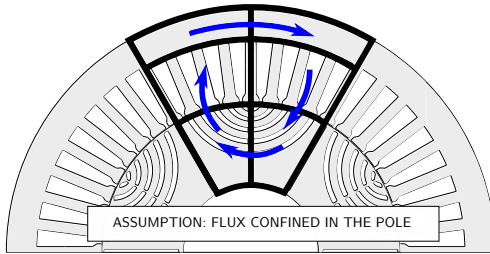


Figure 3.4: Equivalent flux tubes in the SAM.

Secondly, as the SAM is based on the calculation of steady-state parameters, the instantaneous flux density in the air-gap ( $B_{gap}(\theta_{ag}, t)$ ) is not *a priori* available. In order to assess the flux densities in stator teeth, yoke and rotor flux paths, it is considered that the *amplitude* of  $B_{gap}$  waveform around the air-gap is constant, independently of rotor position. To illustrate this assumption, Fig. 3.5 shows some  $B_{gap}$  calculations for distinct rotor positions. It can be remarked that, indeed, the maximum and minimum values remain roughly constants.

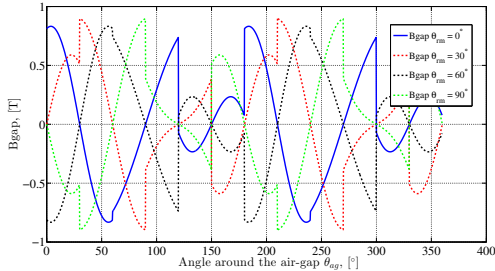


Figure 3.5:  $B_{gap}$  calculation for several positions.

As one is interested in limiting induction, independently of where in the machine the maximum value takes place, the waveform of  $B_{gap}$  at a fixed time  $t = 0s$  is used to estimate the aforementioned flux densities around the machine. This calculation assumes that, if a different time is chosen to assess  $B_{gap}$ , the maximum value of the flux density in stator teeth, yoke and rotor flux paths will be roughly the same than they are at  $t = 0s$ , although it may occur at a different teeth/yoke/flux path.

Obviously, these assumption will incur in errors due to the complex field interaction on this machine as previously discussed. However, this procedure does allow to estimate with acceptable accuracy the magnetic induction levels for a limited linear pre-design model. Since the main goal of this calculation is to restrict the search space for the optimization algorithm, it is considered that the approach used to calculate the flux densities around the machine are sufficient of the purpose of the SAM.

### 3.4.2 Air-gap flux density calculation considering all the six phases excited

Based on the aforementioned assumptions, the flux densities around the machine are calculated from  $B_{gap}(\theta_{ag}, t)$ , defined in (C.5). The procedure to estimate  $B_{gap}$  is similar to the one used on the inductances calculation. The difference is that now balanced three phase currents are applied to grid and control winding and the total MMF contribution from the six phases are taken into account to evaluate  $B_{gap}(\theta_{ag}, t)$ . By using the fundamental component of the three phase MMF function presented in Section 1.2.2.3, the air-gap flux density is given by:

$$B_{gap}(\theta_{ag}, t = 0) = \frac{\mu_0}{2 \cdot gapef} [\mathbb{F}_{3\phi total}(\theta_{ag}, t = 0) - \mathbb{F}_{3\phi total}(\theta_{ag}^{DR}, t = 0)] \quad (3.57)$$

where  $\mathbb{F}_{3\phi total}$  is calculated by using (1.8).

To illustrate to what the  $B_{gap}$  waveform resembles, Fig 3.6 shows one example for  $t = 0s$  at  $\omega_{rm} = 1000rpm$  and rated excitation. In this figure, a comparison between a FEA simulation and the analytical estimation of this parameter is highlighted.

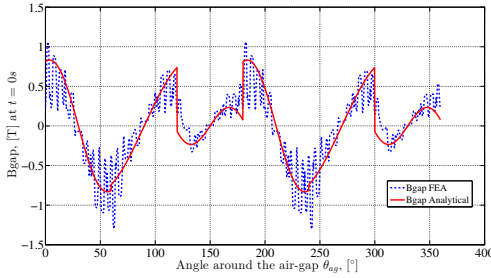


Figure 3.6: Comparison between a  $B_{gap}$  analytical estimation and a FEA simulation for  $\omega_{rm} = 1000rpm$  at  $t = 0s$  and rated excitation.

### 3.4.3 Nomenclature definition for the calculation of flux densities in several parts around the machine

Before starting the calculations of the flux densities, let us define some parameters that will be used in the following discussion, shown in Fig. 3.7.

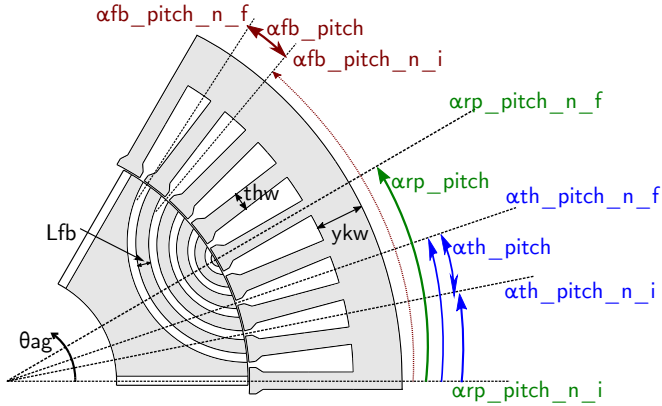


Figure 3.7: Angles definition to calculate flux density around the machine in SAM.

### 3.4.4 Flux density in stator teeth

The inductions in the stator teeth are calculated by assuming that all the flux corresponding to one stator tooth pitch  $\alpha_{th\_pitch}$  passes through the middle of the adjacent stator tooth. One stator tooth pitch is calculated by:

$$\alpha_{th\_pitch} = \frac{2\pi}{N_{sl}} \quad (3.58)$$

where  $N_{sl}$  is the number of stator slots (or equivalently the number of stator teeth).

By using (3.57) and (3.58) the flux passing through a stator teeth can be calculated:

$$\phi_{th\_n} = r_{gap} L_{stkef} \int_{\alpha_{th\_pitch\_n\_i}}^{\alpha_{th\_pitch\_n\_f}} B_{gap}(\theta_{ag}) d\theta_{ag} \quad (3.59)$$

where  $\phi_{th\_n}$  is the flux in the “ $n$ ” tooth,  $\alpha_{th\_pitch\_n\_i}$  and  $\alpha_{th\_pitch\_n\_f}$  are, respectively, the initial and final angles of the “ $n$ ” stator tooth pitch.

The flux density in the “ $n$ ” tooth is calculated by:

$$B_{th\_n} = \frac{\phi_{th\_n}}{th\_area\_middle} \quad (3.60)$$

where  $th\_area\_middle$  is the tooth cross sectional area calculated by

$th\_area\_middle = thw \cdot L_{stkef}$  and  $thw$  is the tooth width at the middle position.

The induction on stator teeth shall be calculated and tested individually at each stator slot in the domain to find the maximum induction level. This is necessary, since the angle  $\theta_{ag}$  where the  $B_{gap}$  amplitude is maximum is not known a priori.

### 3.4.5 Flux density in stator yokes

The flux density in stator yoke can be calculated by assuming that all the flux that enters at one side of the considered rotor pole passes through the respective stator yoke (see Fig. 3.4). The angle of the half rotor pole pitch is given by:

$$\alpha_{rp\_pitch} = \frac{\pi}{P_r} \quad (3.61)$$

The flux in stator yoke can be calculated by:

$$\phi_{rp\_n} = r_{gap} L_{stkef} \int_{\alpha_{rp\_pitch\_n\_i}}^{\alpha_{rp\_pitch\_n\_f}} B_{gap}(\theta_{ag}) d\theta_{ag} \quad (3.62)$$

where  $\phi_{rp\_n}$  is the flux entering the “ $n$ ” half rotor pole,  $\alpha_{rp\_pitch\_n\_i}$  and  $\alpha_{rp\_pitch\_n\_f}$  are, respectively, the initial and final angles of the “ $n$ ” half rotor pole.

The flux density in the “ $n$ ” stator yoke is calculated by:

$$B_{yk\_n} = \frac{\phi_{rp\_n}}{yk\_area} \quad (3.63)$$

where  $yk\_area$  is the stator yoke cross section area calculated by  $yk\_area = ykw \cdot L_{stkef}$  and  $ykw$  is the stator yoke width.

As can be inferred from Fig. 3.4, the number of flux densities to be verified in stator yokes are equal to the number of rotor poles if no symmetry is considered, since it is assumed a  $P_r$  pole machine.

### 3.4.6 Flux density in rotor flux paths

Finally, the induction in the rotor flux paths can be evaluated. The angle corresponding to a flux path is given by:

$$\alpha_{fb\_pitch} = \frac{2\pi}{N_{slr}} \quad (3.64)$$



where  $Nslr$  is the number of rotor slots (or equivalently the number of flux paths).

The flux in a rotor flux path can be calculated by:

$$\phi_{fb\_n} = r_{gap} L_{stkef} \int_{\alpha_{fb\_pitch\_n\_i}}^{\alpha_{fb\_pitch\_n\_f}} B_{gap}(\theta_{ag}) d\theta_{ag} \quad (3.65)$$

where  $\phi_{fb\_n}$  is the flux entering at the “ $n$ ” rotor flux path,  $\alpha_{fb\_pitch\_n\_i}$  and  $\alpha_{fb\_pitch\_n\_f}$  are, respectively, the initial and final angles of the “ $n$ ” rotor flux path.

The flux density in the “ $n$ ” rotor flux path is calculated by:

$$B_{fb\_n} = \frac{\phi_{fb\_n}}{fb\_area} \quad (3.66)$$

where  $fb\_area$  is the rotor flux path cross sectional area calculated by  $fb\_area = Lfb \cdot L_{stkef}$  and  $Lfb$  is the flux path width.

The number of flux densities in the rotor flux path to be calculated are equal to  $Nslr/2$  if no symmetry is considered since it is assumed that they are ideal flux conductors (all the flux entering at one flux path must go out at the other extremity).

### 3.5 Final Considerations

This chapter presented the Global Electromagnetic Model - SAM that relies on the equivalent electric circuit approach to calculate the electromagnetic output parameters of the BDFRM. As a complementary source, it is mentioned that a complete Mathcad <sup>®</sup> spreadsheet implementing SAM and the associated Additional Sizing Equations (to be discussed in Chapter 5) forming the SAM-based Global Sizing and Optimization Model is available in the Appendix G. In Chapter 9, the SAM is coupled to the optimization algorithm and the simulation results are discussed. Next chapter addresses the second model proposed in the BDFRM design process, the Multi-Static Reluctance Network model.



## Chapter 4

# BDFRM Multi-Static Reluctance Network Model (MSRN)

### Abstract

*This chapter presents the Multi-Static Reluctance Network (MSRN) model that relies on the solution of a permeance network to calculate the BDFRM electromagnetic outputs. On the contrary to the Semi-Analytical Model (SAM), the MSRN takes into account magnetic material nonlinearities. As it is also based on semi-analytical equations, it offers an interesting trade-off between precision and computation time when compared to Finite Element Analysis (FEA). The model structure, the air-gap reluctances parametrized in terms of rotor position and the use of symmetry and sources rotation to perform effective multi-static calculating are discussed in the next sections. These steps define a procedure to evaluate the outputs such as phase voltages, power, torque and flux densities in the stator teeth, yoke and in the rotor flux paths by using a multi-static calculations on a reluctance network model.*

## 4.1 Basic principles and requirements to obtain a multi-static reluctance network (MSRN) model

### 4.1.1 General characteristics of the MSRN model

The Multi-Static Reluctance Network (MSRN) is a BDFRM optimization oriented global electromagnetic model (GEMM) that uses the permeance network approach to calculate fluxes, voltages, flux densities and torque. In this model, the electromagnetic domain is discretized in many saturable and linear reluctances (modeling, respectively, iron and air) that represents the existing flux tubes on the device.

Similar to the SAM, the MSRN model is based on semi-analytical approaches: most part of the equations are analytical, but it uses implicit equations and numerical integrals to calculate the outputs as well. These characteristics allow to take into account magnetic material saturation, increasing model accuracy, whereas assuring a good trade-off between precision and computation time.

Before addressing the MSRN model structure, a brief discussion on the use of the reluctance network (RN) approach for solving electromagnetic problems is introduced in the sequence.

### 4.1.2 Electromagnetic principles on modeling by using reluctance networks

The reluctance is a magnetic quantity associated to a volume (or flux tube) that can be defined from Maxwell's equation in the integral form for magnetostatics.

From Maxwell-Ampère's equation, a magnetic scalar potential can be defined:

$$V_{mag} = \oint_c \vec{H} \cdot d\vec{l} \quad (4.1)$$

The magnetic flux in the flux tube is given by:

$$\phi = \iint \vec{B} \cdot d\vec{S} \quad (4.2)$$

Aiming to use reluctances to represent an electromagnetic domain in a discretized way, one can define an *equivalent flux tube* based on the fact that the magnetic flux is conservative, since  $\nabla \cdot \vec{B} = 0$ , with the

following characteristics: the volume is made by a series of equipotential surfaces and all flux lines are assumed to be perpendicular to its surfaces [116]. In other words, an actual flux tube with length  $l$  and with surfaces  $S_i$  in the input and  $S_o$  in the output maybe represented by an equivalent flux tube with length  $L_{eq}$  and surface  $S_{eq}$  so that the reluctance from both flux tubes are the same [117]. Fig. 4.1 illustrates the procedure.

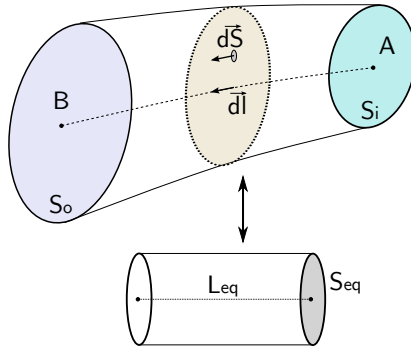


Figure 4.1: Equivalent flux tube.

Equations (4.1) and (4.2) can be simplified by considering the assumptions made for the equivalent flux tube. In this approach,  $\vec{H} \cdot d\vec{l}$  and  $\vec{B} \cdot d\vec{S}$  are equal to the product of their magnitudes since they are collinear vectors. Induction  $B$  is assumed constant for a given excitation inside the equivalent flux tube, so  $\phi = BS_{eq}$ . Thus, by using these equations and the constitutive equation  $\vec{B} = \mu\vec{H}$ ,  $V_{mag}$  can be simplified:

$$V_{mag} = \int_A^B \frac{BS_{eq}}{\mu} \frac{dl}{S_{eq}} = \int_A^B \phi \frac{dl}{\mu S_{eq}} \quad (4.3)$$

The magnetic reluctance of the equivalent flux tube  $\mathfrak{R}$  is then defined as the ratio of the magnetic potential and the magnetic flux, equivalent to the Ohm's law for a magnetic circuit. It represents the material resistance to the flux passing through it. The inverse of  $\mathfrak{R}$  is defined as the magnetic permeance  $P$ .

$$\mathfrak{R} = \frac{1}{P} = \frac{V_{mag}}{\phi} = \frac{L_{eq}}{\mu S_{eq}} \quad (4.4)$$

For a nonlinear reluctance, (4.4) can be re-written in terms of the

flux passing through the reluctance, which is the unknown parameters to be solved in the reluctance network (Hopkinson's law) [111]:

$$\mathfrak{R}(\phi) = \frac{L_{eq}}{\phi} H \left( \frac{\phi}{S_{eq}} \right) \quad (4.5)$$

The use of equation (4.5) implies in the knowledge of the magnetic material characteristics. This can be estimated analytically (one example can be found in [111]) or by using a curve obtained experimentally [84]. In this case, interpolation can be used to define a continuous function by parts.

The reluctances representing the flux tubes in regions containing air can be implement directly by considering the vacuum permeability  $\mu_0$  (air reluctances). Several air reluctances formulas that considers different geometries for the flux path in the air have been proposed in [118]. In this thesis, the air reluctances have been represented by (4.6) with equivalent lengths  $L_{eq}$  and cross-sectional surfaces  $S_{eq}$ .

$$\mathfrak{R}_{air} = \frac{1}{P} = \frac{V_{mag}}{\phi} = \frac{L_{eq}}{\mu_0 S_{eq}} \quad (4.6)$$

where  $\mu_0 = 4\pi 10^{-7}$  [ $H/m$ ] is the vacuum permeability.

The theory behind these definitions allows to define the well known analogy between electric and magnetic circuits. Table 4.1 presents the equivalent quantities when referring to it. The so called Reluctance Network (RN) (also called in the literature Permeance Network) is based on this analogy.

Table 4.1: Analogy between electric and magnetic circuits [111, 104].

<b>Electric</b>	<b>Magnetic</b>
Potential V	Magnetic Potential $V_{mag}$
Current I	Magnetic Flux $\phi$
Resistance R	Reluctance $\mathfrak{R}$
Electric Conductivity $\sigma$	Magnetic Permeability $\mu$
Electric Field $\vec{E}$	Magnetic Field $\vec{H}$
Current Density $\vec{J}$	Flux density $\vec{B}$

The reluctance network provides, for each reluctance, the flux ( $\phi_r$ ) passing through it, the magnetic induction ( $B_r$ ), the respective reluctance ( $\mathfrak{R}_r$ ) and the associated coenergy  $W_{co,r}$ , where the index  $r$  varies from 1 up to the total number of reluctances in the network. Additionally,

the RN also calculates the total system coenergy  $W_{cotot}$ , assuming the contribution of all reluctances, that will be used to calculate the electromagnetic torque. Details on these calculations can be found in [111].

It is clear that representing an electromagnetic domain in a discretized way by reluctances implies in loss of finesse and, probably, accuracy. Not all the domain can be *exactly* represented by an equivalent flux tube, or at least the number of reluctances in the network would be too big to be equivalent to a Finite Element Method mesh. The interest in the RN approach is to define a discretized domain, coarser than one by using Finite Element Analysis (FEA), but, at the same time, being representative to calculate electromagnetic parameters with an acceptable *global* accuracy. For example, by using a RN approach, one is not interested in calculating fluxes in each part of the machine magnetic circuit (teeth, yoke *etc.*) with the highest accuracy. The great interested is in obtaining the global electromagnetic outputs (voltages, torque *etc.*) by a fast and accurate way.

The number of reluctances in the network is fairly arbitrary and application dependent. When building a reluctance network, it is usually recommend to first execute a finite element analysis of the electromagnetic device to identify the main flux tubes in the domain. Then, the associated reluctances of the equivalent magnetic circuit can be defined and connected in an entire network to represent the electromagnetic domain.

### 4.1.3 Hypothesis

To discretize the electromagnetic domain by using a reluctance network and to obtain the performance outputs, the following assumptions are considered in this work:

- The representation of the local phenomena on the magnetic circuit by lumped reluctances are sufficient for solving the electromagnetic problem;
- The magnetic material is lossless from the RN point of view;
- The magnetomotive forces (MMF) produced by currents circulating through the windings distributed in the stator slots can be represented by equivalent sources located within the reluctance network.
- The reluctance rotor is not ideal and the leakage flux is taken into account by lumped air reluctances forming equivalent leakage flux

tubes.

- The machine is considered to be rotating in steady state conditions.

#### 4.1.4 Outputs definition

The MSRN outputs are defined in Table 4.2 and the procedure to calculate them are discussed later in this chapter in Section 4.5.

Table 4.2: Outputs definition of the Multi-Static Reluctance Network Model.

Parameter <sup>1</sup>	Description	Size <sup>2</sup>
$T_{em_{ave}}$	Average value of the electromagnetic torque [ $Nm$ ].	1
$E_{x_{rms}}$	Internal induced rms phase voltage [ $V$ ].	6
$ B_{th_{max}} $	Maximum absolute induction level in stator teeth [ $T$ ]	1
$ B_{yk_{max}} $	Maximum absolute induction level in stator yoke [ $T$ ]	1
$ B_{rt_{max}} $	Maximum absolute induction level in rotor teeth (flux paths) [ $T$ ]	1
$P_{act_{x\_int}}$	Internal active power per phase (calculated from $E_x$ ) [ $W$ ]	6
$V_{x_{rms}}$	Terminal output rms phase voltage (considers the voltage drop in the phase resistances)	6
$P_{act_{x\_ter}}$	Terminal active power per phase (calculated from $V_x$ ) [ $W$ ]	6
$I_{x_{rms}}$	RMS value of the phase currents [ $A$ ]	6
Total size of output vector:		34

<sup>1</sup>  $x$  means the respective phase considered:  $g|a, b, c$  (grid) or  $c|a, b, c$  (control).

<sup>2</sup> The size column means how many outputs are calculated for the respective parameter.

Similarly to the SAM, in the MSRN we are interested in obtaining the electromagnetic behavior of the BDFRM as a function of machine structural physical dimensions and excitation conditions so that we can



further explore this model in an optimization context. Therefore, the MSRN outputs are related to voltages, power, electromagnetic torque and flux densities in several parts of the machine magnetic circuit (e.g. stator teeth, yoke and rotor flux paths).

#### 4.1.5 The need of the voltages as a function of time

Ultimately, the goal of the global electromagnetic models (SAM and MSRN) regarding the phase voltages is to obtain them in steady state conditions. The SAM, for example, assumes that the phase voltages are balanced and it uses a calculation procedure based on a per-phase equivalent electric circuit. This provides sufficiently accurate results for the purposes of its modeling level.

The MSRN differs from the SAM in the design process because it targets a more precise representation of the electromagnetic phenomena in the BDFRM. To reach this goal, it is not possible to assume that the phases are necessarily balanced, since the two set of three phase windings with distinct number of poles are operating at different frequencies, we are dealing with nonlinear magnetic materials and the machine is submitted to a complex magnetic field interaction originated from the flux modulation process occasioned by the rotor. All these effects added together results in a non-uniform distribution of the flux density around the machine at any instant of time, as can be inferred from Fig. 4.2, which shows a FEA simulation of the flux distribution at  $time = 0$  s at rated conditions.

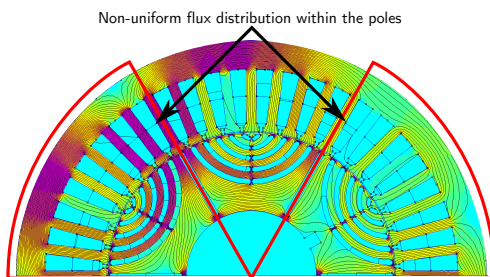


Figure 4.2: Non-uniform flux distribution. Example of a FEA simulation with half symmetry considering a 8-4 stator poles, 6 rotor poles BDFRM machine at rated conditions.

To obtain more precise results when estimating the BDFRM phase voltages independently of the excitation level, the derivative of the

phase flux linkage in terms of the time must be calculate, since:

$$v(t) = \frac{d\lambda(t)}{dt} \quad (4.7)$$

To be able to use (4.7) to calculate the phase voltages, the model must be capable of performing multi-static calculations to assess the instantaneous value of the flux linkage in each phase as a function of the rotor position. The proposed MSRN model discussed in the following sections implements the required effective multi-static calculations by taking into account the movements from the rotor and the rotating magnetic field, carrying them out simultaneously.

#### **4.1.6 Other performance parameters as a function of time**

It is possible to take advantage of the multi-static simulations, necessary to calculate voltage, to obtain all the performance parameters as a function of the simulation time. At each calculated position, the instantaneous value of the phase flux linkages, voltages, electromagnetic torque and flux densities are assessed. From these results, one can estimate the rms voltages, the average torque and the maximum induction in an electrical period. The multi-static calculations also provide means to estimate voltage harmonics and torque ripple if required for a particular application.

#### **4.1.7 MSRN model structure: static and multi-static reluctance networks for taking into account rotor movement and MMF variation in terms of time**

The MSRN uses a static reluctance network (SRN) to calculate its outputs and an air-gap/source rotation model (AGSRM) parametrized in terms of rotor position to take into account multi-static calculations. The SRN solves the electromagnetic problem at each position, whereas the AGSRM manages the air-gap flux tubes and the source rotation, connecting the rotor teeth to the stator teeth at the correct location in terms of rotor movement. Fig. 4.3 outlines the two sub-models used to calculated the BDFRM outputs.

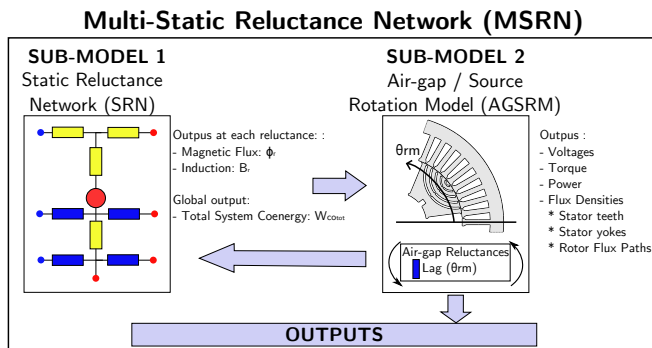


Figure 4.3: Schematic of the MSRN model.

Next sections discuss the modeling of these parts.

## 4.2 Sub-model 1: Static Reluctance Network (SRN)

The SRN contains in a single model the flux tubes used to represent the machine electromagnetic behavior for *any* rotor position within the range  $[0, \psi_{st}]$ . The angle  $\psi_{st}$  is defined as the arc between any two adjacent stator teeth and it is depicted in Fig. 4.4.

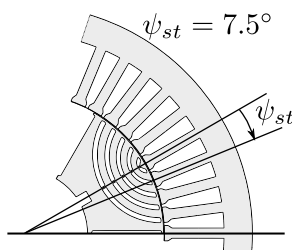


Figure 4.4: Definition of the angle  $\psi_{st}$ .

The angle  $\psi_{st}$  is calculated by <sup>1</sup>:

$$\psi_{st} = 360^\circ / Nsl \quad (4.8)$$

<sup>1</sup>For the considered BDFRM topology,  $\psi_{st} = 360^\circ / 48 = 7.5^\circ$ .

The SRN is divided in three components representing one stator tooth and one slot, one rotor pole and one air-gap model per rotor pole. The latter contains the reluctances used to link one rotor pole to the stator teeth that will have a direct connection within the range  $[0, \psi_{st}]$ .

## 4.2.1 Reluctance network for one stator tooth

### 4.2.1.1 Structural topology and notation

Fig. 4.5 shows the main dimensions related to machine physical dimensions used to calculate the equivalent stator reluctances. The names starting by “a” refers to an angle and the other refers to lengths. Symbol “ $\phi$ ” in this case means that the dimensions refers to the diameter.

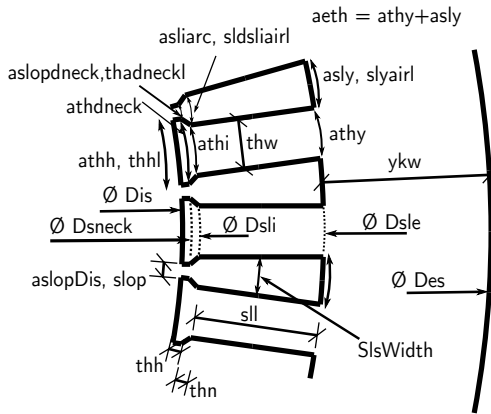


Figure 4.5: Stator slot physical dimensions definitions.

### 4.2.1.2 Associated reluctance network for one stator tooth

Fig. 4.6 shows the RN for one stator tooth and its respective slot.

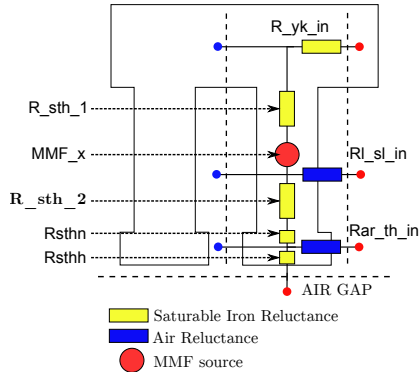


Figure 4.6: Reluctance Network for one stator tooth and its respective slot.

Table 4.3 shows the definitions that have been used to calculate equivalent flux tubes in the stator tooth.

Table 4.3: Reluctances definition for one stator slot.

Reluctance	Length	Cross-sectional area
$R_{yk\_in}$	$\pi(Des + Dsle)/(2Nsl)$	$yk_w \cdot Lstkef$
$R_{sth\_1/2}$	$sll/2$	$th_w \cdot Lstkef$
$R_{sth_n}$	$th_n$	$th_hl \cdot Lstkef$
$R_{sth_h}$	$th_h$	$th_hl \cdot Lstkef$
$R_{l\_sl\_in}$	$3 \cdot SlsWidth$ <sup>(2)</sup>	$sll \cdot Lstkef$
$R_{ar\_th\_in}$	$slop$	$th_h \cdot Lstkef$

where:

$Nsl$                       Number of stator slots  
 $Lstkef$                     Effective core axial length

The magnetomotive force sources  $MMF_x$  are discussed separately in Section 4.3.2 since they are used to perform multi-static calculations.

<sup>2</sup>Factor “3” is found by analytically calculating the stator slot leakage inductance [119]. Refer to Appendix C.3.2 for details.

## 4.2.2 Reluctance network for one rotor pole

### 4.2.2.1 Structural topology and notation

Fig. 4.7 shows the physical dimensions for one rotor pole. Parameters  $L_{xdm}$  are related to the arc length of the flux path (where  $x = 1, 2, 3, 4, 5, 6$ , corresponding to each one of the flux paths).

The similar notation  $L_{ydm}'$  also means the arc length, but it refers to the flux barrier, i.e. the air region among the rotor flux paths.  $L_{ydm}'$  (where  $y = 1, 2, 3, 4, 5$ ) represents the leakage reluctance between flux paths.

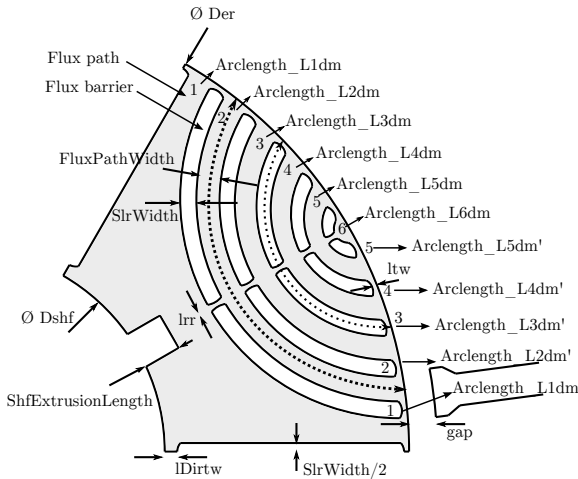


Figure 4.7: Physical dimensions definition for one rotor pole.

### 4.2.2.2 Associated reluctance network for one rotor pole

Fig. 4.8 shows the reluctance network for one rotor pole.

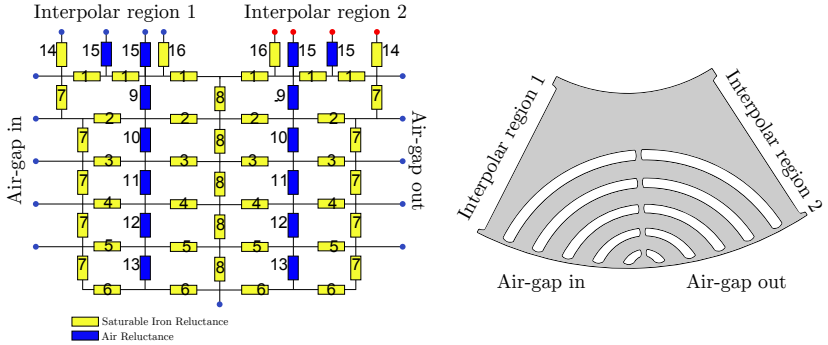


Figure 4.8: Reluctance Network for one rotor pole.

Based on Fig. 4.8 and 4.7, Table 4.4 outlines the definitions that have been used to calculate equivalent flux tubes in the rotor pole component.

Table 4.4: Reluctances definition for one rotor pole.

Reluctance	Length	Cross sectional area
1	$Arclength\_L1dm/6$	$FluxPathWidth \cdot Lstkef$
2	$Arclength\_L2dm/4$	$FluxPathWidth \cdot Lstkef$
3	$Arclength\_L3dm/4$	$FluxPathWidth \cdot Lstkef$
4	$Arclength\_L4dm/4$	$FluxPathWidth \cdot Lstkef$
5	$Arclength\_L5dm/4$	$FluxPathWidth \cdot Lstkef$
6	$Arclength\_L6dm/4$	$FluxPathWidth \cdot Lstkef$
7	$SlrWidth$	$ltw \cdot Lstkef$
8	$SlrWidth$	$lrr \cdot Lstkef$
9	$SlrWidth$	$Arclength\_L1dm' \cdot Lstkef$
10	$SlrWidth$	$Arclength\_L2dm' \cdot Lstkef$
11	$SlrWidth$	$Arclength\_L3dm' \cdot Lstkef$
12	$SlrWidth$	$Arclength\_L4dm' \cdot Lstkef$
13	$SlrWidth$	$Arclength\_L5dm' \cdot Lstkef$
14	$SlrWidth/2$	$ltw \cdot Lstkef$
15	$SlrWidth/2$	$(Der/2 - Dshf/2 - lDirtw - ltw)/2 \cdot Lstkef$
16	$SlrWidth/2$	$lDirtw \cdot Lstkef$

The  $Arclength\_L1dm$  (Reluctance 1) is divided by 6 because there is 6 reluctances on this branch, whereas the remaining branches (2, 3,

4, 5 and 6) are divided by 4, as shown in Fig. 4.8.

### 4.2.3 Air-gap modeling: the choice of the Fourier series to parametrize the reluctances as a function of rotor position

In an electromechanical system in general, nearly all of the energy stored in coupling fields, responsible for electromechanical conversion, are stored in the air-gap [87]. Therefore, modeling the air-gap accurately is one of the most important tasks on machine analysis [120].

The goal of this section is to show how the air-gap reluctances or, more specifically, the *equivalent width* of the flux tube connecting each rotor tooth to each stator tooth can be defined *in terms of rotor position* so that one can perform multi-static calculations. The complete air-gap reluctance network topology used in this work is presented in Section 4.3 when the rotor movement is discussed.

#### 4.2.3.1 Setting the problem: calculation of the flux tube equivalent widths

For modeling the air-gap, it is required to create equivalent flux tubes that connect the stator teeth to the rotor teeth for all the rotor positions to be considered. Fig. 4.9 shows a FEA simulation with the flux lines and the air-gap reluctances required for modeling them by using the reluctance network approach.

#### Required: analytical modeling of the flux tubes

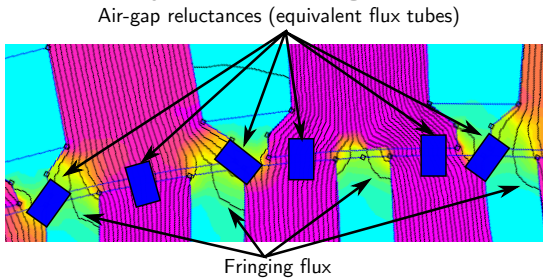


Figure 4.9: The flux lines and the required air-gap reluctances to connect the stator and rotor teeth.

The main goal is to define an equivalent reluctance that represents the path required for the flux lines to circulate between the stator



and the rotor. The reluctance length is the air-gap length ( $gap$ ) and the cross-sectional area is the effective machine axial length ( $L_{stkef}$ ) multiplied by a variable width ( $EqWidth$ ) that takes into account the interface between one stator tooth and the respective rotor tooth. The “ $n$ ” reluctance in the air-gap model is given by:

$$\mathfrak{R}_{gap_n} = \frac{gap}{\mu_0 \cdot L_{stkef} \cdot EqWidth_n} \quad (4.9)$$

The equivalent reluctance width must be calculated individually for each reluctance in the air-gap representing all the possible flux tubes among the stator and rotor teeth for a given position. There are many different approaches that can be used to estimate the equivalent reluctance width, for example: the straight tooth method, trapezoidal method, finite element method, Fourier series method, geometrical and others [121, 120]. Different criteria can be used on the choice of the preferred method such as precision, robustness, computation time, discretization level and time to implement, but the choice is subjective and depends on the application [120]. On this work, the straight tooth and the Fourier series methods have been analyzed and this discussion is presented in the sequence.

#### 4.2.3.2 The straight teeth method (STM)

In the straight tooth method, the equivalent reluctance width is determined by assuming that the flux lines pass straight ahead only through the direct interface among the stator and rotor teeth. The fringing flux is not taken into account. Fig. 4.10 illustrates the 4 possible cases according to the rotor position [121].

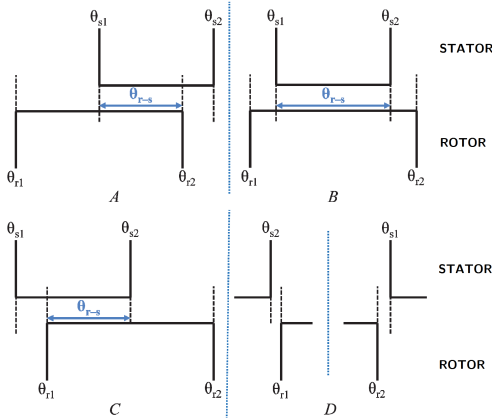


Figure 4.10: Possible cases for the straight tooth method. Adapted from [121].

The equivalent width  $EqWidth$  in the STM is determined by [121]:

$$EqWidth_{STM} = R_{gap} \cdot \theta_{r-s} \quad (4.10)$$

where  $R_{gap}$  is the air-gap radius and the 4 possible angles  $\theta_{r-s}$  are determined as follows:

$$\begin{aligned} \text{Case A} &\rightarrow \theta_{r2} - \theta_{s1} \\ \text{Case B} &\rightarrow \theta_{s2} - \theta_{s1} \\ \text{Case C} &\rightarrow \theta_{s2} - \theta_{r1} \\ \text{Case D} &\rightarrow 0 \end{aligned} \quad (4.11)$$

### 4.2.3.3 Fourier series method (FSM)

#### 4.2.3.3.1 Considering fringing fluxes

Fig. 4.11 shows that *most* of the flux lines indeed respect the assumption made for the straight tooth method (STM). However, in a real device, there are always additional fringing flux lines coming in and out in the vicinity of the main flux tube. Fig. 4.11 depicts the problem, highlighting the fact that the fringing fluxes are not negligible and alternative methods than the STM must be considered for more accurate calculations.

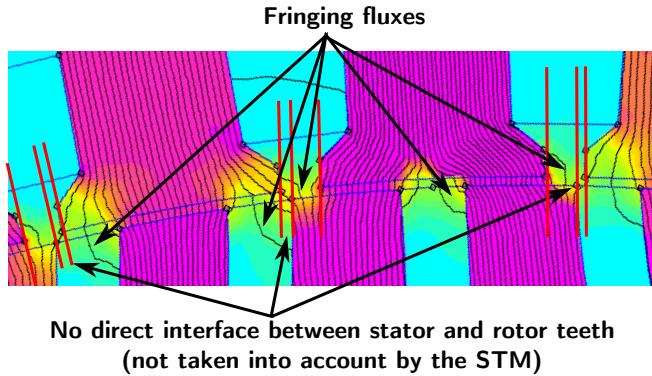


Figure 4.11: Illustration of the fringing flux to be taken into account by the Fourier series method.

To take into account the fringing flux, an approach that can be used is the Fourier series method (FSM). The idea behind using the Fourier series is to slightly increase the effective reluctance width so that the additional flux lines not taken into account by the STM can be accounted for. Fig. 4.12 shows the stator and rotor teeth represented by their respective Fourier series and the resulting equivalent width.

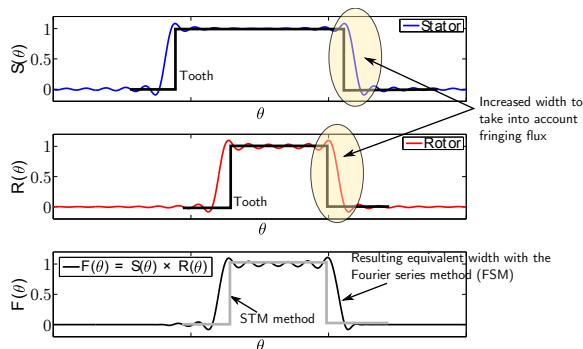


Figure 4.12: Illustration of the Fourier series method.

#### 4.2.3.3.2 Fourier series of a pulse wave

The Fourier series of a pulse wave is used on the modeling of the air-gap reluctances. The pulse wave is characterized by a duty cycle and a period. The amplitude of the pulse wave is set to 1 and its period

is defined in terms of  $\theta_{rm}$ . The definitions and the parameters used to calculate the stator and rotor teeth Fourier series are shown in Fig. 4.13.

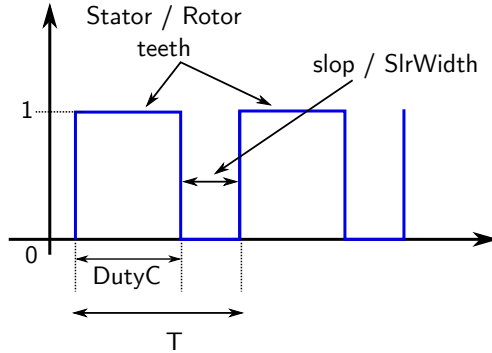


Figure 4.13: Definitions and equivalence of the pulse wave to the stator and rotor teeth.

#### 4.2.3.3.3 Fourier series of the stator tooth

The Fourier series used to analytically represent the stator teeth is:

$$S(\theta) = \sum_{n=1}^{N_{fourier}} \frac{2}{n\pi} \sin\left(\frac{\pi \cdot n \cdot DutyC_s}{T_s}\right) \cos\left(\frac{2\pi n}{T_s} \theta\right) \quad (4.12)$$

where:

$$DutyC_s = \frac{\frac{(2\pi/Nsl) \cdot (Dis/2) - slop/\xi}{Dis/2}}{T_s}$$

$$T_s = \frac{2\pi}{Nsl}$$

$N_{fourier}$	number of Fourier terms used to truncate the series
$DutyC_s$	duty cycle of the stator waveform
$T_s$	period of the stator waveform
$Nsl$	number of stator slots
$Dis$	stator internal diameter
$slop$	slot opening
$\xi$	parameter used to control the pulse wave width (see Fig. 4.14 for details)

#### 4.2.3.3.4 Increasing the equivalent width of the pulse wave: definition of parameter $\xi$

The effect of parameter  $\xi$  can be seen in Fig. 4.14. If  $\xi = 1$ , the duty cycle is defined exactly with respect to the stator or rotor teeth width. The problem is that the smooth transition of the Fourier series results in an equivalent width smaller than required to take into account the fringing flux. To correct this, the  $\xi$  parameters is used to find an equivalent teeth width that allows to take into account the fringing flux, as shown in the second illustration in Fig. 4.14. For the chosen BDFRM topology,  $\xi = 5$  has been used (defined empirically).

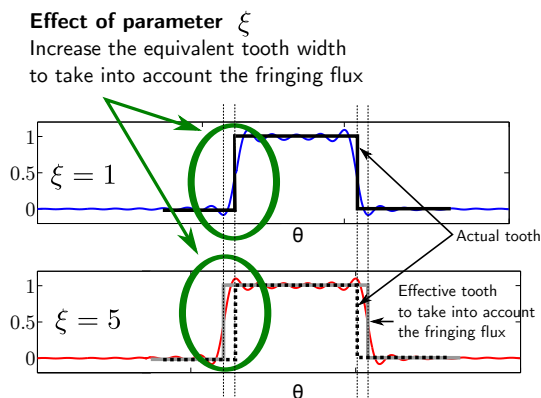


Figure 4.14: The effect of parameter  $\xi$  to take into account the fringing flux.

#### 4.2.3.3.5 Fourier series of the rotor tooth

With the definitions set above, the Fourier series for the rotor waveform is:

$$R(\theta) = \sum_{n=1}^{N_{fourier}} \frac{2}{n\pi} \sin\left(\frac{\pi \cdot n \cdot DutyC_r}{T_r}\right) \cos\left(\frac{2\pi n}{T_r}\theta\right) \quad (4.13)$$

where:

$$DutyC_r = \frac{(2\pi/Nslr) \cdot (Der/2) - SlrWidth/\xi}{Der/2}$$

$$T_r = \frac{2\pi}{Nslr}$$

$DutyC_r$	duty cycle of the rotor waveform
$T_r$	period of the rotor waveform
$Nslr$	number of rotor slots (ducts)
$Der$	rotor external diameter
$SlrWidth$	width of rotor duct

#### 4.2.3.3.6 Equivalent reluctance width by using the Fourier series method

The equivalent angle in the air-gap representing the arc “seen” by the reluctance is found by integrating the result of the multiplication between the stator and rotor waveforms, since the amplitudes of  $S(\theta)$  and  $R(\theta)$  are 1.

$$EqArcAngle = \int_{\theta_i}^{\theta_f} F(\theta)d\theta = \int_{\theta_i}^{\theta_f} S(\theta)R(\theta)d\theta \quad (4.14)$$

where the initial  $\theta_i$  and final  $\theta_f$  integration angles are individually defined in terms of the rotor position  $\theta_{rm}$  for each reluctance being calculated.

Finally, the equivalent reluctance length is given by:

$$EqWidth_{FSM} = EqArcAngle \cdot R_{gap} \quad (4.15)$$

#### 4.2.3.4 The choice of the Fourier series method

In [121, 122], an investigation on three different methods for the modeling of the air-gap in terms of rotor position has been performed: straight teeth method, trapezoidal teeth method and Fourier series method. The best results when compared to FEA have been found

with the Fourier series method and this is the one that has been chosen to be used in this work.

### 4.3 Sub-model 2: Air-gap/Source Rotation Model (AGSRM)

This section introduces the modeling approach used to effectively obtain multi-static calculation for the BDFRM MSRN model. Before addressing the adopted solution, a short review on different strategies used for modeling electrical machines by using reluctance networks is presented.

#### 4.3.1 Different approaches to take into account multi-static calculations and the proposed method used in this thesis

The greatest issue to perform multi-static calculations using the reluctance network approach is on the air-gap modeling. In the literature, some solutions have been discussed and they are briefly described in the sequence.

##### 4.3.1.1 Solution 1: one RN for each rotor position

Probably the most obvious solution is to develop a static reluctance network for each rotor position one wants simulate. The results of each individual solution must be assembled in order to get the outputs in terms of the simulation time. This method, although possible, is very time consuming to develop and difficult to manage considering eventual modifications. For these reasons, it is not considered in this work.

##### 4.3.1.2 Solution 2: rotating the MMF sources by using an electrical angle

It is possible to calculate some important machine parameters such as the average torque by using a single static RN without parameterizing the air-gap reluctances in terms of rotor position. For example, if one is interested only on the average torque capability and not on taking into account the slotting effects, an alternative is to analytically parametrize the MMF source positions as a function of the electrical angle  $\theta_{mmf}$ . When this angle is rotated, keeping constant the excitation currents, it provides the average torque as a function of  $\theta_{mmf}$ .

This approach has been used, for example, by Perez [123] to calculate the average torque capability of the machine being investigated in the referred work.

#### **4.3.1.3 Solution 3: emulating the mechanical rotation of the MMF sources by using a transformation matrix**

Reinbold [101] proposes an approach in which the multi-static calculations are achieved by emulating a mechanical displacement of the mmf sources by using a single RN. A transformation matrix is deduced to correctly link the flux circulating at each stator tooth to the flux linking a phase winding. The results that can be obtained with solutions 2 and 3 are similar, since in both methods the air-gap reluctances are not parametrized in terms of the rotor position. Thus, one can only evaluate the average torque and the fundamental component of the phase voltages, the slotting effects are not taken into account, because the RN is always the same independently of the rotor position.

#### **4.3.1.4 Solution 4: air-gap reluctances connecting all the possible interactions between stator and rotor as a function of rotor position**

Dogan [121, 122] proposes an approach to take into account multi-static calculations for a permanent magnet machine. The idea behind the methodology is to connect all the rotor terminals to all the possible stator terminals in order to provide equivalent flux paths in the air-gap for all rotor positions ( $\theta_{rm}$ ) as illustrated in Fig. 4.15. The equivalent length of the air-gap reluctances are parametrized as a function of  $\theta_{rm}$  so that the equivalent reluctances for any position can be calculated. This approach allows to take into account intermediary rotor steps between adjacent stator teeth and, hence, voltage harmonics and torque ripple can be estimated.



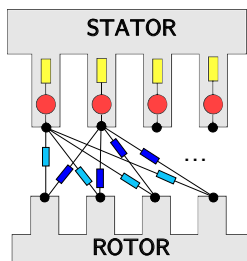


Figure 4.15: Representation of the air-gap reluctances connecting all the possible flux tubes.

This method was interesting in [121, 122] for the permanent magnet machine mostly due to its small model size. From a symmetry point of view, only one quarter of the machine has been considered. Additionally, due to geometry topology, only 6 air-gap reluctances were necessary to connect rotor to stator to take into account multi-static positions. However, if we look into a more general case, machines with complicated rotor/stator designs could lead to prohibitive reluctance network assembly, as it is the case of the BDFRM topology considered in this work,. Fig. 4.16 illustrates the BDFRM problem for a single rotor reluctance.

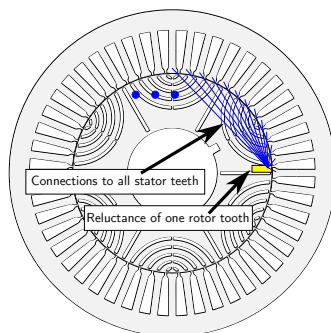


Figure 4.16: Illustration of the approach connecting every rotor tooth to all stator teeth.

Firstly, connecting all the rotor teeth reluctance to all the stator teeth have no *physical* sense, since the great majority of the flux tubes would be inexistent in a practical case. Secondly, although some techniques can be applied to improve convergence [124], the matrix size

to represent the equation system is huge and it would most likely be ill-conditioned, resulting in numerical issues for system solution (considering the investigated BDFRM topology,  $(Nslr \cdot Nsl)/2 = (66 \cdot 48)/2 = 1584$  reluctances would be necessary *only* in the air-gap, assuming half-machine symmetry).

#### 4.3.1.5 The use of symmetry to simplify the reluctance network

It is possible to take advantage of symmetry to simplify the reluctance network when considering rotor movement [101]. Fig. 4.17 illustrates the symmetry principle considering a rotor displacement equivalent to the angle between two adjacent stator teeth ( $\psi_{st}$ ).

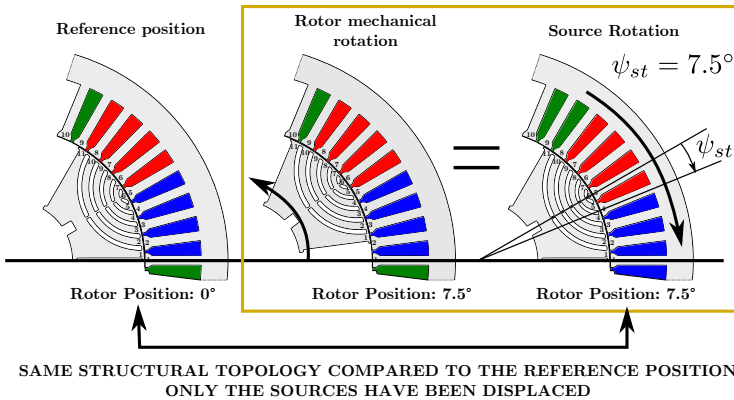


Figure 4.17: Illustration of the symmetry principle due to a rotor displacement of one stator teeth  $\psi_{st}$ .

In Fig. 4.17, the reference position ( $\theta_{rm} = 0^\circ$ ) is defined in the image on the left. The illustration in the middle shows a rotor mechanical displacement in the counterclockwise direction equivalent to one stator tooth  $\psi_{st}$ . Based on this two images, it can be seen that the machine *structural topology* on the right ( $\theta_{rm} = 7.5^\circ$ ) is identical to the reference position ( $\theta_{rm} = 0^\circ$ ), the only difference being the position of the windings that have been displaced in the clockwise direction of an angle  $\psi_{st}$ . If we continue the process, and we turn again the windings of each slot to the next slot in the clockwise direction, we will see that the rotor is exactly at  $\theta_{rm} = 15^\circ$ , without having effectively rotated.

It can be concluded from Fig. 4.17 that the machine topology, and hence the associated reluctance network, is periodic and its period is

given by  $\psi_{st}$ . One can infer from this discussion that whether the air-gap reluctances connecting the rotor pole to the stator teeth are defined in the interval  $[0, \psi_{st}]$  and their equivalent lengths parametrized in terms of  $\theta_{rm}$ , *any* rotor position can be calculated. The only requirement is to rotate the magnetomotive sources of an angle  $\theta_{mmf}$ . The magnetomotive sources modeling and the use of the angle  $\theta_{mmf}$  to rotate them is discussed in Section 4.3.2.

In general, the symmetry principle is also valid for other machines. On the majority of the cases, even if the rotor pole itself has a complicated geometry, the rotor poles around the machine have a repetitive pattern, i.e. they are symmetrical. Thus, by representing the rotor pole once, the pattern is repeated for the other ones and the approach remains valid.

#### **4.3.1.6 Solution 5: developed method - hybridization of the previous solutions to be able to effectively perform multi-static calculations at any rotor position**

None of the previous approaches fit exactly the requirements to accurately calculate the phase voltages in the BDFRM: the absence of intermediary positions (considering the slotting effects) in solutions 2 and 3 and the potential numerical issues in solution 4 must be assessed for this purpose.

In this sense, it is proposed a hybrid method based on the aforementioned previous works [121, 123, 101]: the air-gap reluctances are parametrized in terms of the rotor position and, at the same time, the MMF sources are rotated both electrically (rotating magnetic field) and mechanically (displacing the source positions in the stator slots to take full advantage of the symmetry principle).

To manage the rotor movement within the range defined by the symmetry condition ( $[0, \psi_{st}]$ ) and, from then on, to calculate any rotor position by performing effective multi-static calculations by using the a single SRN, it is required to execute some tasks based on previous solutions:

1. update the rotating magnetic field through the equivalent MMF sources calculated as a function of the time (notice that the simulation time ( $t$ ) and the rotor position ( $\theta_{rm}$ ) are connect through the constant rotor angular speed ( $\omega_{rm}$ ) since we assume steady-state operation);
2. verify if the sources themselves must be rotated to consider a position  $\theta_{rm}$  outside the range  $[0, \psi_{st}]$  by using the same SRN;

3. to calculate the equivalent air-gap reluctances lengths as a function of the rotor mechanical position ( $\theta_{rm}$ ) within the range  $[0, \psi_{st}]$ .

These steps are discussed in the sequence, starting by the MMF sources modeling followed by the air-gap model.

### 4.3.2 AGSRM model - Part 1: magnetomotive sources modeling: assessing the equivalent one for each stator tooth to take into account rotor movement

#### 4.3.2.1 Parameter definitions used to manage the rotor movement

##### 4.3.2.1.1 Rotor position and simulation time

The rotor position ( $\theta_{rm}$ ) is the reference for the multi-static calculations and the remaining parameters are calculated as a function of it. It is incremented of an angle representing the rotor angular step ( $\Delta\theta_{rm}$ ) for the next iteration.

Assuming that the rotor initial position is zero ( $\theta_{rm0} = 0$ ) and that the simulation time starts at  $ts_0 = 0s$  (these assumptions have no impact on the optimization process, since always at least one electrical period is calculated for each winding), the simulation time  $ts$  calculated in terms of the rotor position  $\theta_{rm}$  is given by:

$$ts = \frac{\theta_{rm}}{\omega_{rm}} = \frac{1}{2} \cdot \theta_{rm} \cdot \frac{P_g + P_c}{\omega_g + \omega_c} \quad (4.16)$$

where  $\omega_{rm}$  is:

$$\omega_{rm} = 2 \cdot \frac{\omega_g + \omega_c}{P_g + P_c} \quad (4.17)$$

For the purpose of the optimization studies proposed in this work, it is assumed that the machine operates in steady-state conditions. Therefore, (4.16) connects the parameter simulation time ( $ts$ ) to the rotor position  $\theta_{rm}$  and affect the phase currents as depicted in the sequence:

$$\left. \begin{aligned} i_{ga} &= I_g \cos(\omega_g t s) \\ i_{gb} &= I_g \cos\left(\omega_g t s - \frac{2\pi}{3}\right) \\ i_{gc} &= I_g \cos\left(\omega_g t s + \frac{2\pi}{3}\right) \end{aligned} \right\} \text{Grid} \quad (4.18)$$

$$\left. \begin{aligned} i_{ca} &= I_c \cos(\omega_c t s - \alpha_c) \\ i_{cb} &= I_c \cos\left(\omega_c t s - \alpha_c - \frac{2\pi}{3}\right) \\ i_{cc} &= I_c \cos\left(\omega_c t s - \alpha_c + \frac{2\pi}{3}\right) \end{aligned} \right\} \text{Control} \quad (4.19)$$

These currents are used to calculate the magnetomotive force in Section 4.3.2.3.4.

#### 4.3.2.1.2 Definition of the angles used to manage the multi-static calculations

To perform the multi-static calculations, different angles have been introduced in the MSRN model and it is important to highlight the difference among them. The distinct angles are depicted in Fig. 4.18 for illustration. In this figure, the angle difference between  $\theta_2$  and  $\theta_1$  is defined by the angle between two adjacent stator teeth ( $\psi_{st}$ ) and the time  $t_1$  up to  $t_n$  are calculated considering a constant speed and (4.16).

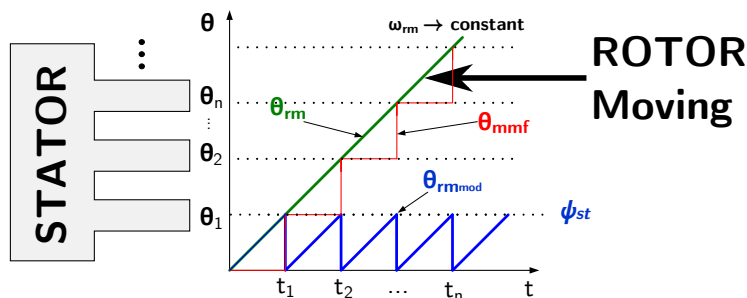


Figure 4.18: Angle definitions used for multi-static calculations.

As previously stated, the  $\theta_{rm}$  is the reference angle that represents the rotor position. Although the number of positions and the discretization<sup>3</sup> of the multi-static modeling is, *a priori*, arbitrary, the calculation of the voltage waveforms and their RMS values imply in the consideration of at least one full electrical period for each winding. For example, let us consider the case where  $\omega_g = \omega_c = 2\pi 50$ . The

<sup>3</sup>The discretization refers to the rotor angular step ( $\Delta\theta_{rm}$ ) among each multi-static calculation.

electrical period in this case is  $T_g = T_c = 0.02$  s for both windings and the rotor speed is  $\omega_{rm} = 1000$  rpm. With this conditions, the rotor position at 0.02 s is  $\theta_{rm} = T_g \times \omega_{rm} = 120^\circ$ . If the adopted rotor step is  $\Delta\theta_{rm} = \psi_{st} = 7.5^\circ$ , the number of positions to be calculated for a full electric period in both windings is 16. If the it is  $\Delta\theta_{rm} = \psi_{st}/2 = 3.75^\circ$ , the number of positions is 32, and so on.

The angle  $\theta_{rm_{mod}}$  is derived from  $\theta_{rm}$ . It is calculated by using the modulo function (4.20), which provides a periodic signal in a form of a sawtooth function, varying from 0 up to  $\psi_{st}$ . It means that the  $\theta_{rm_{mod}}$  is a periodic function with period  $\psi_{st}$ . The angle  $\theta_{rm_{mod}}$  is used to calculated the air-gap equivalent reluctance widths, since, for that purpose, only a rotor movement in the interval  $[0, \psi_{st}]$  is considered.

$$\theta_{rm_{mod}} = \text{modulo}(\theta_{rm}, \psi_{st}) \quad (4.20)$$

The angle  $\theta_{mmf}$  is used to rotated the sources in the clockwise direction every time the  $\theta_{rm}$  parameter completes a period  $\psi_{st}$ , as depicted in Fig. 4.18. It is defined as follows:

$$\theta_{mmf} = N_{mmf} \cdot \psi_{st} \quad (4.21)$$

where  $N_{mmf}$  is an integer number that indicates how many times the sources must be rotated of an angle  $\psi_{st}$  to calculate the rotor position  $\theta_{rm}$  and it is given by:

$$N_{mmf} = \text{Integer} \left( \frac{\theta_{rm}}{\psi_{st}} \right) \quad (4.22)$$

where Integer is a function that returns the integer number of the division.

### 4.3.2.2 Modeling the MMF sources

The modeling of the MMF sources has basically two goals: firstly, they are the electrical excitation of the static reluctance network and must be calculated for this purpose. Secondly, their positions around the air-gap are varied to take advantage of symmetry to simplify the network when performing multi-static simulations. How these tasks are accomplished is discussed in the sequence.

#### 4.3.2.2.1 Three possible approaches for modeling the MMF sources

Three possibilities for modeling the MMF sources have been evaluated in this work:

1. Fundamental component (“fund”): only the fundamental component is considered. It is the same approach used for modeling the SAM MMF sources.
2. Truncating the Fourier series after the first three nonzero MMF harmonics (“harm”): the MMF sources are calculated by using the most significant lower order harmonics to analytically obtain their instantaneous values.
3. Discrete (“disc”): in the discrete method, the Ampère-turns contribution of each slot on the MMF source being calculated is assessed by solving the Ampère’s Law for each one of them. The discrete method results in a rectangular waveform and, therefore, the majority of the MMF harmonics are taken into account.

The “fund” and the “harm” methods are defined by analytical equations, whereas the “disc” is represented by a vector in which each element represents a MMF source. The accuracy of these methods to represent the fundamental and lower order harmonics of the voltage and torque waveforms have been tested and the results are presented in Appendix F. As expected, the “fund” method is limited and can be basically used only to calculate the fundamental component of the output parameters. Regarding harmonic calculations, the “harm” and the “disc” methods present comparable results since the most relevant lower order harmonics are taken into account in both.

Based on the fact that the MSRN performs multi-static simulations to evaluate the rms phase voltages aiming to improve the accuracy obtained with the SAM, it seems reasonable to choose a method that provides more precise results without compromising the computation time. Therefore, the “harm” method has been chosen to implement the MMF sources because it considers the most significant lower order MMF harmonics, improving accuracy, and, from a modeling point of view, it is represented exclusively by analytical equations.

#### **4.3.2.3 Method “harm”: calculating the MMF analytically by using the winding function theory**

##### **4.3.2.3.1 Input parameters used to calculate the MMF sources**

Although the approach to calculate the MMF sources presented in the

sequence is general, it is interesting to illustrate the equations and the respective waveforms through an example. For this purpose, the BDFRM topology, introduced in Chapter 2, and the parameters of the prototype machine introduced in Appendix D are used. Table 4.5 depicts the main input parameters used to calculate the MMF for grid and control windings.

Table 4.5: Input parameters used to calculate the winding functions and the MMF sources.

$N_{slg}$	56	$N_{slc}$	39
$N_{phg}$	448	$N_{phc}$	312
$f_g$	50 Hz	$f_c$	50 Hz
$P_g$	8	$P_c$	4
$I_g$	3.07 A	$I_c$	3.23 A
$\alpha_c$	90 °	$Nsl$	48

where:

$N_{slg} / N_{slc}$	number of turns per slot (grid/control)
$N_{phg} / N_{phc}$	number of turns per phase (grid/control)
$f_g / f_c$	frequency (grid/control)
$P_g / P_c$	number of poles (grid/control)
$I_g / I_c$	amplitude of phase current (grid/control)
$\alpha_c$	phase angle between the three phase system of both windings
$Nsl$	number of stator slots

The “harm” method truncates the Fourier series at the first three non-zero MMF harmonics at each winding. The resulting waveforms that are presented in the sequence compare the methods “harm” and “fund” for illustration purpose. The goal is to highlight the modeling differences that one can obtain by representing only the fundamental component or taking the lower order harmonics into account.

#### 4.3.2.3.2 Windings distribution in the considered BDFRM topology

The MMF are calculated based on the winding function theory. The main aspects regarding this approach are presented in Appendix A.1. The first step for modeling the MMF sources is to identify the winding arrangements around the machine slots.

The windings of the considered BDFRM topology are defined in Fig. 4.19.



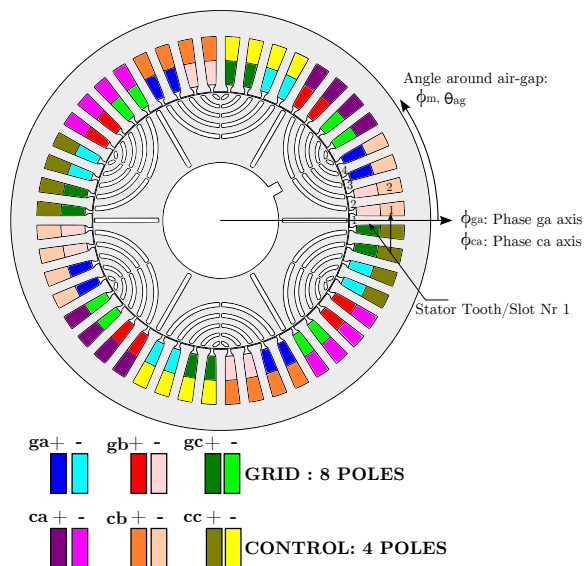


Figure 4.19: Winding definitions for the considered BDFRM topology.

Fig. 4.19 allows to define a vector containing the number of turns per slot for each phase winding. These vectors are shown in Table 4.6. Only the first 24 slots are shown in this table for simplicity since the pattern is repetitive (the chosen machine structural topology defined in Chapter 2 presents half symmetry).

Table 4.6: Number of turns per slot: discrete distribution for each winding.

Slot $i$	$N_{ga}$	$N_{gb}$	$N_{gc}$	$N_{ca}$	$N_{cb}$	$N_{cc}$
1	0	$-N_{slg}$	0	0	$-N_{slc}$	0
2	0	$-N_{slg}$	0	0	$-N_{slc}$	0
3	$N_{slg}$	0	0	0	$-N_{slc}$	0
4	$N_{slg}$	0	0	0	$-N_{slc}$	0
5	0	0	$-N_{slg}$	$N_{slc}$	0	0
6	0	0	$-N_{slg}$	$N_{slc}$	0	0
7	0	$N_{slg}$	0	$N_{slc}$	0	0
8	0	$N_{slg}$	0	$N_{slc}$	0	0
9	$-N_{slg}$	0	0	0	0	$-N_{slc}$
10	$-N_{slg}$	0	0	0	0	$-N_{slc}$
11	0	0	$N_{slg}$	0	0	$-N_{slc}$
12	0	0	$N_{slg}$	0	0	$-N_{slc}$
13	0	$-N_{slg}$	0	0	$N_{slc}$	0
14	0	$-N_{slg}$	0	0	$N_{slc}$	0
15	$N_{slg}$	0	0	0	$N_{slc}$	0
16	$N_{slg}$	0	0	0	$N_{slc}$	0
17	0	0	$-N_{slg}$	$-N_{slc}$	0	0
18	0	0	$-N_{slg}$	$-N_{slc}$	0	0
19	0	$N_{slg}$	0	$-N_{slc}$	0	0
20	0	$N_{slg}$	0	$-N_{slc}$	0	0
21	$-N_{slg}$	0	0	0	0	$N_{slc}$
22	$-N_{slg}$	0	0	0	0	$N_{slc}$
23	0	0	$N_{slg}$	0	0	$N_{slc}$
24	0	0	$N_{slg}$	0	0	$N_{slc}$

\*  $N_{slg}$  and  $N_{slc}$  mean the number of turns per slot for grid and control windings, respectively.

The continuous conductor distribution for each phase can be analytically calculated by [87]:

$$n_x(\theta_{ag}) = \sum_{j=1}^{J_{fourier}} a_j \cos(j\theta_{ag}) + b_j \sin(j\theta_{ag}) \quad (4.23)$$

where:

$x$  denotes a specific winding (e.g.  $ga$ ,  $gb$ ,  $gc$ ,  $ca$ ,... where  $g$  and  $c$  means grid or control, respectively).

$\theta_{ag}$  represents the angle around the air gap.

$J_{fourier}$  is the number of coefficients considered in the series.

The coefficients  $a_j$  and  $b_j$  must be calculated for each phase winding

and are given by, respectively [87]:

$$a_j = \frac{1}{\pi} \sum_{i=1}^{Nsl} N_{x,i} \cos(j\phi_{ys,i}) \quad (4.24)$$

$$b_j = \frac{1}{\pi} \sum_{i=1}^{Nsl} N_{x,i} \sin(j\phi_{ys,i}) \quad (4.25)$$

where index  $i$  refers to the slot being considered.  $\phi_{ys,i}$  is the center of the  $i$ 'th slot (angle) and it is calculated by:

$$\phi_{ys,i} = \pi(2i - 2)/Nsl + \phi_{ys,1} \quad (4.26)$$

where  $\phi_{ys,1}$  is the center (angle) of the slot number 1. For the considered BDFRM topology,  $\phi_{ys,1} = \psi_{st}/2 = 3.75^\circ$  (see Fig. 4.19).

From Table 4.6, the coefficients of Fourier series  $a_j$  and  $b_j$  can be calculated by substituting the parameters  $N_{x,i}$  accordingly.

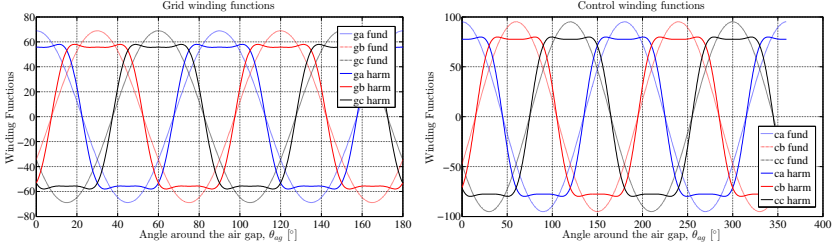
#### 4.3.2.3.3 Calculation of the winding functions for each phase

The winding function of the phase winding  $x$  is given by [87]:

$$w_x(\theta_{ag}) = \frac{1}{2} \int_0^{2\pi/P} n_x(\theta_{ag}) d\theta_{ag} - \int_0^{\theta_{ag}} n_x(\theta_{ag}) d\theta_{ag} \quad (4.27)$$

Equation (4.27) can be solved analytically, recalling that  $n_x(\phi_m)$  is a sum of sinusoidal functions. The results for all of the phases are shown in Appendix F.2.

The resulting winding function waveforms for the grid and control windings are shown in Fig. 4.20a and Fig. 4.20b, respectively. The “fund” and the “harm” methods are plot together for comparison purpose.



(a) Winding function from grid.

(b) Winding function from control.

Figure 4.20: Grid and control winding functions for models *harm* and *fund*. Grid plot presents only half machine ( $180^\circ$ ) for clarity.

It can be seen that the amplitude of the winding function converges to the number of turns per pole  $N_{tp_x}$  of each winding. In the considered case, the number of turns per pole of grid winding is  $N_{tp_g} = N_{phg}/P_g = 448/8 = 56$  and the number of turns per pole of the control winding is  $N_{tp_c} = N_{phc}/P_c = 312/4 = 78$ . It is also possible to remark the differences in the waveforms by comparing the *fund* and *harm* approaches.

#### 4.3.2.3.4 Calculating the MMF by using the winding function theory

The winding function provides means to calculate the magnetomotive forces from each winding. The resulting MMF of a 3-phase winding can be calculated by [87]:

$$\mathbb{F}_s = w_{as}(\theta_{ag})i_{as} + w_{bs}(\theta_{ag})i_{bs} + w_{cs}(\theta_{ag})i_{cs} \quad (4.28)$$

Assuming a balanced three phase current system in both windings, the grid and control winding MMF are given by <sup>4</sup>:

$$\mathbb{F}_g(\theta_{ag}, ts) = w_{ga}(\theta_{ag})i_{ga}(ts) + w_{gb}(\theta_{ag})i_{gb}(ts) + w_{gc}(\theta_{ag})i_{gc}(ts) \quad (4.29)$$

$$\mathbb{F}_c(\theta_{ag}, ts) = w_{ca}(\theta_{ag})i_{ca}(ts) + w_{cb}(\theta_{ag})i_{cb}(ts) + w_{cc}(\theta_{ag})i_{cc}(ts) \quad (4.30)$$

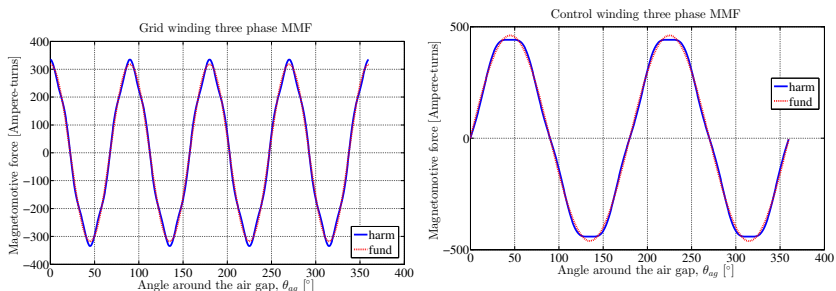
The solution of (4.29) and (4.30) are shown in the Appendix F.3.

<sup>4</sup>The balance three phase currents are defined in (4.18) and (4.19)

The resulting total MMF contribution, considering the effect of grid and control windings simultaneously, is obtained by:

$$\mathbb{F}_t(\theta_{ag}, ts) = \mathbb{F}_g(\theta_{ag}, ts) + \mathbb{F}_c(\theta_{ag}, ts) \quad (4.31)$$

Fig. 4.21a and Fig. 4.21b shows the MMF for the grid and control windings for  $ts = 0s$  as a function of  $\theta_{ag}$ . It is interesting to notice that, although the *fund* and *harm* waveforms are distinct, the difference between them is not so expressive as one could imagine when compared to the difference among the winding functions presented in Fig. 4.20a and Fig. 4.20b.



(a) Grid winding  $3\phi$  MMF ( $ts = 0s$ ). (b) Control winding  $3\phi$  MMF ( $ts = 0s$ ).

Figure 4.21: Grid and control 3-phase magnetomotive forces for *harm* and *fund* models.

Fig. 4.22 shows the global effect of both windings excited simultaneously due to the double winding configuration of the BDFRM for rated conditions at  $ts = 0s$ . Again, both waveforms are similar.

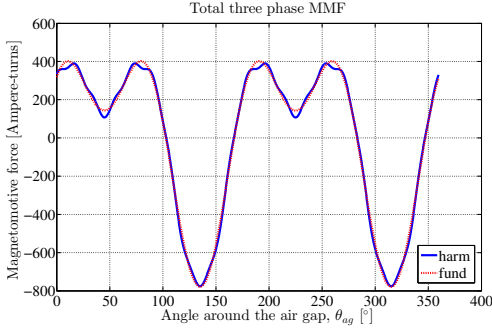


Figure 4.22: Total three phase magnetomotive force versus  $\theta_{ag}$  for  $t_s = 0s$ .

#### 4.3.2.3.5 Discretization of the MMF waveform to define the equivalent source value at each stator tooth

The procedure presented so far allows to calculate the MMF waveform through (4.31) in terms of the simulation time ( $t_s$ ) and of the angle around the air-gap ( $\theta_{ag}$ ). From a practical point of view, the instantaneous value of the equivalent MMF sources of the static reluctance network (SRN) must be obtained through a discretization of the MMF waveform at each stator tooth.

Thus, for the MMF source placed at stator tooth “ $i$ ”, the angle  $\theta_{ag}$  in (4.31) is replaced by:

$$\theta_{ag} = TOOTH\_i_{angle} + \theta_{mmf} \quad (4.32)$$

where  $TOOTH\_i_{angle}$  is the position of the stator tooth “ $i$ ” with respect to the reference angle in the air-gap. This substitution must be done for all the MMF sources in the SRN.

The substitution depicted in (4.32) determines the MMF value at each stator tooth and introduces the angle  $\theta_{mmf}$  into the static reluctance network. This provides means to analytically rotate the sources when necessary to execute the multi-static simulation.

The actual discretized values of the global MMF previously presented in Fig. 4.22 are shown in Fig. 4.23 for  $t_s = 0s$ . To better highlight the differences between the “fund” and “harm” methods, Fig. 4.24a and Fig. 4.24b presents a zoom at the top and at the bottom, respectively.

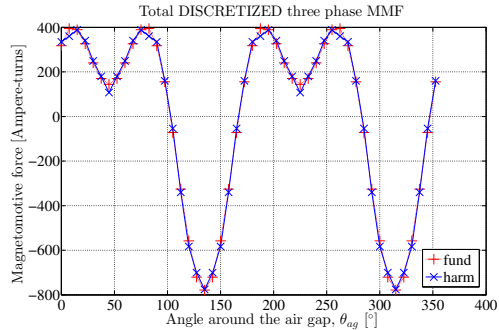


Figure 4.23: Total three-phase magnetomotive force discretized for each slot for  $t = 0s$ .

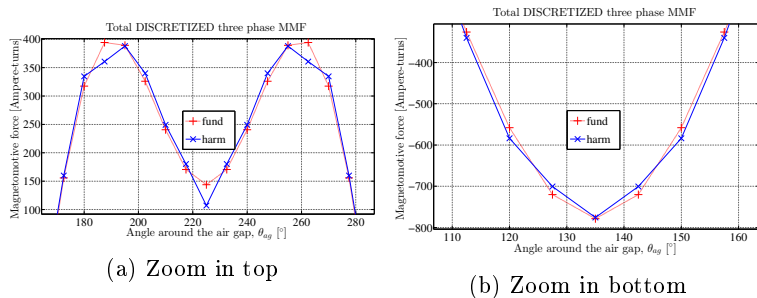


Figure 4.24: Zoomed total three-phase magnetomotive force discretized for each stator slot at  $ts = 0s$ .

### 4.3.3 AGSRM model - Part 2: reluctance network topology of the air-gap

The reluctance network of the air-gap must represent all the possible flux tubes that may exist in the range  $[0, \psi_{st}]$  considering the stator and rotor teeth that are face-to-face and the ones in the vicinity that may eventually provide additional flux paths.

To define the air-gap model, Fig. 4.25 illustrates the rotor at the two extreme positions in the range  $[0, \psi_{st}]$  ( $0^\circ$  and  $7.5^\circ$ ) with the respective number definition corresponding to the rotor and stator terminals that shall be connected through the air-gap.

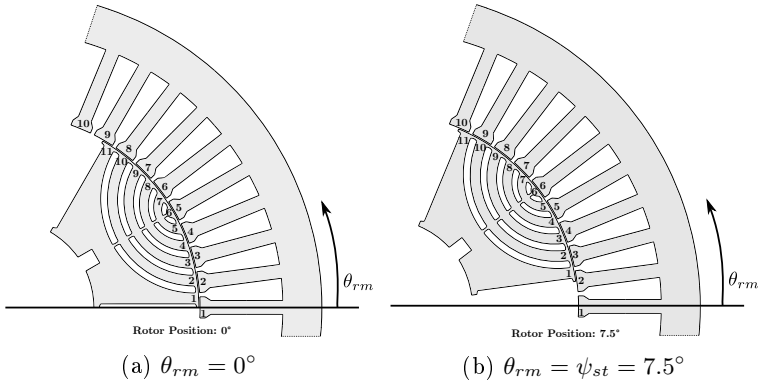


Figure 4.25: Air gap modeling: rotor position  $\theta_{rm} = 0^\circ$  (4.25a) and  $\theta_{rm} = 7.5^\circ$  (4.25b) with the number definitions that are used to calculate the reluctances.

The following approach is used to identify all possible connection between rotor and stator: taking the rotor flux path 1 as an example, from Fig. 4.25a, it is required to assure an air-gap flux tube to the stator teeth 1 and 2. Similarly, observing Fig. 4.25b at  $\psi_{st}$ , the possibilities from rotor flux path 1 are stator teeth 2 and 3. Fig. 4.26 shows a zoom over the referred region. Thus, to connect rotor 1 to stator 1, 2 and 3, three reluctances are required. By applying this procedure for each rotor flux path, from 1 to 11 in the range  $[0, \psi_{st}]$ , all the possible flux tubes connections in the air-gap are identified.

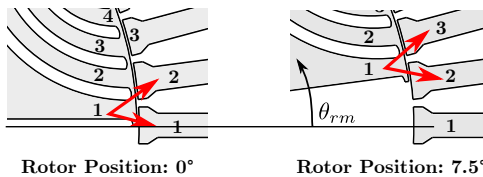


Figure 4.26: Definition of the connection between the rotor flux path 1 and stator teeth 1-2-3.

Fig. 4.27 depicts a simplified and linearized version of stator and rotor teeth indicating the static reluctance network of the air-gap that must be implemented to take into account any rotor position within the interval  $[0, \psi_{st}]$  for each rotor pole.



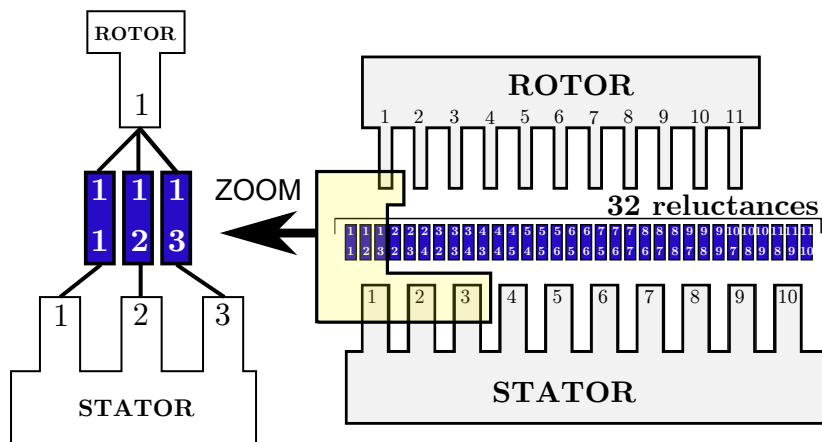


Figure 4.27: Linearize air-gap reluctances model to take into account rotation. Rotor position  $0^\circ$  is represented.

For the considered BDFRM topology, it is required 32 linear reluctances in the air-gap. Each one of them is parametrized regarding their position with respect to the reference angle ( $\theta_{ag}$ ) and the rotor position in terms of the angle  $\theta_{rm_{mod}}$  (Section 4.3.2.1.2). This allows to define the initial ( $\theta_i$ ) and the final ( $\theta_f$ ) integration angles of the Fourier series approach (Section 4.2.3.3.6) in order to calculate the reluctance equivalent widths.

## 4.4 The resulting static reluctance network

Fig. 4.28 depicts the components used to assembly the BDFRM static reluctance network.

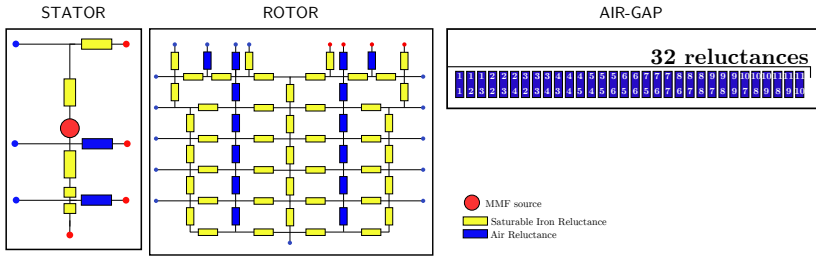


Figure 4.28: The components forming the static reluctance network model.

In total, for the considered BDFRM topology with half symmetry, there are components for 24 stator teeth, 3 rotor poles and 3 air-gap as illustrated in Fig. 4.29.

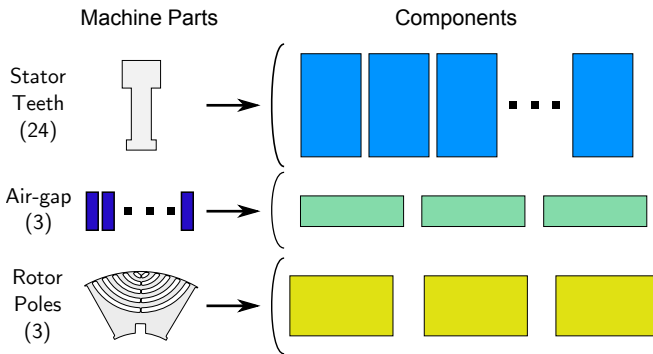


Figure 4.29: The static reluctance network model.

The total number of reluctances on the SRN are given in Table 4.7.

Table 4.7: Total number of reluctance in the network.

Sub-model	Number of Reluctances	Total per sub-system
Stator	$7 \times 24$	168
Rotor	$59 \times 3$	177
Air Gap	$32 \times 3$	96
<b>Total in the Network</b>		<b>441</b>

It is interesting to recall that the hybrid method proposed in Solu-

tion 5 (Section 4.3.1.6) and developed in this thesis has a total of 96 reluctances to represent the air-gap for half machine symmetry. If the method of Solution 4 (Section 4.3.1.4) were used, it would be required 1584 reluctances only in the air-gap. The hybrid solution that uses the symmetry principle, sources rotation and the air-gap modeling as a function of rotor position significantly reduces the number of reluctance ( $\approx 94\%$  reduction), improving numerical stability, for *exactly* the same accuracy.

## 4.5 Outputs calculation

The discussing presented so far addressed the development of a BDFRM multi-static reluctance network model. The following sections describe how the electromagnetic performance outputs defined in the beginning of this chapter (e.g. voltages, torque, flux density and others) are calculated by using the MSRN approach.

### 4.5.1 MSRN model: flowchart of the outputs

The multi-static calculations provide all the electromagnetic performance parameters in terms of the simulation time ( $ts$ ). To determine the outputs, the MSRN model is divided in two parts as illustrated in Fig. 4.30.

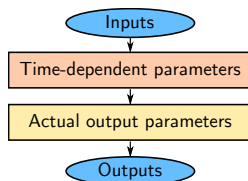


Figure 4.30: Processing steps to calculate the MSRN outputs.

The first part performs the multi-static calculations and obtains the time-dependent results (instantaneous values in terms of  $ts$ ). The second uses these results to assess the actual output parameters (previously defined in Table 4.2) that are calculated within at least one electrical period of grid and control windings, such as the average torque, the RMS voltages and the maximum flux densities.

To illustrate the MSRN calculation procedure, Fig. 4.31 shows the algorithm used to implement it.

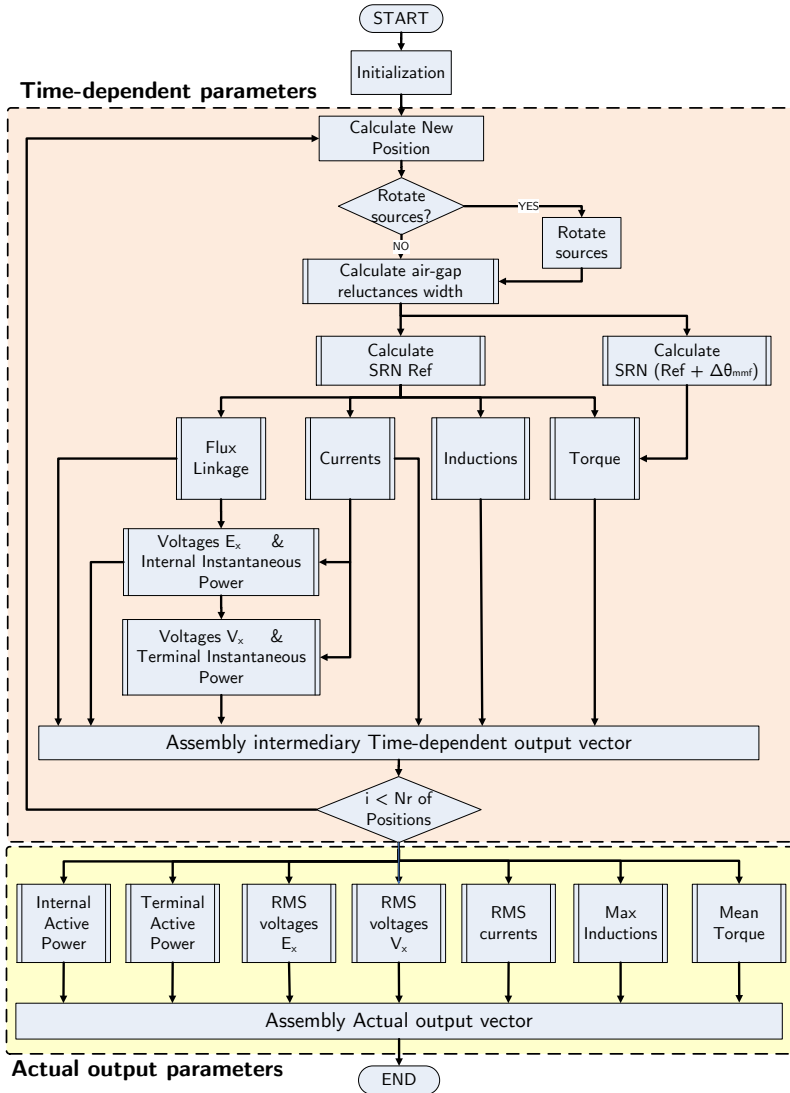


Figure 4.31: MSRN Global Electromagnetic Model Flowchart.

The procedure to calculate each one of the electromagnetic outputs are discussed in the sequence. The following notation is used for this purpose:

$K$  the number of multi-static calculation that are performed  
 $k$  index used to refer to each one of the  $K$  multi-static calculations

## 4.5.2 Electromagnetic torque

### 4.5.2.1 Coenergy variation principle

To obtain the electromagnetic torque, the principle of coenergy variation is used [32]:

$$T_{em} = \left. \frac{\partial W_{co}}{\partial \theta_{rm}} \right|_{i \text{ constant}} \quad (4.33)$$

where  $W_{co}$  is the total system coenergy calculated as an output of the the reluctance network for each position [111] and  $\theta_{rm}$  is the rotor mechanical position.

### 4.5.2.2 Instantaneous torque

In order to use (4.33) to calculate the instantaneous value of the torque, one needs the coenergy *variation*. The reluctance network only provides at each position the total coenergy, but not its derivative in terms of rotor position as it is required. Thus, to evaluate the instantaneous value of the torque, two calculations of the Static Reluctance Network (SRN) are performed at each position:

(i) Reference position  $[k]$ : this calculations refers to the actual rotor position  $\theta_{rm}$  being calculated. The  $W_{co}[k]$  is obtained.

(ii) Position  $[k + \Delta\theta_{mmf}]$ : the source position angle ( $\theta_{mmf}$ ) is incremented of a very small step ( $\Delta\theta_{mmf}$ ). All the remaining parameters stay unchanged, notably the currents, in order to respect the conditions of (4.33). Torque is then calculated by using a finite difference calculation, as shown in (4.34). The SRN model is built considering half symmetry, so the system coenergy and consequently the electromagnetic torque must be multiplied by a factor 2.

$$T_{em}[k] = 2 \times \left. \frac{W_{co}[k + \Delta\theta_{mmf}] - W_{co}[k]}{\Delta\theta_{mmf}} \right|_{i \text{ constant}} \quad (4.34)$$

where  $\Delta\theta_{mmf}$  is a very small angle increment that affect sources position to calculated the system coenergy variation. In this work, the angle displacement has been considered to be  $\Delta\theta_{mmf} = 0.003^\circ$ .

It is worth to recall that the electrical angle  $\theta_{mmf}$  variation to estimate the coenergy derivative has also been used in [123] to calculate torque as previously discussed in Section 4.3.1.2. On that work, changing the  $\theta_{mmf}$  allows to obtain only the machine average torque capability in terms of  $\theta_{mmf}$ , since the air-gap reluctances are not parametrized as a function of rotor position. On the contrary, in this work, the air-gap reluctances are parametrized in terms of  $\theta_{rm}$  and the  $\theta_{mmf}$  angle variation is used to calculate torque at each new rotor position. This yields in the instantaneous torque carrying out the torque ripple characteristic due to the effective multi-static calculations.

#### 4.5.2.3 Average torque

Finally, the average torque  $T_{em_{ave}}$  within an electrical period with  $K$  multi-static positions can be calculated by:

$$T_{em_{ave}} = \frac{1}{K} \sum_{k=1}^K T_{em}[k] \quad (4.35)$$

### 4.5.3 Phase Flux linkage

#### 4.5.3.1 General definition

The phase flux linkage  $\lambda_x$  is calculated by multiplying the total magnetic flux linking the respective phase  $\phi_x$  by the total number of turns per phase ( $Nph_x$ ). Generally:

$$\lambda_x = Nph_x \cdot \phi_x \quad (4.36)$$

where index  $x$  refers to the phase winding (e.g. *ga*, *gb*, *gc*, *ca*, *cb*, *cc*).

Fig. 4.32 depicts the procedure to calculate the phase flux linkages.

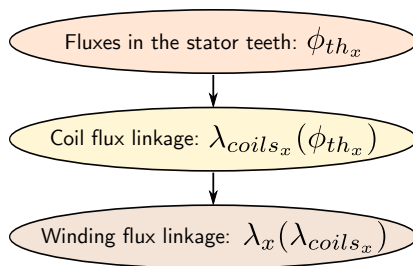


Figure 4.32: Procedure to calculate the phase flux linkages.

The strategy to calculate the flux linkage of phase “ $x$ ” ( $\lambda_x$ ) starts by the identification of the teeth and the associated fluxes ( $\phi_{th_x}$ ) that are linked by the phase being calculated. The fluxes passing through the stator teeth ( $\phi_{th_x}$ ) are used to calculate the flux linkage in each of the coils ( $\lambda_{coils_x}$ ) forming the phase  $x$  and, then, the total flux linkage of the phase winding  $x$  ( $\lambda_x$ ) can be assessed.

Next sections explain these calculations.

#### 4.5.3.2 Magnetic flux in stator teeth

The total magnetic flux  $\phi_x$  linked by phase  $x$  is calculated from the fluxes circulating through the reluctances in the stator teeth ( $\phi_{th}$ ). The magnetic flux  $\phi_{th}$  is directly obtained from the solution of the static reluctance network (SRN) for each rotor position. Fig. 4.33 defines the reluctance in the stator RN topology from which the flux ( $\phi_{th}$ ) is obtained to assess the phase flux linkage.

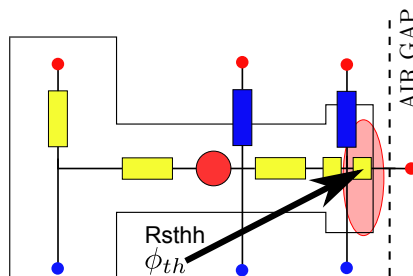


Figure 4.33: Definition of the reluctance that is used to calculate the flux linkage.

### 4.5.3.3 Flux linkage in the coils

To calculate the magnetic flux linking the coils of a phase winding, it is necessary to know the exact winding position in the investigated topology. The procedure is better explained through an example. For this purpose, let us calculate the flux linkage considering the phase  $cb$  of control winding.

Fig. 4.34 depicts the BDFRM with half machine symmetry. For clarity, only the control windings (4 poles) are shown with the respective coils for the phase  $cb$ . In this example, the phases of control winding have 4 coils, thus  $N_{coil_{sc}} = 4$ . The symbol  $Nslc$  refers to the number of conductors in each coil of the control winding.

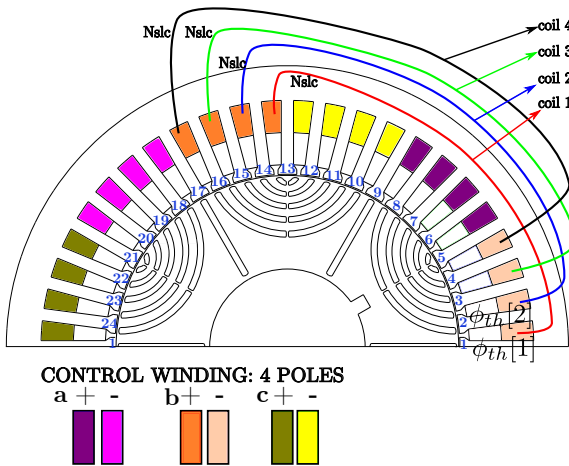


Figure 4.34: Coils forming the the phase  $cb$  of the control winding.

The flux linkage of each coil of phase  $cb$  is calculated by:

$$\begin{aligned}
 \lambda_{coil_{cb}}[1] &= Nslc (\phi_{th_{cb}}[2] + \phi_{th_{cb}}[3] + \cdots \phi_{th_{cb}}[13]) \\
 \lambda_{coil_{cb}}[2] &= Nslc (\phi_{th_{cb}}[3] + \phi_{th_{cb}}[4] + \cdots \phi_{th_{cb}}[14]) \\
 \lambda_{coil_{cb}}[3] &= Nslc (\phi_{th_{cb}}[4] + \phi_{th_{cb}}[5] + \cdots \phi_{th_{cb}}[15]) \\
 \lambda_{coil_{cb}}[4] &= Nslc (\phi_{th_{cb}}[5] + \phi_{th_{cb}}[6] + \cdots \phi_{th_{cb}}[16])
 \end{aligned} \tag{4.37}$$



#### 4.5.3.4 Updating stator teeth indexes to take into account source rotation and the multi-static calculations

When the sources are rotated in order to execute the multi-static calculations, the indexes used to calculate the coil flux linkages must also be updated, since the sources are no longer in their original place. This is achieved by rotating the indexes of the vectors containing the flux information.

Following the example of phase *cb* of control winding, Fig. 4.35 depicts the coil positions when the sources are rotated of an angle  $\psi_{st}$  in the clockwise direction.

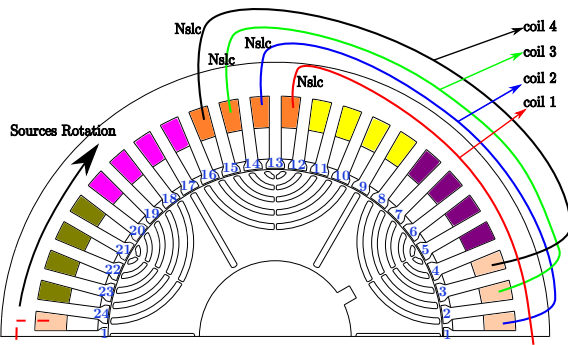


Figure 4.35: Coil positions for phase *cb* of control winding when the sources are rotated of an angle  $\psi_{st}$  in the clockwise direction.

From Fig. 4.35, it can be noticed that the stator teeth indexes must be decremented of one unit, as follows:

$$\begin{aligned}
 \lambda_{coil_{cb}}[1] &= Nslc (\phi_{th_{cb}}[1] + \phi_{th_{cb}}[2] + \cdots \phi_{th_{cb}}[12]) \\
 \lambda_{coil_{cb}}[2] &= Nslc (\phi_{th_{cb}}[2] + \phi_{th_{cb}}[3] + \cdots \phi_{th_{cb}}[13]) \\
 \lambda_{coil_{cb}}[3] &= Nslc (\phi_{th_{cb}}[3] + \phi_{th_{cb}}[4] + \cdots \phi_{th_{cb}}[14]) \\
 \lambda_{coil_{cb}}[4] &= Nslc (\phi_{th_{cb}}[4] + \phi_{th_{cb}}[5] + \cdots \phi_{th_{cb}}[15])
 \end{aligned} \tag{4.38}$$

#### 4.5.3.5 Instantaneous phase flux linkage

Finally, the flux linkage of phase *cb* is calculated by (factor 2 is due to the half symmetry):

$$\lambda_{cb}(\theta_{rm}) = 2 \cdot \sum_{k_{coil}=1}^{N_{coils_c}} \lambda_{coil_{cb}}[k_{coil}](\theta_{rm}) \quad (4.39)$$

where  $N_{coils}$  is the number of coils of the respective phase and  $\lambda_{coil_{cb}}$  is the vector containing the flux linkage of each coil of phase  $cb$ .

The same procedure is applied to all six phases of grid and control windings to calculate the flux linkage. In a general way, it can be stated that the phase flux linkage for the phases of grid and control windings are given by:

$$\lambda_x(\theta_{rm}) = 2 \cdot \sum_{k_{coil}=1}^{N_{coils_x}} \lambda_{coil_x}[k_{coil}](\theta_{rm}) \quad (4.40)$$

where:

$\lambda_x$	flux linkage of phase $x$ ( $x = ga, gb, gc, ca, cb, cc$ )
$N_{coils_x}$	Number of coils of winding $x$

The coils and the associated stator teeth fluxes ( $\phi_{th}$ ) to be used with (4.40) for each one of the BDFRM phase voltages are defined in Appendix B.5.

## 4.5.4 Induced phase voltage $E$

### 4.5.4.1 Instantaneous induced phase voltage $E$

The induced phase voltages  $e_x$  are obtained by considering the phase flux linkage variation with respect to the time given by:

$$e_x = \frac{d\lambda_x}{dt} \quad (4.41)$$

where the index  $x$  represents grid and control winding phases  $a, b$  and  $c$ .

In Section 4.5.3.5, the phase flux linkages  $\lambda_x$  have been calculated in terms of the rotor position and it is possible to use directly these results to calculate the induced phase voltages.

For that purpose, the phase voltages are calculated from (4.41) by employing a central finite difference derivative method as follows <sup>5</sup>:

---

<sup>5</sup>As the phase flux linkage already takes into account half machine symmetry, the factor 2 is intrinsically considered in (4.42).

$$e_x[k] = \frac{\lambda_x[k+1] - \lambda_x[k-1]}{2 \cdot \Delta t} \quad (4.42)$$

where  $\Delta t$  is the equivalent elapsed time between two multi-static calculations for a fixed speed and  $k$  refers to the multi-static calculation (rotor position) being executed.

From the  $ts$  equation (4.16), in steady-state  $\Delta t$  is given by:

$$\Delta t = \frac{\Delta \theta_{rm}}{\omega_{rm}} = \Delta \theta_{rm} \cdot \frac{1}{2} \cdot \frac{P_g + P_c}{\omega_g + \omega_c} \quad (4.43)$$

#### 4.5.4.2 RMS induced phase voltage $E$

The internal induced RMS phase voltages  $E_{x_{rms}}$  are given by:

$$E_{x_{rms}} = \sqrt{\frac{1}{K} \sum_{k=1}^K (e_x[k])^2} \quad (4.44)$$

### 4.5.5 Terminal phase voltage $V$

#### 4.5.5.1 Instantaneous terminal phase voltage $V$

By taking into account the phase winding resistances, the terminal phase voltages (4.45) for the grid and (4.46) for the control can be assigned:

$$v_{gx}[k] = R_g \cdot i_{gx}[k] + \underbrace{e_{gx}[k]}_{\text{Eq. (4.42)}} \quad (4.45)$$

$$v_{cx}[k] = R_c \cdot i_{cx}[k] + \underbrace{e_{cx}[k]}_{\text{Eq. (4.42)}} \quad (4.46)$$

where  $x$  refers to the phases  $a$ ,  $b$  and  $c$  of grid ( $g$ ) or control ( $c$ ) windings.

#### 4.5.5.2 RMS terminal phase voltage $V$

The terminal RMS phase voltages  $v_{x_{rms}}$  are:

$$V_{x_{rms}} = \sqrt{\frac{1}{K} \sum_{k=1}^K (v_x[k])^2} \quad (4.47)$$

## 4.5.6 Real power

Once the phase voltages  $e$  and  $v$  are determined, the internal and terminal instantaneous power output can be calculated by:

$$\begin{aligned} P_{intgx}[k] &= e_{gx}[k] \cdot i_{gx}[k] \\ P_{intcx}[k] &= e_{cx}[k] \cdot i_{cx}[k] \end{aligned} \quad (4.48)$$

$$\begin{aligned} P_{tergx}[k] &= v_{gx}[k] \cdot i_{gx}[k] \\ P_{tercx}[k] &= v_{cx}[k] \cdot i_{cx}[k] \end{aligned} \quad (4.49)$$

The internal active power per phase, calculated from  $E_x$ , is assessed by extracting the mean value of the instantaneous power vectors  $P_{intgx}[k]$  and  $P_{intcx}[k]$ , since we are assuming that the multi-static calculations are made for a full electrical period.

$$\begin{aligned} P_{actgx\_int} &= \frac{1}{K} \sum_{k=1}^K P_{intgx}[k] \\ P_{actcx\_int} &= \frac{1}{K} \sum_{k=1}^K P_{intcx}[k] \end{aligned} \quad (4.50)$$

Similarly, the terminal active power per phase, calculated from  $v_x$  is determined by extracting the mean value of the instantaneous power vectors  $P_{tergx}[k]$  and  $P_{tercx}[k]$ .

$$\begin{aligned} P_{actgx\_int} &= \frac{1}{K} \sum_{k=1}^K P_{intgx}[k] \\ P_{actcx\_int} &= \frac{1}{K} \sum_{k=1}^K P_{intcx}[k] \end{aligned} \quad (4.51)$$

## 4.5.7 Maximum flux density levels in the steel

### 4.5.7.1 Flux densities

The flux densities levels can be calculated in all the reluctances of the network, since we know the fluxes passing through each one of them.

However, to evaluate the flux density at each reluctance on the network could be impractical from a computational point of view. To simplify the problem, some stator and rotor reluctances have been chosen to give a general overview of material magnetization levels around the machine.

Fig. 4.36 shows the reluctances that have been chosen to limit the magnetic material saturation in stator teeth and yokes. Since there are 24 stator slot components such as the one in Fig. 4.36, 48 reluctances are tested in the stator.

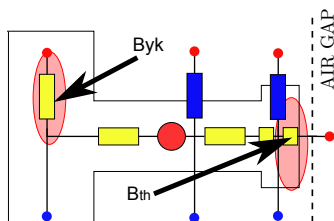


Figure 4.36: Reluctances chosen to limit flux densities in stator teeth ( $B_{th}$ ) and yokes ( $B_{yk}$ ).

In the reluctance rotor, the 6 reluctances highlighted in Fig. 4.37 have been selected in the 3 rotor poles, resulting in a total of 18 flux densities  $B_{rt}$  to limit the flux density.

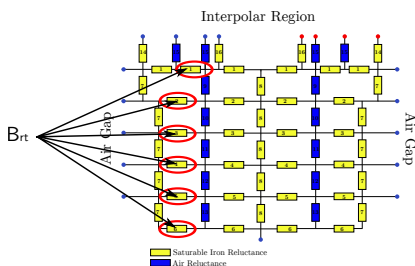


Figure 4.37: Selected reluctances (red circle) to calculate the flux density on the rotor.

All these flux densities are calculated at each rotor position, resulting in a total of  $(24 + 24 + 18) \cdot (K)$  induction levels that are calculated.

#### 4.5.7.2 Absolute maximum inductions levels

The absolute maximum inductions levels for  $|B_{th_{max}}|$ ,  $|B_{yk_{max}}|$  and  $|B_{rt_{max}}|$  are calculated by taking the absolute value of each induction within the vectors  $B_{th}$ [24],  $B_{yk}$ [24] and  $B_{rt}$ [18]. Then, the maximum value in one electrical period is identified to set  $|B_{th_{max}}|$ ,  $|B_{yk_{max}}|$  and  $|B_{rt_{max}}|$  output parameters. These quantities represent the maximum induction that the stator teeth, the yoke and the rotor flux paths can reach considering all performed multi-static calculations (at least one electrical period).

## 4.6 Final Considerations

This chapter presented in details the implementation of the BDFRM Global Electromagnetic Model (GEMM) based on a multi-static reluctance network approach. Starting from the basic principles, it has set forth a procedure to build a static reluctance network (SRN) for the BDFRM. Then, a computationally efficient strategy, using a symmetry principle, is used to take into account rotor movement and effectively perform multi-static calculations. Up to this point, the two BDFRM electromagnetic models have been discussed (SAM and the MSRN). Next chapter discusses the Additional Sizing Equations (ASE) that are used to complete the BDFRM sizing and optimization models.

# Chapter 5

## BDFRM Additional Sizing Equations (ASE)

### Abstract

*The goal of this chapter is to introduce the Additional Sizing Equations (ASE) that are not part of the electromagnetic models SAM and MSRN. They are used to calculate geometrical and performance parameters that are required for designing the BDFRM. The main aspects, hypothesis and considerations are discussed and the reader is referred to Appendix G for a complete implementation of the ASE.*

### 5.1 Definition of the Additional Sizing Equation (ASE) and their role on the global sizing and optimization models

The Additional Sizing Equations (ASE) are analytical expressions that complement the global electromagnetic models (GEMM) SAM and MSRN discussed so far. When the ASE are couple to the GEMM, they form the Global Sizing and Optimization Models (GSOM). Fig. 5.1 illustrates the GSOM based on the SAM and MSRN models as defined in Section 1.5.1.2.

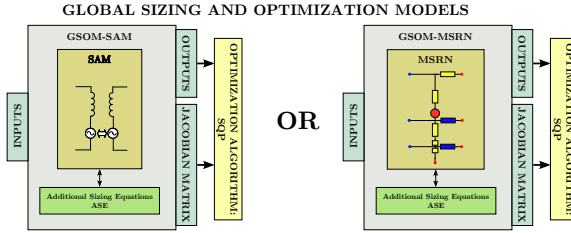


Figure 5.1: Overview of GSOM and GEMM models.

The ASE can be divided in two parts:

1. **Preprocessing:** equations that connect the GSOM inputs to the GEMM inputs.
2. **Post-processing:** equations that uses the results obtained from the GEMM to calculate additional outputs for the GSOM.

Fig. 5.2 depicts the data flow for the ASE.

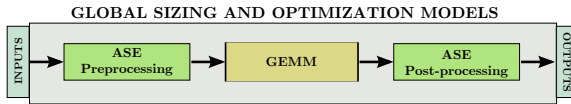


Figure 5.2: Data flow of the GSOM using the ASE.

The analytical equations defining the ASE are basically described by rather simple linear and/or trigonometric expressions derived from the machine structural topology defined in Chapter 2. They are not shown here for simplicity and the interested reader is referred to the Appendix G for details on the ASE. It completely implements in a Mathcad <sup>®</sup> spreadsheet the SAM based Global Sizing and Optimization Model which includes all the Additional Sizing Equations that have been used. The ASE presented in Appendix G are valid for both SAM and MSRN models.

In the following sections, a discussion on the main aspects, hypothesis and definitions that have been used to calculate the ASE is presented.



## 5.2 Preprocessing ASE

### 5.2.1 Geometrical parameters defining machine structural topology

In general, the geometrical parameters that define the machine structural topology are calculated by analytical equations relating the GSOM inputs (e.g. stator external diameter ( $Des$ ), stator internal diameter ( $Dis$ ), air-gap length ( $gap$ ), effective axial length ( $L_{stkef}$ ), yoke width ( $ykw$ ), tooth width ( $thw$ ) and others) to GSOM outputs (e.g. rotor internal diameter ( $Dir$ ), rotor external diameter ( $Der$ ), arc defining the rotor ducts and others). Fig. 5.3 and Fig. 5.4 define the stator and rotor physical parameters that are calculated by the preprocessing ASE. The utilized equation set used to implement them is shown in Appendix G.

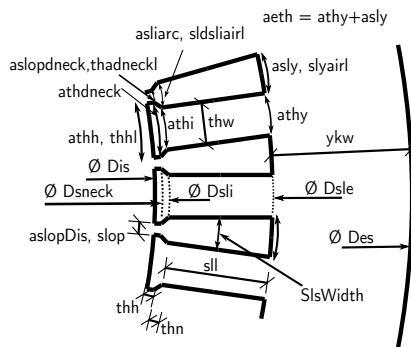


Figure 5.3: Stator slot physical dimensions definitions.

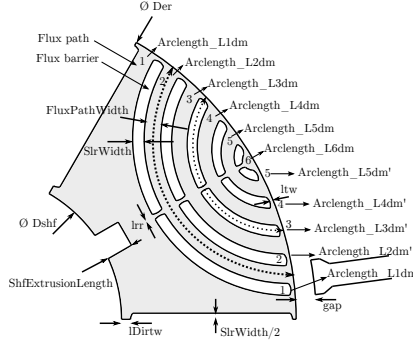


Figure 5.4: Physical dimensions definition for one rotor pole.

## 5.2.2 Electrical parameters

### 5.2.2.1 Phase winding resistances

The phase winding resistances are calculated from the GSOM inputs related to the machine physical dimensions and the number of turns considering copper conductors. The DC resistance can be derived from these parameters considering the BDFRM topology defined in Chapter 2. However, the DC resistance is calculated at ambient temperature ( $t_{amb}$ ) and its value may significantly vary for a full-loaded machine at steady state conditions. Therefore, since a thermal model has not been included in the BDFRM models, it is assumed that the windings at steady state are operating under a temperature defined by the parameter  $t_{sta}$ . The DC resistances are corrected by updating the copper resistivity for  $t_{sta}$  [100].

$$R_x = \rho_{copper}(1 + \alpha_{rho}(t_{sta} - t_{amb})) \times \frac{L_{wire_x}}{S_{cond_x}} \quad (5.1)$$

where  $x$  represents grid or control windings,  $\rho_{copper}$  is the copper resistivity,  $\alpha_{rho}$  is a coefficient representing the evolution of the resistivity in terms of the temperature,  $L_{wire_x}$  is the total wire length (calculated in terms of machine dimensions, winding number of poles and turns) and  $S_{cond_x}$  is the wire cross-sectional area.

### 5.2.2.2 Winding filling factor

The winding filling factor ( $wff$ ) is the ratio between the area occupied by the copper ( $wapsl$ ) and the available area at each slot ( $S_{slot}$ ).

It is given by:

$$wff = \frac{wapsl}{Sslot} = \frac{wapsl_g + wapsl_c}{Sslot} \quad (5.2)$$

where  $wapsl_g$  and  $wapsl_c$  are the areas occupied by the grid and control windings at each slot.

It is a common practice to design a machine to respect the winding filling factor constraint as follows:  $0 < wff < 0.4$ .

### 5.2.2.3 Winding factors

The winding factor ( $K_{w_x}$ ) takes into account the distribution ( $k_{d_x}$ ) and the short pitching ( $k_{p_x}$ ) effects in a phase winding. It is calculated by [88]:

$$K_{w_x} = k_{d_x} \cdot k_{p_x} \quad (5.3)$$

where index  $x$  refers to grid or control windings.

For a full-pitch winding, as it is the case of the BDFRM considered in this work,  $k_{pg} = k_{pc} = 1$ . The  $k_{d_x}$  is calculated by [88]:

$$k_{d_x} = \frac{\sin\left(\frac{\pi}{6}\right)}{q_x \sin\left(\frac{\pi}{6q_x}\right)} \quad (5.4)$$

where  $q_x$  is the number of slots per pole per phase.

For the considered BDFRM,  $q_g = 2$  and  $q_c = 4$ .

### 5.2.3 Specific electric loading and current density

The rms specific electric loading ( $Asel_x$ ) (or linear current density) of a winding  $x$ , as well as the conductor current density ( $J_x$ ) are dimensions of the electrical loading of the machine [37] and must also be assessed to guarantee machine operation under normal conditions.

The  $Asel_x$  can be defined in terms of the number of turns per phase  $Nph_x$ , the winding factor  $K_{w_x}$ , the air-gap radius  $r_{gap}$  and the rms phase current by  $I_{rms_x}$  [11]:

$$Asel_x = \frac{3 \cdot (Nph_x \cdot K_{w_x})}{\pi \cdot r_{gap}} \cdot I_{rms_x} \quad (5.5)$$

The total rms specific electric loading  $Asel$  is calculated by:

$$Asel = Asel_g + Asel_c \quad (5.6)$$

The conductor current density  $J_x$  is calculated by:

$$J_x = \frac{I_{rmsx}}{S_{condx}} \quad (5.7)$$

Empirically, the  $Asel$  parameter is constrained by [ $Asel < 35 - 80 \text{ kA/m}$ ] and the current density by [ $J_x < 3 - 5 \text{ A/m}^2$ ] the for air-cooled non-salient pole synchronous machines [37]. These values are used as the references for the BDFRM.

### 5.2.4 Duct ratio

The duct ratio (DR) is the ratio between the rotor slot width ( $SlrWidth$ ) and the rotor pole pitch [79], given by:

$$DR = \frac{Nslr \cdot SlrWidth}{\pi Der} \quad (5.8)$$

where  $Nslr$  is the number of rotor slots,  $SlrWidth$  is the rotor slot width and  $Der$  is the rotor external diameter.

The duct ratio is an important parameter to be constrained since it highly influences rotor performance. A small DR value means more cross-sectional area available in the rotor flux path and it makes the rotor to saturate at higher excitation levels. On the other hand, as the flux paths are closer to each other, there will be more leakage flux between them and this tends to degrade performance. Obviously there is an optimal value to this parameter. In the literature, the best values for the duct ratio for the BDFRM seems to be in the range [0.38–0, 42] [80, 79].

### 5.2.5 Carter's factor

When calculating analytically many parameters on machine design, usually the air-gap region is simplified by, for example, assuming that there are no open slots in stator and rotor. As mentioned in [37], the flux density always decreases at the slot opening and it is not easy to take this into account analytically. In 1901, F. W. Carter proposed a factor that tries to compensate the decreasing of the flux density at the slot openings. According to Carter's principle, the air-gap seems to be longer than its physical measure.

In this work, the Carter's factor has been used in the Semi-Analytical Model (SAM) to find an effective air-gap and the calculation of this parameter is discussed in Appendix C.4.

## 5.2.6 Leakage inductances

The leakage inductances are associated to the flux that does not participate in the electromechanical energy conversion. The leakage inductances are implemented only in the Semi-Analytical Model (SAM) since the leakage flux is already taken into account in the MSRN model through the definition of the air-reluctances.

Three kinds of leakage inductances based on reference [119] are considered: the slot and tooth top, the zig zag and the differential flux leakage inductances. More details on this topic can be found in [87, 42, 37]. The implemented equations are presented in Appendix C.3.

## 5.2.7 Total active mass and volume

Parameters related to the volume and the resulting total active mass of the BDFRM are calculated based on the machine structural dimensions. The active mass considers only the quantity of the iron and copper materials. The analytical equations used to assess the volume and the active mass are presented in Appendix G considering the iron density of  $7600\text{kg}/\text{m}^3$  and the copper density of  $8960\text{kg}/\text{m}^3$ .

# 5.3 Post-processing ASE

## 5.3.1 Losses calculation

In the BDFRM models, only the copper and iron losses are considered, the mechanical ones (friction, windage, stray losses) are neglected. Therefore, the total losses in the machine are given by:

$$Loss_{CopperIronTotal} = Loss\_Windings + Loss\_Iron \quad (5.9)$$

### 5.3.1.1 Winding losses

The losses associated to the windings  $Loss\_Windings$  are calculated based on electrical circuit theory by:

$$Loss_{Rx} = 3 \cdot Rx \cdot I_{rms_x}^2 \quad (5.10)$$

where  $Loss_{Rx}$  are the total loss of the 3-phase winding  $x$ .

Then, in the BDFRM, the total copper losses are given by:

$$Loss\_Windings = Loss_{Rg} + Loss_{Rc} \quad (5.11)$$

### 5.3.1.2 Iron losses

The analytical estimation of iron losses is a complicated task in any electromagnetic device. There are many approaches that can be used depending on the excitation conditions, especially related to the applied frequencies.

Past researches have shown that the iron losses increase as a function of the excitation frequency, but this relationship is nonlinear and depends on material properties and manufacturing processes. Usually, empirical equations/coefficients are used to give an idea of the whole amount of losses in a device.

In the BDFRM, iron losses are probably more difficult to be analytically evaluated: there are two main flux waves with different number of poles and frequencies [78]. As previously discussed in Section 1.2.4.3, the flux modulation process by the rotor results in a non-sinusoidal air-gap flux density which limits the accuracy of certain methods.

To estimate the total iron losses in the BDFRM, this work proposes the use of Bertotti's method [125] where the losses are segmented in three components: hysteresis, eddy current and excess losses. Since the flux density waveforms in the BDRFM are not sinusoidal, low accuracy may be expected for the absolute value of the losses. However, the main goal of this calculation is actually to correctly identify the tendency of the iron losses when the design parameters are changed during the optimization process rather than calculating them with the highest accuracy. In other words, we are most interested in determining whether the variation of each input parameter increases or decreases the iron losses so that the design can converge for an efficient design. The chosen method is considered sufficient to satisfy this purpose.

Taking these simplifying hypothesis into account, the iron losses in each part  $k$  of the BDFRM magnetic circuit are estimated by [126]:

$$P_{iron_k} = f_{op} \cdot Mass_k \cdot \left[ k_h B_{max_k}^\alpha + \frac{f_{op}}{f_{test}} k_f B_{max_k}^2 + \sqrt{\frac{f_{op}}{f_{test}}} k_e B_{max_k}^{1.5} \right] [W] \quad (5.12)$$

where  $k$  refers to each part of the magnetic circuit in the machine where the maximum induction  $B_{max_k}$  is calculated, i.e. stator teeth ( $th$ ), yokes ( $yk$ ) and rotor flux paths ( $fp$ ). The coefficients  $k_h$ ,  $\alpha$ ,  $k_f$ ,  $k_e$  are magnetic material dependent and are determined by experimental tests. In [127], they have been calculated for a 0.5 mm silicon-iron alloy and these values, depicted in Table 5.1, are used as a first estimative in

this thesis. Parameter  $f_{test}$  in (5.12) refers to the frequency at which these coefficients have been measured. The operating frequency  $f_{op}$  is considered to be equal to the grid frequency  $f_g$  as a first estimative.

Table 5.1: Iron loss coefficients used as a first estimative [127].

$k_h$	$\alpha$	$k_f$	$k_e$
0.0171	1.6353	0.0059	0.0031

Equation (5.12) is then applied to each part around the machine, since their maximum inductions have been calculated by the SAM and the MSRN as shown in the previous chapters.

The total iron losses are determined by in the :

$$Loss\_iron = P_{iron_{th}} + P_{iron_{yk}} + P_{iron_{fp}} \quad (5.13)$$

The implementation of the total iron losses calculation in the SAM is presented in Appendix G.

### 5.3.2 Apparent Power

The apparent power is calculated by using the *internal* induced voltage  $E_{x_{rms}}$  and, taking into account the resistive drop, by using the *terminal* voltage  $V_{x_{rms}}$ . To illustrate the calculations, Fig. 5.5 depicts the single-phase equivalent electric circuit derived in Section 3.2.6 and defines the internal (*int*) and terminal (*ter*) points where power is calculated for each phase. The total apparent power is assessed by assuming the contribution of all the 3 phases.

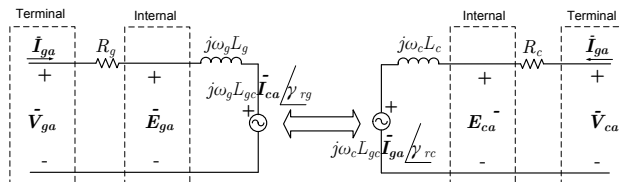


Figure 5.5: BDFRM single-phase Equivalent Electric Circuit.

The internal induced voltages  $E_{x_{rms}}$ , the terminal voltages  $V_{x_{rms}}$ , the phase currents  $I_{x_{rms}}$ , as well as the real power  $P_{act_{x\_int}}$  and  $P_{act_{x\_ter}}$  are outputs of both SAM and the MSRN models. Therefore, it is pos-

sible to apply electrical circuit theory to calculate the reactive power and the power factor for grid and control windings.

Firstly, the magnitude of the 3-phase apparent power phasors for the terminal points at grid and control windings are given by:

$$S_{g3\phi\_ter} = (V_{ga} \cdot I_{ga} + V_{gb} \cdot I_{gb} + V_{gc} \cdot I_{gc}) \quad (5.14)$$

$$S_{c3\phi\_ter} = (V_{ca} \cdot I_{ca} + V_{cb} \cdot I_{cb} + V_{cc} \cdot I_{cc}) \quad (5.15)$$

where  $V$  and  $I$  are the magnitude of the voltage and current rms phasors of each phase.

The reactive power is then given by:

$$Q_{g3\phi\_ter} = \sqrt{S_{g3\phi\_ter}^2 - P_{g3\phi\_ter}^2} \quad (5.16)$$

$$Q_{c3\phi\_ter} = \sqrt{S_{c3\phi\_ter}^2 - P_{c3\phi\_ter}^2} \quad (5.17)$$

The power factor at the terminals are given by:

$$PF_{g3\phi\_ter} = \frac{P_{g3\phi\_ter}}{S_{g3\phi\_ter}} \quad (5.18)$$

$$PF_{c3\phi\_ter} = \frac{P_{c3\phi\_ter}}{S_{c3\phi\_ter}} \quad (5.19)$$

To calculate the internal apparent power  $S_{g3\phi\_int}$  and  $S_{c3\phi\_int}$  (and the associated reactive power, power factor), the same set of equations (5.14)-(5.19) are used, the only difference is that the terminal voltage  $V_{x_{rms}}$  must be replaced by the internal voltage  $E_{x_{rms}}$  in (5.14) and (5.15).

### 5.3.3 Efficiency

The efficiency is defined as the ratio of the output power by the input power as follows.

$$\eta = \frac{P_{out}}{P_{in}} \quad (5.20)$$

To correctly estimate the efficiency,  $P_{out}$  and  $P_{in}$  must be determined as a function of machine operation in motoring or generating conditions.



For *motoring condition*<sup>1</sup>, the input power is supplied by the external terminals and the mechanical power (output) is converted internally in the machine shaft. Therefore:

$$\eta_{motoring} = \frac{P_{g3\phi\_int} + P_{c3\phi\_int} - Loss\_iron}{P_{g3\phi\_ter} + P_{c3\phi\_ter}} \quad (5.21)$$

Notice that, for motoring conditions:

- The real power is positive;
- The copper losses are inherently taken into account in power expressions, since the internal (*int*) and terminal (*ter*) powers are calculated by using  $E_{x_{rms}}$  and  $V_{x_{rms}}$ , respectively;
- The iron losses are taken into account by subtracting them from the internal power.

For *generating condition*<sup>2</sup>, the input power is supplied by the electromechanical conversion in the shaft and the output power is available at machine terminals. Therefore:

$$\eta_{generating} = \frac{P_{g3\phi\_ter} + P_{c3\phi\_ter} + Loss\_iron}{P_{g3\phi\_int} + P_{c3\phi\_int}} \quad (5.22)$$

Notice that, for generating conditions:

- The real power is negative;
- The copper losses are inherently taken into account in power expressions, since the internal (*int*) and terminal (*ter*) powers are calculated by using  $E_{x_{rms}}$  and  $V_{x_{rms}}$ , respectively;
- The iron losses are considered by summing them from the terminal power, since the real power is negative.

## 5.4 Final Considerations

This chapter introduces the Additional Sizing Equations (ASE) that are not part of the electromagnetic models SAM and MSRN. These equations are used to calculate geometrical and output performance

---

<sup>1</sup>Motoring condition implies that the angle  $\phi_{torque} < 0$ , defined in (3.56). Hence, the power and torque is positive.

<sup>2</sup>Generating condition implies that the angle  $\phi_{torque} > 0$ , defined in (3.56). Hence, the power and torque is negative.

parameters that are required for designing the BDFRM. The main aspects, hypothesis and considerations have been discussed and the reader is referred to Appendix G for a complete implementation of the ASE.

This chapter concludes the BDFRM modeling for sizing approach. The next one discusses the coupling and implementation of the Global Electromagnetic Models SAM and MSRN to the ASE, allowing us to define the Global Sizing and Optimization Models that are used in the design procedure.

# Chapter 6

## Implementation of the optimization-oriented models

### Abstract

*This chapter presents the implementation aspects that are used to transform the global electromagnetic models SAM and MSRN into the global sizing and optimization models GSOM-SAM and GSOM-MSRN by coupling them to the additional sizing equations. The use of the software CADES/Reluctool to automatically calculate the Jacobian matrix associated to each model is also discussed, providing means to couple these models to the SQP deterministic optimization algorithm.*

### 6.1 Objectives and requirements for coupling the models with the SQP optimization algorithm

Previous chapters presented the global electromagnetic models (GEMM-SAM and GEMM-MSRN) focusing on their physical modeling assumptions that have been considered in both approaches to determine the BDFRM performance outputs. The additional sizing equations (ASE) that complement them have also been discussed.

As introduced in Section 1.5, the proposed BDFRM design procedure relies on the use of optimization to determine an optimal design that is defined by solving an objective function for a specific application. So that optimization can be effectively applied, we must couple the global electromagnetic models and the additional sizing equations in order to obtain the Global Sizing and Optimization Models (GSOM-SAM and GSOM-MSRN) that can be used in the design process.

The goal of using optimization is to set a constrained outputs problem, define an objective function and let the optimization algorithm iterate to find an optimal design whereas the input parameters are varying within a predefined range. Since *a priori* we may have from some tens up to some thousands constrained outputs, the deterministic gradient-based SQP optimization algorithm has been chosen. Therefore, to be able to use the SQP, one needs to determine not only the GSOM outputs, but also the *Jacobian matrix* containing the partial derivatives of the outputs in terms of the inputs.

Fig. 6.1 illustrates the coupling of the GSOM device model to the SQP.

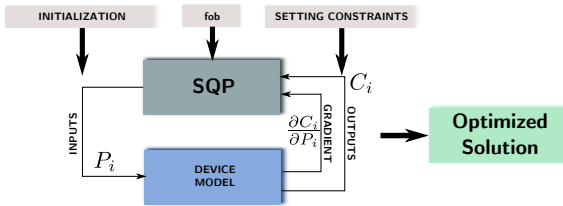


Figure 6.1: Coupling of the GSOM device models to the SQP.

The goal of this chapter is to present how the models have been implemented in order to obtain a software component (code) containing the model equations and the associated Jacobian matrix to be used in the optimization process.

## 6.2 Dedicated optimization software tools

Computer Aid Design (CAD) tools are specialized software that aims to assist the designer on the development process. In the context of this work, it is proposed to use optimization as a design tool and it is out of scope a deeper study on this topic.

In this work, the software CADES [108, 128, 109, 110, 98, 100] and RelucTOOL [111, 112] have been chosen to implement the global

sizing and optimization models (GSOM-SAM and GSOM-MSRN) and manage the coupling to the SQP optimization algorithm. An overview of these tools are described in the sequence.

## 6.2.1 CADES Framework

### 6.2.1.1 Main characteristics

The CADES (Component Architecture for the Design of Engineering Systems) is a framework dedicated to simulation and optimization and it has been initially developed at the Grenoble Electrical Engineering Laboratory (G2ELAB). It allows [101]:

- to develop components (models, libraries) for specific devices targeting the simulation and optimization of the system;
- the portability between the models with different tools (Matlab, Excel, Portunus, Flux, etc.);
- the coupling to different optimization algorithms.

The CADES framework is illustrated in Fig. 6.2.

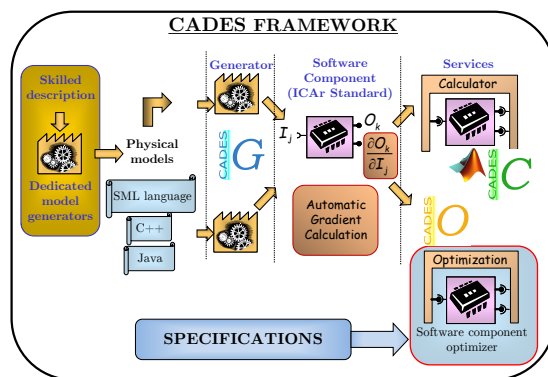


Figure 6.2: Illustration of CADES framework.

### 6.2.1.2 Generating the models: CADES Generator

CADES has a built-in programming environment that allows to code model equations in its specific *sml* language (System Modeling

Language) [129]. The model equations that can be implemented in sml are analytical and/or semi-analytical (numerical integrals, implicit equations *etc.*). One of the greatest advantages of analytical or semi-analytical models is that their partial derivatives can be *exactly* determined, either symbolically or by using derivation theorems [130]. When CADES compiles a model written in sml, it calculates automatically its gradient by using these derivation techniques. The result is an “icar” component [128] containing the model output functions in terms of the inputs, as well as their associated partial derivatives. The icar standard is defined in sub-modules capable of performing tasks of calculation, sensibility analysis, derivation *etc.* [101]. Essentially, it is a Java function and it can be coupled to different software (such as Matlab for example) and to the optimizer module of CADES (discussed in the sequence).

The CADES generator does not allow to code directly conditional (if-else) and loop (for, do-while) programming structures. However, it has built-in modules that allows to automatically derive C functions. To that end, CADES has implemented on it the ADOL-C [131]<sup>1</sup> package for automatic differentiation of C codes, so it is possible to obtain the Jacobian matrix associated to a function containing such programming structures in CADES.

Fig. 6.3 depicts the programming environment of CADES generator.

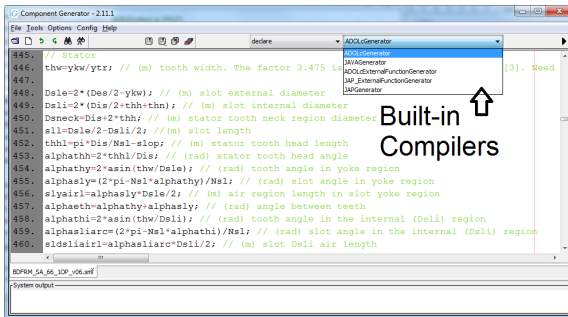
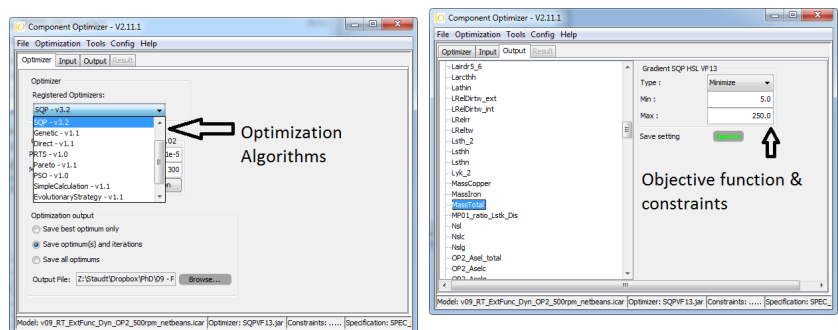


Figure 6.3: Programming environment of CADES generator

<sup>1</sup>Open source community COmputational INfrastructure for Operations Research - COIN-OR, available online in [www.coin-or.org/index.html](http://www.coin-or.org/index.html)

### 6.2.1.3 Coupling the models to the optimization algorithms: CADES Optimizer

The CADES optimizer allows to couple the icar component directly to optimization algorithms. Fig. 6.4 illustrates the optimizer Graphical User Interface (GUI). There are some different optimization algorithms implemented in CADES as shown in Fig. 6.4a. Of special interest for this thesis is the deterministic optimization algorithm version of SQP, the SQP-VF13 [107] (Harwell Subroutine Library). The setting of input values and the associated maximum and minimum ranges, as well as the definition of outputs constraints and the objective function is straightforward as shown in Fig. 6.4b.



(a) Optimization algorithms.

(b) Output constraints and objective function.

Figure 6.4: Graphical User Interface of CADES optimizer.

## 6.2.2 Reluctool - a Computer Aid Design software for building semi-analytical models based on the reluctance network approach

The Reluctool [108, 132, 111, 112, 133] is a CAD software dedicated to the modeling of electromagnetic devices by using the reluctance network approach. It permits to calculate many outputs associated to each reluctance in the network such as fluxes, induction, energy and coenergy taking into account non-linear magnetic materials. To generate the model, the network is transformed into an equation system containing analytical and semi-analytical equations that are solved together with the associated Jacobian matrix that is automatically cal-

culated by Reluctool <sup>2</sup>. This process results in a Java library function. The reluctance network model generated by Reluctool can be imported by CADES generator that automatically manages the coupling of the codes written in sml and the imported functions issued from Reluctool.

Fig. 6.5 depicts the programming environment of Reluctool. It illustrates the implementation of the stator slot reluctance network, the analytical equations used to calculate the parameters required by the model and the predefined components palette that are used to assembly the reluctance network.

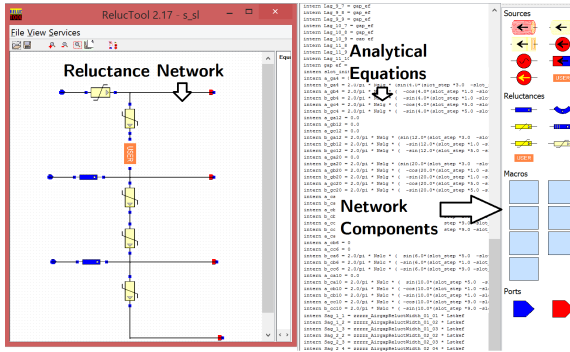


Figure 6.5: Reluctool programming environment

### 6.3 SAM-based Global Sizing and Optimization Model (GSOM-SAM) implementation in CADES

Fig. 6.6 shows the GSOM-SAM, which represents the coupling of the global electromagnetic semi-analytical model (SAM) to the additional sizing equations (ASE).

<sup>2</sup>A procedure to implement a static reluctance network (SRN) adapted to be used with gradient-based optimization algorithms is briefly presented in Appendix B.1



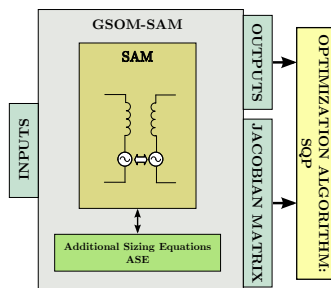


Figure 6.6: Schematic of the GSOM-SAM.

As shown in Chapters 3 and 5, the Semi-Analytical Model (SAM) and the ASE are formed exclusively by analytical and semi-analytical equations. These expressions can be directly implemented in CADES generator by using its specific sml language. Essentially, the GSOM-SAM is the implementation of the SAM and the ASE model equations depicted in Appendix G into CADES. In total, the GSOM-SAM has over 1000 code lines, among which 50 numerical integrals are defined to calculate inductances and flux densities in several parts of the machine magnetic circuit by using the air-gap flux density ( $B_{gap}$ ) results.

The icar component is then automatically created by CADES generator by using the built-in ADOL-C compiler in order to obtain the output/input relationships and the associated gradient. Fig. 6.7 illustrates GSOM-SAM implemented in CADES.

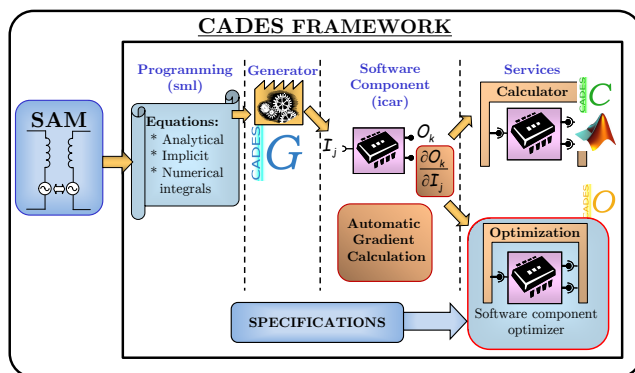


Figure 6.7: SAM implementation using Cades Framework.

## 6.4 MSRN-based Global Sizing and Optimization Model (GSOM-MSRN) implementation in CADES

### 6.4.1 GSOM-MSRN overview

Fig. 6.8 depicts the GSOM-MSRN, which represents the coupling of the global electromagnetic multi-static reluctance network (MSRN) model to the ASE.

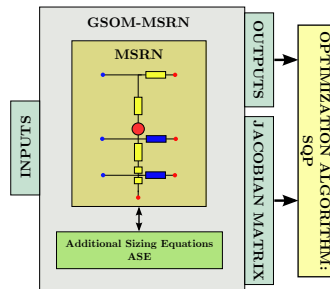


Figure 6.8: Schematic of the GSOM-MSRN.

As discussed in Chapter 4, the MSRN implements a static reluctance network (SRN) and parametrizes the air-gap reluctances as a function of rotor position ( $\theta_{rm}$ ) to take into account rotor movement within an angle between two adjacent stator slots ( $\phi_{st}$ ). The effective multi-static calculations for any rotor position are then achieved by rotating the MMF sources taking advantage of the existent symmetry in the machine topology.

The implementation of the GSOM-MSRN differs from the GSOM-SAM because of the reluctance network modeling approach and the need to take into account the multi-static calculations. Basically, the CADES generator is used to automatically couple the ASE written in `sml` to an imported Java library function containing the MSRN model. However, CADES/Reluctool have some limitations to take into account the rotor movement and these particularizations are discussed in the sequence. Fig. 6.9 depicts the GSOM-MSRN model highlighting the MSRN different sub-models used to take into account rotor movement.

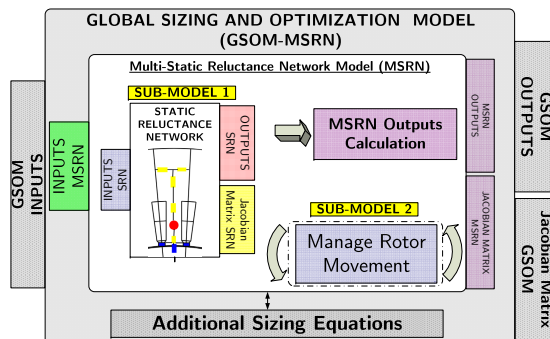


Figure 6.9: GSOM-MSRN: illustration of the sub-models used to take into account rotor movement.

### 6.4.2 Static Reluctance Network (SRN) topology implementation

The Static Reluctance Network (SRN) topology together with the analytical equations used to evaluate the reluctances have been presented in Section 4.2 and they are directly implemented in Reluctool. The model is then compiled to generate a Java library function containing the output/input relationships and their partial derivatives.

The problem with the SRN model is that only a single *specific position* is assessed at any simulation time. As shown in Section 4.5, the MSRN outputs must be calculated as a function of the SRN outputs in terms of rotor position. Therefore, one needs to find a way to call the SRN function for each multi-static simulation, managing the calculation of the air-gap reluctances and the sources rotation. Then, the SRN outputs from each position must be used to evaluate the MSRN outputs and their partial derivatives.

Up to this date, CADES/Reluctool are not capable of managing automatically the rotor movement and this must be manually taken into account in order to generate the MSRN software component that is coupled to the sml code by CADES generator. The limitations of the software tools and the proposed solution are described in the sequence.

### 6.4.3 Limitations of the software tools: the need of manual derivation of the gradient

In order to take advantage of the symmetry principle aiming to reduce the size of the SRN, a procedure to rotate the MMF sources must be implemented. Computationally, the sources are defined in a vector of size  $[1 \times 24]^3$  containing the 24 instantaneously calculated MMF source values that are used to solve the SRN for each position. Thus, to computationally rotate the MMF sources, it is necessary to permute the indexes on the MMF vector whenever required.

However, the limitation of CADES/Reluctool is that, up to this date, they are not capable of dealing with the index permutation required to change the source positions. Therefore, they cannot be used to automatically evaluate the MSRN outputs and the associated Jacobian matrix and these calculations must be manually implemented.

### 6.4.4 Proposed solution

To overcome this limitation, the MSRN software component required to define the GSOM-MSRN in CADES generator is implemented in an external function developed in Java (EJF). The EJF encapsulate the SRN model issued from Reluctool and manages the rotor rotation by calculating the air-gap reluctances and rotating the MMF sources whenever required. To calculate the MSRN outputs and their partial derivatives, the EJF takes advantage of CADES/Reluctool characteristic of automatic code derivation by using the SRN results to evaluate them.

### 6.4.5 The MSRN software component implemented in the external Java function (EJF)

The MSRN outputs<sup>4</sup> are parameters calculated using the results of a full electrical period simulation (e.g. average torque, rms voltages *etc.*). From the optimization algorithm point of view, the SQP calls the EJF function once at each iteration expecting these results, not the instantaneously calculated quantities. Therefore, the EJF must manage internally all the required multi-static simulations to evaluate the MSRN outputs. Fig. 6.10 illustrates the MSRN EJF flowchart.

---

<sup>3</sup>There are one MMF source for each one of the 24 stator teeth for the chosen BDFRM topology with half symmetry.

<sup>4</sup>Refer to Table 4.2 for details on the MSRN outputs.

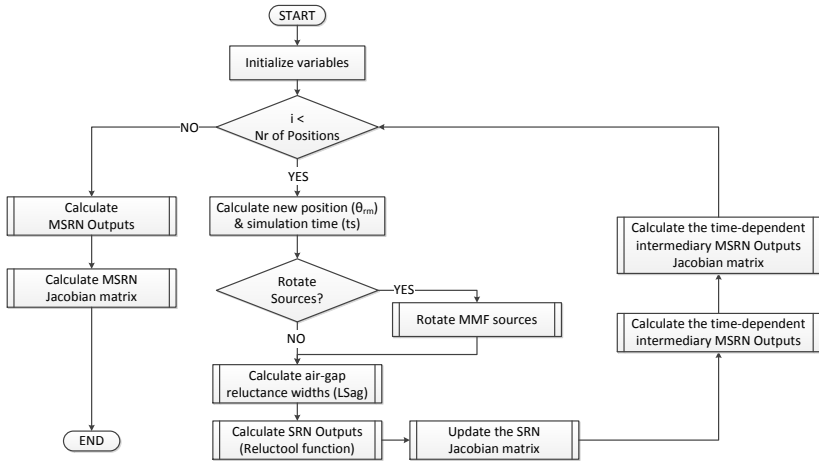


Figure 6.10: MSRN External Java function flowchart.

From Fig. 6.10, it can be noticed that there are some parameters required by the SRN function (Reluctool function) that are calculated at EJF level in terms of MSRN inputs such as the simulation time ( $ts$ ) and the equivalent air-gap reluctances widths  $LSag$ <sup>5</sup> (32 equivalent widths in total). This creates a dependence among the SRN inputs that must be taken into account to calculate the Jacobian matrix. The procedure is outlined in the sequence.

### 6.4.5.1 Considered derivation principles

#### 6.4.5.1.1 Problem setting: SRN inputs calculated in terms of MSRN inputs

As the MSRN outputs are determined as a function of the SRN outputs, their partial derivatives can be defined from the ones of the SRN function, provided by Reluctool. However, since some of SRN inputs are evaluated in terms of MSRN inputs (e.g.  $ts$ ,  $LSag$ ) at the EJF level, this relationship must be taken into account when calculating the MSRN Jacobian matrix. Fig. 6.11 depicts the MSRN input/output flow.

<sup>5</sup>The implementation aspects of the external function used to calculate the equivalent air-gap reluctances widths is discussed in Appendix B.2

### Multi-Static Reluctance Network (MSRN) Model

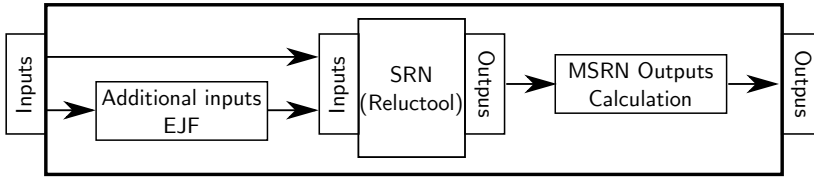


Figure 6.11: MSRN input/output flow.

By default, Reluctool, used to implement the SRN function, assumes that all of its inputs are independent from each other and it generates the associated Jacobian matrix taking this into account. As this is not always the case, the gradient of the SRN function with respect to the created variables in the EJF must be updated so that the MSRN gradient is accurately determined.

#### 6.4.5.1.2 Differential equation to update the Jacobian matrix

For that purpose, the general differential equation is used [102].

Considering  $y = f(x_1, \dots, x_n)$  a multi-variable function, the differential  $dy$  of  $y$  with respect to all input variables  $x_n$  is given by:

$$dy = \frac{\partial y}{\partial x_1} dx_1 + \dots + \frac{\partial y}{\partial x_n} dx_n \quad (6.1)$$

where the terms  $\frac{\partial y}{\partial x_n}$  are the partial derivatives of  $y$  with respect to  $x_n$ .

To illustrate the procedure, let us define the function  $y = f(x_1, x_2)$ , where  $y$  may be thought of one of the SRN outputs:

$$y = f(x_1, x_2) = a \cdot x_1 + b \cdot x_2 \quad (6.2)$$

where  $a$  and  $b$  are constants.

By using (6.1), the derivative of (6.2) with respect to  $x_1$ , assuming  $x_1$  independent of  $x_2$ , is:

$$\frac{dy}{dx_1} = \frac{\partial y}{\partial x_1} + \frac{\partial y}{\partial x_2} \frac{dx_2}{dx_1} = a \quad (6.3)$$

since  $\frac{dx_2}{dx_1} = 0$ .

Equation (6.3) would be the partial derivative calculated by Reluctool since it assumes by default that  $x_1$  is independent of  $x_2$ .

Now, let us assume that, before evaluating function  $f(x_1, x_2)$ ,  $x_2$  is calculated in terms of  $x_1$  by:

$$x_2 = c \cdot x_1 \quad (6.4)$$

Therefore, the derivative of  $y$  with respect to  $x_1$  is:

$$\frac{dy}{dx_1} = \frac{\partial y}{\partial x_1} + \frac{\partial y}{\partial x_2} \frac{dx_2}{dx_1} = a + bc \quad (6.5)$$

since  $\frac{\partial y}{\partial x_2} = b$  and  $\frac{dx_2}{dx_1} = c$ .

The term “ $+bc$ ” in (6.5) is the value that must be summed to the gradient of  $y$  with respect to  $x_1$  to take into account the interdependence of  $x_1$  and  $x_2$ .

This example illustrates the need of updating the SRN Jacobian matrix to use its result to calculate the MSRN Jacobian matrix. For that purpose, (6.1) must be applied to all SRN partial derivatives provided by Reluctool that are related to the SRN inputs that have been created at the EJF level in terms of the MSRN inputs. Details on the specific implementation of the MSRN gradient calculation for each one of its outputs can be found in Appendix B.3.

### 6.4.6 Coupling the MSRN software component to CADES to form the GSOM-MSRN

The MSRN component is created in a form of a Java library function containing the MSRN model output/input relationships and the associated partial derivatives. Computationally, it has exactly the same elements of the external function normally generated by Reluctool. Therefore, CADES can be used to automatically couple the ASE implemented in the sml code to the MSRN model manually coded in the external Java function (EJF). This generates the icar software component required by the CADES optimizer.

Fig. 6.12 illustrates the GSOM-MSRN implementation in Cades.

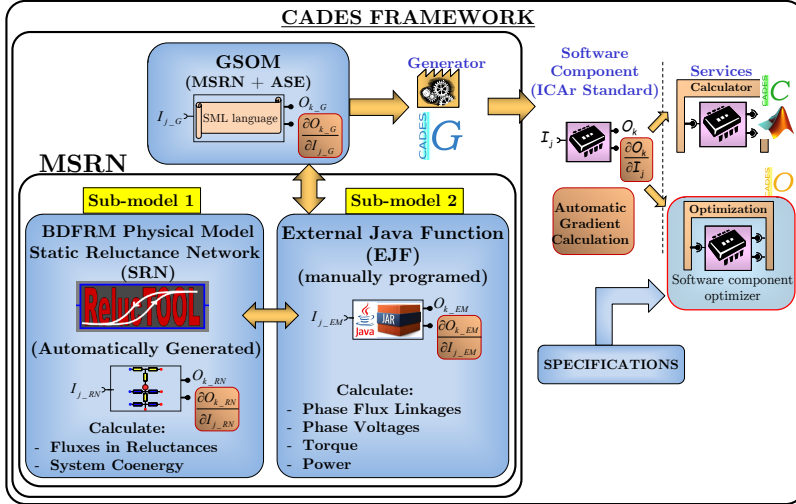


Figure 6.12: MSRN implementation using Cades Framework.

## 6.5 Final considerations

This chapter presented the procedure that have been used to couple the global electromagnetic models SAM and MSRN to the additional sizing equations (ASE) in order to define two optimization models: GSOM-SAM and GSOM-MSRN. The software CADES and Reluctool have been used to implement these models because they can *exactly* calculate the model gradients, either symbolically or by automatic code differentiation, providing means to couple them to the SQP optimization algorithm. The limitations of the software tools and the proposed solution to perform the multi-static calculations of the MSRN model due to the management of source rotation has also been discussed.

Next chapters explore the GSOM-SAM and the GSOM-MSRN discussed so far by first verifying their accuracy confronting their results to the equivalent ones obtained with 2D Finite Element Analysis (FEA) simulations. Then, the experimental results measured on the prototype developed in this thesis are used to validate de models. Finally, the last chapter presents an optimization case study using the proposed procedure.



# Chapter 7

## Simulation results

### Abstract

*The goal of this chapter is to analyze the GSOM-SAM and the GSOM-MSRN by comparing their simulations to 2D Finite Element Analysis. Since the most important constraints for the optimization approach are the global electromagnetic performance outputs (e.g. phase voltages, torque, maximum flux densities), the analysis focuses exclusively on these kind of parameters. Firstly, the machine assumed as the reference to verify the models is introduced together with the nomenclature used in the discussion that follows. Then, the models are examined separately, starting by the GSOM-SAM, in order to discuss their advantages and limitations. A comparison on the simulation time for each model is presented at the end. The comparisons of the results amid the three modeling levels (GSOM-SAM, GSOM-MSRN and FEA) are left to the next chapter, that additionally confront them with experimental results obtained from the prototype.*

### 7.1 Reference machine definition to verify the models

#### 7.1.1 Geometrical and rated performance parameters

The reference machine parameters used to verify the models are the ones of the BDFRM prototype that has been developed in this thesis. This experimental machine is fully discussed in Chapter 8, but

the relevant parameters for the discussion presented in this Chapter are summarized in Table 7.1.

Table 7.1: Reference machine used to compare the semi-analytical models to FEA.

Stator external diameter	235.0 mm
Stator internal diameter	144.24 mm
Effective axial length	69.0 mm
Shaft diameter	65.0 mm
Grid winding total number of turns	448
Control winding total number of turns	312
Air gap length	0.5 mm
Number of stator slots	48
Number of rotor ducts	66
Number of poles grid/control/rotor	8/4/6
Yoke width	14.5 mm
Yoke to stator tooth width ratio	2.826
Stator slot opening	1.6 mm
Rotor slot width	2.727 mm
Control winding wire diameter	0.91186 mm
Grid winding wire diameter	0.91186 mm
Magnetic material in stator and rotor	M400-50A

The BDFRM prototype is designed for 1 *kW* at 1000 *rpm* and the rated electromagnetic parameters are shown in Table 7.2.

Table 7.2: Prototype rated parameters to compare the semi-analytical models to FEA.

Grid winding current ( $I_g$ )	3.07 Apk / 2.17 Arms
Control winding current ( $I_c$ )	3.23 Apk / 2.28 Arms
Grid winding phase voltage ( $V_g$ )	127 Vrms
Control winding current ( $V_c$ )	127 Vrms
Grid winding frequency ( $f_g$ )	50 Hz
Control winding frequency ( $f_c$ )	50 Hz
Maximum speed ( $\omega_{rm}$ )	1000 rpm
Torque max @ Max Speed	9.5 Nm
Rated power @ 1000 rpm	1 kW
Maximum allowed flux density in the magnetic circuit	$B_{n\_max} < 1.5T$

All the simulations presented in the sequence assume that the machine rotor is turning at 1000 rpm, either by proper control or being forced to by external means (e.g. by using a DC machine connected to the shaft).

### 7.1.2 Nomenclature definition

For the discussions that follows throughout this chapter to compare the models, the nomenclature depicted in Table 7.3 is used.

Table 7.3: Nomenclature used to compare the models.

DRI	Ideal Ducted Rotor geometry (see Fig. 7.1)
DRNI	Practical or not ideal ducted rotor geometry (see Fig. 7.1)
NL	Nonlinear magnetic material
LI	Linear magnetic material

Fig. 7.1 illustrates both DRI and DRNI rotors defined in Table 7.3.

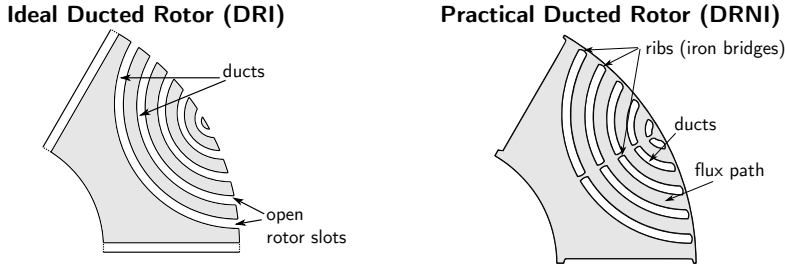


Figure 7.1: Ideal Ducted Rotor (DRI) and Practical Ducted Rotor (DRNI) definitions.

Based on these definitions, two distinct Finite Element Analysis (FEA) simulations considering the DRI and the DRNI rotor possibilities are considered for comparison:

1. FEA DRI LI: it uses the ideal rotor topology with a linear magnetic material with permeability tending to infinite ( $\mu_r = 1E9$ ). This rotor type (idealized) is the closest that one can simulate to approach the hypothesis made to derive the SAM. The goal with this model is to analyze the differences among the analytical and numerical methods with similar considerations for the magnetic material and machine structural topology.
2. FEA DRNI NL: the DRNI is the practical rotor topology, used to build the prototype. This FEA simulation considers nonlinear magnetic materials and it is the closest one to the prototype.

Regarding the results obtained from the semi-analytical models GSOM-SAM and GSOM-MSRN, the curves associated to them in the plots are referred, for simplicity, only by SAM and MSRN, respectively. Table 7.4 summarizes the acronyms, colors and traces used to differentiate the models in the plots.

Table 7.4: Nomenclature used to compare the models.

Acronym	Color	Trace
SAM	blue	—
MSRN	red	-.-
FEA DRI LI	magenta	...
FEA DRNI NL	green	- -

### 7.1.3 Impact of the iron ribs on machine performance

Before presenting the simulation results, it is worth to introduce the effects that the iron ribs, defined in Fig. 7.1, have on machine performance.

These elements are used to increase the mechanical robustness of the rotor, connecting together all the flux paths. At rated conditions, they saturate due to their small dimensions and they have a negligible impact on machine performance. However, at low current levels, the magnetic material on the iron ribs is highly permeable and these components act as magnetic short circuits, degrading the rotor modulation capability.

To illustrate the problem, Fig. 7.2 depicts two FEA simulations with the DRI and the DRNI rotor when a DC current of 1 A is applied only to the phase “a” of control winding. The flux lines have the same resolution in both cases. At this current level, the iron bridges are not saturated and it is clear their role on deviating the flux lines at the air-gap region when the DRNI rotor is used. The differences between the DRI and the DRNI rotor due to this parameters is especially remarked when analyzing the mutual inductance between the grid and control windings as discussed in the sequence.

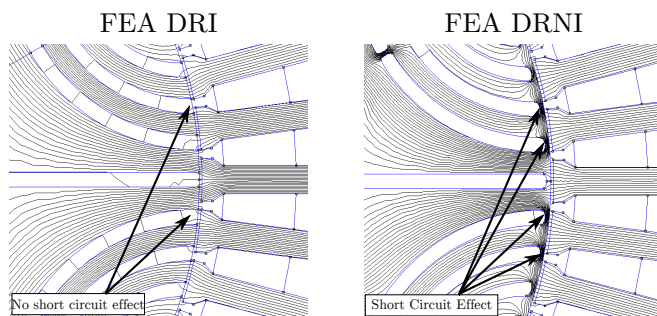


Figure 7.2: FEA simulation illustrating the short-circuit effect on the DRNI rotor for a DC current of 1 A at phase “ca”.

## 7.2 Verifying the GSOM-SAM by comparing its results to the reference FEA model

### 7.2.1 Considered performance parameters

The performance parameters used to verify the GSOM-SAM are listed in the sequence.

- Air-gap flux density ( $B_{gap}$ ) at rated conditions (i.e. both windings are excited and the machine is turning at 1000 rpm);
- Machine inductances;
- Instantaneous induced voltages ( $e_{ga}(t)$  and  $e_{ca}(t)$ ) at rated conditions;
- Open-circuit grid induced rms voltage ( $E_{ga_{rms}}$ ) *versus* control winding 3-phase excitation ( $I_{c3\phi}$ ) ( $I_{g3\phi} = 0$ );
- Open-circuit control induced rms voltage ( $E_{ca_{rms}}$ ) *versus* grid winding 3-phase excitation ( $I_{g3\phi}$ ) ( $I_{c3\phi} = 0$ );
- Induced average electromagnetic torque *versus* grid winding 3-phase excitation ( $I_{g3\phi}$ ), while keeping the control current fixed at the rated value ( $I_{c3\phi} = 3.23$  Apk).

### 7.2.2 Air-gap flux density versus $\theta_{ag}$ at rated conditions

The air-gap flux density estimation is the basis to calculate the EEC inductances and also to obtain the flux density in several parts of the machine. Fig. 7.3 shows a comparison between the approach used to calculate it in SAM and the corresponding FEA results at rated conditions with all the six phases excited at instant  $t_s = 0s$ .

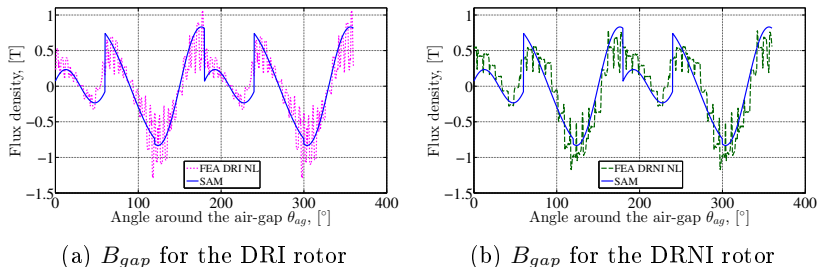


Figure 7.3: SAM: Air-gap flux density  $B_{gap}$  versus  $\theta_{ag}$  at rated excitation.

Fig. 7.3a depicts the results for the DRI LI rotor. It can be noticed that the analytical approach represents a sort of an average curve over the FEA result. If the high frequency flux density variation due to the slotting effect is neglected, it can be concluded that the flux modulation process by the rotor is relatively well represented considering all the idealized hypothesis made for deriving the SAM. Since the machine is operating in the non-saturated region ( $B_{n\_max} < 1.5T$ ) at rated conditions, similar conclusions can be inferred from the FEA DRNI NL rotor in Fig. 7.3b.

### 7.2.3 Inductances

The inductances are used to calculate machine phase voltages in the EEC approach. Table 7.5 outlines the results for the self ( $L_{gm}$ ,  $L_{cm}$ ) and mutual ( $L_{gcmax}$ ) inductances comparing their values to the FEA DRI LI model.

Table 7.5: Inductances comparison.

	SAM [mH]	FEA DRI LI [mH]	Diff [%] *
$L_{gm}$	82.99	73.86	12.4
$L_{cm}$	76.92	78.00	-1.4
$L_{gcmax}$	78.54	71.71	9.5

\* FEA value used as the reference.

Both models used in the comparison are linear and consider similar hypothesis. The results from Table 7.5 indicates that SAM is comparable to a linear FEA model, within a  $\pm 10\%$  range, and reinforces its

usability for early design stages.

To investigate the nonlinear behavior of BDFRM inductances, Fig. 7.4 presents the results for the mutual inductance  $L_{gcmax}$  in terms of the excitation levels. In this curve, the  $L_{gcmax}$  parameters is obtained by exciting only the phase “a” of the grid winding with a DC current ( $I_{gaDC}$ ). The machine is assumed to be turning at 1000 rpm and the induced flux linkage in control winding is calculated, allowing to determine the  $L_{gcmax}$  for many values of  $I_{gaDC}$ . This parameter is directly related to the induced torque through (3.56).

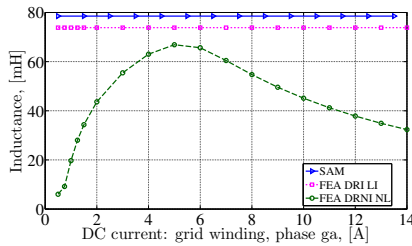


Figure 7.4: Mutual inductance  $L_{gcmax}$  versus excitation current.

The results in Fig. 7.4 confirm the similarities among the linear models and highlights the inductance dependence on the excitation conditions in a practical case. It can be noticed that the peak value of the inductance obtained from FEA DRNI NL model is comparable to the linear ones. However, interestingly at low excitation, the inductance heavily depends on the magnetization level. This can be explained by the short circuit effect of the rotor iron bridges (ribs) when they are not saturated, discussed in Section 7.1.3, that greatly reduces the coupling between the windings and, consequently, the mutual inductance.

## 7.2.4 Induced voltages $e_{ga}$ and $e_{ca}$

The induced voltages  $e_{ga}$  and  $e_{ca}$  are verified by considering the instantaneous values when the machine is operating at rated conditions (both windings are excited) and by calculating the open-circuit rms voltage curve in both windings, assuming a balanced 3-phase current excitation in the winding opposed to the one where the voltages is being calculated.



### 7.2.4.1 Instantaneous induced voltages $e_{ga}$ and $e_{ca}$ at rated conditions

Fig. 7.5a illustrates the instantaneous value of phase voltage  $e_{ga}$  at rated conditions comparing the SAM with both the FEA DRI LI and FEA DRNI NL models. The SAM results are quite similar to the linear FEA model, whereas some amplitude and phase differences can be noticed when it is compared to the FEA DRNI NL. The distinct results are related to the consideration or not of iron nonlinearities and the DRNI rotor, evidencing the limitations of the SAM model due to the idealized modeling assumptions. Similar conclusions can be inferred from Fig. 7.5b which shows the  $e_{ca}$  results.

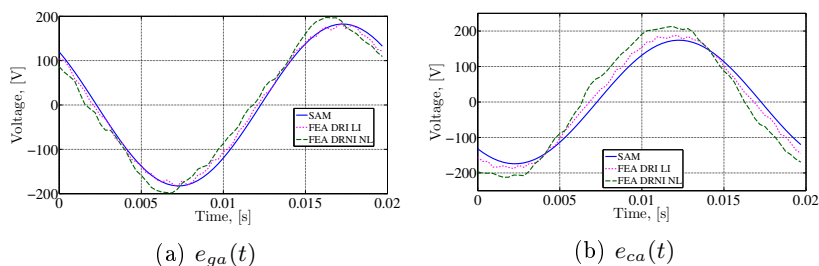


Figure 7.5: SAM: Instantaneous induced voltages  $e_{ga}$  and  $e_{ca}$  at rated conditions.

### 7.2.4.2 Open-circuit induced RMS voltages $E_{ga_{rms}}$ and $E_{ca_{rms}}$ versus excitation currents

The open-circuit RMS voltages  $E_{ga_{rms}} \times I_{c3\phi}$  with  $I_{g3\phi} = 0$  and  $E_{ca_{rms}} \times I_{g3\phi}$  with  $I_{c3\phi} = 0$  are depicted in Fig 7.6a and Fig. 7.6b, respectively. These curves are directly related to the mutual inductance among the windings sets.

In both cases, the linear results of SAM and FEA DRI LI have nearly the same asymptote, the small difference being explained by the distinct modeling approaches: whereas the SAM considers hypothesis to simplify Maxwell's equations and solve the problem globally through analytical equations, the FEA model solve them locally in a discretized domain.

When the FEA DRNI NL is considered, there is a larger difference in the beginning of the magnetization curve due to the iron ribs effect as found for the  $L_{g_{cmax}}$  parameter. Around  $I_{g3\phi} = I_{c3\phi} \approx 3.5$  A

(near the rated values), in both cases, the machine starts to saturate, confirming that the maximum flux density constraint in the machine magnetic circuit at rated conditions is respected ( $B_{n\_max} < 1.5T$ ).

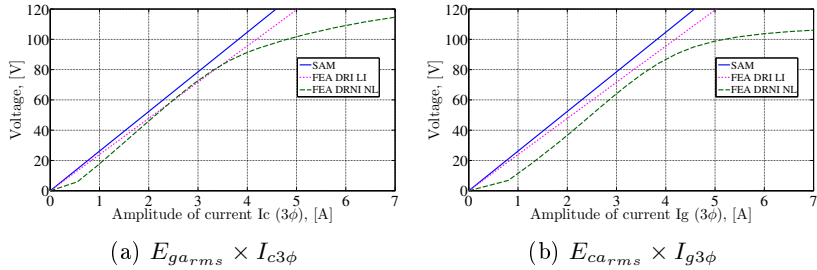


Figure 7.6: SAM: Open-circuit induced RMS voltages  $E_{ga}$  and  $E_{ca}$  versus excitation currents.

## 7.2.5 Induced average electromagnetic torque

The last comparison for the GSOM-SAM refers to the average electromagnetic torque and it is shown in Fig. 7.7. To plot this curve, the amplitude value of the control winding current  $I_{c3\phi}$  is kept fixed at the rated value, while  $I_{g3\phi}$  is changed from 0 up to 6 A.

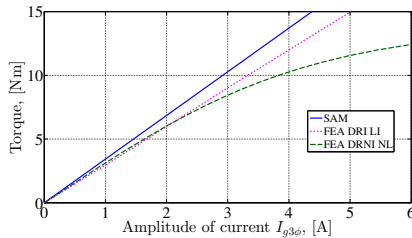


Figure 7.7: SAM: Electromagnetic torque *versus*  $I_{g3\phi}$  at  $I_{c3\phi} = 3.23A$ .

Fig. 7.7 confirms the results obtained for the open-circuit voltages, where the angular coefficients of the SAM and the FEA DRI LI slightly differs. It can be noticed that all the three models presents acceptable results, considering all the idealized assumptions in SAM, to predict BDFRM torque capability up to rated excitation conditions around  $I_{g3\phi} = 3A$ . From then on, FEA DRNI NL starts to diverge due to saturation.

## 7.2.6 Conclusions about the GSOM-SAM

The comparisons of SAM performance when confronted to the reference FEA models confirms that:

- (i) SAM results up to rated conditions are satisfactory if the goal is to use them for specifying a “first-cut” design that is planned to be further refined in the design process.
- (ii) The calculation of the flux densities in several parts of the machine to restrain the optimization search space is working and it is indeed necessary to limit the results at practical and useful values for a linear model.
- (iii) SAM is of course limited for predicting machine performance for operating points above rated conditions since it is a linear model.
- (iv) There may be some limited precision results at low excitation levels due to the effect of iron ribs in the considered BDFRM rotor topology, especially for voltage calculation, due to the nonlinear machine inductances.

## 7.3 Verifying the GSOM-MSRN by comparing its results to the reference FEA model

### 7.3.1 Considered performance parameters

Since the GSOM-MSRN is a nonlinear model implementing the DRNI NL rotor, the following discussion compares its results only to the FEA DRNI NL model. The performance parameters used to verify the GSOM-MSRN are listed in the sequence.

- Air-gap flux density ( $B_{gap}$ ) at rated conditions;
- Mutual inductance between the grid and control windings;
- Instantaneous induced voltages ( $e_{ga}(t)$  and  $e_{ca}(t)$ ) at rated conditions;
- Open-circuit grid induced rms voltage ( $E_{ga_{rms}}$ ) *versus* control winding 3-phase excitation ( $I_{c3\phi}$ ) ( $I_{g3\phi} = 0$ );
- Open-circuit control induced rms voltage ( $E_{ca_{rms}}$ ) *versus* grid winding 3-phase excitation ( $I_{g3\phi}$ ) ( $I_{c3\phi} = 0$ );
- Instantaneous induced electromagnetic torque ( $T_{em}(t)$ ) at rated conditions;

- Induced average electromagnetic torque *versus* grid winding excitation ( $I_{g3\phi}$ ), while keeping the control current fixed at the rated value ( $I_{c3\phi} = 3.23$  Apk).

### 7.3.2 Air-gap flux density versus $\theta_{ag}$ at rated conditions

Fig. 7.8 compares the air-gap flux density results among the models at instant  $t_s = 0s$ . It can be noticed that the MSRN curve accurately envelops the amplitude value of the FEA plot at rated conditions and it does not take into account the high frequency variations on the flux density due to the slotting effect. The latter is not considered in the MSRN model. This result is more accurate than the one obtained with the SAM that nearly represented an average curve over the period as previously shown in Fig. 7.3b.

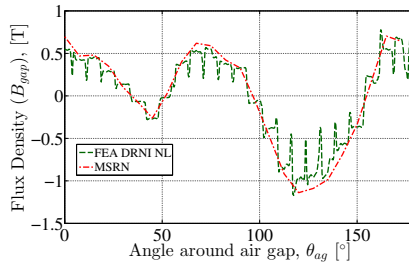


Figure 7.8: MSRN: Air-gap flux density  $B_{gap}$  *versus*  $\theta_{ag}$  at rated excitation.

### 7.3.3 Mutual inductance between grid and control windings

The same procedure described in Section 7.2.3 to calculate the mutual inductance between the grid and control winding is used to generate the FEA and MSRN curves in Fig. 7.9. This plot points out that the strong nonlinear dependence on excitation levels of the mutual inductance is identified by both models, with the MSRN model providing very precise results for the entire current range when compared to FEA.

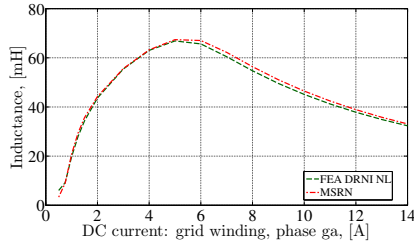


Figure 7.9: Mutual inductance  $L_{gmax}$ .

### 7.3.4 Induced voltages $e_{ga}$ and $e_{ca}$

#### 7.3.4.1 Instantaneous induced voltages $e_{ga}(t)$ and $e_{ca}(t)$ at rated conditions

Next comparison refers to the induced voltages  $e_{ga}(t)$  (Fig. 7.10a) and  $e_{ca}(t)$  (Fig. 7.10b) for an electrical period. In both plots, the results are very near from each other, confirming the good agreement between the FEA and MSRN models. The lower order voltage harmonics are also fairly well represented.

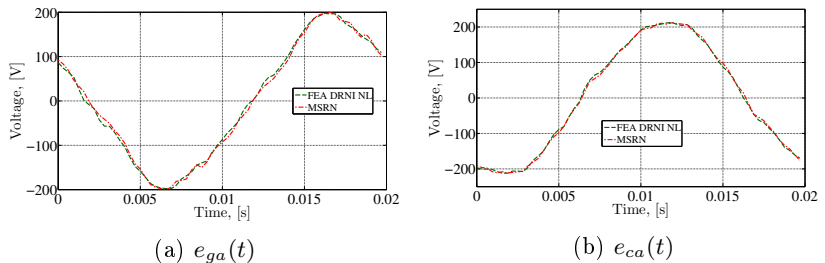


Figure 7.10: MSRN: Instantaneous induced voltages  $e_{ga}$  and  $e_{ca}$  at rated conditions.

#### 7.3.4.2 Open circuit RMS induced voltages $E_{ga}$ and $E_{ca}$ versus the excitation currents

To investigate the MSRN model even further, Fig. 7.11a and Fig. 7.11b depict the open-circuit induced RMS voltages  $E_{ga_{rms}}$  and  $E_{ca_{rms}}$  versus a 3-phase excitation in the opposed winding to the one being assessed. These curves indicate that the differences among the mod-

els are very small, confirming that the MSRN model has an accuracy comparable to the FEA model for the entire current range.

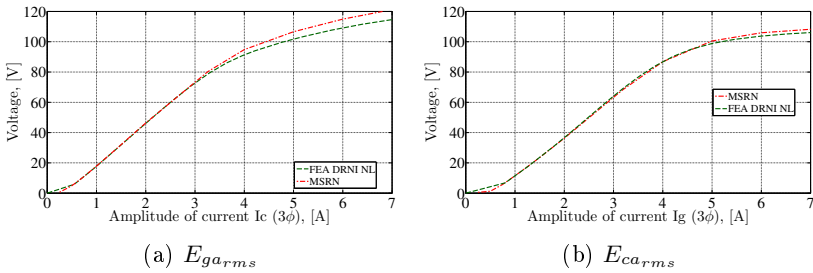


Figure 7.11: MSRN; Open-circuit induced RMS voltages  $E_{ga}$  and  $E_{ca}$  versus excitation currents.

### 7.3.5 Electromagnetic torque

The last comparison refers to the model capability on predicting the instantaneous and the average electromagnetic torque.

#### 7.3.5.1 Instantaneous electromagnetic torque

Fig. 7.12 illustrates the induced torque as a function of the time for a complete rotor mechanical rotation (3 electrical periods). Notice that the maximum torque is accurately represented when compared to the reference FEA model, except, again, for the high frequency gaps due to the slotting effect. This figure also indicates that the MSRN model is capable of estimating the torque ripple if one desires because of the effective multi-static calculations that are performed.

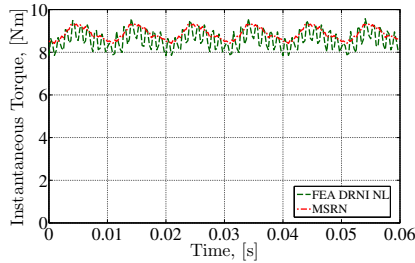


Figure 7.12: MSRN: Instantaneous induced electromagnetic torque at rated conditions.

### 7.3.5.2 Induced average electromagnetic torque

Finally, the induced average torque is plotted as a function of a 3-phase current excitation at grid winding while a 3-phase rated current excitation is kept fixed at the control winding ( $I_{c3\phi} = 3.23A$ ). The results are remarkably good for the entire current range, starting to diverge only for highly saturated operating conditions.

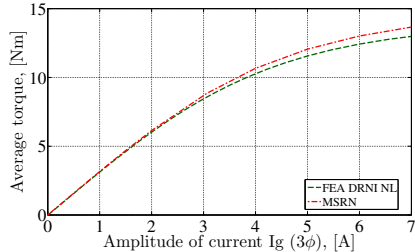


Figure 7.13: MSRN: Electromagnetic torque *versus*  $I_{g3\phi}$  at  $I_{c3\phi} = 3.23A$ .

## 7.3.6 Conclusions about the GSOM-MSRN

Previous sections have shown that the BDFRM MSRN is highly accurate when it is compared to the FEA reference model, evidencing its capability on predicting the global electromagnetic performance parameters such as phase voltages and torque.

Regarding its limitations, the MSRN does not take into account the slotting effects. This is due to its lower discretization level when compared to the FEA model: while the FEA model considers a very

dense mesh to solve Maxwell's equations locally, the MSRN is composed of a much coarser mesh represented by equivalent reluctances.

Another intrinsic MSRN limitation (that is actually shared with the developed FEA model) is the incapability of representing 3-D effects: both evaluate only two dimensional calculations.

To sum up, considering the analysis of the global performance parameters, it can be inferred that the optimization-oriented BDFRM semi-analytical model MSRN is highly accurate when compared to the reference numerical FEA model.

## 7.4 Simulation time comparison

### 7.4.1 Considerations

The parameters of the prototype machine have been used for comparing the computation time spent in each simulation for the three modeling levels (SAM, MSRN and FEA). As the MSRN, the FEA model is implemented with half-machine symmetry and, for an external diameter of 235 *mm*, it yields approximately fifty thousand elements in the finite element mesh.

To compare the computation time among the three modeling approaches, the following assumptions have been considered:

1. For the MSRN and the FEA models, the average time to perform *only one* multi-static calculation has been considered. To find the total simulation time for them, one needs to multiply the resulting value by the number of rotor positions that are calculated in one electrical period. Regarding the SAM, when it is run, it gives the results directly at steady state conditions;
2. The computation time of the optimization-oriented SAM and MSRN models includes the time spent to obtain the Jacobian matrix;
3. The time spent to calculate the FEA model refers only to solve the numerical model. The Jacobian matrix is not calculated.

### 7.4.2 Computation time results

Table 7.6 shows a comparison of the computation time for the three models using an Intel Core i7 4770 @ 3.40 GHz, 8 GB RAM.



Table 7.6: Computation time comparison among the models.

SAM	MSRN	FEA
0.030 s   1100 ×	1.43 s   24 ×	34.37 s

It can be noticed that the SAM is much faster than both models. It provides the final results in about 30 ms, which is around 1100× faster than the FEA model (reference) which takes 34.37s to calculate only one static position. Regarding the MSRN model, it takes 1.43 s to calculate one static position. If we compare the MSRN and the FEA models, for nearly the same global performance parameters accuracy, the MSRN is 24 times faster, including the Jacobian matrix calculation.

## 7.5 Final Considerations

The discussions on this chapter have shown that, due to the different modeling approaches, the GSOM-SAM and GSOM-MSRN have distinct characteristics regarding computation time and precision. The SAM is much faster, but it may provide low precision results depending on the operating excitation level. Regarding the MSRN, it offers a very interesting trade-off between precision and computation time when compared to FEA.

The question that rises is: why not to use directly the MSRN in the design process due to its highly accurate results?

To answer this question, let us recall the design procedure outlined in Section 1.5.1.3 that mentioned the different goals of the SAM and the MSRN. Although possible to use directly the MSRN on the optimization process, the SAM is still much faster, mostly due to the MSRN multi-static computations. Depending on the considered time step, one optimization may take a few hours with the MSRN and just a few seconds with the SAM. Thus, in very early design stages, where the number of parameter uncertainties for the final machine are huge, it is suggested to firstly use the SAM to restrain the search space and to define an initial machine that match all constraints set up in the optimization process. This machine is potentially a good candidate to be used as the starting point in the optimization using the GSOM-MSRN to further refine the design. Since the initial machine may be closer to the optimal one, it eventually reduces the number of iterations (time to convergence), saving time in the development process.

Next chapter examines the model results by confronting them with the experimental ones obtained with the prototype.

# Chapter 8

## BDFRM prototype: design, realization and experimental results used to verify the models

### Abstract

*This chapter presents the optimization approach that has been used to design a BDFRM prototype and examines its experimental results. Firstly, the optimization problem characteristics used to specify the prototype are presented. In the sequence, referring to the results, special attention is given to the mutual inductance, directly related to machine capacity on the electromechanical energy conversion. The main focus is on machine characterization and on the comparison among the measured data and the simulation results obtained with the three modeling levels (GSOM-SAM, GSOM-MSRN and FEA) developed in this thesis. In general, the comparison results are considered satisfactory. However, some discrepancies are identified and a discussion about some hypothesis to explain the differences among the models and the experimental results is presented at the end.*

## **8.1 BDFRM prototype design and realization by using an optimization approach**

### **8.1.1 Prototype specification by using the GSOM-SAM**

In order to validate the models that have been developed in this dissertation, a BDFRM prototype has been specified by using an optimization approach based on the GSOM-SAM. By the time it was manufactured, the GSOM-MSRN was not yet operational and the proposed design procedure could not be fully applied to define it. Next sections outline the optimization problem that has been set for that purpose.

### **8.1.2 Characteristics of the GSOM-SAM used to specify the prototype: objective function and constraints**

The GSOM-SAM equations presented in Appendix G have been implemented in CADES to generate the required optimization model containing the outputs/inputs relationship and the associated Jacobian matrix. For the optimization problem, 10 inputs were left free to vary in a range. Regarding the outputs, 35 have been constrained in a range in the form  $MIN < output < MAX$  resulting in 70 constraints in total. The constrained outputs refers to geometrical and electrical parameters, as well as one objective function.

Fig. summarizes 8.1 the optimization problem characteristics.

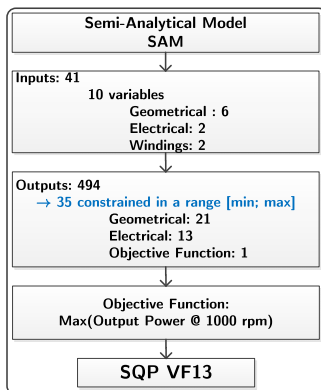


Figure 8.1: GSOM-SAM characteristic for sizing the prototype

### 8.1.3 Variable inputs

The prototype has been specified to fit a specific frame, therefore the stator external diameter ( $D_{es}$ ) has been previously set to 235 mm and the effective machine axial length ( $L_{stkef}$ ) to 69 mm in the optimization problem. The inputs that are left free to vary are defined in Table 8.1. In this table, the column “Range” depicts the minimum, initial and maximum values of the variable inputs using the notation: [min; initial; max]. The symbols are defined in Fig 8.2.

Table 8.1: Optimization problem: variable inputs.

Symbol	Description	Range
Dis	Stator internal diameter	[50; 147.9; 350]
Iphc	Control current amplitude	[0.01; 3; 30]
Iphg	Grid current amplitude	[0.01; 5; 30]
Nphc	Control total number of turns per phase	[8; 144; 600]
Nphg	Grid total number of turns per phase	[8; 144; 600]
SlrWidth	Rotor slot width	[2.5; 2.6; 30]
thh	Stator teeth detail	[2.0; 2.0; 3.0]
thn	Stator teeth detail	[2.0; 2.0; 3.0]
ykw	yoke width	[10.0; 15.0; 60.0]
ytr	yoke to stator tooth width ratio $ytr = ykw/thw$	[2.0; 2.82; 5.0]

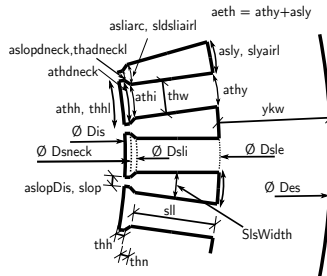


Figure 8.2: Stator slot physical dimensions definitions.

### 8.1.4 Constrained outputs

The constrained outputs refers to geometrical and electrical parameters. The geometrical ones are used to limit some dimensions so that the resulting machine has a physical meaning. For example, the stator internal diameter ( $Dis$ ) cannot be greater than the external one ( $Des$ ), so a constraint of the kind  $condition\_1 = (Des - Dis) > 0$  is created to limit the optimization search space. Similar assumptions are

made for other geometrical constraints in order to limit machine physical dimensions. Additionally, the duct ratio (refer to Section 5.2.4), the cross-sectional area of the slot, the winding filling factor, the ratio between the axial length and the stator internal diameter and the tooth width are also set as geometrical constrained outputs. The electrical constraints refer to the output voltages, the maximum allowed current densities and the maximum inductions in the magnetic circuit. The constrained outputs are summarized in Table 8.2.

Table 8.2: Optimization problem: constrained outputs.

Symbol	Description	Range	Quantity
<b>Geometrical Constraints</b>			
$DuctRatio$	Duct Ratio	[0.37; 0.4]	[1]
$ratio\_L\_Dis$	Lstk/Dis Ratio	[0.6; 3]	[1]
$Sslot$	cross-sectional area of the stator slot	[1; 500]	[1]
$thw$	stator teeth width	[4; 20]	[1]
$wff$	winding filling factor	[0.001; 0.35]	[1]
$Phys\_limit$	Physical limitation constraints (e.g. (Dis-Der) $> 0$ , (Des-Dsle) $> 0$ etc.	constr $> 0$	[16]
<b>Electrical Constraints</b>			
$V_{ca}$	Control winding rms phase voltage	[129.9; 130.0]	[1]
$V_{ga}$	Grid winding rms phase voltage	[129.9; 130.0]	[1]
$J_{wc}$	Current density in control winding	[0.01; 3.5]	[1]
$J_{wg}$	Current density in grid winding	[0.01; 3.5]	[1]
$A_{sel_{total}}$	Linear current density (refer to Section 5.2.3)	[0; 32000]	[1]
$B_{FBx}$	Maximum induction in the rotor flux paths	[0; 1.5]	[6]
$B_{thmax}$	Maximum induction in the stator teeth	[0; 1.5]	[1]
$B_{ykmax}$	Maximum induction in the stator yoke	[0; 1.5]	[1]

### 8.1.5 Objective function and the resulting machine used on the validations

The objective function was set to maximize the output power at 1000 rpm assuming that the machine external dimensions are fixed. The GSOM-SAM is coupled to the SQP-VF13 optimization algorithm that automatically searches the optimal machine that satisfies all the constrained outputs within the optimization search space defined in Table 8.3. It takes 20 iterations (approximately 20 s) to converge and provide the optimal machine.

Table 8.3: Optimization problem: variable inputs.

Symbol	Description	Range	Result
Dis	Stator internal diameter	[50; 147.9; 350]	144.24
Iphc	Control current amplitude	[0.01; 3; 30]	3.23
Iphg	Grid current amplitude	[0.01; 5; 30]	3.07
Nphc	Control total number of turns per phase	[8; 144; 600]	312
Nphg	Grid total number of turns per phase	[8; 144; 600]	448
SlrWidth	Rotor slot width	[2.5; 2.6; 30]	2.727
thh	Stator teeth detail	[2.0; 2.0; 3.0]	2.0
thn	Stator teeth detail	[2.0; 2.0; 3.0]	2.0
ykw	yoke width	[10.0; 15.0; 60.0]	14.5
ytr	yoke to stator tooth width ratio $ytr = ykw/thw$	[2.0; 2.82; 5.0]	2.826

### 8.1.6 Prototype specification

Based on the previous results, the prototype characteristics have been specified. Table 8.4 summarizes its specifications.



Table 8.4: BDFRM prototype characteristics.

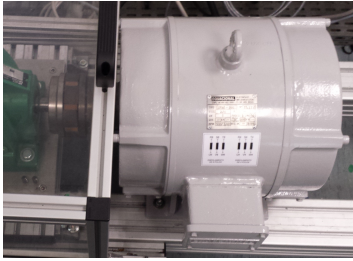
Stator External Diameter	235.0 mm
Stator Internal Diameter	144.24 mm
Effective Axial Length	69.0 mm
Shaft diameter	65.0 mm
Grid winding total number of turns	448
Control winding total number of turns	312
Air gap length	0.5 mm
Number of stator slots	48
Number of rotor ducts	66
Number of poles Grid/Control/Rotor	8/4/6
Yoke width	14.5 mm
Yoke to stator tooth width ratio	2.826
Stator slot opening	1.6 mm
Rotor slot width	2.727 mm
Control winding wire diameter	0.91186 mm
Grid winding wire diameter	0.91186 mm
Magnetic Material in stator and rotor	M400-50A

The prototype rated electromagnetic parameters are depicted in Table 8.5.

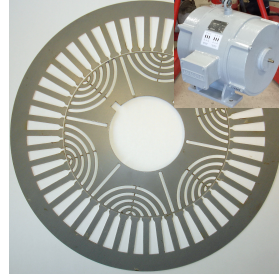
Table 8.5: BDFRM prototype rated parameters (specifications).

Grid winding current ( $I_g$ peak)	3.07 Apk / 2.17 Arms
Control winding current ( $I_c$ peak)	3.23 Apk / 2.28 Arms
Grid winding phase voltage ( $V_g$ rms)	127 V
Control winding current ( $V_c$ rms)	127 V
Maximum speed ( $\omega_{rm}$ )	1000 rpm
Torque max @ Max Speed	9.5 Nm
Rated power @ 1000 rpm	1 kW

Fig. 8.3a shows the prototype that has been manufactured and Fig. 8.3b presents the stator and rotor laminations.



(a) BDFRM prototype.



(b) Prototype stator and rotor laminations.

Figure 8.3: BDFRM 1000 W prototype.

## 8.2 Experimental results obtained from the prototype

All of the experimental results that are presented in this chapter refers to no-load tests. Their goal is to verify the machine behavior, by focusing the analysis on the flux modulation process by the rotor. These kind of tests are associated to the BDFRM mutual inductance among the winding sets  $L_{gcm_{max}}$ . This parameter is one of the most important when assessing BDFRM performance, since the steady state torque, given by (1.19), is directly proportional to it.

### 8.2.1 Preliminary considerations to present the experimental results

Before discussing the experimental results, this section outlines the test workbench used to obtain the experimental data and the nomenclature used to compare the results with the models previously presented.

#### 8.2.1.1 Test workbench

The test workbench used to perform the tests is shown in Fig 8.4. The utilized equipments includes a DC machine used to drive the machine shaft and impose a fixed speed, AC and DC voltage sources and measurement equipments (oscilloscope, multimeter, current and voltage probes).

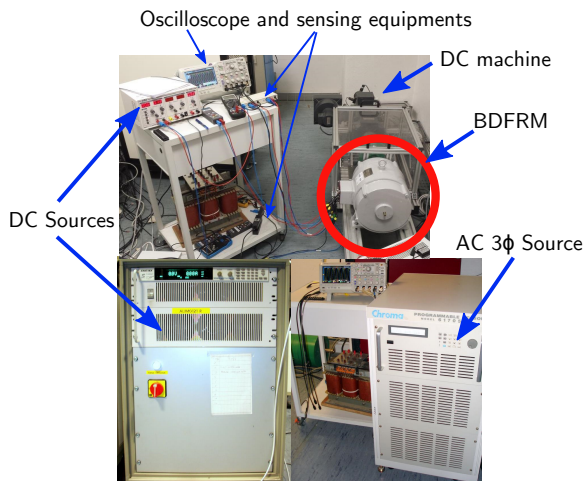


Figure 8.4: Test workbench.

### 8.2.1.2 Nomenclature definition

The following nomenclature is used in the sequence for discussing the results:

$ga$	→	Phase $A$ of grid winding
$gb$	→	Phase $B$ of grid winding
$gc$	→	Phase $C$ of grid winding
$ca$	→	Phase $A$ of control winding
$cb$	→	Phase $B$ of control winding
$cc$	→	Phase $C$ of control winding
$PROT$	→	Results obtained by experiments on the prototype
$FEA$	→	Results obtained from the FEA DRNI NL model
$MSRN$	→	Results obtained from the GSOM-MSRN model
$SAM$	→	Results obtained from the GSOM-SAM

### 8.2.2 Mutual inductance test setup

To calculate the mutual inductance, a DC current is applied to one of the three phases at one side (grid or control) and all the other five phases are left opened. The machine is externally driven by a DC machine at a constant fixed speed. Then, the three phase voltages are measured in the opposite side of the one that is being excited.

For example, if a DC current is applied to  $ga$  ( $I_{ga_{DC}}$ ), the voltage is measured at the three phases in the control winding set. Similarly, if a DC current is applied to  $ca$  ( $I_{ca_{DC}}$ ), the three phase voltages are measured at grid side.

To effectively calculate the mutual inductance, the measured voltages are post-processed by integrating the voltage waveform to obtain the phase mutual flux linkage, since  $v = \frac{d\lambda}{dt}$ . When performing this calculation, one needs to compensate the offset that may arise due to the integration process.

The mutual flux linkage waveform is (ideally) a sinusoidal function of the rotor position. Therefore, to assess  $L_{gcmax}$ , the maximum value of flux waveform is identified and it is divided by the DC current that has been applied to the excitation winding. The result is the maximum value of the mutual inductance  $L_{gcmax}$ .

### 8.2.3 Voltage measured at control side, 500 rpm, $I_{ga_{DC}}$ excitation

To illustrate the procedure, Fig. 8.5 shows the oscilloscope screenshot with the induced voltages waveforms in control winding due to a  $I_{ga_{DC}} \approx 6 A$  at 500 rpm. In this test, the machine is externally driven at  $\omega_{rm} = 500 rpm$ . It can be noticed that the electrical period of the voltage waveform is 20 ms, satisfying the speed condition (1.18) as expected.

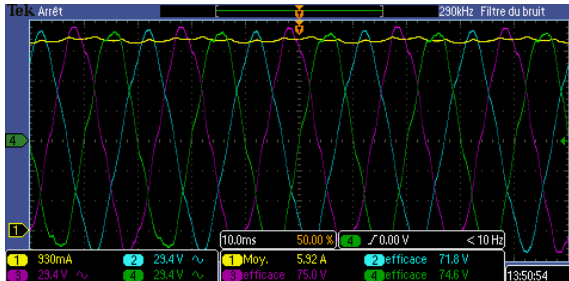


Figure 8.5: Oscilloscope screenshot: induced voltages in control winding at 500 rpm and  $I_{ga_{DC}} \approx 6A$ .

- $Ch1 \rightarrow I_{ga_{DC}} = 5.92A$
- $Ch2 \rightarrow V_{ca}$
- $Ch3 \rightarrow V_{cb}$
- $Ch4 \rightarrow V_{cc}$

## 8.2.4 Mutual inductance between the winding sets

### 8.2.4.1 Comparison between mutual inductances measured at grid and control sides at 500 rpm

Fig. 8.6 shows the  $L_{gcm\max}$  parameter measured at phase  $ca$  when a DC current is applied to  $ga$  and compares its result by measuring the same parameter at phase  $ga$  when a DC current is applied to  $ca$ . Both tests are performed when the machine is turning at 500 rpm.

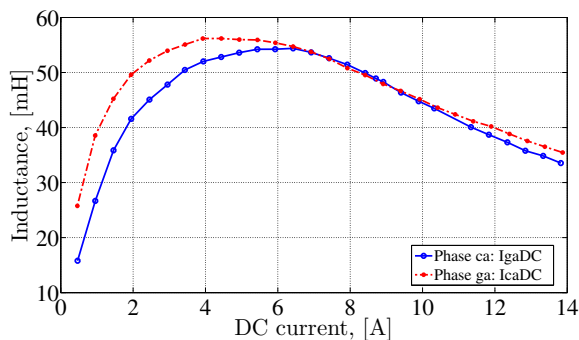


Figure 8.6: Mutual inductances comparison: grid *versus* control at 500rpm.

Ideally, one would expect that both results would be the same. However, it is interesting to notice that the mutual inductance measured from control and grid sides, although similar from each other, presents a small difference, mainly in the first part of the curve (low excitation). This difference can be explained by the nonlinear effect introduced by the iron bridges previously discussed in Section 7.1.3 and recalling the distinct number of poles nature of this machine<sup>1</sup>. Magnetically, especially at low excitation, the way one winding is induced differs from the other.

This phenomenon can be confirmed through Finite Element Analysis. The DRNI rotor is replaced by the DRI, which does not have the iron bridges, with the same nonlinear material used on the DRNI simulation. Fig. 8.7 depicts two calculations for the mutual inductance by using FEA simulations for excitations at grid  $I_{gaDC}$  and control  $I_{caDC}$  windings considering the DRI rotor. It can be seen that the

<sup>1</sup> $P_g = 8$ ,  $P_c = 4$  and the number of slots per pair of poles per phase is, respectively, 4 and 8. Refer to Fig. 2.8 for the actual position of the windings around the machine air-gap.

mutual inductances, when calculated from both sides, are nearly the same for a case without the iron bridges as one would expect.

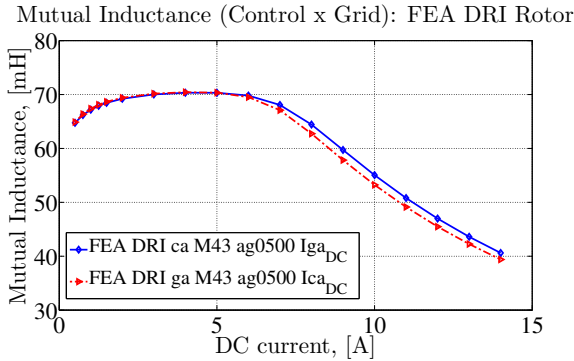
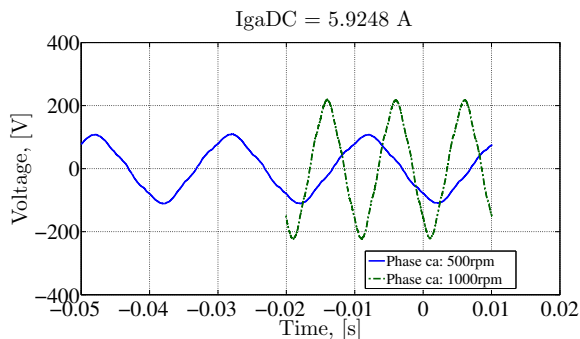


Figure 8.7: Mutual inductances comparison by using a Finite Element Analysis in a Ideal Ducted Rotor (DRI): grid *versus* control at 500rpm.

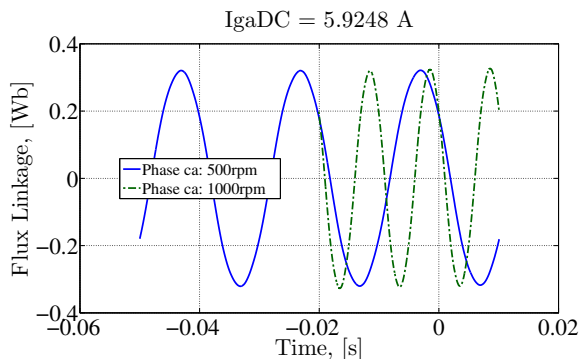
#### 8.2.4.2 Investigating the speed influence: mutual inductances at 500 rpm and 1000 rpm

The next test investigates the influence of the speed on determining the mutual inductance. Since the induced currents in the iron (eddy currents) are proportional to the frequency, this parameter could eventually impact on the measured data.

Fig. 8.8a and Fig. 8.8b present the voltage and flux linkage waveforms in phase *ca* of control winding for a DC excitation  $I_{ga_{DC}} \approx 6 A$ , respectively, at speeds 500 and 1000 rpm. The differences in the voltage amplitude and frequency can be remarked, since the voltages are induced at 100 Hz when the rotor is rotating at 1000 rpm and at 50 Hz when it is at 500 rpm for the considered number of poles combination.



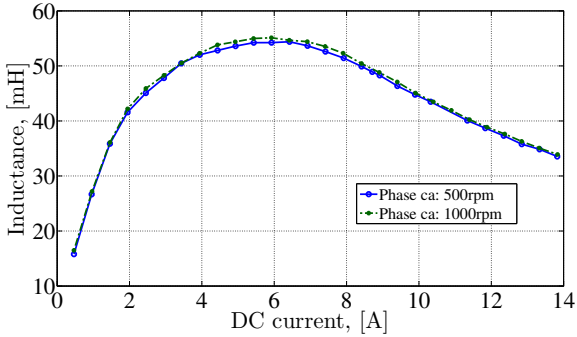
(a) Voltage waveform measured at control side at  $I_{ga_{DC}} \approx 6$  A.



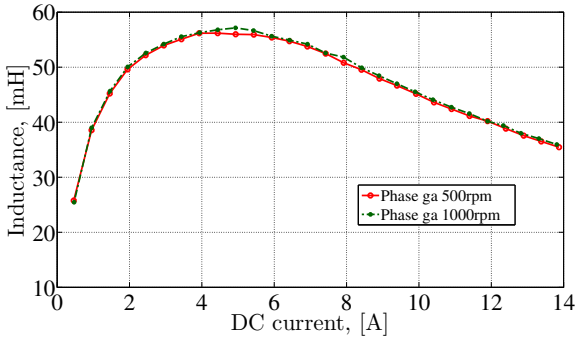
(b) Flux linkage waveform measured at control side at  $I_{ga_{DC}} \approx 6$  A.

Figure 8.8: Voltage and flux linkage waveforms in control side at  $I_{ga_{DC}} \approx 6$  A and at 500 and 1000 rpm.

Fig. 8.9a depicts the results obtained at *ca* due to a  $I_{ga_{DC}}$  excitation and Fig. 8.9b the ones at *ga* due to a  $I_{ca_{DC}}$  excitation.



(a) Measured mutual inductance in control winding at 500 and 1000 rpm.



(b) Measured mutual inductance in grid winding at 500 and 1000 rpm.

Figure 8.9: Comparison of mutual inductances in grid and control windings measured at 500 and 1000 rpm.

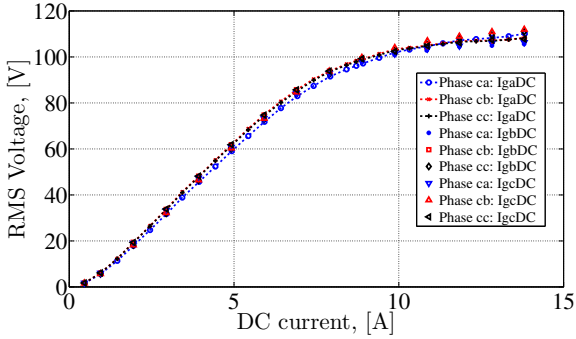
As can be noticed, the speed and, consequently, the induced frequency, has nearly no effect on the determination of the mutual inductance for speeds up to 1000 rpm.



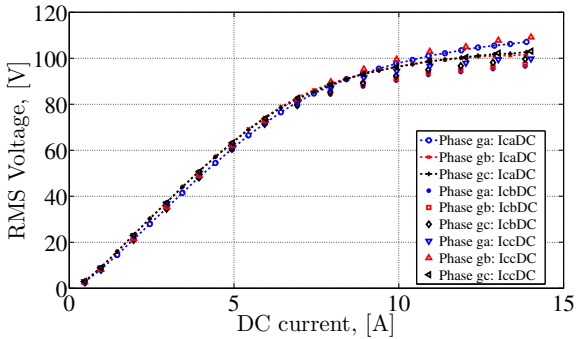
### **8.2.5 Open-circuit induced RMS voltage in grid and control sides due to a DC excitation at the respective opposite side at 500 rpm**

The last section dedicated exclusively to the experimental data plots the open-circuit induced RMS voltages as a function of single phase DC excitations in the opposite winding set to the one being measured.

Fig. 8.10a shows the RMS voltage in the three phases of control side, considering a DC excitation on each phase of grid winding individually. Similarly, Fig. 8.10b presents the RMS voltage in the three phases of grid side, considering a DC excitation on each phase of control winding individually.



(a) Open-circuit RMS voltage in control winding at 500 rpm.



(b) Open-circuit RMS voltage in grid winding at 500 rpm.

Figure 8.10: Open-circuit RMS voltages measured in grid and control sides at 500 rpm for DC excitations.

The goal of these figures is to verify if all the phases are balanced and that a DC excitation in any of the other phases produces comparable results. It can be concluded that indeed, independently of the phase that the DC current is applied, the induced RMS voltages are basically the same among the phases. These results allow to consider only one of the phases when comparing the experimental data to the simulation results in the next sections.

## 8.3 Confronting the experimental and simulation results

This section depicts some comparisons among experimental data measured on the prototype (PROT) and simulation results obtained from the 2D finite element model (FEA), the multi-static reluctance network model (MSRN) and the semi-analytical model (SAM).

### 8.3.1 Nomenclature

Table 8.6 shows the nomenclature used to designate the curves in the following plots when comparing the simulation results to the experimental data. Regarding the FEA models previously discussed, only the FEA DRNI NL is used. Thus, for simplicity, it is identified just by FEA.

Table 8.6: Nomenclature used to compare the models.

Acronym	Color	Trace
SAM	blue	—
MSRN	red	-.-
FEA	green	--
PROT	black	×

### 8.3.2 Mutual inductances

Fig. 8.11 depicts the mutual inductances obtained from the distinct sources and Table 8.7 compares the different results between the models and the prototype considering only their maximum possible values for the mutual inductance.

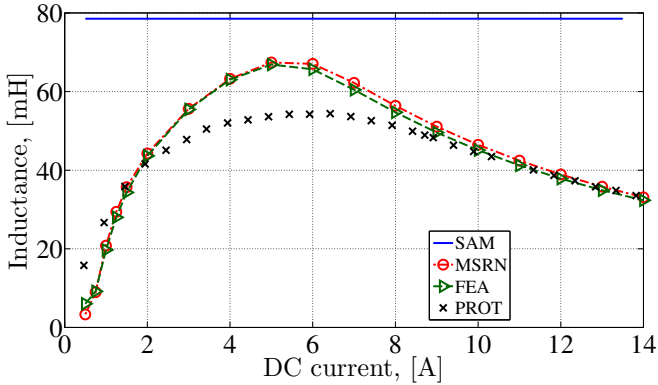


Figure 8.11: Mutual inductance  $L_{gcmx}$  calculated from the FEA, SAM and MSRN models compared to the prototype results. Measured at  $ca$  with DC excitation at  $ga$ .

Table 8.7: Comparison of maximum values of  $L_{gcmx}$  obtained with the prototype and the different models.

	Prototype	FEA	MSRN	SAM
	54.39 <i>mH</i>	66.89 <i>mH</i>	67.40 <i>mH</i>	78.54 <i>mH</i>
Diff % Prototype	-	+23.0 %	+23.9 %	+44.4 %
Diff % FEA	-	-	+0.76 %	+17.4 %

From Fig. 8.11 and Table 8.7, it can be noticed that the MSRN and the FEA models have a good agreement. Even the SAM (linear) falls within an acceptable range when compared to the nonlinear models. However, when the models are compared to the prototype, there is clearly an important difference of around 23 % for the worst case that must be further investigated.

### 8.3.3 Open-circuit induced RMS voltage due to a single phase DC excitation

Fig. 8.12 illustrate the results for the induced RMS voltages due to a single phase DC excitation.

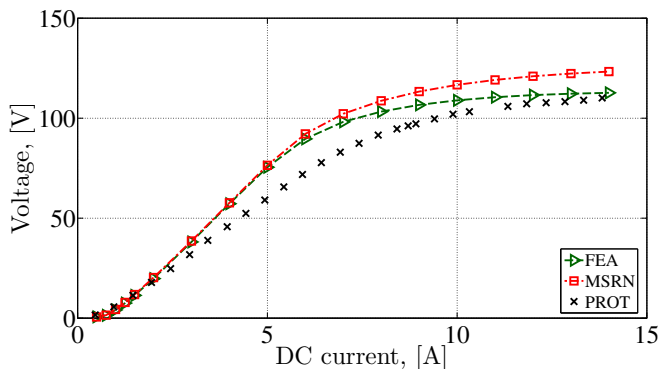


Figure 8.12: Open-circuit induced RMS voltage calculated from FEA, SAM and MSRN models compared to the prototype results. Measured at  $ca$  with DC excitation at  $ga$ .

Again, some differences among the models and the prototype are remarked, especially at the point of maximum permeability. It represents roughly the same operating point with the maximum deviation of the mutual inductance in Fig. 8.11.

### 8.3.4 Instantaneous open-circuit induced voltages at control and grid windings due to a 3-phase excitation

So far, the models have been compared by using a single phase DC excitation. This section investigates the open-circuit induced voltages by feeding the excitation windings with balanced sinusoidal 3-phase currents.

To start, Fig. 8.13a presents the instantaneous open-circuit induced voltage  $e_{ga}(t)$  for all the three models and the prototype for a rated excitation at the control winding. Similarly, Fig. 8.13b shows the open-circuit induced voltage  $e_{ca}(t)$  considering the excitation at the grid winding.

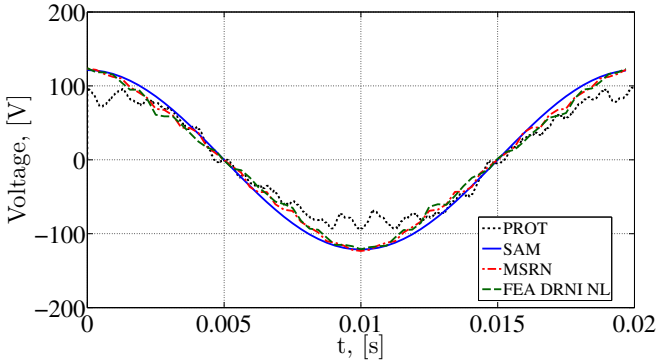
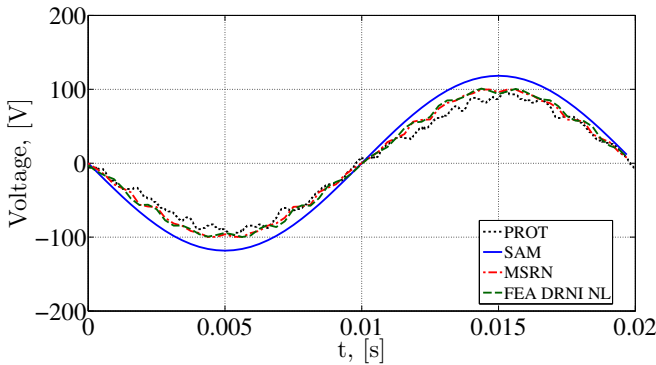
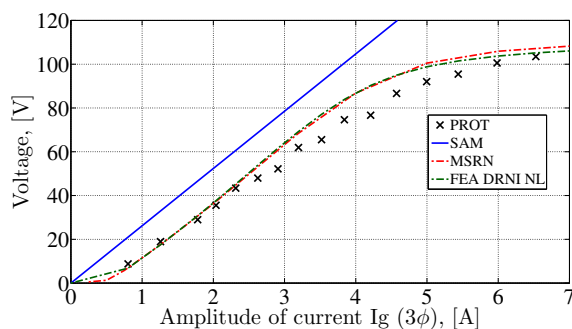
(a)  $e_{ga}(t)$  at  $I_{g3\phi} = 0A$  &  $I_{c3\phi} = 3.28A$ (b)  $e_{ca}(t)$  at  $I_{g3\phi} = 3.2A$  &  $I_{c3\phi} = 0A$ 

Figure 8.13: Instantaneous open-circuit induced voltages at  $e_{ga}$  and  $e_{ca}$ .

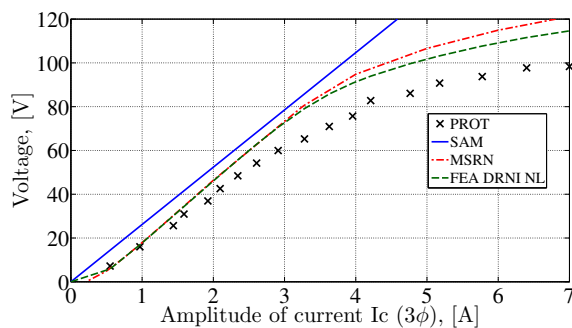
It can be inferred that the instantaneous induced voltage simulation results are representative to predict the prototype behavior and each one of them is limited by its inherent modeling approach and associated accuracy level. However, there are some differences among the simulation and experimental data mostly due to the reduced value of the mutual inductance in the prototype.

### 8.3.5 Open-circuit induced RMS voltages at control and grid windings as a function of the excitation currents

To further analyze the open-circuit induced voltages, Fig. 8.14a shows the open-circuit induced RMS  $E_{ca}$  voltage as a function of the 3-phase currents applied to the grid winding for the three models and the prototype. Similarly, Fig. 8.14b depicts the induced voltage at  $E_{ga}$  for control winding 3-phase excitation.



(a)  $E_{ca}$  (RMS) versus  $I_{g3\phi}$



(b)  $E_{ga}$  (RMS) versus  $I_{c3\phi}$

Figure 8.14: RMS open-circuit induced voltages  $E_{ga}$  and  $E_{ca}$  in terms of the excitation currents.

Again, Fig. 8.14 indicates the limitations of the linear SAM model and highlights the capability of the MSRN and FEA models on predicting the prototype behavior. Although the results are considered

sufficiently accurate for modeling and optimization purposes, there is clearly a difference among the curves that are directly related to the mutual inductance as introduced in the previous sections. A general discussion on these aspects is presented in the sequence.

## 8.4 Discussions on the experimental and simulation results

### 8.4.1 Preliminary conclusions

To discuss the differences among the simulation and experimental results, let us define three distinct current ranges shown in Fig. 8.15 based on the mutual inductance comparisons previously presented in Fig. 8.11.

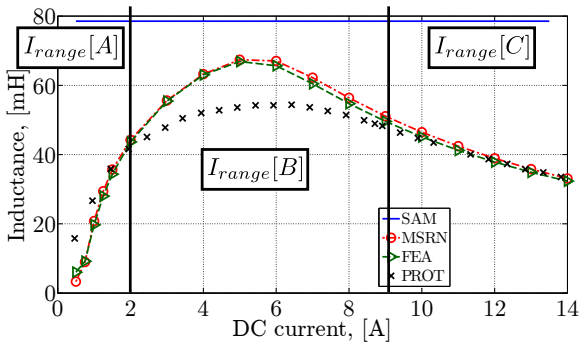


Figure 8.15: Definition of the current ranges to discuss the results.

The current ranges are:

1.  $I_{range}[A]$  for currents from 0.5 up to 2.0 A;
2.  $I_{range}[B]$  for currents from 2.0 up to 9.0 A;
3.  $I_{range}[C]$  for currents from 9.0 up to 14.0 A.

Based on these definitions, the following observations can be made:

- $I_{range}[C]$  indicates that, when the magnetic material saturates in the machine, the prototype as well as the FEA and MSRN models converges to the same asymptote. At this excitation level, as the magnetic material used in the prototype and in the models



have similar saturation points, its characteristics have nearly no influence on the results.

- Similar conclusions cannot be directly inferred for ranges  $I_{range}[A]$  and  $I_{range}[B]$ . Considering first  $I_{range}[A]$ , for low values of excitation currents, it is interesting to notice that the prototype presents higher (better) values for the mutual inductance. At  $I_{range}[B]$ , this tendency is inversed, with the simulation values reaching a peak which is around 23 % higher than the one obtained with the prototype.
- The FEA and the MSRN models present coherent results among each other and provide the same tendency observed in the prototype. Some differences should be expected, since, even if they take into account many nonlinear phenomena, they always have some intrinsic simplifications that could lead to these differences. However, it is important to investigate the most likely reasons of the distinct results to better understand the model capabilities and their limitations. Some possible hypothesis that may lead to this discrepancies are discussed in the sequence.

## 8.4.2 Hypothesis investigation for the differences found between the models and the prototype results

### 8.4.2.1 Three-dimensional effects not taken into account

The first hypothesis that can be raised to explain the differences is the influence of three-dimensional effects in the actual prototype that are not taken into account in the 2D FEA and MSRN models. The currents circulating in the end windings could somehow impacts the mutual inductance, keeping in mind that the prototype external diameter is 235 mm and the effective axial length is 69 mm (3.4× greater). However, the end windings are relatively far from the iron parts and, consequently, the end winding leakage inductances, which gives a general idea of the influence of the end windings on machine performance, are usually not very high [37]. Thus, although it is possible that the end windings currents have some influence on the mutual inductance, it is unlikely that they explain alone the differences between the models and the experimental results for the entire current range. A 3D finite element analysis would confirm or discard this statement and this

study is proposed as a future work to further investigate the BDFRM prototype.

#### 8.4.2.2 Manufacturing tolerance of the air-gap

In any electrical machine, the air-gap length have a great impact on performance. Therefore, another possible hypothesis to explain the differences is the manufacturing tolerance of the air-gap length (*gap*).

The prototype has been specified with a small air-gap length of  $gap = 0.5 \text{ mm}$  and a tolerance of  $\pm 0.02 \text{ mm}$ . To investigate the effective impact of the air-gap length on the mutual inductance and on the induced open-circuit RMS voltage, some different air-gap lengths have been simulated in the FEA (reference) model.

Four different values of air-gap length are considered:  $0.5 \text{ mm}$ ,  $0.525 \text{ mm}$ ,  $0.55 \text{ mm}$  and  $0.575 \text{ mm}$ . Although these values extrapolates the tolerance, it is interesting to notice their influences on the machine performance. To indicate them in the curves, the acronym *ag0000* is used. The number after *ag* divided by a factor 1000 gives the air-gap in millimeters. For example, *ag0500* means  $0.5 \text{ mm}$ .

Fig. 8.16a and Fig. 8.16b presents, respectively, the mutual inductance and the induced open-circuit RMS voltages in control winding due to an  $Iga_{DC}$  current

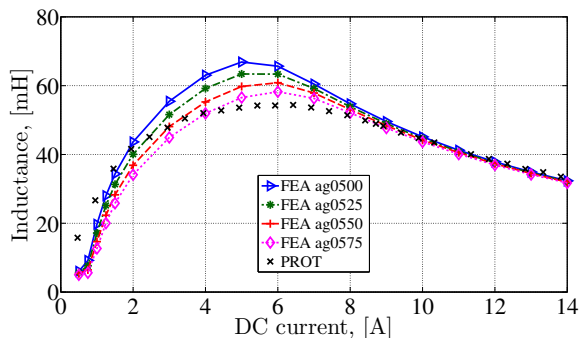
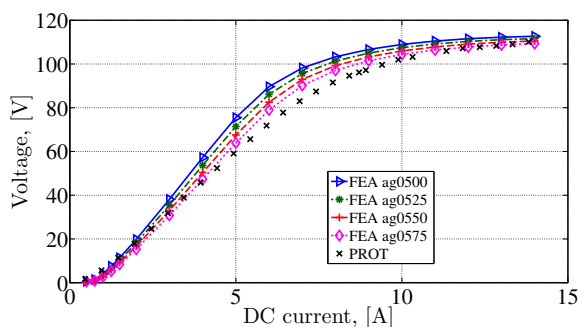
(a)  $L_{gmax}$ (b)  $V_{rms}$ 

Figure 8.16: Mutual inductance and RMS voltages calculated from the FEA considering different air-gap lengths.

The first conclusion that can be drawn from Fig. 8.16 is that the air-gap length is quite important for determining the peak value of the mutual inductance in current range  $I_{range}[B]$ . Additionally, it can be noticed that the air-gap length has nearly no influence at the beginning and at the end of the magnetization curve, for  $I_{range}[A]$  and  $I_{range}[C]$ , respectively. Although the air-gap length can indeed explain some of the divergences between the models and the prototype, this hypothesis alone is not consistent for the entire current range.

### 8.4.2.3 Degradation of the magnetic material due to the laser-cutting manufacturing process

#### 8.4.2.3.1 The problem

It is well known in the literature that the manufacturing processes (punching, laser cutting) used to produce the iron sheets may degrade magnetic material performance. Often, a stress relief annealing is employed to improve/restore magnetic material characteristics after the cutting. Such process has not been applied to the BDFRM prototype, because the material used on sheet insulation would not resist.

Belhadj *et al.* [134] investigated the laser cutting process impact on the microstructure and on magnetic properties of non-oriented grain electrical steels. It has been found, for the tested samples with a width of 5 mm, that the laser induces a strong permeability drop, between 14% up to 30% depending on sample type, which is usually linked to an increase on the coercive field. They also noticed that to reach an induction level of 1.5 T, higher field strength are required for the samples that have been cut with the laser when compared to the samples that have been cut by a punching process. Similar conclusions regarding the permeability drop on electrical steels due to manufacturing processes such as the laser cutting have been found in [135]. The impact of the manufacturing process especially over small width strips have been highlighted.

#### 8.4.2.3.2 The BDFRM prototype rotor lamination

The iron sheets of the BDFRM prototype have been manufactured by using a laser cutting process. Therefore, another hypothesis that can be raised is that the machine performance has been degraded due to the this manufacturing process. For the BDFRM, the rotor is a potential candidate to be severely affected. Fig. 8.17 shows a sample of the rotor lamination used to build the prototype.

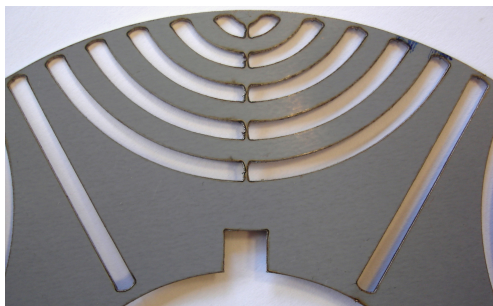


Figure 8.17: Rotor lamination: effect of the laser cutting process.

The BDFRM rotor laminations have been affected by many laser cuts in order to produce all the flux barriers specified in the project. The flux paths have a width of  $3.87\text{ mm}$  and, based on the literature [135, 134], the permeability drop for such a small width can be significant. The impact of laser cutting process can be even higher for the rotor region containing the narrowest cuts, for example, the iron bridges on the rotor air-gap region with widths smaller than  $1\text{ mm}$ .

#### 8.4.2.3.3 Simplified procedure to investigate the hypothesis validity: a new rotor model

To simplify the investigation of this hypothesis, it is assumed that the laser cutting process affects mostly the narrowest regions, smaller than  $1\text{ mm}$ . On the proposed simulation, it is considered that the flux paths regions would not suffer a great impact on performance. As the rotor periphery (air-gap region) contains the small iron bridges to connect the flux path for mechanical robustness, with widths of around  $0.8\text{ mm}$ , it seems reasonable to assume that this region could be severely influenced by the laser cutting process, more than the remaining part of the rotor. It is also important to remark that the laser passes through this region twice: the first to define the air-gap itself and the second one to define the rotor ducts (slots), which could further increase the magnetic material degradation.

To simulate this effect, a modified rotor FEA model is developed. In this model, the region around the air-gap associated to the iron ribs is set with a different material, with a great reduction on its permeability. Fig. 8.18 highlights the region supposedly affected by the laser cutting.

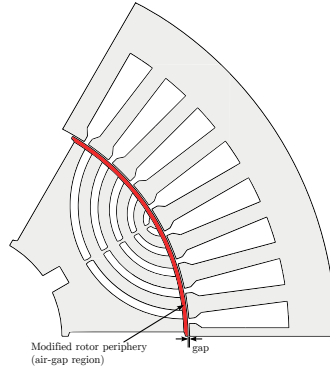
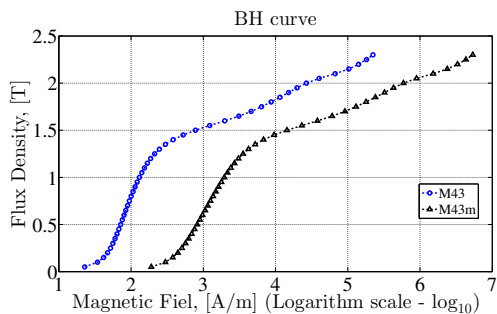


Figure 8.18: Air-gap region potentially influenced by the laser-cut process during BDFRM prototype manufacturing.

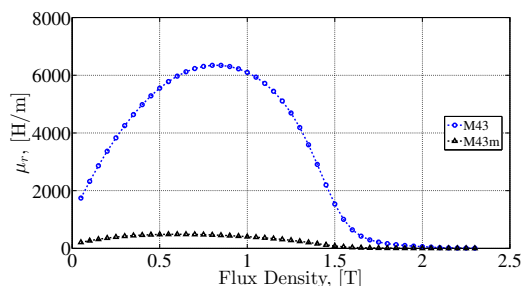
#### 8.4.2.3.4 Magnetic material considered in the modified air-gap region

The magnetic material  $M43$  (M400-50A) is the one used to build the prototype and it has been set in all the models presented so far. Although the hypothesis of material degradation on the air-gap region seems reasonable, it is very hard to quantitatively determine the permeability drop due to the laser process for such small widths. That is because the laser impact on material also depends on the unknown parameters used on the laser beam applied to cut the steel.

As a work-around, a magnetic material has been empirically defined (referred as  $M43m$ ). It is derived from the  $M43$  material to test an hypothesis raised in this section. The comparison among the magnetic materials are shown in Fig. 8.19a for the BH magnetization curves and in Fig. 8.19b for the relative magnetic permeability.



(a) BH magnetization curves.



(b) Relative permeability.

Figure 8.19: Magnetic materials characteristics.

To test the hypothesis, the material *M43m* has been set to the region highlighted in Fig 8.18. The remaining iron parts in the machine model remains unchanged and the *M43* material originally used in the simulations is set to these regions.

#### 8.4.2.3.5 Comparing the experimental data to the simulated hypothesis

Fig. 8.20a and Fig. 8.20b shows the results obtained for the mutual inductance and the induced open-circuit RMS voltage, respectively, for the modified air-gap FEA model considering the same four air-gap lengths as defined previously:  $0.5 \text{ mm}$ ,  $0.525 \text{ mm}$ ,  $0.55 \text{ mm}$  and  $0.575 \text{ mm}$ . The original FEA model with  $0.5 \text{ mm}$  is also shown for comparison.

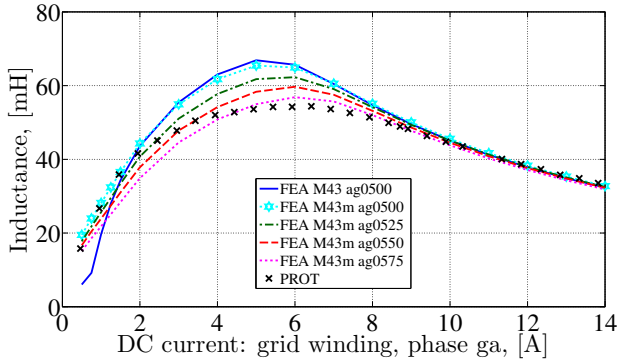
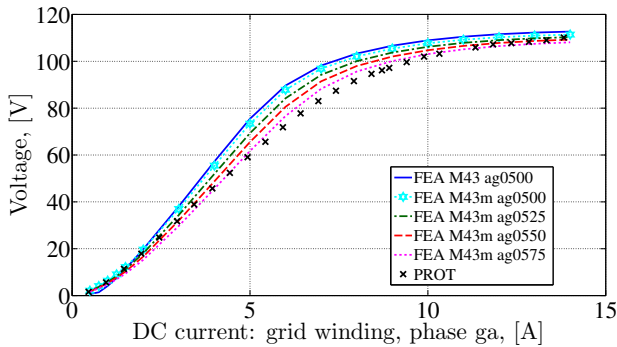
(a)  $L_{gmax}$ (b)  $V_{rms}$ 

Figure 8.20: Mutual inductance and RMS voltages calculated from the FEA considering the *M43m* material in the air-gap region.

The following remarks can be deduced:

- The modified air-gap has nearly no influence on  $I_{range}[B]$ , where the mutual inductance has its peak value.
- For region  $I_{range}[A]$ , the results are quite different. For the modified air-gap model, the prototype and the model have now very similar results. One possible interpretation for this result is that a much worst material in the air-gap region actually improves performance at low current levels. Next section analyses in details this argument.



### 8.4.2.3.6 The impact of the degraded material in the air-gap region on the short-circuit effect induced by the iron ribs

The iron ribs (bridges), as introduced in Section 7.1.3, induce a magnetic short-circuit in the air-gap region for low excitation levels. At this conditions, the highly permeable magnetic material at these points is not saturated and this effect reduces the mutual inductance.

However, considering the hypothesis of the modified air-gap due to the laser cutting process, the magnetic permeability of the  $M43m$  is much lower than the one of  $M43$ . Thus, the short circuit effect is greatly reduced on the modified model for low excitation (when the magnetic material is not saturated). To illustrate this effect, Fig. 8.21 shows the original and the modified air-gap FEA simulations for an excitation of  $I_{gaDC} = 1\text{ A}$  (at  $I_{range}[A]$ ). The flux lines in both figures have the same resolution.

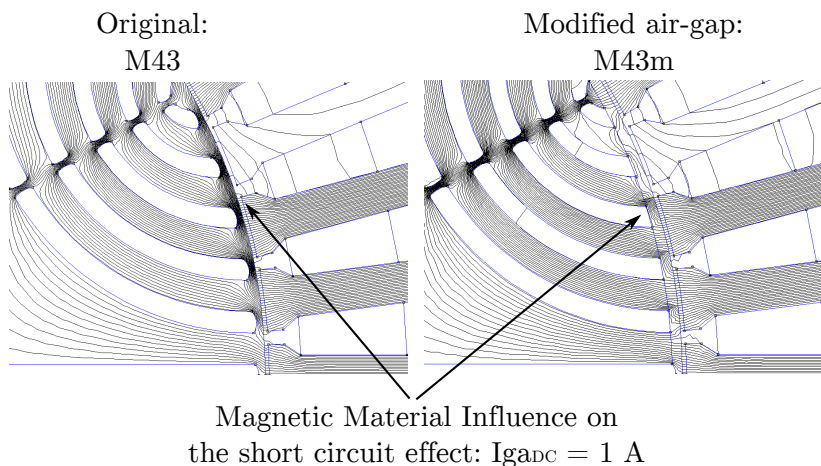


Figure 8.21: Original and modified air-gap models simulations for  $I_{gaDC} = 1\text{ A}$ .

Notice that, since the iron is much less permeable with the  $M43m$  material, the short-circuit effect is reduced in  $I_{range}[A]$  current range.

As previously observed in Fig. 8.20, the modified air-gap simulation has a limited influence at the  $I_{range}[B]$  current range. To investigate this, Fig. 8.22 shows the original and the modified air-gap FEA simulations for  $I_{gaDC} = 6\text{ A}$ . The flux lines in both figures have the same resolution.

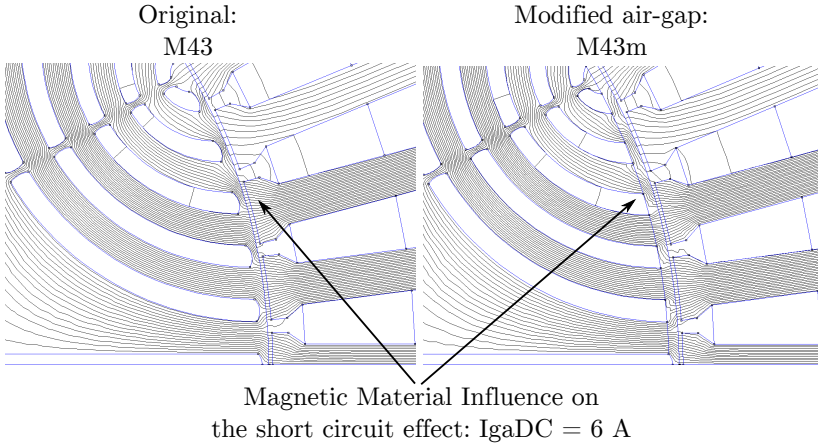


Figure 8.22: Original and modified air-gap models simulations for  $I_{gaDC} = 6 \text{ A}$ .

Fig. 8.22 shows that for the  $I_{range}[B]$  current range the modified air-gap FEA model has a reduced influence when compared to the  $I_{range}[A]$ . This is consistent with the results presented in Fig. 8.20.

This result is in accordance with the hypothesis on which the laser cutting process degrades the magnetic material in the air-gap region, since the prototype and model results are coherent among each other for the  $I_{range}[A]$ . A deteriorated rotor air-gap region would explain the differences in the initial range, where the short circuit effect is much more significant for lower currents. When the material in the iron bridges saturates at  $I_{range}[B]$  for the original FEA model, the differences between the models are not significant.

#### 8.4.2.3.7 Consideration of the limit case: using the DRI rotor to eliminate the iron bridges on the simulation

The influence of the air-gap region is evidenced if the limit case is considered, i.e. taking into account a rotor without the iron bridges. Fig 8.23 shows a FEA simulation considering the DRI rotor set with the nonlinear magnetic material *M43*. In this FEA calculation, the air-gap is kept at  $0.5 \text{ mm}$  for comparison.

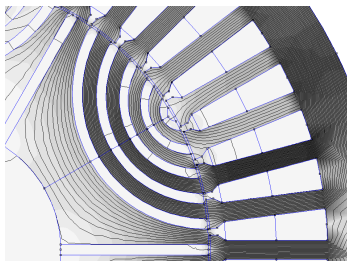


Figure 8.23: FEA simulation with the DRI rotor set with the nonlinear *M43* material for  $I_{gaDC} = 6$  A.

Fig. 8.24a and Fig. 8.24b shows the FEA results obtained for the mutual inductance and the induced open-circuit RMS voltage, respectively, for the modified air-gap model and for an ideal ducted rotor (DRI).

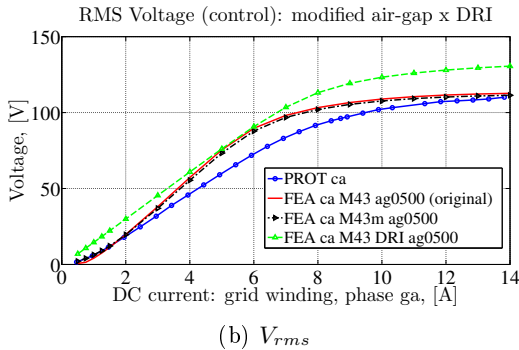
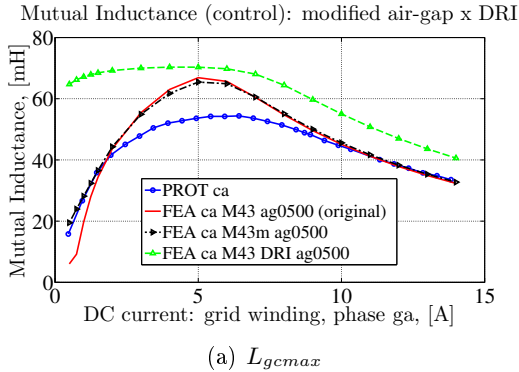


Figure 8.24: Mutual inductance and RMS voltages calculated from the FEA considering the *M43m* material and a DRI rotor in the air-gap region.

The influence of the iron bridges in the beginning of the magnetization curve at  $I_{range}[A]$  is straightforward to be noticed. As the iron bridges are absent in the DRI model, the mutual inductance has a nearly linear behavior up to region  $I_{range}[C]$ , where the machine starts to saturate. At the maximum value, around  $I_{gaDC} \approx 6 A$  at  $I_{range}[B]$ , the mutual inductance from the original, the modified air-gap and the DRI models are similar.

#### 8.4.2.3.8 Conclusions about the hypothesis of magnetic material degradation due to the laser cutting process

The results presented so far strongly indicates that the manufacturing process plays an important role on the prototype performance. It seems

that the laser cutting has degraded rotor performance and that this effect is the most likely explanation to the differences amid the models and experimental results for the initial part of the curve ( $I_{range}[A]$ ).

The difference on the  $I_{range}[B]$  is probably linked to the air-gap length as shown in Fig. 8.20a and in Fig. 8.20b. Even if the mechanical tolerance is limited to  $\pm 0.02$  mm, a possible explanation would be a further deteriorated magnetic material than the *M43m* in the rotor air-gap region. It is worth to recall that the *M43m* material was empirically defined. As the actual magnetic characteristics of this region is very hard (or even impossible) to determine, one could imagine many variations to this material to fit the prototype behavior. This is not, however, the goal of this discussion.

Just to give an example, from Fig. 8.20, the FEA simulation with an air-gap of 0.55 mm with the modified air-gap model nearly matches the prototype results. Even though an air-gap of 0.55 mm is beyond the original manufacturing tolerances, one could imagine an air-gap further deteriorated by the laser cutting process in the sense that, for the  $I_{range}[B]$ , the relative permeability of the magnetic material would be so low (approaching the permeability of the air) that the rotor would have a performance equivalent to an air-gap of 0.55 mm. As the width of the iron bridges are 0.8 mm, in the extreme case where the material would be so affected that it would approach the vacuum permeability  $\mu_0$ , the air-gap could be of up to 1.3 mm (0.5 + 0.8 mm). This is obviously not the case, but this example illustrate that an equivalent effective air-gap length of 0.55 mm would not be an impossible hypothesis considering material degradation due to the laser cutting process. A different material of the *M43m*, with much lower permeability at  $I_{range}[B]$  could further approximate the models results to the ones of the prototype.

Although this discussion is in a sense coherent to explain the discrepancies between models and the prototype, it is very hard to prove with the current prototype. Only a systematic study on the magnetic material properties that would take into account the laser cutting effect for very small widths, lower than 1 mm, could provide definitive conclusions. Such a study is beyond the scope of the thesis and this deeper investigation is proposed as a future work.

The main objective of this section was to present some possible hypothesis to the differences between models and prototype. It is clear that the manufacturing process could potentially impact machine performance and special attention should be given to the BDFRM rotor design. As a general design guideline, a solution which could reduce

the short circuit effects through the iron bridges is needed, eventually reducing or completely removing them. An optimized BDFRM rotor relies not only on the electromagnetic design, but also on the mechanical aspects and possibilities to improve robustness, whereas keeping satisfactory performance.

## 8.5 Final considerations

This chapter presented the characteristics of an optimization problem that has been defined using the GSOM-SAM to specify a BDFRM prototype. The experimental results obtained from this machine have been presented, focusing on the investigation of the flux modulation process by the reluctance rotor. The mutual inductance among the winding sets has been extensively investigated. Then, the simulation results obtained from the BDFRM models that have been developed in this thesis have been confronted to the experimental ones. Although the results were in a sense satisfactory to validate the models, there have been differences that demanded further investigation. A discussion on the most likely hypothesis have been performed, indicating the significant role of the manufacturing process on machine performance.

At this point, the modeling, implementation and validation of the models have been presented. The next and last chapter of this thesis illustrates with a case study the use of the proposed methodology to design a BDFRM by employing the GSOM-SAM and GSOM-MSRN for wind power applications.

## Chapter 9

# BDFRM design by using the proposed optimization procedure: a case study

### Abstract

*The goal of this chapter is to illustrate with a case study all the development stages in the BDFRM design procedure that has been proposed in this thesis. To remain consistent with the models already verified and validated with experimental results, a wind turbine with a power level compatible to the one of the prototype has been chosen in order to expose the development stages based on the tree modeling levels. The discussion starts by introducing the application requirements and defining the wind turbine that is supposed to be coupled to the BDFRM. Then, the use of GSOM-SAM and GSOM-MSRN in the design process is examined, focusing on the optimization models characteristics (number of constraints, time to convergence). A Pareto front strategy is used to analyze a multi-objective problem, where the objective functions are the total active mass and the efficiency. At the end, an optimal machine is chosen and the simulation results are verified by using FEA.*

## 9.1 Wind energy system overview: system topology

The main advantage of considering the BDFRM on wind power application is the possibility of using a partially-rated power converter (around 1/3 of total system capacity) which greatly reduces the converter cost. An additional advantage refers to the robust structure, without the need of brushes and slip rings as it is the case of the traditional Doubly-Fed Induction Machine (DFIG). The wind power system topology on which the BDFRM is considered is outlined in Fig. 9.1.

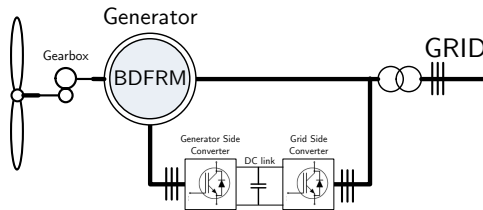


Figure 9.1: Variable speed, wind turbine topology with a Brushless Doubly Fed Reluctance Machine and a partial-scale power converter.

Based on this topology, the wind turbine and the BDFRM are specified in the following sections.

## 9.2 Wind turbine

### 9.2.1 Turbine power coefficient ( $C_p$ ) and tip-speed ratio ( $\lambda$ )

The wind turbine rotor performance is usually represented by the power coefficient  $C_p$ , which represents the ratio between the power available in the rotor and the power available in the wind [14]:

$$C_p = \frac{\text{Rotor power}}{\text{Power in the wind}} = \frac{P_{turbine}}{\frac{1}{2}\rho_{air}Av_{wind}^3} \quad (9.1)$$

where  $P_{turbine}$  is the power available in the rotor,  $\rho_{air}$  is the air density,  $A$  is the swept area by the blades and  $v_{wind}$  is the wind speed.

The theoretical maximum value of  $C_p$  is known as the Betz limit and it is given by (9.2). More realistic values of  $C_p$  for practical wind turbines falls within the range 25-45%.



$$C_{p,max} = \frac{16}{27} = 0.5926 \quad (9.2)$$

Another parameter used to characterize wind turbines is the tip-speed ratio ( $\lambda$ ), given by [15]:

$$\lambda = \frac{\omega R}{v_{wind}} \quad (9.3)$$

where  $R$  is the radius to tip of rotor and  $\omega$  is the rotational speed of rotor.

The power coefficient,  $C_p$ , and the tip-speed ratio,  $\lambda$ , are dimensionless and are used to describe the performance of any size of wind turbine rotor [15]. The  $C_p$  versus  $\lambda$  curve gives important information on turbine capability. A generic equation (9.4) can be used to analytically determine this relationship for a wind turbine [136]:

$$C_p(\lambda, \beta) = c_1 \left( \frac{c_2}{\lambda_i} - c_3\beta - c_4 \right) e^{-\frac{c_5}{\lambda_i}} + c_6\lambda \quad (9.4)$$

where  $\beta$  is the pitch angle and  $\lambda_i$  can be calculated by:

$$\frac{1}{\lambda_i} = \frac{1}{\lambda + 0.08\beta} - \frac{0.035}{\beta^3 + 1} \quad (9.5)$$

Coefficients  $c_1$ ,  $c_2$ ,  $c_3$ ,  $c_4$ ,  $c_5$  and  $c_6$  depends on the turbine aerodynamics and are empirically obtained.

## 9.2.2 The choice of the wind turbine: main characteristics

The prime mover that drives the generator shaft on this case study has been based on the commercially available Excel 1kW wind turbine from Bergey's<sup>1</sup> [137] since it matches the defined power level. The wind turbine characteristics have been obtained from manufacturer datasheet and are summarized in Table 9.1.

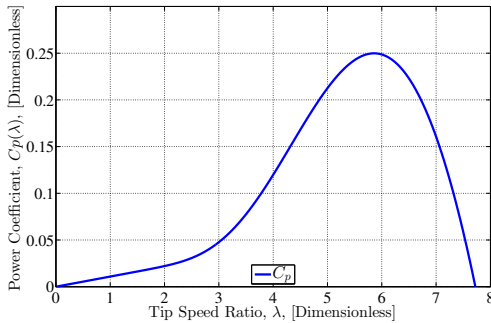
---

<sup>1</sup><http://bergey.com/products/wind-turbines/bergey-excel-1> Accessed on 27/03/2015

Table 9.1: Characteristics of Bergey's Excel 1kW Wind Turbine.

Rated Power	1 kW
Start-up wind speed	3 m/s
Rated wind speed	11 m/s
Furling wind speed	13 m/s
Rotor diameter	2.5 m
Rated rotor speed (without gearbox)	490 rpm

Based on manufacturer data, the  $C_p$  curve from Bergey's Excel 1 wind turbine has been analytically estimated by using (9.4). Fig. 9.2 depicts the result.

Figure 9.2: Estimated  $C_p$  curve for the wind turbine used as the reference.

To plot Fig. 9.2, the parameters listed in Table 9.2 have been used.

Table 9.2: Parameters used to plot the power coefficient  $C_p$  for the chosen turbine.

$c_1$	$c_2$	$c_3$	$c_4$	$c_5$	$c_6$	$\beta$
0.7105	250	0.4	25	26	0.010868	$0^\circ$

Fig. 9.2 clearly indicates that the  $C_p$  is maximum only for one specific value of  $\lambda$ . This means that there is an optimal operating point where the goal is to keep fixed the nominal value of  $\lambda$  defined when the  $C_p$  is maximum independently of wind speed. For the wind turbine depicted in Fig. 9.2, this point corresponds to  $C_{pmax} = 0.2498$  and  $\lambda_{C_{pmax}} = 5.856$ . From (9.3), it can be noticed that this maximum

power point extraction can be tracked by varying generator shaft speed. This kind of control is known as the Maximum Power Point Tracking (MPPT) and it represents the main interest on operating wind turbines at variable speed.

### 9.2.3 Maximum Power Point Tracking (MPPT) curve for the chosen turbine

The wind turbine power curve can be plotted as a function of the shaft speed for several wind speed as shown in Fig. 9.3.

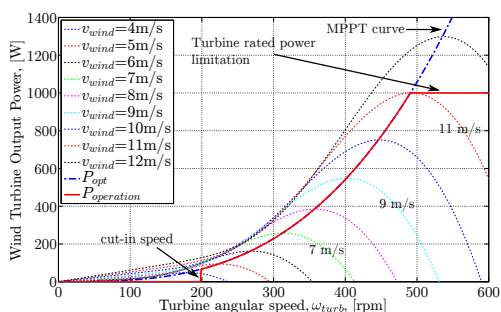


Figure 9.3: Power x speed for different winds.

The optimum curve for a Maximum Power Point Tracking (MPPT) control for this turbine is the one that connects the maximum points for each wind speed. It corresponds to the operation at maximum  $C_p$  and, from (9.1) and (9.3), it can be calculated by:

$$P_{turb} = K_{opt} \times \omega_{turb}^3 \quad (9.6)$$

where  $K_{opt} = \frac{1}{2} \times C_{pmax} \times \rho_{air} \times A \times \left( \frac{R}{\lambda_{C_{pmax}}} \right)^3 = 0.0073056$  for the chosen turbine.

In practice, the wind turbine cannot operate over the MPPT curve for all wind speed. When it reaches rated power, the power being converted is limited to protect the wind turbine and the electrical generator as illustrated in Fig. 9.3.

## 9.3 The BDFRM design procedure: constraints and operating points definition

### 9.3.1 Three modeling levels: GSOM-SAM, GSOM-MSRN and FEA

The goal of this section is to apply the proposed methodology based on three modeling levels to design a Brushless Doubly-Fed Reluctance Machine that fits the application requirements. Fig. 9.4, initially shown in Section 1.2.2.3, depicts the procedure.

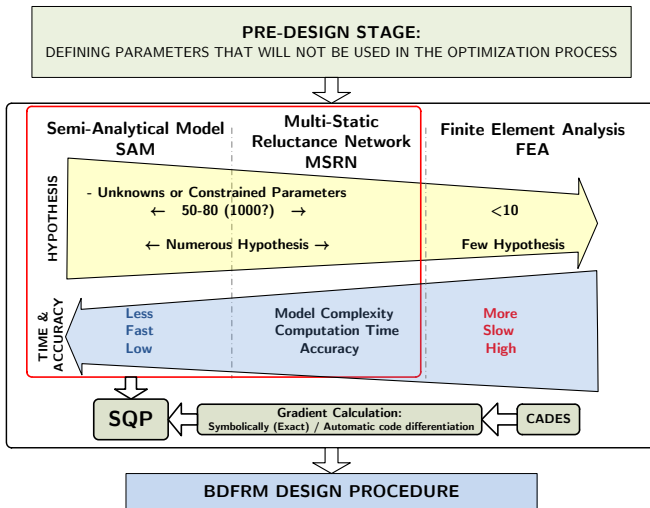


Figure 9.4: Proposed three modeling levels approach.

Based on the wind turbine characteristics previously discussed, the design constraints are set up and the development stages outlined in Fig. 9.4 are presented in the following sections.

### 9.3.2 Pre-design

The pre-design stage refers to the starting point, where the machine parameters that are considered fixed for the optimization studies are chosen. Chapter 2 introduced some pre-design guidelines, indicating the good and bad choices for the number of poles and slots combination. Although some other variation could be eventually used, to

remain consistent with the rest of this dissertation, the same parameters previously defined have been chosen and they are shown in Table 9.3.

Table 9.3: Fixed parameters (not considered in the optimization).

Parameter	Description	Value
$Nsl$	Number of stator slots	48
$Nslr$	Number of rotor slots	66
$P_g$	Number of poles of the grid winding	8
$P_c$	Number of poles of the control winding	4
$P_r$	Number of poles of the rotor	6

### 9.3.2.1 BDFRM rated speed definition

From the wind power system topology depicted in Fig. 9.1, it is assumed that the generator is operating connected to a power system at frequency 50  $Hz$ . Thus, from the machine operating principles, the choice of the number of poles implies through (9.7) that the synchronous speed, defined at  $f_c = 0$   $Hz$ , is 500  $rpm$  and the maximum speed, when  $f_c = 50$   $Hz$ , is 1000  $rpm$ .

$$\left. \begin{aligned} P_r &= \frac{P_g + P_c}{2} \\ \omega_{rm} &= \frac{\omega_g + \omega_c}{P_r} \end{aligned} \right\} \text{Positive case} \quad (9.7)$$

From the BDFRM speed range, from 0 up to 1000  $rpm$ , it would be possible to directly couple it to the wind turbine without gearbox since the latter is rated at 490  $rpm$ . However, if we analyze the BDFRM power expressions, presented in Section 1.2.3.2, it can be concluded that the best operating angular speeds with respect to efficiency are in the supersynchronous range (i.e. from synchronous up to maximum speed). The relationship among the real power at each winding set can be written in terms of the slip<sup>2</sup> as:

$$P_{3\phi c_{int}} = -sP_{3\phi g_{int}} \quad (9.8)$$

<sup>2</sup>In the BDFRM, the slip is defined as  $s = -\frac{\omega_c}{\omega_g}$

Equation (9.8) indicates that, below synchronous speed, the machine efficiency is reduced because some of the real power is just taken from grid winding and returned back to the power system via the secondary incurring in losses along the way [57].

The decision on using or not a gearbox is application dependent. Since the goal of this chapter is to illustrate the proposed BDFRM design procedure rather than providing an ultimate response for this choice, the generator rated angular speed is defined at 750 rpm because it is more favorable to the BDFRM operation. This implies in a control winding frequency of  $f_c = 25 \text{ Hz}$ . Then, the internal real power at this operating point at the control winding is half of the real power at grid winding ( $P_{c3\phi} = \frac{1}{2}P_{g3\phi}$ ) and 1/3 of total power being converted by the system. Therefore, in order to couple the wind turbine rated speed (490 rpm), defined in Table 9.1, to the generator rated speed, a gearbox with ratio 1.53 is considered.

### 9.3.2.2 BDFRM rated power definition

The generator rated power is based on wind turbine specifications. According to the manufacturer datasheet, the turbine can reach a peak power of nearly 1200 W [137]. To be able to eventually withstand this additional power, the BDFRM rated power is defined to 1200 W. At rated speed (750 rpm), this implies in a torque of 15.28 Nm.

### 9.3.2.3 Constraints and operating points definition (OP)

In variable speed wind power applications, the generator speed range is usually limited in the range  $\pm 30\%$  around rated speed since a fractionally rated converter can then be employed [49, 57, 70]. Assuming that the machine operates the majority of the time within this range, it is possible to define three essential operating points (OP) for BDFRM variable speed operation and they are summarized in Table 9.4.

Table 9.4: Operating points (OP) definition.

	Symbol	OPm30	OPrated	OPp30
Torque [Nm]	$T_{em}$	15.28	15.28	11.46
Total real power [W]	$P_{out_{3\phi}}$	800	1200	1200
Grid frequency [Hz]	$f_g$	50	50	50
Control frequency [Hz]	$f_c$	0	25	50
Speed [rpm]	$\omega_{rm}$	500	750	1000
Slip	$s$	0	-1/2	-1
Grid real power [W]	$P_{out_{3\phi g}}$	$\approx$	$\approx 2/3 \times P_{out_{3\phi}}$	$\approx 1/2 \times P_{out_{3\phi}}$
Control real power [W]	$P_{out_{3\phi c}}$	$\approx 0$	$\approx 1/3 \times P_{out_{3\phi}}$	$\approx 1/2 \times P_{out_{3\phi}}$

From “OPm30” (500 rpm) up to “OPrated” (750 rpm) the machine is specified to be capable of producing constant rated torque. With respect to the wind turbine operation, the control system works in MPPT mode, tracking the maximum power extraction efficiency. From “OPrated” up to “OPp30” (1000 rpm) the machine output power is limited to 1200 W and the BDFRM operates in field weakening mode, reducing proportionally the torque capability in terms of generator speed.

Table 9.4 highlights the fact that, under these conditions, the power converter rating connected to the control winding can be half of total real power system capacity (the worst case is at “OPp30”)<sup>3</sup>. To better illustrate the wind power generating system formed by the turbine and the BDFRM, Fig. 9.5 and Fig. 9.6 shows, respectively, the resulting power the torque curve characteristics.

<sup>3</sup>The converter rating could be further reduced if the generator output power requirement at 1000 rpm were decreased. At this speed level the wind turbine is already above rated speed and the furling system is actuating to reduce the available power in the shaft

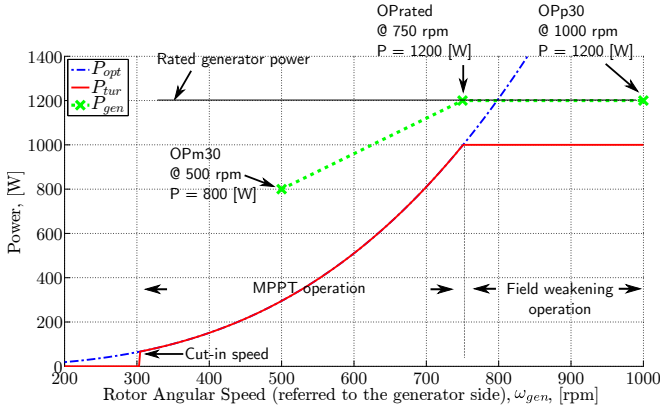


Figure 9.5: Power characteristics.

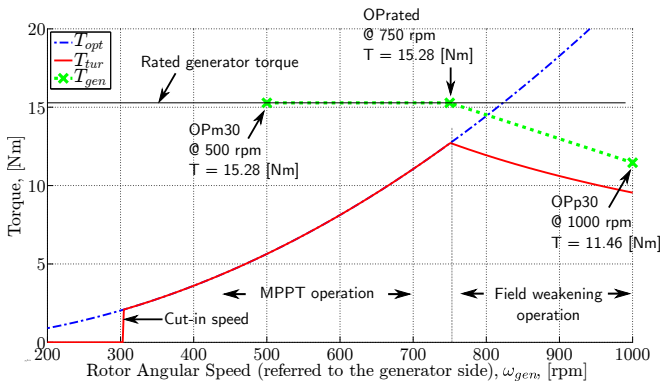


Figure 9.6: Torque characteristics.

### 9.3.3 General optimization constraints

The discussion presented so far allows to define the optimization constraints based on the machine operating points. Additionally, some others design constraints must be set. These constraints refers to electrical and mechanical limitations such as the output voltages, current densities, maximum allowed flux density and minimum stator teeth width. Table 9.5 summarizes these design requirements that are used as constraints in the optimization problem.



Table 9.5: BDFRM specifications used as constraints.

Description	Value
Rated Power @ 750 rpm [W]	-1200
Rated Torque @ 750 rpm [Nm]	-15.28
Rated Power @ 500 rpm [W]	-800
Rated Torque @ 500 rpm [Nm]	-15.28
Rated Power @ 1000 rpm [W]	-1200
Rated Torque @ 1000 rpm [Nm]	-11.46
Grid Winding Phase Voltage [ $V_{rms}$ ]	128
Control Winding Phase Voltage Range [ $V_{rms}$ ]	0-128
Grid Winding Frequency [Hz]	50
Torque angle (generating)	90 °
Maximum allowed current density [ $A/mm^2$ ]	3.5
Maximum Specific Electric Loading [ $A/mm$ ]	32000.0
Maximum allowed flux density on iron [T]	1.6
Maximum Slot Filling Factor	0.35
Minimum stator teeth width [mm]	4.00

### 9.3.4 The use of the Pareto front strategy to assess contradictory objectives

In this work, two main objective functions are used to set the optimization problem and design the BDFRM: minimize the mass and maximize efficiency. Since these are contradictory objectives, a Pareto front strategy is used to find the best trade-off among them<sup>4</sup>.

For all the optimizations presented in the sequence, the Pareto front is calculated by using the following procedure:

With the input/output constraints set, two optimizations are run:

- (i) Mass minimization with no constraint on the efficiency (“Min-Mass”);
- (ii) Efficiency maximization with no constraint on the total active mass (“MaxEff”).

Steps (i) and (ii) allows to define the two Pareto Front extremities. Then, the objective function is set to minimize the total active mass

<sup>4</sup>This is not a limitation, since all the output parameters could be a candidate to be further explored in a Pareto sense to define an optimized design (e.g. Power Factor, torque density, etc.).

for the discretized values of the efficiency within the two Pareto Front extremities by using the SQP algorithm.

## **9.4 The use of GSOM-SAM in early design stages to define a “first-cut” design**

The first step in the design procedure is to use GSOM-SAM to define a “first-cut” machine that respect all the constraints. In order to define this initial design, two objective functions are explored: minimize the mass and maximize efficiency, whereas keeping in both cases the output torque constant. This initial optimization is performed only for “OPrated” at 750 rpm.

### **9.4.1 GSOM-SAM optimization results: Pareto front to identify the best trade-off between total active mass and efficiency at rated conditions**

#### **9.4.1.1 Model characteristics**

The GSOM-SAM used in this case study is essentially the same as the one discussed in Appendix D for specifying the prototype. The differences are in the degrees of freedom, since some dimensions that have been fixed on that case to fit a specific frame are now variable inputs (e.g. stator external diameter, shaft diameter, axial length, wire diameter *etc.*). Fig. 9.7 summarizes the optimization problem characteristics.

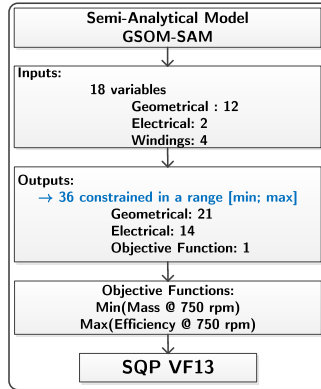


Figure 9.7: GSOM-SAM characteristic for the case study

The GSOM-SAM has been implemented in CADES and an icar component (model and Jacobian matrix) has been generated with 18 inputs that are left free to vary within a range. Regarding the outputs, 36 have been constrained in a range in the form  $MIN < output < MAX$  resulting in 72 constraints in total. The constrained outputs refers to geometrical and electrical parameters, as well as one objective function. For a complete list of the optimization constraints refer to Appendix E.1.

#### 9.4.1.2 GSOM-SAM Pareto front: total active mass *versus* efficiency

The Pareto front obtained with the GSOM-SAM at rated speed 750 rpm is presented in Fig. 9.8.

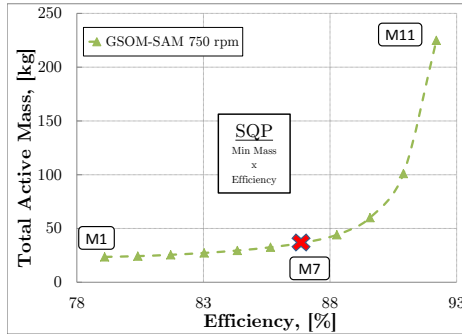


Figure 9.8: GSOM-SAM Pareto front Mass versus Efficiency at rated conditions.

Fig. 9.9 depicts the three machines highlighted in Fig. 9.8 on the Pareto front to assess the external dimensions evolution in terms of the required efficiency.

### GSOM-SAM machines on the Pareto front

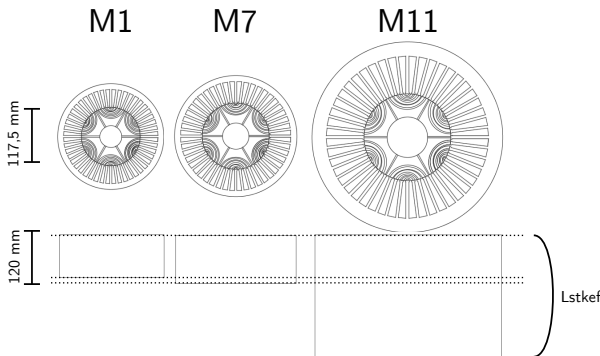


Figure 9.9: GSOM-SAM Pareto front Mass versus Efficiency at rated conditions: resulting machines.

#### 9.4.2 The chosen “first-cut” machine design using the GSOM-SAM to be further explored

The Pareto front allows to analyze two opposing objectives and provide means to the designer to choose the best trade-off among them.

From Fig. 9.8, machine number 7 has been chosen, since a considerable gain in efficiency is obtained without compromising the mass constraint. The resulting values of this machine design can be found in Appendix E.1.3.

## 9.5 Refining the design: GSOM-MSRN to obtain accurate results whereas using deterministic optimization

### 9.5.1 GSOM-MSRN optimization results: Pareto front to identify the best trade-off between total active mass and efficiency at rated conditions

#### 9.5.1.1 Model characteristics

The GSOM-MSRN aims to further refine the “first-cut” design obtained by using the GSOM-SAM. This initial machine is used as the starting point for the optimization problem set up in the GSOM-MSRN. The model is compiled and coupled by Cades to the SQP optimization algorithm. Fig. 9.10 depicts its main characteristics regarding the input/output constraints. It has 21 variable inputs and 36 constrained outputs.

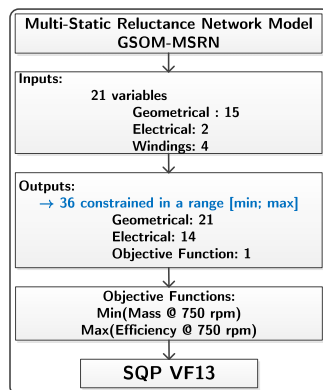


Figure 9.10: GSOM-MSRN characteristic for the case study.

### 9.5.1.2 GSOM-MSRN Pareto front: total active mass *versus* efficiency

The Pareto front obtained by using the GSOM-MSRN for “OPrated” is presented in Fig. 9.11. For comparison purpose, the Pareto front previously obtained with the GSOM-SAM is also shown.

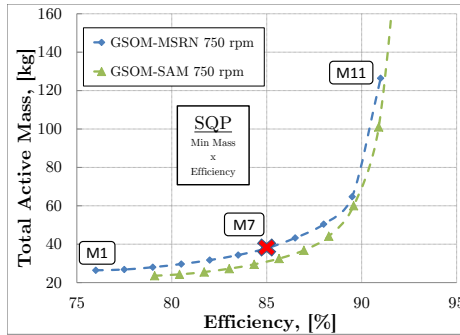


Figure 9.11: GSOM-MSRN Pareto front Mass versus Efficiency at rated conditions.

It is possible to remark that the Pareto Front for GSOM-SAM is slightly shifted to the right when compared to the GSOM-MSRN. As the models use different principles to calculate their outputs, some divergence is expected. Nevertheless, from this comparison, it is clear that both models present the same *tendency* regarding mass and efficiency.

Fig. 9.12 illustrates the highlighted machines in Fig. 9.11 on the GSOM-MSRN Pareto front. It is possible to realize the changes in machine external dimensions in terms of the efficiency constraint.

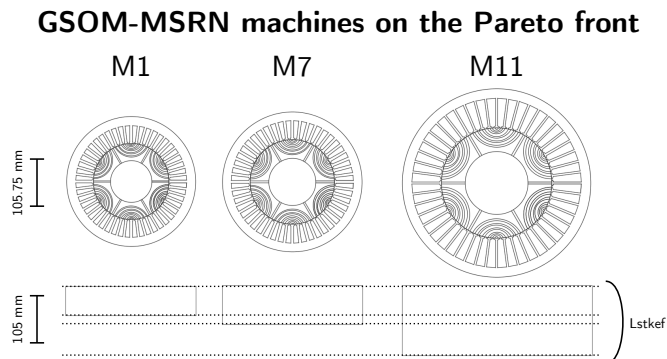


Figure 9.12: GSOM-MSRN Pareto front Mass versus Efficiency at rated conditions: resulting machines.

### 9.5.1.3 The chosen machine design for rated conditions at 750 rpm

Considering Fig. 9.11, one interesting choice that presents a good trade-off between Mass and Efficiency is machine number 7. The resulting values of this machine design can be found in Appendix E.2.

## 9.5.2 GSOM-MSRN optimization results: Pareto front to identify the best trade-off between total active mass and efficiency for the three operating points solved simultaneously

### 9.5.2.1 Model characteristics

Up to now, only BDFRM operation at rated conditions at 750 rpm has been considered in the design. The chosen machine number 7 from Fig. 9.11, for example, is optimal only at OPrated.

An alternative way to find the best machine by optimization for all operating points (OP) defined in Table 9.4 is to solve all of them simultaneously. This leads to a unique design that satisfies the all the optimization constraints for the 3 OP at the same time. Obviously, this procedure increases model complexity, number of constraints and computation time, especially if using the MSRN with multi-static calculations. To illustrate the problem, Table 9.6 presents a comparison between MSRN characteristics that considers one or three operating points simultaneously. There are 64 outputs constrained in a

range (128 in total) for 3 OPs against 36 (72 in total) with only 1 OP. Notwithstanding, the use of a deterministic optimization algorithm and analytical/semi-analytical approaches makes this a reasonable task.

Table 9.6: MSRN characteristics: models with one or three operating points.

	<b>MSRN OP</b>	<b>1 MSRN 3 OP</b>
<b>Total Nr of Variable Inputs</b>	<b>21</b>	<b>25</b>
Geometrical	15	15
Electrical	2	6
Windings	4	4
<b>Total Nr of Constrained Outputs in a range</b>	<b>36</b>	<b>64</b>
Geometrical	21	21
Electrical	14	42
Objective Function	1	1

### 9.5.2.2 Global efficiency equation at the 3 OP

To perform this last optimization refinement by solving the 3 OPs simultaneously, a global efficiency equation has been defined:

$$\text{Global Efficiency} = K_A \times \eta_{500rpm} + K_B \times \eta_{750rpm} + K_C \times \eta_{1000rpm} \quad (9.9)$$

where  $\eta$  indicates the efficiency constraint at each operating point and the coefficients  $K_A$ ,  $K_B$  and  $K_C$  provides the weight that one wishes to give for machine operation at the specific OP. Their sum is  $K_A + K_B + K_C = 1$ .

One possible way to determine  $K_A$ ,  $K_B$  and  $K_C$  values is assessing the wind probability at each one of the speeds. In this work, the following values have been used:  $K_A = 0.6$ ,  $K_B = 0.3$  and  $K_C = 0.1$ . This choice roughly indicates that, in the majority of the time, it is assumed that the wind drives the generator within the range from 500 rpm up to 750 rpm (the speeds are referred to the generator side).



### 9.5.2.3 GSOM-MSRN Pareto front: total active mass *versus* global efficiency for 3 OP

To perform this optimization, machine number 7 defined in Fig. 9.12 is used as the starting point. The Pareto front considering the three operating points simultaneously and the global efficiency equation is presented in Fig. 9.13.

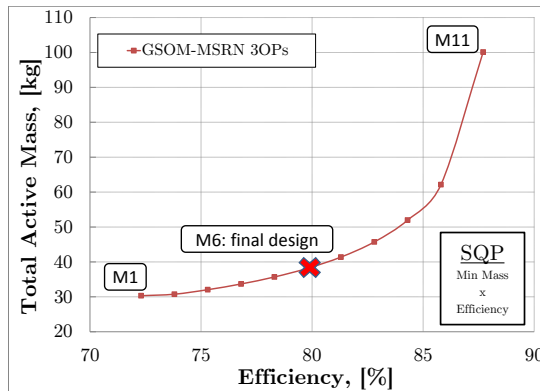


Figure 9.13: GSOM-MSRN Pareto front Mass versus Global Efficiency at 3 OP simultaneously.

Fig. 9.14 shows the resulting machines on the Pareto front.

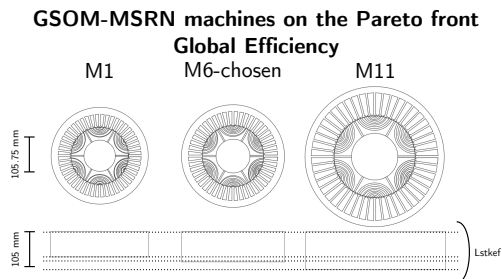


Figure 9.14: GSOM-MSRN Pareto front Mass versus Global Efficiency at 3 OP simultaneously.

### 9.5.2.4 The BDFRM final design

The total active mass *versus* global efficiency Pareto front depicted in Fig. 9.13 allows to define the best trade-off among these contradictory objectives. Therefore, machine 6 is chosen because it provides a reasonable global efficiency according to (9.9) whereas not spending too much in total active mass. Additionally, this machine satisfies all constraints from Table 9.5 at the three operating points. The resulting values of BDFRM final design can be found in Appendix E.3. Table 9.7 illustrates its main parameters.

Table 9.7: BDFRM final design: main characteristics.

Stator External Diameter		307.36 mm
Stator Internal Diameter		183.36 mm
Effective Axial Length		85.85 mm
Grid winding total number of turns		240
Control winding total number of turns		200
Air gap length		0.5 mm
Number of stator slots		48
Number of rotor ducts		66
Number of poles Grid/Control/Rotor		8/4/6
Yoke width		20.1 mm
Yoke to stator tooth ratio		3.43
Control Winding Peak Current	OPm30	5.23 A
Grid Winding Peak Current	OPm30	8.46 A
Control Winding Peak Current	OPrated	4.75 A
Grid Winding Peak Current	OPrated	8.22 A
Control Winding Peak Current	OPp30	3.28 A
Grid Winding Peak Current	OPp30	8.14 A

## 9.6 Verifying optimization results with the reference model: finite element analysis (FEA)

The last part of the procedure is to test and verify the optimization results by using the reference FEA model. The BDFRM final design depicted in Table 9.7 is used for that purpose. The electromagnetic parameters that are considered for this analysis are the air-gap flux

density, the induced phase voltages and the instantaneous torque at rated conditions. The simulations consider the three models (GSOM-SAM, GSOM-MSRN and FEA). They are presented in the sequence only for the “OPrated” at 750 rpm for simplicity, since a complete model verification procedure has been previously presented.

### 9.6.1 Air-gap flux density

Fig. 9.15 depicts the air-gap flux density. It can be inferred that the resulting machine designed with the MSRN model accurately matches the FEA simulation, except for the high frequency slotting effect calculated by the latter.

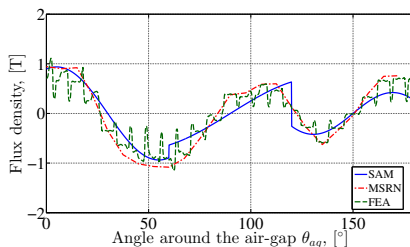


Figure 9.15: Air gap flux density  $B_{gap}$  at OPrated: 750 rpm.

### 9.6.2 Phase voltages at rated conditions

Similar conclusions can be deduced for the induced phase voltages at rated conditions. Fig. 9.16 presents the results for the grid and control winding voltages. Since the simulation is performed at 750rpm, it can be notice the difference in frequency among the waveforms, since, at this speed,  $f_g = 50 \text{ Hz}$  and  $f_c = 25 \text{ Hz}$ .

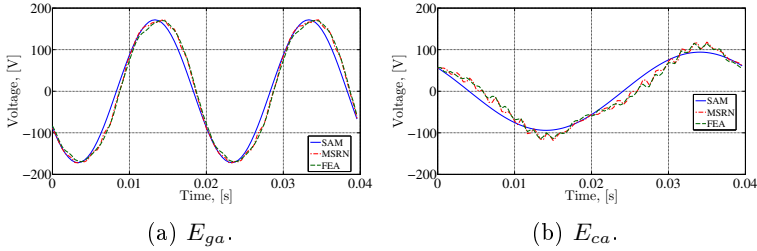


Figure 9.16: Induced phase voltage  $E_{ga}$  and  $E_{ca}$  at OPrated: 750 rpm.

### 9.6.3 Instantaneous torque at rated conditions

The last simulation that is presented is the induced electromagnetic torque in Fig. 9.17. Notice that its value is negative, since the machine is operating as a generator. The MSRN provides a good representation of this parameter, except for the high frequency slotting effect that is remarked in the FEA waveform.

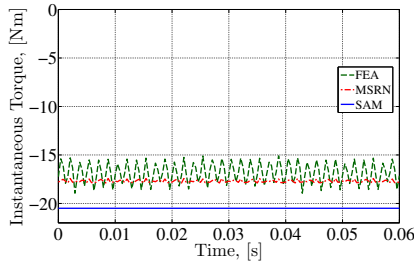


Figure 9.17: Instantaneous electromagnetic torque at OPrated: 750 rpm.

It can be concluded from the comparisons among the three modeling levels that the BDFRM final design optimized by using the GSOM-MSRN presents precise results when compared to FEA for the global performance parameters such as voltages and torque.

## 9.7 Simulation time comparisons among the three modeling levels

The procedure based on the three modeling levels approach is based on the premise that the SAM is very fast and the MSRN provides a

good trade-off among precision and computation time. To give some insight about the time spent in the optimization process, Table 9.8 outlines a comparison among the optimization models discussed in this chapter. The calculations have been performed in an Intel Core i7 4770 @ 3.40 GHz, 8 GB RAM.

Table 9.8: Optimization time and number of iteration (iter) comparison between models.

	SAM		MSRN “OPrated”		MSRN 3 OP	
	Iter	Time	Iter	Time	Iter	Time
(i) Min-Mass	38	50 s	21	5043 s	12	4669 s
(ii) MaxEff	48	53 s	34	7443 s	18	6747 s

Table 9.8 reinforces the assumptions made. The GSOM-SAM takes less than a minute to provide the final result. Therefore, it can be used in early stages to test many design variations when highly accurate results are not necessarily required. Then, SAM results are used as the starting point for the GSOM-MSRN model. Notice that the number of iterations has been slightly reduced in the latter, probably because the starting values have been firstly optimized by SAM and they are closer to the solution. The GSOM-MSRN takes from 1h30min up to around 2h to converge. This is because, for each iteration, 96 multi-static calculations are performed for the “OPrated” operation point at 750 rpm. Once the best design calculated by using the GSOM-MSRN for rated conditions is chosen, its parameters are used as the initial values for the 3 OP optimization. The number of iteration is further reduced and the optimizer takes from 1h up to 2h to converge. When 3 OP are considered, 192 multi-static calculations are performed (96 for “OPrated” at 750 rpm, 32 for “OPm30” at 500 rpm and 64 for “OPp30” at 1000 rpm). In any of the cases, the optimization times are reasonable, especially for the MSRN 3OP case, where a constrained input/output problem with more than a hundred constraints are taken into account to solve the optimization problem.

## 9.8 Final Considerations

This chapter presented a case study that applies all the development stages in the BDFRM design procedure proposed in this thesis. For that purpose, it has been considered a low power wind turbine. Nevertheless, the methodology is general and could be used for designing *a priori* a machine at any power level. Regarding the models, especially for the GSOM-MSRN, it could be necessary to perform minor modifications in order to take into account differences in the magnetic circuit that eventually may be necessary for high power machines (for example eliminating the rotor iron ribs). The application of the design procedure for a high power machine (e.g. 2MW) is proposed as a future work.

The methodology starts by the definition of the application requirements and, based on that, the BDFRM design constraints are defined. A Pareto front strategy is used throughout the chapter to identify the best trade-off among the total active mass and the machine efficiency for all the optimizations.

Following the design procedure, some optimizations using the fast GSOM-SAM are performed. A “first-cut” design is defined and used as the starting point for the GSOM-MSRN model. The optimization performed with the GSOM-MSRN yields an optimal machine at rated conditions. However, since the machine operates in variable speed application, this design is further refined by assuming a global efficiency constraint that takes into account simultaneously three operating points. Then, one machine on the Pareto front of the GSOM-MSRN with 3 OP is chosen as the BDFRM final design and it is verified by using the reference FEA model.

It can be concluded from the comparisons among the three modeling levels that the BDFRM final design presents highly accurate results when compared to FEA. This highlights the powerful capability of the developed models coupled to optimization to solve a constrained input/output optimization problem by using the SQP deterministic algorithm.

General Conclusion  
&  
Perspectives





# General Conclusion and Perspectives

## General Conclusions

This thesis is inserted in the context of wind power applications. The outlined approach to develop it was to identify and study a cost-effective and robust electrical generator solution that can be potentially used to replace the Doubly-Fed Induction Generator (DFIG) in the system topology that uses a fractionally rated power converter. Based on a literature review, the Brushless Doubly-Fed *Reluctance* Machine (BDFRM) has been chosen as the electrical generator to be investigated.

Two major bottlenecks have been identified for this research:

1. to master BDFRM optimized design;
2. to assess the advantages and drawbacks of the BDFRM with respect to other solutions in wind power comparing the system solution as a whole.

From this initial investigation, it has been defined as the main objective to assess and contribute on the solution of bottleneck 1, by proposing a BDFRM design procedure based on a deterministic optimization approach.

The first part of this thesis, presented in Chapter 1, refers to a literature review on wind power generating systems, focusing on the application requirements, market trends and technological issues for the different system topologies. The BDFRM basic operating principles and its use on this kind of application have been discussed.

The second part depicts the BDFRM electromagnetic modeling aspects. Firstly, the criteria to choose the design parameters that are

fixed in the optimization process are discussed in Chapter 2. This allowed to define the BDFRM structural topology that has been used throughout the thesis to develop the models, the prototype and the optimization studies. Once the main parameters of the topology are chosen, the global electromagnetic models (GEMM) are presented. Chapter 3 introduces the first model to be used in the BDFRM design process, the Semi-Analytical Model (SAM). The SAM is a linear model that relies on the equivalent electric circuit approach to calculate the electromagnetic output parameters of the BDFRM. Then, Chapter 4 depicts the second model, the Multi-Static Reluctance Network (MSRN) model. The MSRN is based on a reluctance network approach that is capable of performing multi-static simulations. This chapter introduces a computationally efficient strategy that uses a symmetry principle to take into account rotor movement and effectively perform multi-static calculations. To finalize the BDFRM modeling, Chapter 5 shows the complementary Additional Sizing Equations (ASE). The ASE are used to calculate geometrical and output performance parameters that are required for designing the BDFRM. The phase resistances, the iron losses estimation, Carter's factor, leakage inductances, apparent power expressions and efficiency calculation are some examples of the ASE that are discussed in this chapter.

Once the BDFRM modeling aspects have been presented, the third part of the thesis explains how the models have been implemented in order to be used in an optimization context. It also presents the simulation results, comparing the SAM and MSRN performance outputs to the ones obtained with the reference Finite Element Analysis (FEA) model. In Chapter 6, the SAM and the MSRN are coupled to the ASE to form the Global Sizing and Optimization Models GSOM-SAM and GSOM-MSRN. The software CADES and Reluctool have been used to implement these models because they can exactly calculate the model gradients, either symbolically or by automatic code differentiation, providing means to couple them to the SQP optimization algorithm. The limitations of the software tools and the proposed solution to perform the multi-static calculations of the MSRN model due to the management of source rotation have also been discussed. Then, the simulation results obtained with the GSOM-SAM and the GSOM-MSRN are confronted to the equivalent ones obtained with 2D Finite Element Analysis (FEA) simulations in Chapter 7. From this verification, it can be concluded that the SAM has a limited accuracy level and it is recommended to be used in early design stages, where the designer is most interested in fast computation times to test many design varia-

tion than in obtaining the results with the highest possible accuracy. The MSRN, on the contrary, presents remarkably precise results when compared to FEA, yielding a very interesting trade-off among accuracy and computation time.

The fourth part is dedicated to the presentation of the prototype that has been developed in this thesis by using an optimization approach and this is discussed in Chapter 8. By the time the prototype was specified, the GSOM-MSRN was not yet operational and the proposed BDFRM design procedure could not be fully applied. Thus, only the GSOM-SAM has been used to specify it and the optimization problem used to perform this task is outlined in this chapter. Then, the experimental results obtained from this machine have been presented, focusing on the investigation of the flux modulation process by the reluctance rotor, especially the mutual inductance among the winding. The simulation results obtained from the BDFRM models have been confronted to the experimental ones. Although the results were in a sense satisfactory to validate the models, there have been differences that demanded further investigation. A discussion on the most likely hypothesis for that has been performed, indicating the significant role of the manufacturing process on machine performance. Also, of special concern was the effect of the rotor iron bridges that induces a sort of magnetic short-circuit when they are not saturated. An improved rotor design should provide means to mitigate their degrading effects and, at the same time, guarantee the required mechanical robustness.

The fifth and last part recalls the thesis proposal and presents through a case study the complete design procedure based on the three modeling levels (GSOM-SAM, GSOM-MSRN and FEA). Starting from the application requirements, the methodology is applied and the final design is refined step by step by using the developed BDFRM models. The optimization goal is defined as a multi-objective problem, where the objective functions are the total active mass minimization and efficiency maximization. Since these are contradictory objectives, a Pareto front strategy is applied in order to define the final optimal design for that specific application. From this case study, it can be concluded that the obtained the BDFRM final design presents highly accurate results when compared to FEA, highlighting the powerful capability of the developed models coupled to optimization to solve a constrained input/output optimization problem by using the SQP deterministic algorithm.

The proposed BDFRM design procedure in this thesis is valid for any power level. Regarding the models, they have been verified by

using a low power prototype (1kW), but there is no restriction *a priori* on using them for designing higher power machines. For that purpose, it may be eventually necessary, however, to adapt them by performing minor modifications, especially in the static reluctance network, to take into account differences in the magnetic circuit that may exist (for example, by eliminating the rotor iron bridges).

The power level on which the prototype has been specified is not, *a priori*, the best option for the BDFRM compared to other generator technologies. The greatest interest on using a system topology with a reduced scale power converter is in the high power range, where the cost of the involved power electronics are an important part of the total system cost. The most logical application of the BDFRM would be in high power turbines, since at this power level the converter cost is very significant. For low power wind turbines, the use of permanent magnet machines are usually preferred due to the higher torque density that one can obtain. However, one could eventually also think about the use of the BDFRM for small wind turbines. Since the converter costs can be reduced and the use of permanent magnets avoided, the overall solution cost could be advantageous for the BDFRM, even if the machine itself will most likely have a greater volume.

Notwithstanding, this discussing recalls bottleneck 2, that states that the advantages and drawbacks of the BDFRM with respect to other solutions in wind power should be assessed comparing the system solution as a whole. The definition of the best solution for a specific application must take into account many factors, among them:

- Application power level;
- Power electronics costs;
- Availability and costs of raw materials (permanent magnets, for example);
- Manufacturing, operation and maintenance costs;
- System robustness;
- The use or not of a gearbox;
- Generator torque density;
- System efficiency.

The conclusion about the best solution considering simultaneously all these elements and others is not obvious. This thesis focused in the first part of the study: contribute on the development of a design procedure in order to define an optimal BDFRM for a specific application. This initial study must be further pursued, analyzing the wind power generating system as a whole and comparing different technologies. Up to this date, it can be said that the BDFRM is potentially a good candidate to be used in wind power systems, but the technical and economical aspects on this choice must be still assessed and compared to different solutions.

The investigation of bottleneck 2 is out of the scope of this thesis. This discussion allows us to state the perspectives of this research.

## Perspectives

The results obtained with this thesis allow to outline some interesting perspectives to pursue further the investigation on the use of the BDFRM on wind power generating systems as follows.

### **To address bottleneck 2**

The first study that is placed in perspective is the investigation of the BDFRM advantages and drawbacks when compared to other solutions. This thesis developed the BDFRM modeling basis that can be applied to compare it to different solutions within the same framework. Assuming that similar models are available for the other relevant machines, a Pareto front strategy is suggested to evaluate the distinct technologies. Thus, induction, permanent magnet and reluctance machines could be effectively compared within the context of wind power generation, providing an interesting basis for taking decision about the best solution.

### **Improve the losses model and include a thermal model**

As it has been discussed in Section 5.3.1.2, the modeling of the iron losses are a quite difficult task in any electromagnetic device and this task is even harder on the BDFRM due to the different frequency/pole numbers nature of the machine. The study of iron losses in the BDFRM is likely to generate a thesis by itself and refinements on the modeling of the losses are proposed as a future research. Additionally, it would be interesting to complement the losses model with a thermal model,

capable of estimating the temperature rise in the machine in terms of excitation conditions.

## **Integrate the pre-design stage in the optimization process**

In the proposed design procedure, the pre-design stage defines the machine structural topology by determining the number of stator and rotor slots and the number of the poles in the windings. One study that is proposed in perspective is the integration of the pre-design stage into the optimization process, in which these parameters are not fixed. A higher number of poles combination could, for example, eliminate the need of a gearbox to connect the generator to the wind turbine, depending on rated speed of the latter.

## **Consideration of control aspects on the optimization**

The torque angle has been considered fixed at  $\phi_{torque} = \pm 90^\circ$  in all the optimizations that have been performed (the  $\pm$  signal specifies motoring or generating operation). This condition implies that the machine is operating at the maximum torque per amperes condition. However, this is not necessarily the best operating point for the machine, especially if the power factor constraints are considered [57]. Vector control techniques associated to the design process are proposed to be investigated in a future work.

## **Specify a high power 2MW machine by using the proposed design procedure**

Another interesting study that is proposed in perspective is the use of the BDFRM design procedure to specify a high power 2MW machine. Wind turbines on this power level are found in large generating parks and such study could provide a better insight on the validity of the developed models for designing BDFRM machines at this power level. A reference for this study is [8].

## **Utilization of different optimization algorithms**

The optimization models have been coupled exclusively to the Sequential Quadratic Programming (SQP) deterministic optimization algorithm because it allows to manage many constraints in the design

process. As discussed in Section 1.4.3.4.1, the optimized solution of this kind of algorithm are dependent on the initial values and it may eventually be trapped by a local minimum. The proposed optimization technique depicted in this thesis could be further improved by using an hybrid algorithm as introduced in Section 1.4.3.4.3. Hybridization may be one suitable alternative to take full advantage of fast computation time and capacity to deal with many constraints of the deterministic type, whereas introducing an aleatory aspect on the definition of the starting point of the calculation (initial values) by using an stochastic algorithm. Cades offers support for this kind of optimization.

### **New researches exploring the developed BDFRM prototype**

One of the results of this thesis is the BDFRM prototype. This machine can be used as the basis for new researches in the field, exploring, for example, BDFRM control aspects, iron losses on this kind of machine and new modeling techniques.





# Bibliography

- [1] H. Li and Z. Chen, “Overview of different wind generator systems and their comparisons,” *IET Renewable Power Generation*, vol. 2, no. 2, 2008, p. 123. doi: 10.1049/iet-rpg:20070044
- [2] T. Burton, N. Jenkins, D. Sharpe, and E. Bossanyi, *Wind Energy Handbook*, 2nd ed. Chichester: John Wiley & Sons, Ltd, 2011. ISBN 978-0-470-69975-1
- [3] A. D. Hansen and L. H. Hansen, “Wind turbine concept market penetration over 10 years (1995-2004),” *Wind Energy*, vol. 10, no. 1, Jan. 2007, pp. 81–97. doi: 10.1002/we.210
- [4] E. Schulz and R. Betz, “Use of Doubly Fed Reluctance Machines in Wind Power Generation,” in *2006 12th International Power Electronics and Motion Control Conference*. IEEE, Aug. 2006, pp. 1901–1906. doi: 10.1109/EPEPEMC.2006.4778683. ISBN 1-4244-0121-6
- [5] D. G. Dorrell, A. M. Knight, and R. E. Betz, “Improvements in Brushless Doubly Fed Reluctance Generators Using High-Flux-Density Steels and Selection of the Correct Pole Numbers,” *IEEE Transactions on Magnetics*, vol. 47, no. 10, Oct. 2011, pp. 4092–4095. doi: 10.1109/TMAG.2011.2159300
- [6] H. Chaal and M. Jovanovic, “Practical Implementation of Sensorless Torque and Reactive Power Control of Doubly Fed Machines,” *IEEE Transactions on Industrial Electronics*, vol. 59, no. 6, Jun. 2012, pp. 2645–2653. doi: 10.1109/TIE.2011.2161065
- [7] H. Liu and L. Xu, “Comparison study of Doubly Excited Brushless Reluctance Machine with different rotor pole numbers,” in *2009 IEEE 6th International Power Electronics and Motion*

- Control Conference*. IEEE, May 2009, pp. 830–835. doi: 10.1109/IPEMC.2009.5157499. ISBN 978-1-4244-3556-2
- [8] D. G. Dorrell and M. Jovanovic, “On the Possibilities of Using a Brushless Doubly-Fed Reluctance Generator in a 2 MW Wind Turbine,” in *2008 IEEE Industry Applications Society Annual Meeting*. IEEE, Oct. 2008, pp. 1–8. doi: 10.1109/O8IAS.2008.73. ISBN 978-1-4244-2278-4
- [9] D. G. Dorrell, I. Scian, E. M. Schulz, R. B. Betz, and M. Jovanovic, “Electromagnetic Considerations in the Design of Doubly-Fed Reluctance Generators for use in Wind Turbines,” in *IECON 2006 - 32nd Annual Conference on IEEE Industrial Electronics*. IEEE, Nov. 2006, pp. 4272–4277. doi: 10.1109/IECON.2006.348077. ISBN 1-4244-0390-1. ISSN 1553-572X
- [10] L. Xu, B. Guan, H. Liu, L. Gao, and K. Tsai, “Design and control of a high-efficiency Doubly-Fed Brushless machine for wind power generator application,” in *2010 IEEE Energy Conversion Congress and Exposition*. IEEE, Sep. 2010, pp. 2409–2416. doi: 10.1109/ECCE.2010.5617911. ISBN 978-1-4244-5286-6
- [11] A. M. Knight, R. E. Betz, and D. G. Dorrell, “Design and Analysis of Brushless Doubly Fed Reluctance Machines,” *IEEE Transactions on Industry Applications*, vol. 49, no. 1, Jan. 2013, pp. 50–58. doi: 10.1109/TIA.2012.2229451
- [12] E. Schulz and R. Betz, “Optimal torque per amp for brushless doubly fed reluctance machines,” in *Fortieth IAS Annual Meeting. Conference Record of the 2005 Industry Applications Conference, 2005.*, vol. 3. IEEE, 2005, pp. 1749–1753. doi: 10.1109/IAS.2005.1518683. ISBN 0-7803-9208-6
- [13] T. Ackermann, *Wind Power in Power Systems*, T. Ackermann, Ed. Stockholm: John Wiley & Sons, Ltd, 2005. ISBN 0470855088
- [14] J. F. Manwell, J. G. McGowan, and A. L. Rogers, *Wind Energy Explained - Theory, Design and Application*. Chichester: John Wiley & Sons, Ltd, 2002. ISBN 0471499722
- [15] O. Anaya-Lara, N. Jenkins, J. Ekanayake, P. Cartwright, and M. Hughes, *Wind Energy Generation Modelling and Control*, 1st ed. United Kingdom: Wiley, 2009. ISBN 9780470714331

- [16] K. Marvel, B. Kravitz, and K. Caldeira, “Geophysical limits to global wind power,” *Nature Climate Change*, vol. advance on, Sep. 2012. doi: 10.1038/nclimate1683
- [17] EIA, “International energy statistics database (2011),” in *U.S. Energy Information Administration. Accessed December 2014.* <http://www.eia.gov/cfapps/ipdbproject/IEDIndex3.cfm?tid=44&pid=44&cid=10000>, 2014.
- [18] GWEC, “Global Wind Energy Outlook,” in <http://www.gwec.net/publications/global-wind-energy-outlook/global-wind-energy-outlook-2014/>. Global Wind Energy Council and Greenpeace International, 2014.
- [19] CRESESB, “Centro de Referência para Energia Solar e Eólica Sérgio de Salvo Brito,” in *Available in: http://www.cresesb.cepel.br/index.php?link=/atlas\_eolico\_brasil/atlas.htm* Accessed in 23-novembre-2014, 2001.
- [20] M. B. d. C. Salles, “Modelagem e Análises de Geradores Eólicos de Velocidade Variável Conectados em Sistemas de Energia Elétrica,” Ph.D. dissertation, Escola Politécnica da Universidade de São Paulo, 2009.
- [21] ANEEL, *Atlas da Energia Elétrica*, 3rd ed. Brasilia: ANEEL, 2008.
- [22] CBEE, “CENTRO BRASILEIRO DE ENERGIA EÓLICA,” in *Universidade Federal de Pernambuco. Available in www.eolica.com.br and http://www.aneel.gov.br/aplicacoes/Atlas/energia\_eolica/6\_6.htm* Accessed on 23 november 2014, 2000.
- [23] ABEEólica, “Energia Eólica atinge 5GW de capacidade instalada no Brasil,” in *Associação Brasileira de Energia Eólica, Accessed on 14-november 2014.* <http://www.portalabeeolica.org.br/index.php/releases-menu/2471-brazil-windpower-2014-abertura.html>, 2014.
- [24] Eletronorte, “SNPTEE: Brasil precisará investir R\$ 450 bilhões no setor elétrico nos próximos 20 anos, afirma presidente da Eletrobras ([http://www.eln.gov.br/opencms/opencms/modulos/noticia/noticia\\_0563.html?uri=/modulos/home\\_noticias.html](http://www.eln.gov.br/opencms/opencms/modulos/noticia/noticia_0563.html?uri=/modulos/home_noticias.html)),” p. <http://www.eln.gov.br/opencms/opencms/modulos/noti>, 2011.

- [25] M. Tsili and S. Papathanassiou, "A review of grid code technical requirements for wind farms," *IET Renewable Power Generation*, vol. 3, no. 3, 2009, p. 308. doi: 10.1049/iet-rpg.2008.0070
- [26] P. Kundur, *Power System Stability And Control*, 1st ed. McGraw-Hill, Inc., 1994. ISBN 0-07-035958-x
- [27] J. S. Thongam and M. Ouhrouche, "MPPT Control Methods in Wind Energy Conversion Systems," *Fundamental and Advanced Topics in Wind Power*, 2011. doi: 10.5772/21657
- [28] Z. Chen, J. M. Guerrero, and F. Blaabjerg, "A Review of the State of the Art of Power Electronics for Wind Turbines," pp. 1859–1875, 2009.
- [29] R. Pena, J. Clare, and G. Asher, "Doubly fed induction generator using back-to-back PWM converters and its application to variable-speed wind-energy generation," *IEE Proceedings - Electric Power Applications*, vol. 143, no. 3, 1996, p. 231. doi: 10.1049/ip-epa:19960288
- [30] T. J. E. Miller, *Electronic Control of Switched Reluctance Machines*, 1st ed., T. J. E. Miller, Ed. Oxford, UK: Newnes Power Engineering Series. Newnes, 2001. ISBN 0 7506 50737
- [31] Y. Rahim, J. Fletcher, and N. Hassanain, "Performance analysis of salient-pole self-excited reluctance generators using a simplified model," *IET Renewable Power Generation*, vol. 4, no. 3, 2010, p. 253. doi: 10.1049/iet-rpg.2009.0075
- [32] M. P. Kazmierkowski, R. Krishnan, F. Blaabjerg, and J. D. Irwin, *Control in Power Electronics: Selected Problems*, 1st ed., R. E. Betz, Ed. Chapter 8: Edited by Robert E. Betz. Academic Press, 2002, p. 544. ISBN 0124027725
- [33] D. Torrey, "Variable-reluctance generators in wind-energy systems," in *Proceedings of IEEE Power Electronics Specialist Conference - PESC '93*. Seattle, WA , USA: IEEE, 1993, pp. 561–567. doi: 10.1109/PESC.1993.471982. ISBN 0-7803-1243-0
- [34] —, "Switched reluctance generators and their control," *IEEE Transactions on Industrial Electronics*, vol. 49, no. 1, 2002, pp. 3–14. doi: 10.1109/41.982243

- [35] R. Cardenas, W. Ray, and G. Asher, "Switched reluctance generators for wind energy applications," in *Proceedings of PESC '95 - Power Electronics Specialist Conference*, vol. 1. IEEE, 1995, pp. 559–564. doi: 10.1109/PESC.1995.474864. ISBN 0-7803-2730-6
- [36] R. Cardenas, R. Pena, M. Perez, J. Clare, G. Asher, and P. Wheeler, "Control of a Switched Reluctance Generator for Variable-Speed Wind Energy Applications," *IEEE Transactions on Energy Conversion*, vol. 20, no. 4, Dec. 2005, pp. 781–791. doi: 10.1109/TEC.2005.853733
- [37] J. Pyrhönen, T. Jokinen, and V. Hrabovcova, *Design of Electrical Machines*, 1st ed. John Wiley & Sons, Ltd, 2008. ISBN 978-0-470-69516-6 (H/B)
- [38] K.-C. Kim, J. S. Ahn, S. H. Won, J.-P. Hong, and J. Lee, "A Study on the Optimal Design of SynRM for the High Torque and Power Factor," *IEEE Transactions on Magnetics*, vol. 43, no. 6, Jun. 2007, pp. 2543–2545. doi: 10.1109/TMAG.2007.893302
- [39] A. I. Alolah, "Capacitance requirements for three phase self-excited reluctance generators," in *Generation, Transmission and Distribution, IEE Proceedings C*, vol. 138, no. 3, 1991, pp. 193–198. ISBN 0143-7046
- [40] Y. Liao, L. Xu, and L. Zhen, "Design of a doubly fed reluctance motor for adjustable-speed drives," *IEEE Transactions on Industry Applications*, vol. 32, no. 5, 1996, pp. 1195–1203. doi: 10.1109/28.536883
- [41] F. Runcos, "Modelagem, projeto e análise de máquinas assíncronas trifásicas duplamente alimentadas sem escovas," Doutorado, Universidade Federal de Santa Catarina, Florianópolis, 2006.
- [42] P. C. Roberts, "A Study of Brushless Doubly-Fed ( Induction ) Machines," Ph.D. dissertation, University of Cambridge, 2004.
- [43] J. Poza, "Modélisation, Conception et Commande d'une Machine Asynchrone Sans Balais Doublement Alimentée pour la Generation a vitesse variable," Ph.D. dissertation, University of Grenoble, 2003.

- [44] R. E. Betz and M. G. Jovanovic, "Introduction to Brushless Doubly Fed Reluctance Machines. The Basic Equations," <ftp://vcs2.newcastle.edu.au/Papers/BDFRM-Review.pdf>. University of Newcastle, NSW, 2308, Australia., Aalborg, Denmark, Tech. Rep., 1998.
- [45] —, "Introduction to the Space Vector Modeling of the Brushless Doubly Fed Reluctance Machine," *Electric Power Components and Systems*, vol. 31, no. 8, Aug. 2003, pp. 729–755. doi: 10.1080/15325000390219785
- [46] L. Xu, F. Liang, and T. Lipo, "Transient model of a doubly excited reluctance motor," *IEEE Transactions on Energy Conversion*, vol. 6, no. 1, Mar. 1991, pp. 126–133. doi: 10.1109/60.73799
- [47] F. Liang, L. Xu, and T. Lipo, "D-q analysis of a variable speed doubly AC excited reluctance motor," *Electric Machines and Power Systems*, vol. 19, 1991, pp. 125–138.
- [48] E. J. Koshinski, "Máquina trifásica de relutância duplamente alimentada a sem escovas," Mestrado, Universidade Federal de Santa Catarina, 2008.
- [49] M. Jovanovic and R. Betz, "The use of doubly fed reluctance machines for large pumps and wind turbines," *IEEE Transactions on Industry Applications*, vol. 38, no. 6, Nov. 2002, pp. 1508–1516. doi: 10.1109/TIA.2002.804749
- [50] S. Brothers and F. Lydall, "Siemens Brothers & Co. Ltd. and Francis Lydall. Improvements in polyphase induction motors." in *British Patent No.: 16839*, 1902.
- [51] L. Hunt, "A new type of induction motor," *Journal of the Institution of Electrical Engineers*, vol. 39, no. 186, Sep. 1907, pp. 648–667. doi: 10.1049/jiee-1.1907.0074
- [52] —, "The Cascade Induction Motor," *Electrical Engineers, Journal of the Institution of*, vol. 52, no. 230, 1914, pp. 406–426. doi: 10.1049/jiee-1.1914.0031
- [53] F. Creedy, "Some developments in multi-speed cascade induction motors," *Journal of the Institution of Electrical Engineers*, vol. 59, no. 301, May 1921, pp. 511–532. doi: 10.1049/jiee-1.1921.0036

- [54] A. Broadway and L. Burbridge, "Self-cascaded machine: a low-speed motor or high-frequency brushless alternator," *Proceedings of the Institution of Electrical Engineers*, vol. 117, no. 7, 1970, p. 1277. doi: 10.1049/piee.1970.0247
- [55] A. Broadway, "Cageless induction machine," *Proceedings of the Institution of Electrical Engineers*, vol. 118, no. 11, 1971, p. 1593. doi: 10.1049/piee.1971.0290
- [56] A. Broadway, B. Cook, and P. Neal, "Brushless cascade alternator," *Proceedings of the Institution of Electrical Engineers*, vol. 121, no. 12, 1974, p. 1529. doi: 10.1049/piee.1974.0317
- [57] R. E. Betz and M. G. Jovanović, "Theoretical analysis of control properties for the brushless doubly fed reluctance machine," *IEEE Transactions on Energy Conversion*, vol. 17, no. 3, Sep. 2002, pp. 332–339. doi: 10.1109/TEC.2002.801997
- [58] R. Spee, A. Wallace, and H. Lauw, "Performance simulation of brushless doubly-fed adjustable speed drives," in *Conference Record of the IEEE Industry Applications Society Annual Meeting*. IEEE, 1989, pp. 738–743. doi: 10.1109/IAS.1989.96730
- [59] A. Wallace, R. Spee, and H. Lauw, "Dynamic modeling of brushless doubly-fed machines," in *Conference Record of the IEEE Industry Applications Society Annual Meeting*. IEEE, 1989, pp. 329–334. doi: 10.1109/IAS.1989.96672
- [60] A. Kusko and C. B. Somuah, "Speed Control of a Single-Frame Cascade Induction Motor with Slip-Power Pump Back," *IEEE Transactions on Industry Applications*, vol. IA-14, no. 2, Mar. 1978, pp. 97–105. doi: 10.1109/TIA.1978.4503502
- [61] R. Betz and M. Jovanovic, "The brushless doubly fed reluctance machine and the synchronous reluctance machine—a comparison," *IEEE Transactions on Industry Applications*, vol. 36, no. 4, 2000, pp. 1103–1110. doi: 10.1109/28.855966
- [62] S. Ademi and M. Jovanovic, "Vector control strategies for brushless doubly-fed reluctance wind generators," in *2012 2nd International Symposium On Environment Friendly Energies And Applications*. IEEE, Jun. 2012, pp. 44–49. doi: 10.1109/EFEA.2012.6294084. ISBN 978-1-4673-2911-8

- [63] —, “Vector control strategies for brushless doubly-fed reluctance wind generators,” in *2012 2nd International Symposium On Environment Friendly Energies And Applications*. IEEE, Jun. 2012, pp. 44–49. doi: 10.1109/EFEA.2012.6294084. ISBN 978-1-4673-2911-8
- [64] M. Hassan and M. Jovanovic, “Improved scalar control using flexible DC-Link voltage in Brushless Doubly-Fed Reluctance Machines for wind applications,” in *2012 2nd International Symposium On Environment Friendly Energies And Applications*. IEEE, Jun. 2012, pp. 482–487. doi: 10.1109/EFEA.2012.6294037. ISBN 978-1-4673-2911-8
- [65] M. Jovanovic, “Sensored and sensorless speed control methods for brushless doubly fed reluctance motors,” *Electric Power Applications, IET*, vol. 3, no. 6, 2009, pp. 503–513. doi: 10.1049/iet-epa.2008.0227
- [66] M. G. Jovanovic and D. G. Dorrell, “Sensorless Control of Brushless Doubly-Fed Reluctance Machines using an Angular Velocity Observer,” in *2007 7th International Conference on Power Electronics and Drive Systems*. IEEE, Nov. 2007, pp. 717–724. doi: 10.1109/PEDS.2007.4487782. ISBN 978-1-4244-0644-9
- [67] M. Jovanovic and E. Levi, “Encoderless direct torque controller for limited speed range applications of brushless doubly fed reluctance motors,” *IEEE Transactions on Industry Applications*, vol. 42, no. 3, May 2006, pp. 712–722. doi: 10.1109/TIA.2006.872955
- [68] S. Ademi and M. Jovanovic, “Theoretical and experimental evaluation of vector control for doubly-fed reluctance generators,” in *2014 International Conference on Electrical Machines (ICEM)*. IEEE, Sep. 2014, pp. 936–942. doi: 10.1109/ICELMACH.2014.6960293. ISBN 978-1-4799-4389-0
- [69] —, “Robust vector controllers for brushless doubly-fed wind turbine generators,” in *2014 IEEE International Energy Conference (ENERGYCON)*. IEEE, May 2014, pp. 1–8. doi: 10.1109/ENERGYCON.2014.6850397. ISBN 978-1-4799-2449-3
- [70] —, “Vector Control Methods for Brushless Doubly-Fed Reluctance Machines,” *IEEE Transactions on Industrial Elec-*



- tronics*, vol. 62, no. 1, 2014, pp. 96 – 104. doi: 10.1109/TIE.2014.2327564
- [71] —, “Maximum torque per inverter ampere control of brushless doubly-fed reluctance generators for wind turbines,” in *2014 International Symposium on Power Electronics, Electrical Drives, Automation and Motion*. IEEE, Jun. 2014, pp. 883–888. doi: 10.1109/SPEEDAM.2014.6871984. ISBN 978-1-4799-4749-2
- [72] W. K. Song and D. G. Dorrell, “Improved Direct Torque Control method of brushless doubly-fed reluctance machines for wind turbine,” in *2013 IEEE International Symposium on Industrial Electronics*. IEEE, May 2013, pp. 1–5. doi: 10.1109/ISIE.2013.6563747. ISBN 978-1-4673-5193-5
- [73] F. Valenciaga and P. F. Puleston, “Variable Structure Control of a Wind Energy Conversion System Based on a Brushless Doubly Fed Reluctance Generator,” *IEEE Transactions on Energy Conversion*, vol. 22, no. 2, Jun. 2007, pp. 499–506. doi: 10.1109/TEC.2006.875447
- [74] F. Valenciaga and C. Evangelista, “2-Sliding active and reactive power control of a wind energy conversion system,” *IET Control Theory & Applications*, vol. 4, no. 11, 2010, p. 2479. doi: 10.1049/iet-cta.2009.0437
- [75] T. Fukami, M. Momiyama, K. Shima, R. Hanaoka, and S. Takata, “Steady-State Analysis of a Dual-Winding Reluctance Generator With a Multiple-Barrier Rotor,” *IEEE Transactions on Energy Conversion*, vol. 23, no. 2, Jun. 2008, pp. 492–498. doi: 10.1109/TEC.2008.918656
- [76] E. Schulz and R. Betz, “Optimal rotor design for brushless doubly fed reluctance machines,” in *38th IAS Annual Meeting on Conference Record of the Industry Applications Conference, 2003.*, vol. 1. IEEE, 2003, pp. 256–261. doi: 10.1109/IAS.2003.1257511. ISBN 0-7803-7883-0
- [77] I. Scian, D. Dorrell, and P. Holik, “Assessment of Losses in a Brushless Doubly-Fed Reluctance Machine,” *IEEE Transactions on Magnetics*, vol. 42, no. 10, Oct. 2006, pp. 3425–3427. doi: 10.1109/TMAG.2006.879068

- [78] D. G. Dorrell, A. M. Knight, and R. E. Betz, "Issues with the design of brushless doubly-fed reluctance machines: Unbalanced magnetic pull, skew and iron losses," in *2011 IEEE International Electric Machines & Drives Conference (IEMDC)*. IEEE, May 2011, pp. 663–668. doi: 10.1109/IEMDC.2011.5994890. ISBN 978-1-4577-0060-6
- [79] D. G. Dorrell, A. M. Knight, W. K. Song, and R. E. Betz, "Saturation and Ducting Effects in a Brushless Doubly-Fed Reluctance Machine," *IEEE Transactions on Magnetics*, vol. 49, no. 7, Jul. 2013, pp. 3933–3936. doi: 10.1109/TMAG.2013.2251458
- [80] T. Staudt, F. Wurtz, N. J. Batistela, and P. Kuo-Peng, "Influence of rotor design and geometric parameter variation on global performance of Brushless Doubly-Fed Reluctance Machines," in *2014 International Conference on Electrical Machines (ICEM)*. September 2-5, Berlin: IEEE, Sep. 2014, pp. 537–543. doi: 10.1109/ICELMACH.2014.6960232. ISBN 978-1-4799-4389-0
- [81] A. M. Knight, R. E. Betz, and D. Dorrell, "Design principles for brushless doubly fed reluctance machines," in *IECON 2011 - 37th Annual Conference of the IEEE Industrial Electronics Society*. IEEE, Nov. 2011, pp. 3602–3607. doi: 10.1109/IECON.2011.6119894. ISBN 978-1-61284-972-0
- [82] A. M. Knight, R. E. Betz, W. K. Song, and D. G. Dorrell, "Brushless doubly-fed reluctance machine rotor design," in *2012 IEEE Energy Conversion Congress and Exposition (ECCE)*. IEEE, Sep. 2012, pp. 2308–2315. doi: 10.1109/ECCE.2012.6342466. ISBN 978-1-4673-0803-8
- [83] M.-F. Hsieh, I.-H. Lin, and D. Dorrell, "Magnetic Circuit Modeling of Brushless Doubly-Fed Machines<newline/> With Induction and Reluctance Rotors," pp. 2359–2362, 2013.
- [84] M.-F. Hsieh, I.-H. Lin, Y.-C. Hsu, and R. A. McMahon, "Design of Brushless Doubly-Fed Machines Based on Magnetic Circuit Modeling," *IEEE Transactions on Magnetics*, vol. 48, no. 11, Nov. 2012, pp. 3017–3020. doi: 10.1109/TMAG.2012.2204866
- [85] H. Gorginpour, H. Oraee, and R. A. McMahon, "A Novel Modeling Approach for Design Studies of Brushless Doubly Fed Induction Generator Based on Magnetic Equivalent Circuit,"

- IEEE Transactions on Energy Conversion*, vol. 28, no. 4, Dec. 2013, pp. 902–912. doi: 10.1109/TEC.2013.2278486
- [86] T. Staudt, L. Scanu, F. Wurtz, N. J. Batistela, P. Kuo-Peng, and N. Sadowski, “Brushless Doubly-Fed Reluctance Machine Optimization using Reluctance Networks,” in *Conference on the Computation of Electromagnetic Fields - COMPUMAG*, Budapest, 2013.
- [87] P. C. Krause, O. Wasynczuk, S. D. Sudhoff, and S. Pekarek, *Analysis of Electric Machinery and Drive Systems*, 3rd ed. Piscataway, New Jersey: Wiley-IEEE Press, 2013. ISBN 978-1-118-02429-4
- [88] C.-M. Ong, *Dynamic Simulation of Electric Machinery*, 1st ed., P. Hall, Ed., New Jersey, 1997, p. 688. ISBN 0137237855
- [89] J. Morren and S. W. H. de Haan, “Short-Circuit Current of Wind Turbines With Doubly Fed Induction Generator,” *IEEE Transactions on Energy Conversion*, vol. 22, no. 1, Mar. 2007, pp. 174–180. doi: 10.1109/TEC.2006.889615
- [90] J. Lopez, P. Sanchis, X. Roboam, and L. Marroyo, “Dynamic Behavior of the Doubly Fed Induction Generator During Three-Phase Voltage Dips,” *IEEE Transactions on Energy Conversion*, vol. 22, no. 3, Sep. 2007, pp. 709–717. doi: 10.1109/TEC.2006.878241
- [91] T. Long, S. Shao, P. Malliband, E. Abdi, and R. A. McMahon, “Crowbarless Fault Ride-Through of the Brushless Doubly Fed Induction Generator in a Wind Turbine Under Symmetrical Voltage Dips,” *IEEE Transactions on Industrial Electronics*, vol. 60, no. 7, Jul. 2013, pp. 2833–2841. doi: 10.1109/TIE.2012.2208437
- [92] J. Morren and S. DeHaan, “Ridethrough of Wind Turbines with Doubly-Fed Induction Generator During a Voltage Dip,” *IEEE Transactions on Energy Conversion*, vol. 20, no. 2, Jun. 2005, pp. 435–441. doi: 10.1109/TEC.2005.845526
- [93] G. Pannell, D. J. Atkinson, and B. Zahawi, “Minimum-Threshold Crowbar for a Fault-Ride-Through Grid-Code-Compliant DFIG Wind Turbine,” *IEEE Transactions on Energy Conversion*, vol. 25, no. 3, Sep. 2010, pp. 750–759. doi: 10.1109/TEC.2010.2046492

- [94] J. Lopez, E. Gubia, E. Olea, J. Ruiz, and L. Marroyo, "Ride Through of Wind Turbines With Doubly Fed Induction Generator Under Symmetrical Voltage Dips," *IEEE Transactions on Industrial Electronics*, vol. 56, no. 10, Oct. 2009, pp. 4246–4254. doi: 10.1109/TIE.2009.2028447
- [95] S. Hu, X. Lin, Y. Kang, and X. Zou, "An Improved Low-Voltage Ride-Through Control Strategy of Doubly Fed Induction Generator During Grid Faults," *IEEE Transactions on Power Electronics*, vol. 26, no. 12, Dec. 2011, pp. 3653–3665. doi: 10.1109/TPEL.2011.2161776
- [96] T. Long, S. Shao, E. Abdi, R. A. McMahon, and S. Liu, "Asymmetrical Low-Voltage Ride Through of Brushless Doubly Fed Induction Generators for the Wind Power Generation," *IEEE Transactions on Energy Conversion*, vol. 28, no. 3, Sep. 2013, pp. 502–511. doi: 10.1109/TEC.2013.2261818
- [97] D. Meeker, "FEMM 4.2 Magnetism, Electrostatics, Heat Flow, and Current Flow," in <http://www.femm.info/wiki/HomePage>, 2014.
- [98] B. Delinchant, "Un Environnement à base de Composants, Intégrant le Concepteur et ses Outils, pour de Nouvelles Méthodes de CAO," Ph.D. dissertation, Institut National Polytechnique de Grenoble - INPG. French. <tel-00332801>, 2003.
- [99] R. Carlson and F. Wurtz, "The concepts of sizing and optimization model: Applied to the optimal design of a Permanent Magnet Generator," in *International Aegean Conference on Electrical Machines and Power Electronics and Electromotion, Joint Conference*. Istanbul, Turkey: IEEE, Sep. 2011, pp. 651–656. doi: 10.1109/ACEMP.2011.6490676. ISBN 978-1-4673-5003-7
- [100] F. Wurtz, "Une Nouvelle Approche pour la Conception Sous Contraintes de Machines Electriques," Ph.D. dissertation, INSTITUT NATIONAL POLYTECHNIQUE DE GRENOBLE, 1996.
- [101] V. Reinbold, "Méthodologie de dimensionnement d'un moteur électrique pour véhicules hybrides - Optimisation conjointe des composants et de la gestion d'énergie," Ph.D. dissertation, Univ. Grenoble Alpes, G2Elab-CNRS, F-38000 Grenoble, France, 2014.

- [102] V. Fischer, "COMPOSANTS LOGICIELS POUR LE DIMENSIONNEMENT EN GENIE ELECTRIQUE. APPLICATION A LA RESOLUTION D'EQUATIONS DIFFERENTIELLES," Ph.D. dissertation, Institut National Polytechnique de Grenoble - INPG. French. <tel-00386169>, 2004.
- [103] G. Meunier, *The Finite Element Method for Electromagnetic Modeling*, G. Meunier, Ed. London: ISTE Ltd, 2008. ISBN 9781848210301
- [104] N. Ida and J. a. P. A. Bastos, *Electromagnetics and Calculations of Fields*, 2nd ed. New York: Springer Verlag, 1997. ISBN 0-387-94877-5
- [105] S. N'Tshuika, "Optimisation de Gammes: Application à la Conception des Machines Synchrones à Concentration de Flux," Ph.D. dissertation, Université de Grenoble, 2011.
- [106] J. Nocedal and S. J. Wright, *Numerical Optimization*, P. Glynn and S. M. Robinson, Eds. New York, Berlin, Heidelberg: Springer, 1999. ISBN 0387987932
- [107] M. J. D. Powell, *Mathematical Programming Essays in Honor of George B. Dantzig Part II - On the quadratic programming algorithm of Goldfarb and Idnani*, ser. Mathematical Programming Studies, R. W. Cottle, Ed. Berlin, Heidelberg: Springer Berlin Heidelberg, 1985, vol. 25, pp. 46–61. ISBN 978-3-642-00920-4
- [108] Cades, "Cades Reference Manual v2.11.1," in *Cades Framework - <http://vesta-system.cades-solutions.com/>*. Grenoble: Vesta-Systems, 2014.
- [109] E. Atienza, "Méthodologie et outils pour le dimensionnement. Modeling and Simulation," Ph.D. dissertation, Institut National Polytechnique de Grenoble - INPG, 2003.
- [110] L. Gerbaud, "Gentiane : une Plate-Forme pour la Conception des Ensembles Machine- Convertisseur-Commande," Ph.D. dissertation, Grenoble University, HDR, 2000.
- [111] B. du Peloux, "Modelisation des Actionneurs Electromagnetiques par Reseaux de Reluctances. Creation d'un Outil Metier Dedie au Predimensionnement par Optimisation," doctorat, Université Joseph Fourier. Institut National Polytechnique de Grenoble, 2006.

- [112] L. Albert, “Modélisation et optimisation des alternateurs à griffes Application au domaine automobile,” Ph.D. dissertation, INSTITUT NATIONAL POLYTECHNIQUE DE GRENOBLE, 2004.
- [113] T. Staudt, F. Wurtz, N. J. Batistela, and P. Kuo-Peng, “A New Approach on the Design and Optimization of Brushless Doubly-Fed Reluctance Machines,” in *Symposium de Génie Electrique, SGE*, Cachan, 2014.
- [114] D. G. Dorrell, “Design Requirements for Doubly-Fed Reluctance Generators,” in *2007 7th International Conference on Power Electronics and Drive Systems*. IEEE, Nov. 2007, pp. 981–988. doi: 10.1109/PEDS.2007.4487823. ISBN 978-1-4244-0644-9
- [115] A. Vagati, M. Pastorelli, G. Francheschini, and S. Petrache, “Design of low-torque-ripple synchronous reluctance motors,” *IEEE Transactions on Industry Applications*, vol. 34, no. 4, 1998, pp. 758–765. doi: 10.1109/28.703969
- [116] B. Nedjar, “Modélisation basée sur la méthode des réseaux de perméances en vue de l’optimisation de machines synchrones à simple et à double excitation,” Ph.D. dissertation, ECOLE NORMALE SUPERIEURE DE CACHAN, 2012.
- [117] T. RAMINOSOA, “OPTIMISATION DES PERFORMANCES DES MACHINES SYNCHRO-RELUCTANTES PAR RESEAUX DE PERMEANCES,” Génie Electrique, Institut National Polytechnique de Lorraine, Oct. 2006.
- [118] H. Rothers, *Electromagnetic devices*. New-York, USA: JohnWiley and Sons, 1941.
- [119] A. Foggia, “Méthodes de calcul des inductances de fuites,” *Techniques de l’ingénieur Généralités sur les machines électriques tournantes*, vol. base docum, no. ref. article : d3440, Feb. 1999, pp. 1–20.
- [120] N. Bracikowski, “Modélisation multi-physique par modèles à constantes localisées ; application à une machine synchrone à aimants permanents en vue de son dimensionnement,” Ph.D. dissertation, Ecole Centrale de Lille, 2012.
- [121] H. Dogan, “Méthodologie de Conception des Machines Synchrones à Aimants Permanents - Application au Véhicule Electrique avec Chargeur Rapide Embarqué,” Ph.D. dissertation, Université de Grenoble, 2013.

- [122] H. Dogan, L. Garbuio, H. Nguyen-Xuan, B. Delinchant, A. Foggia, and F. Wurtz, "Multistatic Reluctance Network Modeling for the Design of Permanent-Magnet Synchronous Machines," *IEEE Transactions on Magnetics*, vol. 49, no. 5, May 2013, pp. 2347–2350. doi: 10.1109/TMAG.2013.2243426
- [123] S. Perez, "Contribution au dimensionnement optimal d'alternateur à griffes sans aimant - Apport des alliages FeCo," Ph.D. dissertation, Université de Grenoble - Laboratoire de Génie Electrique de Grenoble - G2ELAB, 2013.
- [124] H. Nguyen-Xuan, H. Dogan, S. Perez, L. Gerbaud, L. Garbuio, and F. Wurtz, "Efficient Reluctance Network Formulation for Electrical Machine Design Using Optimization," *IEEE Transactions on Magnetics*, vol. 50, no. 2, Feb. 2014, pp. 869–872. doi: 10.1109/TMAG.2013.2282407
- [125] G. Bertotti, "GENERAL PROPERTIES OF POWER LOSSES IN SOFT FERROMAGNETIC MATERIALS." *IEEE Transactions on Magnetics*, vol. 24, no. 1, 1987, pp. 621–630. doi: 10.1109/20.43994
- [126] P. Armando, "BANCADA PARA ENSAIOS DE MATERIAIS FERROMAGNÉTICOS EM CHAPA ÚNICA SOB CAMPOS ROTACIONAIS," Ph.D. dissertation, Universidade Federal de Santa Catarina, 2007.
- [127] F. B. R. MENDES, "Análise de Medidas de Perdas Magnéticas em Lâminas de Aço ao Silício FLORIANÓPOLIS," Ph.D. dissertation, Universidade Federal de Santa Catarina, 2004.
- [128] B. Delinchant, D. Duret, L. Estrabaut, L. Gerbaud, H. Nguyen Huu, B. Du Peloux, H. Rakotoarison, F. Verdier, and F. Wurtz, "An optimizer using the software component paradigm for the optimization of engineering systems," *COMPEL - The international journal for computation and mathematics in electrical and electronic engineering*, vol. 26, no. 2, Apr. 2007, pp. 368–379. doi: 10.1108/03321640710727728
- [129] P. Enciu, F. Wurtz, and L. Gerbaud, "Proposal of a Language for Describing Differentiable Sizing Models for Electromagnetic Devices Design," in *14th Biennial IEEE Conference on Electromagnetic Field Computation - CEFC*, Chicago, May 9-12, 2010.

- [130] P. Enciu, F. Wurtz, L. Gerbaud, and B. Delinchant, "Automatic differentiation for electromagnetic models used in optimization," *COMPTEL: The International Journal for Computation and Mathematics in Electrical and Electronic Engineering*, vol. 28, no. 5, 2009, pp. 1313–1326. doi: 10.1108/03321640910969557
- [131] COIN-OR, "COmputational INfrastructure for Operations Research - AdolC Project (<http://www.coin-or.org/projects/ADOL-C.xml>)," 2014.
- [132] B. du Peloux, L. Gerbaud, F. Wurtz, V. Leconte, and F. Dorschner, "Automatic generation of sizing static models based on reluctance networks for the optimization of electromagnetic devices," *IEEE Transactions on Magnetics*, vol. 42, no. 4, Apr. 2006, pp. 715–718. doi: 10.1109/TMAG.2006.872010
- [133] A. Delale, L. Albert, L. Gerbaud, and F. Wurtz, "Automatic Generation of Sizing Models for the Optimization of Electromagnetic Devices Using Reluctance Networks," *IEEE Transactions on Magnetics*, vol. 40, no. 2, Mar. 2004, pp. 830–833. doi: 10.1109/TMAG.2004.824908
- [134] A. Belhadj, P. Baudouin, F. Breaban, A. Deffontaine, M. Dewulf, and Y. Houbaert, "Effect of laser cutting on microstructure and on magnetic properties of grain non-oriented electrical steels," *Journal of Magnetism and Magnetic Materials*, vol. 256, no. 1-3, Jan. 2003, pp. 20–31. doi: 10.1016/S0304-8853(01)00937-4
- [135] R. Siebert, J. Schneider, and E. Beyer, "Laser Cutting and Mechanical Cutting of Electrical Steels and its Effect on the Magnetic Properties," *IEEE Transactions on Magnetics*, vol. 50, no. 4, Apr. 2014, pp. 1–4. doi: 10.1109/TMAG.2013.2285256
- [136] H. Voltolini, "Modelagem e Controle de Geradores de Indução Duplamente Alimentados com Aplicação em Sistemas Eólicos," Ph.D. dissertation, Universidade Federal de Santa Catarina, 2007.
- [137] Bergey, "BWX Excel 1 Wind Turbine - Owner's Manual," *Owner's Manual*, 2015, pp. 1–136.
- [138] N. L. Schmitz and D. W. Novotny, *Introductory Electromechanics*. New York: Roland, 1965.



- [139] G. W. Stagg and A. H. El-Abiad, *Computer methods in power system analysis*. McGraw-Hill series in electronic systems: McGraw-Hill, 1968. ISBN 67012963
- [140] C. Coutel, F. Wurtz, and J. Bignon, “A comparative study of two methods for constrained optimisation with analytical models dealing with implicit parameters,” *IEEE Transactions on Magnetics*, vol. 35, no. 3, May 1999, pp. 1738–1741. doi: 10.1109/20.767365



# Appendix A

## Winding Function Theory

### A.1 Introduction

The winding function is a physical measure of the number of times a winding links the flux in a particular position around the air gap [87].

The winding function concept is an very interesting method on machine analysis and it was first discussed in [138]. According to Liang *et al.* [47] and Xu *et al.* [46], the winding function approach represents the placement of winding turns along the air gap periphery [47, 46], being particularly convenient for the analysis of unusual machines since it assumes no symmetry in the placement of any machine coil in the slots.

According to Krause *et al.* [87], the winding function has at least three important uses.

- To determine the Magnetomotive force (MMF) caused by distributed windings;
- To determine how much flux links a winding;
- To calculate winding inductances.

Many authors have used this concept on the analysis of the Brushless Doubly-Fed Reluctance Machine (BDFRM). Liang *et al.* [47] and Xu *et al.* [46] applied this technique to analytically calculate inductances and this approach was further used by Betz *et al.* [45, 44] on BDFRM analysis.

In this thesis, this concept has also been used to calculate the winding's MMF, flux linkages and inductances in the developed models. For

this reason, the basic concepts and equations used to calculate the Semi-analytical Model (SAM) (Chapter 3) and the Multi-Static Reluctance Network Model (MSRN) (Chapter 4) are presented here. The winding function approach introduced in this appendix is based mostly on [87] where it is presented a deduction of the mathematical definition of the winding function. The most important concept and equations addressed in [87] for the purpose of this work will be presented in this appendix and the details can be found on this reference. The same nomenclature will be used for clarity.

Fig. A.1 is used as a reference for parameters definitions for the BDFRM.

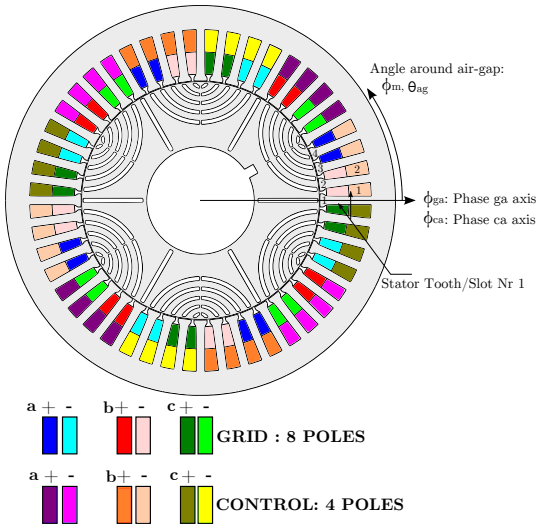


Figure A.1: Parameters for winding function definition considering the BDFRM.

## A.2 Distributed windings

In order to calculate the winding function, the first step is to define the conductor distribution analytically.

The number of conductors of each phase in the slots can be considered a discrete description of a winding and can be given by [87]:

$$n_x(\phi_m) = \sum_{i=1}^{S_y} N_{x,i} \delta(\phi_m - \phi_{ys,i}) \quad (\text{A.1})$$

$$\phi_{ys,i} = \pi(2i - 2)/S_y + \phi_{ys,1} \quad (\text{A.2})$$

where:

$\delta(\cdot)$	is the unit impulse function
$x$	denotes a specific winding (e.g. $ga$ , $gb$ , $gc$ , $ca$ ,... where $g$ and $c$ means grid or control, respectively).
$i$	defines the $i$ 'th slot
$S_y$	Number of stator slots (Nsl)
$N_{x,i}$	represents the number of turns of phase $x$ at slot $i$
$\phi_m$	represents the angle around the air gap referred to the winding position. (Fig. A.1)
$\phi_{ys,1}$	corresponds the center (angle) of first slot
$\phi_{ys,i}$	corresponds the center (angle) of slot $i$ 'th

An idealized representation of conductor distribution may be given by a single-sided Fourier series [87]:

$$n_x(\phi_m) = \sum_{j=1}^{J_{fourier}} a_j \cos(j\phi_m) + b_j \sin(j\phi_m) \quad (\text{A.3})$$

where:

$J_{fourier}$       Number of terms of the Fourier Series

The coefficients of the Fourier series are:

$$a_j = \frac{1}{\pi} \int_0^{2\pi} n_x(\phi_m) \cos(j\phi_m) d\phi_m \quad (\text{A.4})$$

$$b_j = \frac{1}{\pi} \int_0^{2\pi} n_x(\phi_m) \sin(j\phi_m) d\phi_m \quad (\text{A.5})$$

By substituting (A.1) into (A.4) and (A.5) it is found:

$$a_j = \frac{1}{\pi} \sum_{i=1}^{S_y} N_{x,i} \cos(j\phi_{ys,i}) \quad (\text{A.6})$$

$$b_j = \frac{1}{\pi} \sum_{i=1}^{S_y} N_{x,i} \sin(j\phi_{ys,i}) \quad (\text{A.7})$$

### A.3 Winding Function

The winding function of the phase  $x$  ( $w_x$ ) can then be calculated by the following equation [87]:

$$w_x(\phi_m) = \frac{1}{2} \int_0^{2\pi/P} n_x(\phi_m) d\phi_m - \int_0^{\phi_m} n_x(\phi_m) d\phi_m \quad (\text{A.8})$$

where  $P$  is the number of poles of the winding.

For a given winding discrete distribution, (A.3) together with (A.8) can be used to calculate the winding function.

### A.4 Magnetomotive force

The Magnetomotive force (MMF) of a winding three phase winding in the stator can be calculate from the winding function theory by:

$$\mathbb{F}_s = w_{as}(\phi_{sm})i_{as} + w_{bs}(\phi_{sm})i_{bs} + w_{cs}(\phi_{sm})i_{cs} \quad (\text{A.9})$$

where  $s$  means the stator and  $i_{as}$ ,  $i_{bs}$  and  $i_{cs}$  are the instantaneous balanced three phase currents that are given in a general form by:

$$\begin{aligned} i_{as}(t) &= \sqrt{2}I_{s_{rms}} \cos(\omega_e t + \phi_a) \\ i_{bs}(t) &= \sqrt{2}I_{s_{rms}} \cos(\omega_e t + \phi_a - 2\pi/3) \\ i_{cs}(t) &= \sqrt{2}I_{s_{rms}} \cos(\omega_e t + \phi_a + 2\pi/3) \end{aligned} \quad (\text{A.10})$$

where:

$I_{s_{rms}}$	is the rms magnitude of each phase current
$\omega_e$	is the ac electrical frequency
$\phi_a$	is the phase of the a-phase current

### A.5 Flux linkage and inductances

The winding function can be used to determine the flux linkage and the self and mutual inductances of the windings. To that end, idealized assumptions must be considered to derive analytically the equations, such as to neglect iron non-linearities and to assume that it is infinitely permeable and that the magnetic field is uniform in the air gap. The slotting effects are also not taken into account directly in the integral,

but an usual way to consider these effects is by using the Carter's coefficient [87].

The general expressions to calculate the flux linkage and inductances by using winding function theory are [44, 87]:

$$\lambda_{ij} = \int_0^{2\pi} B_i(\phi_m) w_j(\phi_m) r_{gap} L_{stkef} d\phi_m \quad (\text{A.11})$$

$$L_{ij} = \frac{\lambda_{ij}}{I_i} \quad (\text{A.12})$$

where  $i$  and  $j$  are the phase indexes (self and mutual inductances maybe be calculated by this approach),  $L$  is the respective inductance,  $I_i$  is the current used to generate the flux linkage,  $r_{gap}$  is the air-gap radius and  $L_{stkef}$  is the machine effective axial length.

By using (A.13), derived from Ampère's law:

$$\begin{aligned} \mathbb{F}_{i_{gap}}(\phi_m) &= \\ &= w_i(\phi_m) i_i \\ &= H_{i_{gap}}(\phi_m) \cdot g(\phi_m) \\ &= \frac{1}{\mu_0} B_{i_{gap}}(\phi_m) \cdot g(\phi_m) \end{aligned} \quad (\text{A.13})$$

where:

$$\begin{aligned} H_{i_{gap}} &\rightarrow \text{magnetic field in air-gap due to phase } i \\ B_{i_{gap}} &\rightarrow \text{magnetic flux density in air-gap due to phase } i \end{aligned}$$

and (A.11), it can be seen that the self and mutual inductances  $L_{ij}$  between windings can be alternatively found by (A.14) [46, 47, 44, 45, 87] if one knows the inverse air-gap function  $g^{-1}$ .

$$L_{ij} = \mu_0 r_{gap} L_{stkef} \int_0^{2\pi} g^{-1}(\phi_m) w_i(\phi_m) w_j(\phi_m) d\phi_m \quad (\text{A.14})$$

where:

$$\begin{aligned} w_i(\phi_m) &\triangleq \text{winding function of phase "i"} \\ w_j(\phi_m) &\triangleq \text{winding function of phase "j"} \\ g^{-1}(\phi_m) &\triangleq \text{inverse air-gap function (see (1.1))} \\ \mu_0 &\triangleq \text{vacuum permeability} \end{aligned}$$





# Appendix B

## Implementation of a gradient-based reluctance network

### B.1 Gradient-Based Reluctance Network: optimization by deterministic algorithms

#### B.1.1 Introduction

This appendix introduces how a Reluctance Network can be implemented in order to be coupled to gradient based optimization algorithms. The proposed procedure is based on the work of Du Peloux [111, 132], that developed a dedicated tool called RelucTOOL [111, 132, 112, 133]. This software allows to implement the static reluctance network function (SRN) of the MSRN model, by assembling the equivalent magnetic circuit in a similar way than one would do for an electric circuit simulator. Details on the implementation can be found on the aforementioned references, but the main parts of the derivable reluctance network, essential for the purpose of this work, are presented here.

The first step on the reluctance network implementation is to define a topology to represent the equivalent magnetic circuit of the device. Considering its geometry, the electromagnetic domain is discretized in many reluctances defining the existing flux paths in the domain. Based on the electric equivalent magnetic circuit topology, graph theory

together with Kirchhoff Law are used to do a topological analysis of the Reluctance Network (the terms related to graph theory *elements, nodes, path, tree, branches, links, loops, basic loops* used in the sequence are defined in Section B.4 based on [139]):

### B.1.2 Gradient-based reluctance network implementation: the use of the implicit equation theorem

Considering a circuit with only reluctances and magnetic potential sources, the Ampère's law is applied on each loop of the circuit [111]:

$$[V_{mag}] = [\mathfrak{R}][\phi] + [M] \quad (\text{B.1})$$

where:

$[V_{mag}]$	magnetic potential vector in the extremities of the circuit branch
$[\mathfrak{R}]$	diagonal matrix of reluctances for each branch
$[\phi]$	magnetic flux vector for the branches of the circuit
$[M]$	magnetomotive force vector

The topological analysis of the circuit, based on graph theory, results in an independent equation system given in matrix form by [111]:

$$[B][\mathfrak{R}][B]^T[\phi_M] + [B][M] = 0 \quad (\text{B.2})$$

where:

$[B]$	basic loops matrix
$[\phi_M]$	magnetic flux vector for the links of the circuit

This system can be stated in the general form of an implicit equation system  $[F]$  of dimension  $k = a - n + 1$ , where  $a$  is the number of elements and  $n$  is the number of nodes.

$$[F] = \begin{cases} f_1(\phi_{M_1}, \dots, \phi_{M_k}, p_1, \dots, p_m) = 0 \\ \vdots \\ f_k(\phi_{M_1}, \dots, \phi_{M_k}, p_1, \dots, p_m) = 0 \end{cases} \quad (\text{B.3})$$

where:

$p_i$	input parameters
$\phi_{M_j}$	flux in the loops that corresponds to the unknowns to find
$m$	number of input parameters

As the reluctances representing iron are nonlinear functions with respect to the fluxes  $\phi$ , this equation system is solved numerically. Two methods for solving the implicit equation system have been presented

and compared in [140, 132]. The preferred solution was a Newton-Raphson coupled to minimization of the implicit system norm [132].

The most important difference on this approach to implement the reluctance network is the calculation of the gradient of the equation system that represents the machine electromagnetic behavior. For this, it is used the implicit equation theorem [111]. From the topological analysis, the analytical equation for  $f_k(\phi_{M_1}, \dots, \phi_{M_k}, p_1, \dots, p_m)$  are known. According to the theorem of implicit equation, although a non-linear routine is used for solving the system, the derivatives can be *symbolically* derived and are given by:

$$\begin{bmatrix} \frac{\partial \phi_{M_1}}{\partial p_1} & \dots & \frac{\partial \phi_{M_1}}{\partial p_m} \\ \vdots & & \vdots \\ \frac{\partial \phi_{M_k}}{\partial p_1} & \dots & \frac{\partial \phi_{M_k}}{\partial p_m} \end{bmatrix} = \begin{bmatrix} \frac{\partial f_1}{\partial \phi_{M_1}} & \dots & \frac{\partial f_1}{\partial \phi_{M_k}} \\ \vdots & & \vdots \\ \frac{\partial f_k}{\partial \phi_{M_1}} & \dots & \frac{\partial f_k}{\partial \phi_{M_k}} \end{bmatrix}^{-1} \cdot \begin{bmatrix} \frac{\partial f_1}{\partial p_1} & \dots & \frac{\partial f_1}{\partial p_m} \\ \vdots & & \vdots \\ \frac{\partial f_k}{\partial p_1} & \dots & \frac{\partial f_k}{\partial p_m} \end{bmatrix} \quad (\text{B.4})$$

System energy  $W$ , coenergy  $W_{co}$  and their derivatives can also be calculated symbolically by summing the contribution of all reluctances in the network (linear and non-linear reluctances). The procedure to do so can be found in [111].

## B.2 Implementation of the Fourier series used to calculate the air-gap reluctance widths

The Fourier series method used to calculate the air-gap reluctance widths  $LSag$  have been discussed in Section 4.2.3.3. The function used to implement them is coded in C language because it requires conditionals (*if-else*) and repetition (*for*) programming structures. So that one can obtain the equivalent widths  $LSag$  and their associated partial derivatives (required to update the MSRN Jacobian matrix as discussed in Section 6.4.5.1), this C function is compiled by the ADOL-C external function generator available in CADES.

This external function returns a vector with 32 equivalent lengths and it has the following inputs:

$$\begin{aligned}
\text{vector<adouble> } L_{Sag_{XY}} = & \text{CalcAGEqWidth\_FourierSeries}( \\
& \text{adouble } \theta_{rm_{mod}}, \\
& \text{adouble } slop, \\
& \text{adouble } SlrWidth, \\
& \text{adouble } Dis, \\
& \text{adouble } gap)
\end{aligned}
\tag{B.5}$$

where  $\theta_{rm_{mod}}$  is the current rotor position, calculated periodically by the modulo function. The input parameters  $slop$ ,  $SlrWidth$ ,  $Dis$  and  $gap$  represent machine geometry and are defined in Fig. 4.5 and Fig. 4.7.

It has been found that truncating the Fourier series at  $N_{fourier} = 15$  in (4.12) and (4.13) provides accurate results for the chosen BDFRM topology.

## B.3 MSRN Jacobian matrix calculation

This section presents the calculation of the MSRN Jacobian matrix discussed in Chapter 6 using the MSRN output equations depicted in Chapter 4.

### B.3.0.1 Definitions

For the following discussion, Table B.1 sets forth the nomenclature that has been used to designate the distinct input and output vectors existent in the MSRN model.

Table B.1: Indexes definition for models.

Index	Range	Description
$k$	1: $K$	$K$ : Number of Positions (iterations) of the multi-static calculations
$n$	1: $N$	$N$ : Number of inputs of reluctance network function
$m$	1: $M$	$M$ : Number of outputs of reluctance network function
$i$	1: $I$	$I$ : Number of inputs of MSRN
$o$	1: $O$	$O$ : Number of outputs of MSRN
$s$	1: $S$	$S$ : Number of intermediary (time-dependent) outputs of MSRN
$r$	1: $R$	$R$ : Number of reluctances in the reluctance network function
$x$	1: $X$	$X$ : Number of connection in rotor side for the air-gap reluctances (see Fig. 4.27)
$y$	1: $Y$	$Y$ : Number of connection in stator side for the air-gap reluctances (see Fig. 4.27)
$xy$	1: $N\mathfrak{R}_{ag}$	$N\mathfrak{R}_{ag}$ : Number of air-gap reluctances (see Fig. 4.27)

These indexes are used for the following corresponding vector:

$$\begin{aligned}
 I_{MSRN}[i] &\rightarrow \text{“}i_{th}\text{” input of MSRN} \\
 O_{MSRN}[o] &\rightarrow \text{“}o_{th}\text{” output of MSRN} \\
 S_{MSRN}[s] &\rightarrow \text{“}s_{th}\text{” intermediary (time-dependent) output of} \\
 &\quad \text{MSRN at rotor position } k \\
 N_{SRN}[n] &\rightarrow \text{“}n_{th}\text{” input of SRN} \\
 M_{SRN}[m] &\rightarrow \text{“}m_{th}\text{” output of SRN at rotor position } k
 \end{aligned}$$

The output parameters represented by  $S_{MSRN}[s]$  are calculated as a function of time for each multi-static rotor position. They gather all the intermediary outputs (Torque, Flux Linkage, Voltages, Inductions, Current, Power,...) in a single vector and place the results for each position in the sequence. Table B.2 indicates how this vector is assembled. When the index  $s$  is varied, it assigns all intermediary outputs in the  $S_{MSRN}[s]$  vector.

Table B.2: Intermediary outputs vector  $S_{MSRN}$  definition for the Multi-Static Reluctance Network Model.

Parameter	Description	Size
$S_{MSRN}[T_{em}[k]]$	Electromagnetic torque $[Nm]$ .	$1 \cdot K$
$S_{MSRN}[\lambda_x[k]]$	Phase flux linkage $[Wb]$ .	$6 \cdot K$
$S_{MSRN}[E_x[k]]$	Internal induced phase voltage $[V]$ .	$6 \cdot K$
$S_{MSRN}[B_{th}[k]]$	Induction level in stator teeth $[T]$	$24 \cdot K$
$S_{MSRN}[B_{yk}[k]]$	Induction level in stator yoke $[T]$	$24 \cdot K$
$S_{MSRN}[B_{rt}[k]]$	Induction level in rotor teeth (flux paths) $[T]$	$18 \cdot K$
$S_{MSRN}[I_x[k]]$	Phase current value $[A]$	$6 \cdot K$
$S_{MSRN}[P_{inst_x\_int}[k]]$	Internal instantaneous power per phase (calculated from $E_x$ ) $[W]$	$6 \cdot K$
$S_{MSRN}[V_x[k]]$	Terminal output phase voltage (considers the voltage drop in $R_{g/c}$ per phase)	$6 \cdot K$
$S_{MSRN}[P_{inst_x\_ter}[k]]$	Terminal instantaneous power per phase (calculated from $V_x$ ) $[W]$	$6 \cdot K$
Total size of output vector:		$103 \cdot K$

All the outputs in Table B.2 are calculated as a function of the rotor position  $k$ .  $x$  means the respective phase considered:  $g|a, b, c$  (grid) or  $c|a, b, c$  (control). The size column means how many outputs are calculated for the respective parameter.

### B.3.1 Updating the SRN Jacobian matrix obtained from Reluctool

The MSRN requires the partial derivatives from MSRN outputs in terms of MSRN inputs as shown in (B.6).

$$\text{Required for MSRN: } \frac{\partial O_{MSRN}[O]}{\partial I_{MSRN}[I]} \quad (\text{B.6})$$

However, the static reluctance network function (SRN) provides the partial derivatives of SRN outputs in terms of SRN inputs, depicted in (B.7).

$$\text{Obtained from SRN: } \frac{\partial M_{SRN}[M]}{\partial N_{SRN}[N]} \quad (\text{B.7})$$

In order to use the partial derivatives of the SRN outputs to calculate the ones of the MSRN outputs, one needs to update the SRN Jacobian matrix as discussed in Section 6.4.5.1 by using the differential equation as follows:

$$dy = \frac{\partial y}{\partial x_1} dx_1 + \dots + \frac{\partial y}{\partial x_n} dx_n \quad (\text{B.8})$$

where the terms  $\frac{\partial y}{\partial x_n}$  are the partial derivatives of  $y$  with respect to  $x_n$ .

The first step in the procedure is to calculate the partial derivatives of SRN outputs  $M_{SRN}[m]$  in terms of MSRN inputs  $I_{MSRN}[i]$  for each multi-static position, since only the partial derivatives with respect to  $N_{SRN}[n]$  are known a priori.

To calculate the outputs and their partial derivatives, the reluctance network function assumes that all of its input parameters are independent from each other. However, this is not the case when some additional SRN inputs are created as a function of MSRN inputs aiming to manage rotor movement.

This is the case with the SRN input parameters that are calculated as a function of MSRN inputs:  $ts$  (calculated by (4.16)) and all the air-gap reluctances represented by  $LSag_{XY}$  (calculated by (B.5)). Parameter  $ts$  is a function of MSRN inputs  $\omega_g$  and  $\omega_c$  and the  $LSag_{XY}$  are a function of MSRN inputs  $gap$ ,  $slop$ ,  $SlrWidth$  and  $Dis$ .

There are two distinct cases to calculate the derivatives based on the input type and they are analyzed separately.

1. common inputs between MSRN and SRN function  $\omega_g$ ,  $\omega_c$ ,  $gap$  that are used to calculate  $ts$  and  $LSag_{XY}$ .
2. additional MSRN inputs that are not directly SRN inputs, but are used to calculate the air-gap reluctances  $LSag_{XY}$  for SRN function  $slop$ ,  $SlrWidth$  and  $Dis$

### B.3.1.1 CASE 1: SRN inputs are equal to the MSRN inputs

The MSRN inputs that are also SRN inputs and are used to calculate  $ts$  and  $LSag_{XY}$  are  $\omega_g$ ,  $\omega_c$ ,  $gap$ .

The SRN input parameter  $ts$  is calculated from (4.16). The  $ts$  derivatives in terms of  $\omega_g$  and  $\omega_c$  are:

$$\frac{dts}{d\omega_g} = \frac{dts}{d\omega_c} = -\frac{1}{2} \cdot \theta_{rm} \cdot \frac{P_g + P_c}{(\omega_g + \omega_c)^2} \quad (\text{B.9})$$

The partial derivatives of the “ $m_{th}$ ” output from the SRN function  $M_{SRN}[m]$  due to the dependence of  $ts$  in terms of  $\omega_g$  and  $\omega_c$  are given by:

$$\underbrace{\frac{dM_{SRN}[m]}{d\omega_g}}_{\text{updated}} = \underbrace{\frac{\partial M_{SRN}[m]}{\partial \omega_g}}_{\text{SRN}} + \underbrace{\frac{\partial M_{SRN}[m]}{\partial ts}}_{\text{SRN}} \cdot \underbrace{\frac{dts}{d\omega_g}}_{\text{Eq. (B.9)}} \quad (\text{B.10})$$

$$\underbrace{\frac{dM_{SRN}[m]}{d\omega_c}}_{\text{updated}} = \underbrace{\frac{\partial M_{SRN}[m]}{\partial \omega_c}}_{\text{SRN}} + \underbrace{\frac{\partial M_{SRN}[m]}{\partial ts}}_{\text{SRN}} \cdot \underbrace{\frac{dts}{d\omega_c}}_{\text{Eq. (B.9)}} \quad (\text{B.11})$$

The implemented function (B.5) that calculates SRN input parameters  $LSag_{xy}$  and their derivatives in terms of  $\theta_{rm_{mod}}$ ,  $slop$ ,  $StrWidth$ ,  $Dis$  and  $gap$  are presented in Section B.2. The partial derivative of the “ $m_{th}$ ” output of the SRN function  $M_{SRN}[m]$  due to the dependence of  $LSag_{xy}$  in terms of  $gap$  is:

$$\underbrace{\frac{dM_{SRN}[m]}{dgap}}_{\text{updated}} = \underbrace{\frac{\partial M_{SRN}[m]}{\partial gap}}_{\text{SRN}} + \sum_{xy=1}^{N\mathfrak{R}_{ag}} \left( \underbrace{\frac{\partial M_{SRN}[m]}{\partial LSag_{xy}}}_{\text{SRN}} \cdot \underbrace{\frac{dLSag_{xy}}{dgap}}_{\text{Eq. (B.5)}} \right) \quad (\text{B.12})$$

recalling that  $LSag_{xy}$  represents a vector of size 32 containing the air-gap reluctances lengths that are used to take into account rotor movement.

Equations (B.10), (B.11) and (B.12) update the SRN partial derivatives for the MSRN input parameters  $\omega_g$ ,  $\omega_c$  and  $gap$ , respectively. Next step is to calculate the SRN partial derivatives with respect to the additional (extra) MSRN inputs  $slop$ ,  $StrWidth$  and  $Dis$ .



### B.3.1.2 CASE 2: SRN partial derivatives with respect to the additional MSRN inputs

The procedure to obtain these derivatives is similar to the one applied in (B.12). The only difference is that the term regarding the partial derivative of SRN output  $M_{SRN}[m]$  with respect to  $slop$ ,  $SlrWidth$  and  $Dis$  is zero, because they are not inputs of SRN function. The derivative of the  $m_{th}$  output of the SRN function  $M_{SRN}[m]$  due to the dependence of  $LSag_{xy}$  in terms of  $slop$ ,  $SlrWidth$  and  $Dis$  are, respectively:

$$\underbrace{\frac{dM_{SRN}[m]}{dslop}}_{\text{updated}} = \underbrace{\frac{\partial M_{SRN}[m]}{\partial slop}}_{=0} + \sum_{xy=1}^{N\mathfrak{R}_{ag}} \left( \underbrace{\frac{\partial M_{SRN}[m]}{\partial LSag_{xy}}}_{\text{SRN}} \cdot \underbrace{\frac{dLSag_{xy}}{dslop}}_{\text{Eq. (B.5)}} \right) \quad (\text{B.13})$$

$$\underbrace{\frac{dM_{SRN}[m]}{dSlrWidth}}_{\text{updated}} = \underbrace{\frac{\partial M_{SRN}[m]}{\partial SlrWidth}}_{=0} + \sum_{xy=1}^{N\mathfrak{R}_{ag}} \left( \underbrace{\frac{\partial M_{SRN}[m]}{\partial LSag_{xy}}}_{\text{SRN}} \cdot \underbrace{\frac{dLSag_{xy}}{dSlrWidth}}_{\text{Eq. (B.5)}} \right) \quad (\text{B.14})$$

$$\underbrace{\frac{dM_{SRN}[m]}{dDis}}_{\text{updated}} = \underbrace{\frac{\partial M_{SRN}[m]}{\partial Dis}}_{=0} + \sum_{xy=1}^{N\mathfrak{R}_{ag}} \left( \underbrace{\frac{\partial M_{SRN}[m]}{\partial LSag_{xy}}}_{\text{SRN}} \cdot \underbrace{\frac{dLSag_{xy}}{dDis}}_{\text{Eq. (B.5)}} \right) \quad (\text{B.15})$$

The Jacobian matrix update procedure described by (B.10), (B.11), (B.12), (B.13), (B.14) and (B.15) permits to use these values in the calculation of intermediary MSRN outputs  $S_{MSRN}[s]$  for each rotor position. One can assign:

$$\frac{\partial M_{SRN}[m]}{\partial I_{MSRN}[i]} = \underbrace{\frac{\partial M_{SRN}[m]}{\partial N_{SRN}[n]}}_{\text{updated}} \quad (\text{B.16})$$

Next sections explain how the MSRN Jacobian matrix is calculated from the model equations.

## B.3.2 Calculation of the MSRN output partial derivatives

### B.3.2.1 Electromagnetic Torque

#### B.3.2.1.1 Instantaneous torque

From (4.34), the electromagnetic torque partial derivatives according to MSRN inputs are given by:

$$\frac{\partial T_{em}[k]}{\partial I_{MSRN}[i]} = \frac{2}{\Delta\theta_{mmf}} \left( \frac{\partial W_{co}[k + \Delta\theta_{mmf}]}{\partial I_{MSRN}[i]} - \frac{\partial W_{co}[k]}{\partial I_{MSRN}[i]} \right) \Big|_{i \text{ constant}} \quad (\text{B.17})$$

where:

$$\frac{\partial W_{co}[k + \Delta\theta_{mmf}]}{\partial I_{MSRN}[i]} = \underbrace{\frac{\partial W_{co}[k + \Delta\theta_{mmf}]}{\partial N_{SRN}[n]}}_{\text{updated}} \quad (\text{B.18})$$

$$\frac{\partial W_{co}[k]}{\partial I_{MSRN}[i]} = \underbrace{\frac{\partial W_{co}[k]}{\partial N_{SRN}[n]}}_{\text{updated}} \quad (\text{B.19})$$

#### B.3.2.1.2 Mean torque

Then, from (4.35):

$$\frac{\partial T_{emmean}}{\partial I_{MSRN}[i]} = \frac{1}{K} \sum_{k=1}^K \frac{\partial T_{em}[k]}{\partial I_{MSRN}[i]} \quad (\text{B.20})$$

#### B.3.2.2 Flux Linkage

The partial derivatives of the flux linkage according to MSRN inputs are calculated base on (4.40) as follows:

$$\frac{\partial \lambda_{gx}[k]}{\partial I_{MSRN}[i]} = 2 \cdot \sum_{k_{coil}=1}^{N_{coils}} \frac{\partial (Nslg \cdot \phi_{coil_{gx}}[k_{coil}])}{\partial I_{MSRN}[i]} \quad (\text{B.21})$$

$$\frac{\partial \lambda_{cx}[k]}{\partial I_{MSRN}[i]} = 2 \cdot \sum_{k_{coil}=1}^{N_{coils}} \frac{\partial (Nslc \cdot \phi_{coil_{cx}}[k_{coil}])}{\partial I_{MSRN}[i]} \quad (\text{B.22})$$

The number of turns per slot ( $Nslg$  and  $Nslc$ ) are calculated at the MSRN external Java function as a function of the MSRN inputs representing the total number of turns per phase  $Nphg$  and  $Nphc$  as follows:

$$Nslg = \frac{6}{Nsl} \cdot Nphg \quad (\text{B.23})$$

$$Nslc = \frac{6}{Nsl} \cdot Nphc \quad (\text{B.24})$$

Therefore, this dependence must also be taken into account to update the MSRN Jacobian matrix. The derivatives of  $Nslg$  and  $Nslc$  in terms of  $Nphg$  and  $Nphc$  are:

$$\frac{dNslg}{dNphg} = \frac{dNslc}{dNphc} = \frac{6}{Nsl} \quad (\text{B.25})$$

The flux linkage partial derivatives with respect to  $Nslg$  and  $Nslc$  are given by, respectively:

$$\begin{aligned} \frac{\partial \lambda_x[k]}{\partial I_{MSRN}[Nphg]} &= \frac{\partial \lambda_x[k]}{\partial Nphg} = \\ &= 2 \cdot \sum_{k_{coil}=1}^{N_{coils}} \left( \frac{\partial (Nslg)}{\partial I_{MSRN}[Nphg]} \cdot \phi_{coil_x}[k_{coil}] \right) \\ &+ 2 \cdot \sum_{k_{coil}=1}^{N_{coils}} \left( \frac{\partial (\phi_{coil_x}[k_{coil}])}{\partial I_{MSRN}[Nphg]} \cdot Nslg \right) \end{aligned} \quad (\text{B.26})$$

$$\begin{aligned} \frac{\partial \lambda_x[k]}{\partial I_{MSRN}[Nphc]} &= \frac{\partial \lambda_x[k]}{\partial Nphc} = \\ &= 2 \cdot \sum_{k_{coil}=1}^{N_{coils}} \left( \frac{\partial (Nslc)}{\partial I_{MSRN}[Nphc]} \cdot \phi_{coil_x}[k_{coil}] \right) \\ &+ 2 \cdot \sum_{k_{coil}=1}^{N_{coils}} \left( \frac{\partial (\phi_{coil_x}[k_{coil}])}{\partial I_{MSRN}[Nphc]} \cdot Nslc \right) \end{aligned} \quad (\text{B.27})$$

The partial derivatives of  $\lambda_{gx}$  and  $\lambda_{cx}$  for the remaining  $I_{MSRN}[i]$

inputs, different of  $Nphg$  and  $Nphc$ , are given by (B.28) if the phase flux linkage being calculated is from grid winding and by (B.29) if the phase flux linkage is from control winding:

$$\frac{\partial \lambda_{gx}[k]}{\partial I_{MSRN}[i]} = 2 \cdot \sum_{k_{coil}=1}^{N_{coils}} \left( \frac{\partial (\phi_{coil_{gx}}[k_{coil}])}{\partial I_{MSRN}[i]} \cdot Nslg \right) \quad (\text{B.28})$$

$$\frac{\partial \lambda_{cx}[k]}{\partial I_{MSRN}[i]} = 2 \cdot \sum_{k_{coil}=1}^{N_{coils}} \left( \frac{\partial (\phi_{coil_{cx}}[k_{coil}])}{\partial I_{MSRN}[i]} \cdot Nslc \right) \quad (\text{B.29})$$

### B.3.2.3 Induced phase voltage $E$

#### B.3.2.3.1 Instantaneous induced phase voltage $E$

The induced phase voltage derivatives with respect to  $I_{MSRN}[i]$  are calculated from (4.42) and are given by (B.30) for all inputs, except for the inputs  $I_{MSRN}[\omega_g]$  and  $I_{MSRN}[\omega_c]$  that are given, respectively, by (B.32) and (B.33), since the  $\Delta t$  (4.43) parameter depends on these values.

$$\frac{\partial e_{g,cx}[k]}{\partial I_{MSRN}[i]} = \frac{1}{2 \cdot \Delta t} \cdot \left( \frac{\partial \lambda_{g,cx}[k+1]}{\partial I_{MSRN}[i]} - \frac{\partial \lambda_{g,cx}[k-1]}{\partial I_{MSRN}[i]} \right) \quad (\text{B.30})$$

The derivative of  $\Delta t$  with respect to  $\omega_g$  and  $\omega_c$  is:

$$\frac{d\Delta t}{d\omega_g} = \frac{d\Delta t}{d\omega_c} = -\frac{1}{2} \Delta \theta_{rm} \cdot \frac{P_g + P_c}{(\omega_g + \omega_c)^2} \quad (\text{B.31})$$

Thus:

$$\begin{aligned} \frac{\partial e_{g,cx}[k]}{\partial I_{MSRN}[\omega_g]} &= \frac{1}{2 \cdot \Delta t} \cdot \left( \frac{\partial \lambda_{g,cx}[k+1]}{\partial I_{MSRN}[i]} - \frac{\partial \lambda_{g,cx}[k-1]}{\partial I_{MSRN}[i]} \right) \\ &\quad - \frac{1}{2} \cdot \left( \frac{\lambda_{g,cx}[k+1] - \lambda_{g,cx}[k-1]}{(\Delta t)^2} \right) \cdot \frac{d\Delta t}{d\omega_g} \end{aligned} \quad (\text{B.32})$$

$$\begin{aligned} \frac{\partial e_{g,cx}[k]}{\partial I_{MSRN}[\omega_c]} &= \frac{1}{2 \cdot \Delta t} \cdot \left( \frac{\partial \lambda_{g,cx}[k+1]}{\partial I_{MSRN}[i]} - \frac{\partial \lambda_{g,cx}[k-1]}{\partial I_{MSRN}[i]} \right) \\ &\quad - \frac{1}{2} \cdot \left( \frac{\lambda_{g,cx}[k+1] - \lambda_{g,cx}[k-1]}{(\Delta t)^2} \right) \cdot \frac{d\Delta t}{d\omega_c} \end{aligned} \quad (\text{B.33})$$

### B.3.2.3.2 RMS induced phase voltage $E$

From (4.44):

$$\frac{\partial E_{g,cx_{rms}}}{\partial I_{MSRN}[i]} = \frac{\sum_{k=1}^K e_{g,cx}[k] \cdot \frac{\partial e_{g,cx}[k]}{\partial I_{MSRN}[i]}}{K \cdot E_{g,cx_{rms}}} \quad (\text{B.34})$$

where  $K$  is the number of rotor positions.

### B.3.2.4 Terminal phase voltage $V$

#### B.3.2.4.1 Instantaneous terminal phase voltage $V$

In order to calculate the terminal voltages  $v_{gx}$  and  $v_{cx}$  by using from (4.45), the phase resistances must be provided to the MSRN external Java function as input. Therefore, the partial derivative of MSRN outputs with respect to the  $R_g$  and  $R_c$  parameters must also be assessed. Except for the terminal voltages, the partial derivatives of all other MSRN output parameters in terms of the resistances are zero. Only the terminal phase voltages  $v_{gx}$  and  $v_{cx}$  depend on this parameter.

The partial derivatives from (4.45) with respect to  $I_{MSRN}$  are given by (B.35), except for the input  $R_g$  that are given by (B.36).

$$\frac{\partial v_{gx}[k]}{\partial I_{MSRN}[i]} = R_g \cdot \frac{\partial i_{gx}[k]}{\partial I_{MSRN}[i]} + \frac{\partial e_{gx}[k]}{\partial I_{MSRN}[i]} \quad (\text{B.35})$$

$$\begin{aligned} \frac{\partial v_{gx}[k]}{\partial I_{MSRN}[R_g]} &= i_{gx}[k] + R_g \cdot \underbrace{\frac{\partial i_{gx}[k]}{\partial I_{MSRN}[R_g]}}_{=0} + \underbrace{\frac{\partial e_{gx}[k]}{\partial I_{MSRN}[R_g]}}_{=0} = i_{gx}[k] \end{aligned} \quad (\text{B.36})$$

Similarly, the partial derivatives from (4.46) with respect to  $I_{MSRN}$  are given by (B.37), except for the input  $R_c$  that are given by (B.38).

$$\frac{\partial v_{cx}[k]}{\partial I_{MSRN}[i]} = R_c \cdot \frac{\partial i_{cx}[k]}{\partial I_{MSRN}[i]} + \frac{\partial e_{cx}[k]}{\partial I_{MSRN}[i]} \quad (\text{B.37})$$

$$\frac{\partial v_{cx}[k]}{\partial I_{MSRN}[R_c]} = i_{cx}[k] + R_c \cdot \underbrace{\frac{\partial i_{cx}[k]}{\partial I_{MSRN}[R_c]}}_{=0} + \underbrace{\frac{\partial e_{cx}[k]}{\partial I_{MSRN}[R_c]}}_{=0} = i_{cx}[k] \quad (\text{B.38})$$

### B.3.2.4.2 RMS terminal phase voltage $V$

From (4.47):

$$\frac{\partial V_{g,cx_{rms}}}{\partial I_{MSRN}[i]} = \frac{\sum_{k=1}^K v_{g,cx}[k] \cdot \frac{\partial v_{g,cx}[k]}{\partial I_{MSRN}[i]}}{K \cdot V_{g,cx_{rms}}} \quad (\text{B.39})$$

where  $K$  is the number of rotor positions.

### B.3.2.5 Currents

The instantaneous phase currents are calculated inside the MSRN function to evaluate the instantaneous terminal voltages and the power as shown in the sequence. Therefore, their partial derivatives must also be calculated since they are used to compose the Jacobian matrix of the aforementioned parameters.

The three phase currents are:

$$\begin{aligned} i_{ga}[k] &= I_g \cos(\omega_g ts[k]) \\ i_{gb}[k] &= I_g \cos(\omega_g ts[k] - 2\pi/3) \\ i_{gc}[k] &= I_g \cos(\omega_g ts[k] + 2\pi/3) \end{aligned} \quad (\text{B.40})$$

$$\begin{aligned} i_{ca}[k] &= I_c \cos(\omega_c ts[k] - \alpha_c) \\ i_{cb}[k] &= I_c \cos(\omega_c ts[k] - 2\pi/3 - \alpha_c) \\ i_{cc}[k] &= I_c \cos(\omega_c ts[k] + 2\pi/3 - \alpha_c) \end{aligned} \quad (\text{B.41})$$

where:

$\alpha_c$

is the phase difference between the two sets of three phase windings

Since the currents depend only on the MSRN input parameters  $I_g$ ,  $I_c$ ,  $\omega_g$ ,  $\omega_c$  and  $\alpha_c$ , the MSRN partial derivatives are non-zero only for these parameters and their calculations are shown in the sequence.

### B.3.2.5.1 Partial derivative with respect to $I_g$ and $I_c$ :

$$\begin{aligned}\frac{\partial i_{ga}[k]}{\partial I_g} &= \cos(\omega_g ts[k]) \\ \frac{\partial i_{gb}[k]}{\partial I_g} &= \cos(\omega_g ts[k] - 2\pi/3) \\ \frac{\partial i_{gc}[k]}{\partial I_g} &= \cos(\omega_g ts[k] + 2\pi/3)\end{aligned}\tag{B.42}$$

$$\begin{aligned}\frac{\partial i_{ca}[k]}{\partial I_c} &= \cos(\omega_c ts[k] - \alpha_c) \\ \frac{\partial i_{cb}[k]}{\partial I_c} &= \cos(\omega_c ts[k] - 2\pi/3 - \alpha_c) \\ \frac{\partial i_{cc}[k]}{\partial I_c} &= \cos(\omega_c ts[k] + 2\pi/3 - \alpha_c)\end{aligned}\tag{B.43}$$

### B.3.2.5.2 Partial derivative with respect to $\alpha_c$ :

$$\begin{aligned}\frac{\partial i_{ca}[k]}{\partial \alpha_c} &= I_c \sin(\omega_c ts[k] - \alpha_c) \\ \frac{\partial i_{cb}[k]}{\partial \alpha_c} &= I_c \sin(\omega_c ts[k] - 2\pi/3 - \alpha_c) \\ \frac{\partial i_{cc}[k]}{\partial \alpha_c} &= I_c \sin(\omega_c ts[k] + 2\pi/3 - \alpha_c)\end{aligned}\tag{B.44}$$

### B.3.2.5.3 Partial derivative with respect to $\omega_g$ and $\omega_c$ :

$$\begin{aligned}\frac{\partial i_{ga}[k]}{\partial \omega_g} &= -I_g \sin(\omega_g ts[k]) \cdot \left( ts[k] + \omega_g \cdot \frac{dts}{d\omega_g} \right) \\ \frac{\partial i_{gb}[k]}{\partial \omega_g} &= -I_g \sin(\omega_g ts[k] - 2\pi/3) \cdot \left( ts[k] + \omega_g \cdot \frac{dts}{d\omega_g} \right) \\ \frac{\partial i_{gc}[k]}{\partial \omega_g} &= -I_g \sin(\omega_g ts[k] + 2\pi/3) \cdot \left( ts[k] + \omega_g \cdot \frac{dts}{d\omega_g} \right)\end{aligned}\tag{B.45}$$

$$\begin{aligned}
\frac{\partial i_{ca}[k]}{\partial \omega_c} &= -I_c \sin(\omega_c ts[k] - \alpha_c) \cdot \left( ts[k] + \omega_c \cdot \frac{dts}{d\omega_c} \right) \\
\frac{\partial i_{cb}[k]}{\partial \omega_c} &= -I_c \sin(\omega_c ts[k] - 2\pi/3 - \alpha_c) \cdot \left( ts[k] + \omega_c \cdot \frac{dts}{d\omega_c} \right) \\
\frac{\partial i_{cc}[k]}{\partial \omega_c} &= -I_c \sin(\omega_c ts[k] + 2\pi/3 - \alpha_c) \cdot \left( ts[k] + \omega_c \cdot \frac{dts}{d\omega_c} \right)
\end{aligned} \tag{B.46}$$

### B.3.2.5.4 Partial derivative of the rms current values

The partial derivatives of the RMS value of phase currents  $i_{g,cx_{rms}}$  are:

$$I_{g,cx_{rms}} = \sqrt{\frac{1}{K} \sum_{k=1}^K (i_{g,cx}[k])^2} \tag{B.47}$$

$$\frac{\partial I_{g,cx_{rms}}}{\partial I_{MSRN}[i]} = \frac{\sum_{k=1}^K i_{g,cx}[k] \cdot \frac{\partial i_{g,cx}[k]}{\partial I_{MSRN}[i]}}{K \cdot I_{g,cx_{rms}}} \tag{B.48}$$

### B.3.2.6 Real Power

The instantaneous power per phase are calculated from (4.48) for the internal and from (4.49) for the terminal power. Their partial derivatives are, respectively:

$$\begin{aligned}
\frac{\partial P_{intgx}[k]}{\partial I_{MSRN}[i]} &= \frac{\partial e_{gx}[k]}{\partial I_{MSRN}[i]} \cdot i_{gx}[k] + \frac{\partial i_{gx}[k]}{\partial I_{MSRN}[i]} \cdot e_{gx}[k] \\
\frac{\partial P_{intcx}[k]}{\partial I_{MSRN}[i]} &= \frac{\partial e_{cx}[k]}{\partial I_{MSRN}[i]} \cdot i_{cx}[k] + \frac{\partial i_{cx}[k]}{\partial I_{MSRN}[i]} \cdot e_{cx}[k]
\end{aligned} \tag{B.49}$$

$$\begin{aligned}
\frac{\partial P_{tergx}[k]}{\partial I_{MSRN}[i]} &= \frac{\partial v_{gx}[k]}{\partial I_{MSRN}[i]} \cdot i_{gx}[k] + \frac{\partial i_{gx}[k]}{\partial I_{MSRN}[i]} \cdot v_{gx}[k] \\
\frac{\partial P_{tercx}[k]}{\partial I_{MSRN}[i]} &= \frac{\partial v_{cx}[k]}{\partial I_{MSRN}[i]} \cdot i_{cx}[k] + \frac{\partial i_{cx}[k]}{\partial I_{MSRN}[i]} \cdot v_{cx}[k]
\end{aligned} \tag{B.50}$$



Therefore, from (4.50) and (4.51), the real power per phase is:

$$\begin{aligned}\frac{\partial P_{act_{gx\_int}}}{\partial I_{MSRN}[i]} &= \frac{1}{K} \sum_{k=1}^K \frac{\partial P_{intgx}[k]}{\partial I_{MSRN}[i]} \\ \frac{\partial P_{act_{cx\_int}}}{\partial I_{MSRN}[i]} &= \frac{1}{K} \sum_{k=1}^K \frac{\partial P_{intcx}[k]}{\partial I_{MSRN}[i]}\end{aligned}\tag{B.51}$$

$$\begin{aligned}\frac{\partial P_{act_{gx\_ter}}}{\partial I_{MSRN}[i]} &= \frac{1}{K} \sum_{k=1}^K \frac{\partial P_{tergx}[k]}{\partial I_{MSRN}[i]} \\ \frac{\partial P_{act_{cx\_ter}}}{\partial I_{MSRN}[i]} &= \frac{1}{K} \sum_{k=1}^K \frac{\partial P_{tercx}[k]}{\partial I_{MSRN}[i]}\end{aligned}\tag{B.52}$$

### B.3.2.7 Flux density in several parts of the machine

#### B.3.2.7.1 Instantaneous inductions levels

The flux densities at the selected reluctances in stator teeth ( $B_{th}$ ), stator yokes ( $B_{yk}$ ) and rotor flux path ( $B_{rt}$ ) are calculated directly by the static reluctance network as shown in Section 4.5.7 and are part of vector  $M_{SRN}[m]$ . The SRN Jacobian matrix updated values may be used directly to calculate their absolute maximum values required by the MSRN outputs.

#### B.3.2.7.2 Absolute maximum inductions levels

The partial derivatives of  $|B_{th,max}|$ ,  $|B_{yk,max}|$  and  $|B_{rt,max}|$  are obtained from the partial derivatives of  $B_{th}$ [24],  $B_{yk}$ [24] and  $B_{rt}$ [18] that are calculated as discussed in Section 4.5.7 for all rotor positions. The absolute maximum value is obtained by comparing among each other all the values within the vectors  $B_{th}$ [24],  $B_{yk}$ [24] and  $B_{rt}$ [18]. Once the maximum absolute value has been identified, the partial derivative to be used in the Jacobian matrix of MSRN output vector  $O_{MSRN}$  is the one corresponding to the identified maximum induction. However, before assigning the partial derivatives to the MSRN Jacobian matrix, one should take into account the use of the absolute value function, shown in Fig. B.1. If the  $x$  value is positive,  $|x|$  derivative is also positive. Oppositely, if  $x$  is negative,  $|x|$  derivative is negative, as shown in (B.53).

$$\begin{aligned} \frac{d|x|}{dx} &= +1 & \left| \begin{array}{l} x > 0 \\ \hline x < 0 \end{array} \right. \end{aligned} \quad (\text{B.53})$$

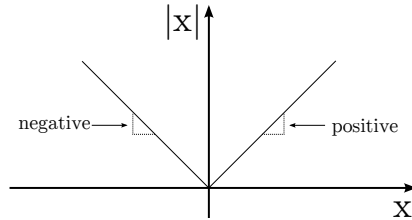


Figure B.1: Absolute value function.

The partial derivatives of  $|B_{th_{max}}|$ ,  $|B_{yk_{max}}|$  and  $|B_{rt_{max}}|$  are given by (B.54):

$$\begin{aligned} \frac{\partial |B_{max}|}{\partial I_{MSRN}[i]} &= + \frac{\partial B_{max}}{\partial I_{MSRN}[i]} & \left| \begin{array}{l} \text{if } B_{max} > 0 \\ \hline \text{if } B_{max} < 0 \end{array} \right. \end{aligned} \quad (\text{B.54})$$

where  $B_{max}$  can be  $B_{th_{max}}$ ,  $B_{yk_{max}}$  or  $B_{rt_{max}}$ .

## B.4 Graph theory definitions

This section presents the definitions used on the discussions regarding graph theory. These definitions have been taken from reference [139].

Graph theory is used to describe the geometrical structure of a network. To do so for an electrical circuit or a network, one can replace the network components by single lines. These lines are called *elements* and their terminals are called *nodes*. A node and an element are *incident* if a node is a terminal of the element.

A *graph* represents the geometrical interconnection of the elements of a network and a *subgraph* is any subset of elements of the graph.

A *path* is a subgraph of connected elements with no more than two elements connected to any one node. A graph is *connected* if and only if there is a path between every pair of nodes. A connected subgraph containing all nodes of a graph but no closed path is called a *tree*. The elements of a tree are called *branches* and form a subset of the elements of the connected graph. The elements of the connected graph that are not included in the tree are called *links*. If a link is added to the tree, the resulting graph contains one closed path, called a *loop*. Loops which contain only one link are independent and are called *basic loops*.

## B.5 Definition of the coil vectors to calculate the phase flux linkage in the MSRN model

This section refers to the calculation of the phase flux linkage presented in Section 4.5.3.

Fig. B.2 shows the grid and control windings definition for the BDFRM MSRN model. The Static Reluctance Network function (SRN) returns the flux passing through the reluctance  $R_{sthh}$ , defined in Fig. 4.33. These fluxes are designated by the terms  $\phi_{th_x}$  for all the phases of grid and control windings ( $x = ga, gb, gc, ca, cb, cc$ ).

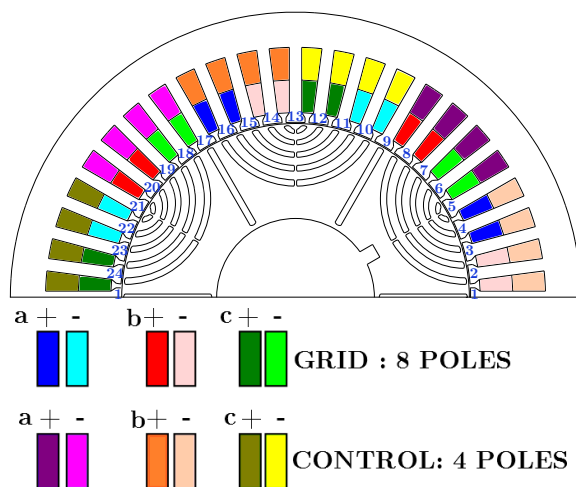


Figure B.2: Flux linkage calculation for all of the phases from grid and control windings at initial position ( $0 \leq \theta_{rm} < \psi_{st} = 360/Nsl$ ).

Table B.3 defines the vectors  $\phi_{coil_x}[k_{coil}]$  representing the magnetic flux passing through a coil and are used to calculate the phase flux linkage  $\lambda_x$ . They are based on the winding configuration depicted in Fig. B.2. Recalling that:

$$\lambda_{coil_x}[k_{coil}] = Nsl_{g,c} \cdot \phi_{coil_x}[k_{coil}] \quad (\text{B.55})$$

where  $\lambda_{coil_x}[k_{coil}]$  is the flux linkage of the coil being calculated and  $Nsl_{g,c}$  represents the number of conductor in a slot for the grid or control windings.

Table B.3: Definition of the stator teeth fluxes  $\phi_{th_{g,cx}}$  that are part of each coil  $\phi_{coil_{g,cx}}[k_{coil}]$  in the BDFRM.

<b>Coil</b> $\phi_{coil_x}[k_{coil}]$	<b>Vector of the indexes that points to flux <math>\phi_{th_x}</math> passing through reluctance <math>R_{sthh}</math> (SRN model), according to Fig. B.2</b>
$\phi_{coil_{ga}}[1]$	22 23 24 1 2 3
$\phi_{coil_{ga}}[2]$	23 24 1 2 3 4
$\phi_{coil_{ga}}[3]$	10 11 12 13 14 15
$\phi_{coil_{ga}}[4]$	11 12 13 14 15 16
$\phi_{coil_{gb}}[1]$	2 3 4 5 6 7
$\phi_{coil_{gb}}[2]$	3 4 5 6 7 8
$\phi_{coil_{gb}}[3]$	14 15 16 17 18 19
$\phi_{coil_{gb}}[4]$	15 16 17 18 19 20
$\phi_{coil_{gc}}[1]$	6 7 8 9 10 11
$\phi_{coil_{gc}}[2]$	7 8 9 10 11 12
$\phi_{coil_{gc}}[3]$	18 19 20 21 22 23
$\phi_{coil_{gc}}[4]$	19 20 21 22 23 24
$\phi_{coil_{ca}}[1]$	18 19 20 21 22 23 24 1 2 3 4 5
$\phi_{coil_{ca}}[2]$	19 20 21 22 23 24 1 2 3 4 5 6
$\phi_{coil_{ca}}[3]$	20 21 22 23 24 1 2 3 4 5 6 7
$\phi_{coil_{ca}}[4]$	21 22 23 24 1 2 3 4 5 6 7 8
$\phi_{coil_{cb}}[1]$	2 3 4 5 6 7 8 9 10 11 12 13
$\phi_{coil_{cb}}[2]$	3 4 5 6 7 8 9 10 11 12 13 14
$\phi_{coil_{cb}}[3]$	4 5 6 7 8 9 10 11 12 13 14 15
$\phi_{coil_{cb}}[4]$	5 6 7 8 9 10 11 12 13 14 15 16
$\phi_{coil_{cc}}[1]$	10 11 12 13 14 15 16 17 18 19 20 21
$\phi_{coil_{cc}}[2]$	11 12 13 14 15 16 17 18 19 20 21 22
$\phi_{coil_{cc}}[3]$	12 13 14 15 16 17 18 19 20 21 22 23
$\phi_{coil_{cc}}[4]$	13 14 15 16 17 18 19 20 21 22 23 24



# Appendix C

## Analytical calculation of the flux density in air-gap, leakage inductances and effective air-gap

### C.1 Air-gap flux density calculation for a radially laminated ducted rotor

The technique proposed by Knight *et al.* [81, 82, 11] has been chosen to estimate analytically the air-gap flux density in the Semi-Analytical Model (SAM). The procedure is described in the aforementioned references, but the basic equations are shown in the sequence based on these works.

The idea behind this approach is to consider the ducted rotor as a perfect flux guide, similar to the axially laminated rotor without the possibility of significant eddy currents in the laminations [11].

Fig. C.1 shows a linearized rotor pole with the angle definition.

From C.1, it can be inferred that the following relationship among the angles hold, considering  $\theta_{rm0}$  as the initial rotor position.

$$\theta_{ag}^{DR} = \theta_{ag} + \lambda_r - 2\sigma_r \quad (C.1)$$

The parameter  $\lambda_r$  is the arc angle corresponding to one rotor pole, defined by

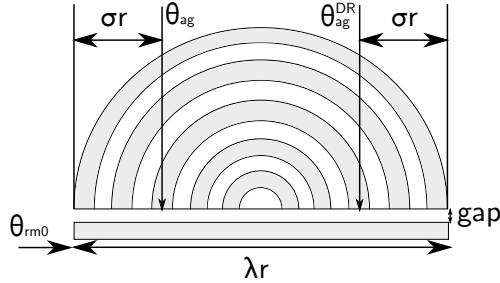


Figure C.1: Angles definition to calculate flux density around the machine in SAM. Adapted from [82].

$$\lambda_r = \frac{2\pi}{P_r} \quad (\text{C.2})$$

where  $P_r$  is the number of rotor poles.

The angle  $\sigma_r$  is the arc between the initial position of the rotor pole and  $\theta_{ag}$ . Notice that it is also the same arc angle in the other extremity of the rotor from  $\theta_{ag}^{DR}$  up to the end of the rotor pole. This is the case, since we are considering a symmetric rotor.

The angle  $\sigma_r$  is a periodic function with respect to the rotor pole  $\lambda_r$ . Thus, it can be calculated by:

$$\sigma_r = \text{mod}(\theta_{ag} - \theta_{rm0}, \lambda_r) \quad (\text{C.3})$$

As it is assumed an infinitely permeable magnetic material (idealized rotor), the magnetomotive force  $\mathbb{F}$  through any flux path is given by the difference between the  $\mathbb{F}$  at the two flux path extremities in the air-gap C.4.

$$\mathbb{F}_{fp} = \mathbb{F}(\theta_{ag}) - \mathbb{F}(\theta_{ag}^{DR}) \quad (\text{C.4})$$

From Ampere's law, it can be deduced that the air-gap flux density is given by C.5.

$$B_{gap}(\theta_{ag}, t) = \frac{\mu_0}{2 \cdot \text{gap}} [\mathbb{F}_p(\theta_{ag}, t) - \mathbb{F}_p(\theta_{ag}^{DR}, t)] \quad (\text{C.5})$$

where:



$gap$	$\triangleq$	air-gap length.
$\theta_{ag}^{DR}$	$\triangleq$	angle around the machine air-gap periphery corresponding to the other extremity of the flux path starting at position $\theta_{ag}$ .
$\mathbb{F}_p$	$\triangleq$	magnetomotive force MMF. In (3.12), $p$ may refer to a single or a three phase MMF.

Therefore, if one knows the magnetomotive force around the air-gap, it is possible to use (C.5) to calculate the air-gap flux density at any rotor position and at any time considering an idealized ducted rotor, similar to the one depicted in Fig. 1.17(c). In the BDFRM with two sets of three phase windings, the  $\mathbb{F}$  can be analytically calculated by (1.8). This approach is general and it is also valid for single phase excitation, as used to calculate BDFRM inductances in Chapter 3. Example of the use of the analytical estimation of  $B_{gap}$  to calculate inductances and flux densities around the machine are presented in Appendix G.

## C.2 Strategy to evaluate coupling effectiveness among different number of poles possibilities

Knight *et al.* [81, 82, 11] propose a solution to quantitatively determine the coupling factors for different combinations of number of poles in order to help the designer to choose the most appropriated solution for a specific application. The procedure presented in the aforementioned references is briefly described in the sequence and it is used to define the number of poles combination of the machine topology that will be investigated in this thesis.

### C.2.0.8 Quantifying the coupling factors for different poles combinations assuming an idealized RLDR by using the Fourier series method

#### C.2.0.8.1 The use of a normalized air-gap flux density function

This strategy assumes an idealized version of the radially laminated ducted rotor (RLDR) in the calculations. To evaluate the coupling factors, the references [81, 82, 11] define a normalized function  $\beta$ , that is the ratio between the air-gap flux density  $B_{gap}$  (C.5) calculated by using the RLDR for each combination of the number of poles and the

*amplitude* of the air-gap flux density that one would obtain if a round rotor were used, represented by  $B_{round}^{pk}$ . The normalized function is defined by:

$$\beta(\theta_{ag}) = \frac{B_{gap}}{B_{round}^{pk}} \quad (C.6)$$

### C.2.0.8.2 The air-gap flux density considering a uniform and solid (round) rotor

Equation (C.6) also requires the amplitude of the air-gap flux density from a uniform and solid (round) rotor, represented by  $B_{round}$  and given by [88]:

$$\begin{aligned} B_{round}(\theta_{ag}, t) &= \frac{\mu_0}{gap} \mathbb{F}_{3\phi}(\theta_{ag}, t) \\ &= \frac{\mu_0}{gap} M_{3j} \cos\left(\omega_j t - \frac{P_j}{2} \theta_{ag} + \phi_{aj}\right) \end{aligned} \quad (C.7)$$

Particularly, we are interested in the amplitude of (C.7), which is given by:

$$B_{round}^{pk} = \frac{\mu_0}{gap} M_{3j} \quad (C.8)$$

### C.2.0.8.3 The resulting normalized function for the RLDR

The fundamental component of the magnetomotive force of a three phase winding set “ $j$ ” used to calculate  $B_{gap}$  is given by:

$$\mathbb{F}_{3\phi j}(\theta_{ag}, t) = M_{3j} \cos\left(\omega_j t - \frac{P_j}{2} \theta_{ag} + \phi_{aj}\right) \quad (C.9)$$

where:

- $P_j$  → number of poles
- $M_{3j}$  → amplitude of the fundamental magnetomotive force considering the contribution of the three phases of winding “ $j$ ”. It is calculated by (1.6)
- $\phi_{aj}$  → reference position of winding “ $j$ ” (phase a axis)

Notice that  $\mathbb{F}_{3\phi_j}$  and consequently  $B_{gap}$  in (C.5) is a function of  $\theta_{ag}$  and  $t$ . At this time, it is investigated the coupling factors due to the spatial harmonics to define the number of poles, thus the parameter time can be set to  $t = 0s$  for the following analysis. The reference axis  $\phi_{aj}$  of the three phase windings are zero according to the definition presented in Fig. 2.6 and Fig. 2.7.

Substituting (C.5) and (C.8) into (C.6) results in:

$$\begin{aligned}\beta_j(\theta_{ag}) &= \frac{B_{gap}(\theta_{ag})}{\frac{\mu_0}{g} M_{3j}} \\ &= \frac{[\mathbb{F}(\theta_{ag}) - \mathbb{F}(\theta_{ag}^{DR})]}{2M_{3j}} \\ &= \frac{1}{2} \left[ \cos\left(\frac{P_j}{2}\theta_{ag}\right) - \cos\left(\frac{P_j}{2}\theta_{ag}^{DR}\right) \right]\end{aligned}\tag{C.10}$$

where  $\theta_{ag}$  and  $\theta_{ag}^{DR}$  are defined in Fig. C.1 and index  $j$  may refer to grid or control windings.

#### C.2.0.8.4 Using the Fourier series approach to calculate the coupling factors

The magnitude of the Fourier series can be used to estimate the rotor capability to provide coupling between the windings. The general idea proposed in [11, 81, 82] is to calculate the air-gap flux density of space order  $i$  produced as a result of the modulation of the MMF harmonic of space order  $j$  by the rotor structure. This modulation is defined in terms of a coupling factor  $C_{ij}$  between the three phase winding sets <sup>1</sup>.

The amplitude of the air-gap flux density of space harmonic  $i$ ,  $B_i$ , can be calculated by:

$$B_i^{pk} = C_{ij} \frac{\mu_0}{g} M_{3j}^{pk}\tag{C.11}$$

The parameter  $C_{ij}$  can be calculate by the magnitude of the corresponding space harmonic obtained by using the Fourier Series approach:

$$C_{ij} = \sqrt{a_{ij}^2 + b_{ij}^2}\tag{C.12}$$

---

<sup>1</sup> $i$  and  $j$  may be  $c$  or  $g$ , representing control or grid windings, respectively

$$a_{ij} = \frac{1}{\pi} \int_0^{2\pi} \beta_j(\theta_m) \cos\left(\frac{P_i}{2}\theta_m\right) d\theta_m \quad (\text{C.13})$$

$$b_{ij} = \frac{1}{\pi} \int_0^{2\pi} \beta_j(\theta_m) \sin\left(\frac{P_i}{2}\theta_m\right) d\theta_m \quad (\text{C.14})$$

The resulting coupling factors are presented in Table 2.1 for several number of poles combinations.

## C.3 Leakage inductances

### C.3.1 Estimation of the leakage inductances per phase for the SAM

Three kinds of leakage inductances based on reference [119] are considered: the slot and tooth top, the zig zag and the differential flux leakage inductances. More details on this topic can be found in [87, 42, 37].

Based on the definitions presented in Fig. C.2, the slot and tooth top leakage inductance are given by [119] (C.15) and (C.16) for grid and control windings, respectively:

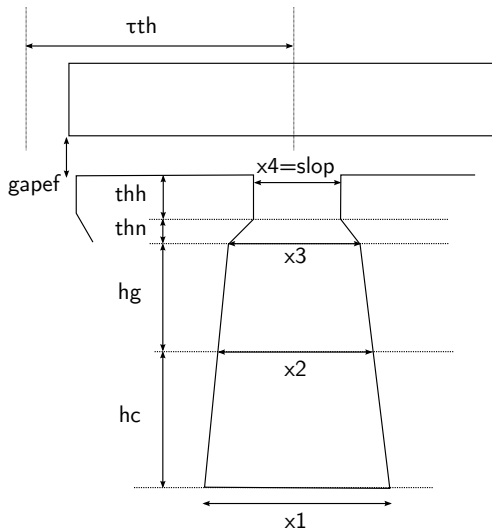


Figure C.2: Leakage inductances calculation.

For the grid winding, assumed to be placed near the air-gap:

$$L_{slg} = \mu_0 \cdot Nslg^2 \cdot L_{stkef} \cdot \left[ \frac{2hg}{3(x2 + x3)} + \frac{thn}{x3 - x4} \ln \left( \frac{x3}{x4} \right) + \frac{thh}{x4} + \frac{gapef}{\tau_{th}} \right] \quad (C.15)$$

For the control winding, assumed to be placed near the stator yoke:

$$L_{slc} = \mu_0 \cdot Nslc^2 \cdot L_{stkef} \cdot \left[ \frac{2hc}{3(x1 + x2)} + \frac{2hg}{(x2 + x3)} + \frac{thn}{x3 - x4} \ln \left( \frac{x3}{x4} \right) + \frac{thh}{x4} + \frac{gapef}{\tau_{th}} \right] \quad (C.16)$$

where  $Nslg$  and  $Nslc$  are, respectively, the number of conductors in one slot for the grid and control windings and  $\tau_{th}$  is given by (C.17).

$$\tau_{th} = \frac{2\pi}{Nsl} \cdot r_{gap} \quad (C.17)$$

The zig zag inductance refers to the coupling where the flux density path zig-zags between teeth on opposing sides of the air gap [42] and can be calculated by [119]:

$$L_{lzg} = \mu_0 \cdot Nslg^2 \cdot L_{stkef} \cdot \frac{(\tau_{th} - slop)^2}{8 \cdot gapef \cdot \tau_{th}} \quad (C.18)$$

$$L_{lzc} = \mu_0 \cdot Nslc^2 \cdot L_{stkef} \cdot \frac{(\tau_{th} - slop)^2}{8 \cdot gapef \cdot \tau_{th}} \quad (C.19)$$

The leakage inductance due to the differential flux is given by [119]:

$$L_{ldg} = 0.0025 \cdot \mu_0 \cdot Nslg^2 \cdot L_{stkef} \cdot \frac{\tau_{wgdem}^2}{\pi^2 \cdot gapef \cdot \tau_{th}} \quad (C.20)$$

where  $\tau_{wgdem} = \frac{2\pi}{P_g} \cdot r_{gap}$

$$L_{ldc} = 0.0025 \cdot \mu_0 \cdot Nslc^2 \cdot L_{stkef} \cdot \frac{\tau_{wcdem}^2}{\pi^2 \cdot gapef \cdot \tau_{th}} \quad (C.21)$$

where  $\tau_{wcdem} = \frac{2\pi}{P_c} \cdot r_{gap}$

The total leakage inductance is obtained by accounting the number of slots used to assembly the each phase windings windings.

$$L_{lg} = \frac{Nsl}{3} \cdot (L_{slg} + L_{lzg} + L_{ldg}) \quad (C.22)$$

$$L_{lc} = \frac{Nsl}{3} \cdot (L_{sllc} + L_{lzc} + L_{ldc}) \quad (\text{C.23})$$

where  $Nsl$  is the number of stator slots.

The leakage inductances previously defined are an attempt to estimate this parameter to be used with the Semi-Analytical model (SAM). The analytical calculation of the leakage inductances from the structural dimensions of the machine is a rather demanding task [37], where many idealized hypothesis shall be assumed. The results presented here are considered sufficient for the purpose of the SAM.

### C.3.2 Equivalent reluctance to take into account the stator slot leakage flux for the MSRN model

This section outlines the calculation of an equivalent slot reluctance that takes into account the leakage flux among two stator teeth and it is based on reference [119].

For the discussion that follows, let us consider the definitions in the simplified stator slot of Fig. C.3.

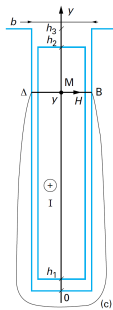


Figure C.3: Simplified stator slot. Adapted from [119].

The goal of this calculation is to obtain analytically the stator slot leakage flux and associate a reluctance to it. For that purpose, let us assume that the magnetic material is infinitely permeable and that the magnetic field distribution in the slot is given by the one presented in Fig. C.4.

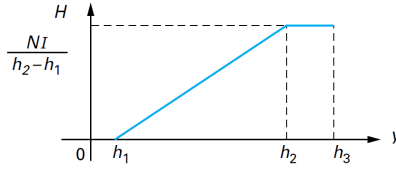


Figure C.4: Considered magnetic field distribution in the stator slot. Adapted from [119].

From Fig. C.4 and by applying Ampère's law to the slot depicted in Fig. C.3, one gets:

$$\int H dl = bH(y) \quad (\text{C.24})$$

Two distinct regions can be assessed:

(i)  $h_1 < y < h_2$ :

$$H(y) = \frac{NI}{b} \left( \frac{y - h_1}{h_2 - h_1} \right) \quad (\text{C.25})$$

(ii)  $y > h_2$ :

$$H(y) = \frac{NI}{b} \quad (\text{C.26})$$

where  $N$  is the number of turns in the slot.

The differential flux linkage  $\lambda_l$  "seen" by the winding in terms of  $dy$  is given by:

$$d\lambda_l = \mu_0 \underbrace{\frac{N}{h_2 - h_1} (y - h_1)}_{N(y)} LH(y) dy \quad (\text{C.27})$$

where  $L$  is the machine axial length.

Substituting (C.25) and (C.26) into (C.27) and integrating from 0 up to  $h_3$  yields:

$$\lambda_l = \mu_0 L \frac{N^2 I}{b} \left[ \int_{h_1}^{h_2} \left( \frac{y - h_1}{h_2 - h_1} \right)^2 dy + \int_{h_2}^{h_3} dy \right] \quad (\text{C.28})$$

Solving:

$$\lambda_l = \mu_0 L \frac{N^2 I}{b} \left[ \frac{h_2 - h_1}{3} + (h_3 - h_2) \right] \quad (\text{C.29})$$

The slot leakage inductance is defined by  $L_l = \lambda_l / I$ . Therefore:

$$L_l = \frac{\lambda_l}{I} = \frac{N\phi}{I} = \mu_0 L \frac{N^2}{b} \left[ \frac{h_2 - h_1}{3} + (h_3 - h_2) \right] \quad (\text{C.30})$$

Based on the considered idealized assumptions, the reluctance can be estimated in terms of the magnetomotive force as follows:

$$MMF = NI = \phi \mathfrak{R} \rightarrow \mathfrak{R} = \frac{NI}{\phi} \therefore \mathfrak{R} = \frac{N^2}{L_l} \quad (\text{C.31})$$

If we simplify further our analytical expression assuming that  $h_1 = 0$  and  $h_2 = h_3$ , the equivalent slot reluctance using the result from (C.30) and (C.31) is given by:

$$\mathfrak{R} = 3 \times \frac{b}{\mu_0 L h_3} \quad (\text{C.32})$$

Only analytical approaches have been considered and, therefore, many idealized assumptions have been taken into account to be able to solve Ampère's law locally to derive (C.32). It gives an approximation that can be used as a first estimative of the local effect of the air reluctance connecting two adjacent stator teeth at the slot. The reluctance *Rl\_sl\_in* in Fig. C.5 represents the inductance that is calculated by (C.32).



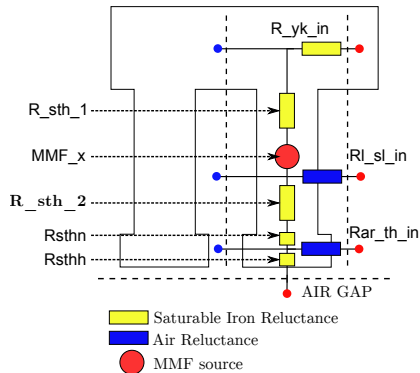


Figure C.5: Reluctance Network for one stator tooth and its respective slot.

Notice that (C.32) yields a factor 3 to calculate the stator slot reluctance. This result is used to assemble the reluctance network in Chapter 4 in Table 4.3.

## C.4 Carter's Factor

In this work, the Carter's coefficient is calculated based on the approach presented in [37] and it assumes that both stator and rotor have open slots.

Carter's coefficient for the stator:

$$K_{cs} = \frac{\tau_{th}}{\tau_{th} - slop \cdot \kappa_s} \quad (\text{C.33})$$

where  $\kappa_s$  is given by (C.34) and  $\tau_{th}$  by (C.17).

$$\kappa_s = \frac{2}{\pi} \left[ \text{atan} \left( \frac{slop}{2 \cdot gap} \right) - \left( \frac{2 \cdot gap}{slop} \right) \ln \cdot \left( \sqrt{1 + \left( \frac{slop}{2 \cdot gap} \right)^2} \right) \right] \quad (\text{C.34})$$

Similarly, for the rotor:

$$K_{cr} = \frac{\tau_{thr}}{\tau_{thr} - SlrWidth \cdot \kappa_r} \quad (\text{C.35})$$

where  $\kappa_r$  is given by (C.36),  $\tau_{thr}$  by (C.37) and  $SlrWidth$  is the rotor

slot width.

$$\kappa_r = \frac{2}{\pi} \left[ \operatorname{atan} \left( \frac{SlrWidth}{2 \cdot gap} \right) - \left( \frac{2 \cdot gap}{SlrWidth} \right) \ln \cdot \left( \sqrt{1 + \left( \frac{SlrWidth}{2 \cdot gap} \right)^2} \right) \right] \quad (\text{C.36})$$

$$\tau_{thr} = \frac{2\pi}{Nslr} \cdot r_{gap} \quad (\text{C.37})$$

The total Carter's factor is:

$$K_{cTotal} = K_{cs} \cdot K_{cr} \quad (\text{C.38})$$

Consequently, the *gapef* parameter is given by:

$$gapef = K_{cTotal} \cdot gap \quad (\text{C.39})$$

# Appendix D

## BDFRM prototype characteristics: reference machine used for model comparisons

### D.1 Main characteristics and rated parameters

In this thesis, a BDFRM prototype, presented in Chapter 8, has been conceived with the goal of validating the models that have been developed. It has been designed for 1 *kW* at 1000 *rpm* and its parameters are used as the reference ones to compare the models. They are summarized in Table D.1 and in Table D.2.

Table D.1: Reference machine used to compare the semi-analytical models to FEA.

Stator external diameter	235.0 mm
Stator internal diameter	144.24 mm
Effective axial length	69.0 mm
Shaft diameter	65.0 mm
Grid winding total number of turns	448
Control winding total number of turns	312
Air gap length	0.5 mm
Number of stator slots	48
Number of rotor ducts	66
Number of poles grid/control/rotor	8/4/6
Yoke width	14.5 mm
Yoke to stator tooth width ratio	2.826
Stator slot opening	1.6 mm
Rotor slot width	2.727 mm
Control winding wire diameter	0.91186 mm
Grid winding wire diameter	0.91186 mm
Magnetic material in stator and rotor	M400-50A

Table D.2: Prototype rated parameters to compare the semi-analytical models to FEA.

Grid winding current ( $I_g$ )	3.07 Apk / 2.17 Arms
Control winding current ( $I_c$ )	3.23 Apk / 2.28 Arms
Grid winding phase voltage ( $V_g$ )	127 Vrms
Control winding current ( $V_c$ )	127 Vrms
Grid winding frequency ( $f_g$ )	50 Hz
Control winding frequency ( $f_c$ )	50 Hz
Maximum speed ( $\omega_{rm}$ )	1000 rpm
Torque max @ Max Speed	9.5 Nm
Rated power @ 1000 rpm	1 kW
Maximum allowed flux density in the magnetic circuit	$B_{n\_max} < 1.5T$

# Appendix E

## Optimization constraints for the case study

### E.1 GSOM-SAM constraints for the case study

#### E.1.1 Variable inputs

Regarding the GSOM-SAM, the inputs that are left free to vary are defined in Table E.1. In this table, in the column “Range”, the values follows the notation: [min; initial; max]. The symbols are defined in Fig E.1. The initial values corresponds to the ones of the prototype.

Table E.1: Optimization problem: variable inputs.

Symbol	Description	Range
DcondWc	Control winding wire diameter	[0.5; 0.91186; 4.0 ]
DcondWg	Grid winding wire diameter	[0.5; 0.91186; 4.0 ]
Des	Stator external diameter	[200.0; 235.0; 420.0]
Dis	Stator internal diameter	[100; 144.24; 350]
Dshf	Shaft diameter	[20; 65; 300]
gap	air-gap length	[0.5; 0.5; 0.8]
Lstkef	Effective axial length	[50; 69; 300]
Nphc	Control total number of turns per phase	[20; 312; 1000]
Nphg	Grid total number of turns per phase	[20; 448; 1000]
Iphc	Control current amplitude	[0.1; 3.23; 100]
Iphg	Grid current amplitude	[0.1; 3.07; 100]
slop	Slot opening	[1.0; 1.6; 4.6]
FBAngle	arc angle of the rotor flux barrier	[90; 120; 150]
SlrWidth	Rotor slot width	[2.5; 2.73; 6.0]
thh	Stator teeth detail	[2.0; 2.0; 4.0]
thn	Stator teeth detail	[2.0; 2.0; 4.0]
ykw	yoke width	[10.0; 14.5; 80.0]
ytr	yoke to stator tooth width ratio $ytr = ykw/thw$	[2.0; 2.83; 5.0]

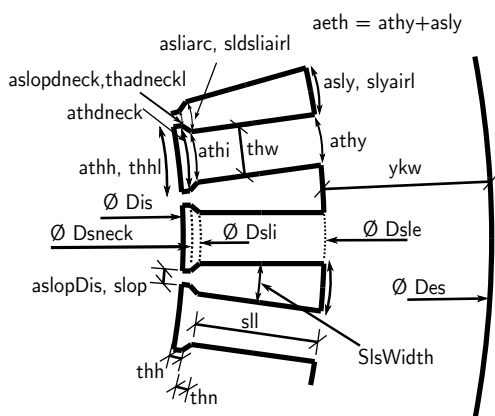


Figure E.1: Stator slot physical dimensions definitions.

### **E.1.2 Constrained outputs**

The GSOM-SAM is used to optimize the machine at 750 rpm. The geometrical constraints are used to limit machine dimensions so that the resulting machine has a physical meaning. For example, the stator internal diameter (Dis) cannot be greater than the external one (Des), so a constraint is created to limit the optimization search space considering this restriction. Similar assumptions are made for all geometrical constraints in order to limit machine physical dimensions. Additionally, the general constraints presented in Table 9.5 apply.

The constrained outputs are summarized in Table E.2.



Table E.2: Optimization problem: constrained outputs.

Symbol	Description	Range	Quantity
<b>Geometrical Constraints</b>			
$DuctRatio$	Duct Ratio (refer to Section 5.2.4)	[0.36; 0.42]	[1]
$ratio\_L\_Dis$	Lstk/Dis Ratio	[0.6; 3]	[1]
$Sslot$	cross-sectional area of the stator slot	[1; 500]	[1]
$thw$	stator teeth width	[4; 20]	[1]
$wff$	winding filling factor	[0.001; 0.35]	[1]
$Phys\_limit$	Physical limitation constraints (e.g. (Dis-Der) $> 0$ , (Des-Dsle) $> 0$ etc.	constr $> 0$	[16]
<b>Electrical Constraints</b>			
$T_{em}$	Electromagnetic torque	[-15.32; -15.28]	[1]
$V_{ca}$	Control winding rms phase voltage	[0; 130.0]	[1]
$V_{ga}$	Grid winding rms phase voltage	[128.0; 130.0]	[1]
$J_{wc}$	Current density in control winding	[0.01; 3.5]	[1]
$J_{wg}$	Current density in grid winding	[0.01; 3.5]	[1]
$A_{sel\_total}$	Linear current density (refer to Section 5.2.3)	[0; 32000]	[1]
$B_{FBx}$	Maximum induction in the rotor flux paths	[0; 1.6]	[6]
$B_{thmax}$	Maximum induction in the stator teeth	[0; 1.6]	[1]
$B_{ykmax}$	Maximum induction in the stator yoke	[0; 1.6]	[1]

### E.1.3 The chosen “first-cut” machine design using the GSOM-SAM to be further explored

Table E.3 shows the chosen “first-cut” machine design using the GSOM-SAM to be further explored in the optimization process by the GSOM-MSRN.

Table E.3: Optimization result: the chosen “first-cut” machine design using the GSOM-SAM.

Symbol	Description	Range	Result
DcondWc	Control winding wire diameter	[0.5; 0.91186; 4.0 ]	1.26
DcondWg	Grid winding wire diameter	[0.5; 0.91186; 4.0 ]	1.47
Des	Stator external diameter	[200.0; 235.0; 420.0]	268.0
Dis	Stator internal diameter	[100; 144.24; 350]	146.3
Dshf	Shaft diameter	[20; 65; 300]	57.55
gap	air-gap length	[0.5; 0.5; 0.8]	0.5
Lstkef	Effective axial length	[50; 69; 300]	107.76
Nphc	Control total number of turns per phase	[20; 312; 1000]	384
Nphg	Grid total number of turns per phase	[20; 448; 1000]	288
Iphc	Control current amplitude	[0.1; 3.23; 100]	2.9
Iphg	Grid current amplitude	[0.1; 3.07; 100]	4.5
slop	Slot opening	[1.0; 1.6; 4.6]	2.15
FBAngle	arc angle of the rotor flux barrier	[90; 120; 150]	90.0
SlrWidth	Rotor slot width	[2.5; 2.73; 6.0]	2.5
thh	Stator teeth detail	[2.0; 2.0; 4.0]	2.0
thn	Stator teeth detail	[2.0; 2.0; 4.0]	2.0
ykw	yoke width	[10.0; 14.5; 80.0]	13.7
ytr	yoke to stator tooth width ratio $ytr = ykw/thw$	[2.0; 2.83; 5.0]	2.82

## **E.2 GSOM-MSRN machine for the case study: the chosen one at rated conditions at 750 rpm**

Table E.4 shows the chosen machine at rated conditions at 750 rpm by using the GSOM-MSRN model.

Table E.4: GSOM-MSRN optimization result: the chosen one at rated conditions at 750 rpm.

Symbol	Description	Range	Result
DcondWc	Control winding wire diameter	[0.5; 1.26; 4.0 ]	1.56
DcondWg	Grid winding wire diameter	[0.5; 1.47; 4.0 ]	1.61
Des	Stator external diameter	[200.0; 268.0; 420.0]	310.3
Dis	Stator internal diameter	[100; 146.3; 350]	188.54
Dshf	Shaft diameter	[20; 57.55; 300]	104.2
gap	air-gap length	[0.5; 0.5; 0.8]	0.5
lDirtw	DRNI rotor parameter defined in Fig. 4.7	[0.8; 2.0; 2.0]	0.8
lrr	DRNI rotor parameter defined in Fig. 4.7	[0.8; 0.8; 2.0]	0.8
Lstkef	Effective axial length	[50; 107.76; 300]	82.68
ltw	DRNI rotor parameter defined in Fig. 4.7	[0.8; 0.8; 2.0]	0.8
Nphc	Control total number of turns per phase	[20; 384; 1000]	224
Nphg	Grid total number of turns per phase	[20; 288; 1000]	280
Iphc	Control current amplitude	[0.1; 2.9; 100]	5.08
Iphg	Grid current amplitude	[0.1; 4.5; 100]	6.26
slop	Slot opening	[1.0; 2.15; 4.6]	2.29
FBAngle	arc angle of the rotor flux barrier	[90; 90; 150]	90.0
SlrWidth	Rotor slot width	[2.5; 2.5; 6.0]	3.75
thh	Stator teeth detail	[2.0; 2.0; 4.0]	2.0
thn	Stator teeth detail	[2.0; 2.0; 4.0]	2.0
ykw	yoke width	[10.0; 13.7; 80.0]	19.31
ytr	yoke to stator tooth width ratio $ytr = ykw/thw$	[2.0; 2.82; 5.0]	3.28

### **E.3 GSOM-MSRN optimization results at the 3 OP: the chosen final design**

Table E.5 shows the chosen machine when the three operating points are solved simultaneously.

Table E.5: GSOM-MSRN optimization result at the 3 OP: the chosen final design.

Symbol	Description	Range	Result
DcondWc	Control winding wire diameter	[0.5; 1.56; 4.0 ]	1.49
DcondWg	Grid winding wire diameter	[0.5; 1.61; 4.0 ]	1.79
Des	Stator external diameter	[200.0; 310.3; 420.0]	307.36
Dis	Stator internal diameter	[100; 188.54; 350]	183.36
Dshf	Shaft diameter	[20; 104.2; 300]	101.0
gap	air-gap length	[0.5; 0.5; 0.8]	0.5
lDirtw	DRNI rotor parameter defined in Fig. 4.7	[0.8; 0.8; 2.0]	0.8
lrr	DRNI rotor parameter defined in Fig. 4.7	[0.8; 0.8; 2.0]	0.8
Lstkef	Effective axial length	[50; 82.68; 300]	85.85
ltw	DRNI rotor parameter defined in Fig. 4.7	[0.8; 0.8; 2.0]	0.8
Nphc	Control total number of turns per phase	[20; 224; 1000]	200
Nphg	Grid total number of turns per phase	[20; 280; 1000]	240
Iphc_OPm30	Control current amplitude	[0.1; 5.08; 100]	5.23
Iphg_OPm30	Grid current amplitude	[0.1; 6.26; 100]	8.46
Iphc_OPp30	Control current amplitude	[0.1; 5.08; 100]	3.28
Iphg_OPp30	Grid current amplitude	[0.1; 6.26; 100]	8.14
Iphc_OPrated	Control current amplitude	[0.1; 5.08; 100]	4.75
Iphg_OPrated	Grid current amplitude	[0.1; 6.26; 100]	8.22
slop	Slot opening	[1.0; 2.29; 4.6]	2.47
FBAngle	arc angle of the rotor flux barrier	[90; 90; 150]	90.0
SlrWidth	Rotor slot width	[2.5; 3.75; 6.0]	3.65
thh	Stator teeth detail	[2.0; 2.0; 4.0]	2.0
thn	Stator teeth detail	[2.0; 2.0; 4.0]	2.0
ykw	yoke width	[10.0; 20.1; 80.0]	20.1
ytr	yoke to stator tooth width ratio $ytr = ykw/thw$	[2.0; 3.28; 5.0]	3.43

# Appendix F

## Different approaches and comparison for modeling the MMF sources

### F.1 Analysis of different methods to calculate the MMF sources

The magnetomotive force (MMF) sources are the electrical excitation of the static reluctance network. Modeling accurately this element is essential to well represent all involved phenomena.

In this work, three possibilities for modeling the MMF sources have been evaluated (refer to Section 4.3.2.2.1) as follows:

1. Fundamental component (“fund”): only the fundamental component is considered. It is the same approach used for modeling the SAM MMF sources.
2. Truncating the Fourier series after the first three nonzero MMF harmonics (“harm”): the MMF sources are calculated by using the most significant lower order harmonics to analytically obtain their instantaneous values.
3. Discrete (“disc”): in the discrete method, the Ampère-turns contribution of each slot on the MMF source being calculated is

assessed by solving the Ampère’s Law for each one of them. The discrete method results in a rectangular waveform and, therefore, the majority of the MMF harmonics are taken into account.

### F.1.1 Parameters used in the simulation

To investigate the different modeling approaches, the parameters defined for the prototype presented in Chapter 8 are used. Table F.1 shows the prototype’s parameters that are used to calculate the MMF for grid and control windings.

Table F.1: Parameters used to calculate winding functions.

$N_{slg}$	56	$N_{slc}$	39
$N_{phg}$	448	$N_{phc}$	312
$f_g$	50 Hz	$f_c$	50 Hz
$P_g$	8	$P_c$	4
$I_g$	3.07 A	$I_c$	3.23 A
$\alpha_c$	90 °	$N_{sl}$	48

where:

$N_{slg}$ and $N_{slc}$	number of turns per slot (grid/control)
$N_{phg}$ and $N_{phc}$	number of turns per phase (grid/control)
$f_g/f_c$	frequency (grid/control)
$P_g/P_c$	number of poles (grid/control)
$I_g/I_c$	amplitude of phase current (grid/control)
$\alpha_c$	phase angle between the three phase system of both windings
$N_{sl}$	number of stator slots

### F.1.2 Modeling the magnetomotive force

#### F.1.2.1 Continuous methods: fundamental component versus fundamental plus lower order harmonics

The two continuous methods for implementing the MMF sources in the MSRN are analyzed: “fund” and “harm”. These methods are implemented by using the winding function theory as described in Section



4.3.2.3. The “fund” method is a particular case of the “harm” method in which only the first non-zero coefficients of (4.24) and (4.25) are taken into account (only the fundamental component is used).

### F.1.2.2 Discrete method: calculating the MMF contribution of each slot at each stator tooth

Based on the winding position defined in Fig. 2.8, Fig. F.1 shows the global MMF contribution at each stator tooth by solving the Ampère’s law at each slot for both windings. This method is referred to “disc” in the following figures.

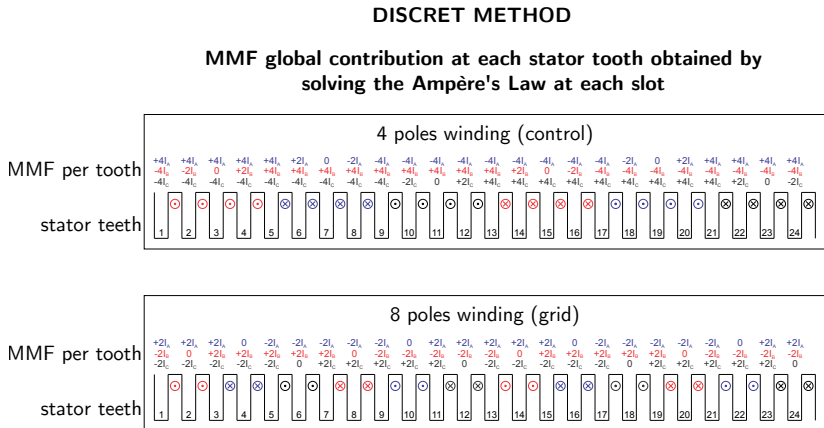


Figure F.1: Global MMF sources at each stator tooth.

### F.1.3 Comparisons of the MMF source modeling

To compare the effects of the three MMF modeling approaches, an harmonic analysis of the induced voltage and the torque is presented in the sequence. A Finite Element Analysis (FEA) is used as the reference for comparison and the methods *disc*, *fund* and *harm* are implemented. This tests have been performed in the Multi-Static Reluctance Network.

For this analysis, the simulation parameters depicted in Table F.1 have been considered. Additionally, it has been considered that the angular speed was fixed at  $1000rpm$ , because at this speed  $f_c = f_g = 50Hz$ . These frequencies are convenient for this analysis, since the electric period from both windings are equal. The rotor step that have

been considered was  $0.468750^\circ$ , which means for this speed a time step of  $7.8125 \cdot 10^{-5} s$ . This results in a sampling frequency of  $F_s = 12.8 kHz$ .

### F.1.3.1 Voltage analysis

Starting by voltage waveforms, Fig. F.2 shows one electric period for phase-a grid voltage  $v_{ga}$  and for phase-a control voltage  $v_{ca}$ . In time domain, it can be notice that the fundamental component is accurately represent for all different methods, but it is hard to address the harmonics effects.

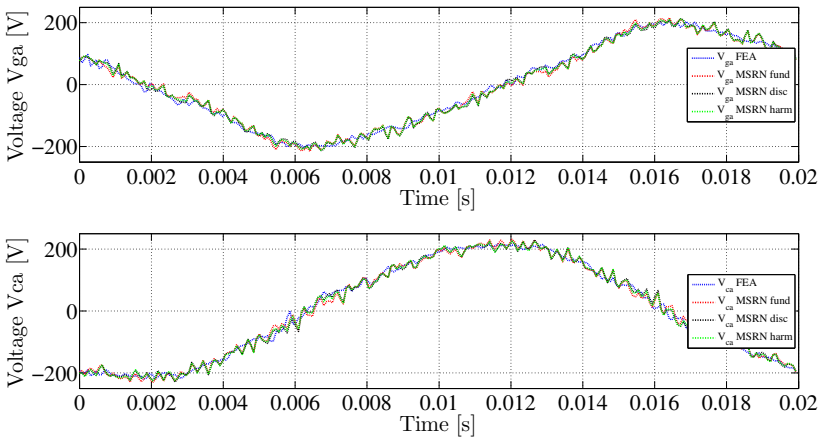


Figure F.2: Induced phase-a grid voltage  $v_{ga}$  and phase-a control voltage  $v_{ca}$ .

To evaluate the differences between the models, the amplitude of the single-sided fast Fourier transform for each phase has been calculated and the results are shown for harmonics 1 up to 11 in Fig. F.3.

Fig. F.3a confirms what has been inferred from the time domain analysis: The fundamental component of the induced voltage is remarkably well estimated for all the RN models for all 6 phases. It is interesting to notice that the phase are not 100 % equilibrated and symmetric. This is due to the consideration of the non-linearities in the model.

Fig. F.3b represents the third harmonic and, although still not far from the FEA reference model, the *fund* model is the one which presents the most diverging results. It is from the 7th-harmonic depicted in Fig. F.3d that this result seems more evident. It is clear that

the *fund* model is limited when one is searching to calculate higher order harmonics. This is expected, since the source itself represents only the first harmonic. What is interesting to notice is that the *harm* model presents similar results to the *disc* model in a general way.

Considering the phase voltages results, it is possible to infer that, in a general way, the differences between the *disc* and *harm* models to represent harmonics up to the 11th order are small and one could use both with similar accuracy. The *fund* model is limited on the representation of higher order harmonics.

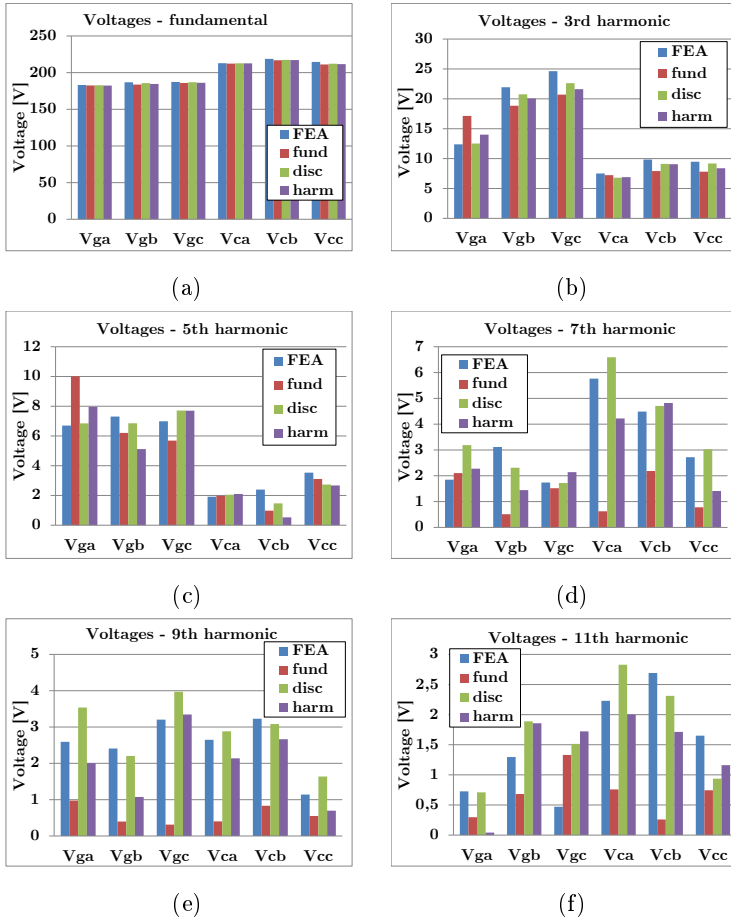


Figure F.3: Harmonic analysis for induced voltages in the BDFRM models.

### F.1.3.2 Torque analysis

Regarding torque, Fig. F.4 shows the time domain results for all the three models and the FEA result. The difference in the mean values for the reluctance network models compared to the FEA model is around 4 %. From the time domain, it is noticed that the multi-static reluctance network model allows to calculate the torque ripple, however, the slotting effects calculated in the FEA model are not considered.

This is due to the air-gap discretization difference between the models. Whereas the FEA model discretizes the domain in a much finer mesh, the reluctance network uses only 32 reluctances per rotor pole to do the same.

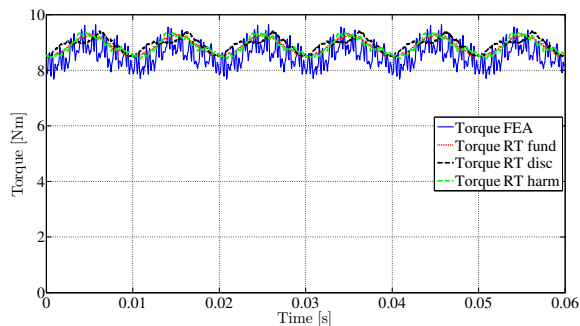


Figure F.4: Electromagnetic torque: comparison between the models.

To better analyze the difference between the MMF modeling approaches, Fig. F.5b presents the torque harmonics for the 2nd, 4th, 6th and 8th harmonics. Similar conclusions that have been made for the voltage case can be inferred for the torque. The higher the harmonics, the worst is the representation of *fund* model. Comparing *harm* and *disc*, both models have similar results.

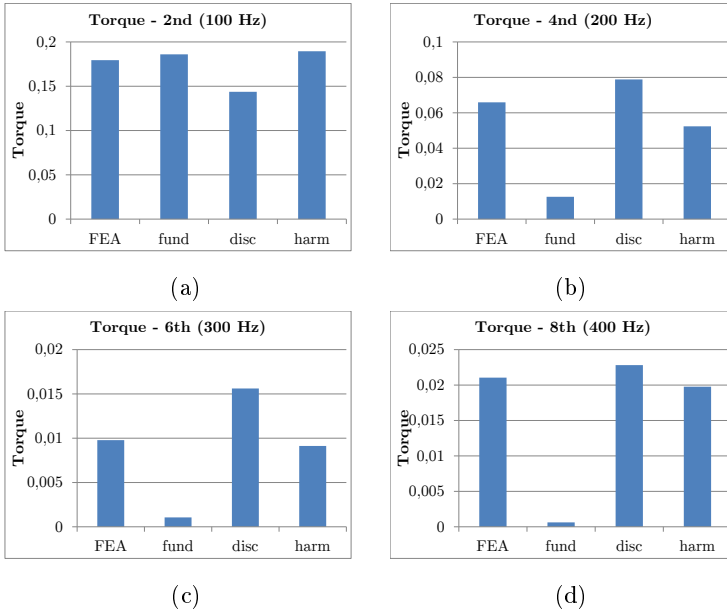


Figure F.5: Harmonic analysis for electromagnetic torque in the BDFRM models.

### F.1.4 Definition of the MMF sources modeling approach to be implemented in the MSRN

The “fund” method that considers only the fundamental component is limited and can be basically used only to calculate the first harmonic of the output parameters. Regarding harmonics calculations, the “harm” and the “disc” methods present comparable results since the most relevant lower order harmonics are taken into account in both. Because the “harm” offers accurate results and it is represented by analytical equations, what greatly simplifies the model implementation, it has been chosen to represent the MMF sources in the MSRN model.

## F.2 Analytical solution of equation (4.27) to calculate the winding functions for each phase using the “harm” method introduced in Section 4.3.2.3

As shown in Section 4.3.2.3.3, the winding functions can be calculated for each phase winding by using (4.27), repeated here in (4.27).

$$w_x(\theta_{ag}) = \frac{1}{2} \int_0^{2\pi/P} n_x(\theta_{ag}) d\theta_{ag} - \int_0^{\theta_{ag}} n_x(\theta_{ag}) d\theta_{ag} \quad (\text{F.1})$$

The analytical solution of (F.1) can be found, recalling that  $n_x(\phi_m)$  is a sum of sinusoidal functions. The results are presented in Fig. F.6 and in Fig. F.7 in the sequence. They have been calculated by using the Maple  $\text{\textcircled{R}}$  software.

$$\begin{aligned}
&> \text{wasg} := \frac{1}{2} \int_0^{\frac{2\pi}{Pg}} \text{nasgdTheta\_ag} - \int_0^{\text{Theta\_ag}} \text{nasgdTheta\_ag} \\
\text{wasg} &:= -\frac{1}{8} b\_ga4 - \frac{1}{24} b\_gal2 - \frac{1}{40} b\_ga20 + \frac{1}{8} a\_ga4 \sin\left(\frac{8\pi}{Pg}\right) - \frac{1}{8} b\_ga4 \cos\left(\frac{8\pi}{Pg}\right) \\
&+ \frac{1}{24} a\_gal2 \sin\left(\frac{24\pi}{Pg}\right) - \frac{1}{24} b\_gal2 \cos\left(\frac{24\pi}{Pg}\right) + \frac{1}{40} a\_ga20 \sin\left(\frac{40\pi}{Pg}\right) - \frac{1}{40} b\_ga20 \cos\left(\frac{40\pi}{Pg}\right) \\
&- \frac{1}{4} a\_ga4 \sin(4 \text{Theta\_ag}) + \frac{1}{4} b\_ga4 \cos(4 \text{Theta\_ag}) - \frac{1}{12} a\_gal2 \sin(12 \text{Theta\_ag}) \\
&+ \frac{1}{12} b\_gal2 \cos(12 \text{Theta\_ag}) - \frac{1}{20} a\_ga20 \sin(20 \text{Theta\_ag}) + \frac{1}{20} b\_ga20 \cos(20 \text{Theta\_ag}) \\
&> \text{wbsg} := \frac{1}{2} \int_0^{\frac{2\pi}{Pg}} \text{nbsgdTheta\_ag} - \int_0^{\text{Theta\_ag}} \text{nbsgdTheta\_ag} \\
\text{wbsg} &:= -\frac{1}{8} b\_gb4 - \frac{1}{24} b\_gb12 - \frac{1}{40} b\_gb20 + \frac{1}{8} a\_gb4 \sin\left(\frac{8\pi}{Pg}\right) - \frac{1}{8} b\_gb4 \cos\left(\frac{8\pi}{Pg}\right) \\
&+ \frac{1}{24} a\_gb12 \sin\left(\frac{24\pi}{Pg}\right) - \frac{1}{24} b\_gb12 \cos\left(\frac{24\pi}{Pg}\right) + \frac{1}{40} a\_gb20 \sin\left(\frac{40\pi}{Pg}\right) - \frac{1}{40} b\_gb20 \cos\left(\frac{40\pi}{Pg}\right) \\
&- \frac{1}{4} a\_gb4 \sin(4 \text{Theta\_ag}) + \frac{1}{4} b\_gb4 \cos(4 \text{Theta\_ag}) - \frac{1}{12} a\_gb12 \sin(12 \text{Theta\_ag}) \\
&+ \frac{1}{12} b\_gb12 \cos(12 \text{Theta\_ag}) - \frac{1}{20} a\_gb20 \sin(20 \text{Theta\_ag}) + \frac{1}{20} b\_gb20 \cos(20 \text{Theta\_ag}) \\
&> \text{wcsg} := \frac{1}{2} \int_0^{\frac{2\pi}{Pg}} \text{ncsgdTheta\_ag} - \int_0^{\text{Theta\_ag}} \text{ncsgdTheta\_ag} \\
\text{wcsg} &:= -\frac{1}{8} b\_gc4 - \frac{1}{24} b\_gc12 - \frac{1}{40} b\_gc20 + \frac{1}{8} a\_gc4 \sin\left(\frac{8\pi}{Pg}\right) - \frac{1}{8} b\_gc4 \cos\left(\frac{8\pi}{Pg}\right) \\
&+ \frac{1}{24} a\_gc12 \sin\left(\frac{24\pi}{Pg}\right) - \frac{1}{24} b\_gc12 \cos\left(\frac{24\pi}{Pg}\right) + \frac{1}{40} a\_gc20 \sin\left(\frac{40\pi}{Pg}\right) - \frac{1}{40} b\_gc20 \cos\left(\frac{40\pi}{Pg}\right) \\
&- \frac{1}{4} a\_gc4 \sin(4 \text{Theta\_ag}) + \frac{1}{4} b\_gc4 \cos(4 \text{Theta\_ag}) - \frac{1}{12} a\_gc12 \sin(12 \text{Theta\_ag}) \\
&+ \frac{1}{12} b\_gc12 \cos(12 \text{Theta\_ag}) - \frac{1}{20} a\_gc20 \sin(20 \text{Theta\_ag}) + \frac{1}{20} b\_gc20 \cos(20 \text{Theta\_ag})
\end{aligned}$$

Figure F.6: Winding functions of the grid winding.

In Fig. F.6,  $w_xsg$  are the winding functions of the grid winding, where  $x$  indicates phases a, b and c.  $n_xsg$  are calculated by (4.23),  $\text{Theta\_ag} = \theta_{ag}$  and the coefficients  $a\_gx_i$ ,  $b\_gx_i$  are the first three non-zero ones calculated by (4.24) and (4.25) for the grid winding.



$$\begin{aligned}
& \text{> } w_{asc} := \frac{1}{2} \cdot \int_0^{\frac{2 \cdot \pi}{Pc}} n_{asc} d\theta_{ag} - \int_0^{\theta_{ag}} n_{asc} d\theta_{ag} \\
w_{asc} & := -\frac{1}{4} b_{ca2} - \frac{1}{12} b_{ca6} - \frac{1}{20} b_{ca10} + \frac{1}{4} a_{ca2} \sin\left(\frac{4 \pi}{Pc}\right) - \frac{1}{4} b_{ca2} \cos\left(\frac{4 \pi}{Pc}\right) \\
& + \frac{1}{12} a_{ca6} \sin\left(\frac{12 \pi}{Pc}\right) - \frac{1}{12} b_{ca6} \cos\left(\frac{12 \pi}{Pc}\right) + \frac{1}{20} a_{ca10} \sin\left(\frac{20 \pi}{Pc}\right) - \frac{1}{20} b_{ca10} \cos\left(\frac{20 \pi}{Pc}\right) \\
& - \frac{1}{2} a_{ca2} \sin(2 \theta_{ag}) + \frac{1}{2} b_{ca2} \cos(2 \theta_{ag}) - \frac{1}{6} a_{ca6} \sin(6 \theta_{ag}) \\
& + \frac{1}{6} b_{ca6} \cos(6 \theta_{ag}) - \frac{1}{10} a_{ca10} \sin(10 \theta_{ag}) + \frac{1}{10} b_{ca10} \cos(10 \theta_{ag}) \\
& \text{> } w_{bsc} := \frac{1}{2} \cdot \int_0^{\frac{2 \cdot \pi}{Pc}} n_{bsc} d\theta_{ag} - \int_0^{\theta_{ag}} n_{bsc} d\theta_{ag} \\
w_{bsc} & := -\frac{1}{4} b_{cb2} - \frac{1}{12} b_{cb6} - \frac{1}{20} b_{cb10} + \frac{1}{4} a_{cb2} \sin\left(\frac{4 \pi}{Pc}\right) - \frac{1}{4} b_{cb2} \cos\left(\frac{4 \pi}{Pc}\right) \\
& + \frac{1}{12} a_{cb6} \sin\left(\frac{12 \pi}{Pc}\right) - \frac{1}{12} b_{cb6} \cos\left(\frac{12 \pi}{Pc}\right) + \frac{1}{20} a_{cb10} \sin\left(\frac{20 \pi}{Pc}\right) - \frac{1}{20} b_{cb10} \cos\left(\frac{20 \pi}{Pc}\right) \\
& - \frac{1}{2} a_{cb2} \sin(2 \theta_{ag}) + \frac{1}{2} b_{cb2} \cos(2 \theta_{ag}) - \frac{1}{6} a_{cb6} \sin(6 \theta_{ag}) \\
& + \frac{1}{6} b_{cb6} \cos(6 \theta_{ag}) - \frac{1}{10} a_{cb10} \sin(10 \theta_{ag}) + \frac{1}{10} b_{cb10} \cos(10 \theta_{ag}) \\
& \text{> } w_{csc} := \frac{1}{2} \cdot \int_0^{\frac{2 \cdot \pi}{Pc}} n_{csc} d\theta_{ag} - \int_0^{\theta_{ag}} n_{csc} d\theta_{ag} \\
w_{csc} & := -\frac{1}{4} b_{cc2} - \frac{1}{12} b_{cc6} - \frac{1}{20} b_{cc10} + \frac{1}{4} a_{cc2} \sin\left(\frac{4 \pi}{Pc}\right) - \frac{1}{4} b_{cc2} \cos\left(\frac{4 \pi}{Pc}\right) \\
& + \frac{1}{12} a_{cc6} \sin\left(\frac{12 \pi}{Pc}\right) - \frac{1}{12} b_{cc6} \cos\left(\frac{12 \pi}{Pc}\right) + \frac{1}{20} a_{cc10} \sin\left(\frac{20 \pi}{Pc}\right) - \frac{1}{20} b_{cc10} \cos\left(\frac{20 \pi}{Pc}\right) \\
& - \frac{1}{2} a_{cc2} \sin(2 \theta_{ag}) + \frac{1}{2} b_{cc2} \cos(2 \theta_{ag}) - \frac{1}{6} a_{cc6} \sin(6 \theta_{ag}) \\
& + \frac{1}{6} b_{cc6} \cos(6 \theta_{ag}) - \frac{1}{10} a_{cc10} \sin(10 \theta_{ag}) + \frac{1}{10} b_{cc10} \cos(10 \theta_{ag})
\end{aligned}$$

Figure F.7: Winding functions of the control winding.

In Fig. F.7,  $w_x sc$  are the winding functions of the control winding, where  $x$  indicates phases a, b and c.  $n_x sc$  are calculated by (4.23) and the coefficients  $a_{cx_i}$ ,  $b_{cx_i}$  are the first three non-zero ones calculated by (4.24) and (4.25) for the control winding.

### F.3 Analytical solution of the magnetomotive forces for grid and control windings using the “harm” method introduced in Section 4.3.2.3

The magnetomotive forces MMF from each phase winding can be calculated by (4.29) and (4.30), repeated here in (F.2) and (F.3), for the grid and control phases, respectively.

$$\mathbb{F}_g(\theta_{ag}, ts) = w_{ga}(\theta_{ag})i_{ga}(ts) + w_{gb}(\theta_{ag})i_{gb}(ts) + w_{gc}(\theta_{ag})i_{gc}(ts) \quad (\text{F.2})$$

$$\mathbb{F}_c(\theta_{ag}, ts) = w_{ca}(\theta_{ag})i_{ca}(ts) + w_{cb}(\theta_{ag})i_{cb}(ts) + w_{cc}(\theta_{ag})i_{cc}(ts) \quad (\text{F.3})$$

The analytical solution of the contribution of each phase in (F.2) to the total MMF of the grid winding is shown in Fig. F.8 considering balanced three-phase currents. The total contribution  $\mathbb{F}_g(\theta_{ag}, ts) = Fwg3\phi$  is depicted in Fig. F.9. The analytical calculations have been obtained from Maple  $\text{\textcircled{R}}$ .

>  $F_{wga} := wasg \cdot iga$

$$\begin{aligned}
 F_{wga} := & \left( -\frac{1}{8} b_{ga4} - \frac{1}{24} b_{ga12} - \frac{1}{40} b_{ga20} + \frac{1}{8} a_{ga4} \sin\left(\frac{8\pi}{Pg}\right) - \frac{1}{8} b_{ga4} \cos\left(\frac{8\pi}{Pg}\right) \right. \\
 & + \frac{1}{24} a_{ga12} \sin\left(\frac{24\pi}{Pg}\right) - \frac{1}{24} b_{ga12} \cos\left(\frac{24\pi}{Pg}\right) + \frac{1}{40} a_{ga20} \sin\left(\frac{40\pi}{Pg}\right) - \frac{1}{40} b_{ga20} \cos\left(\frac{40\pi}{Pg}\right) \\
 & - \frac{1}{4} a_{ga4} \sin(4 \Theta_{ag}) + \frac{1}{4} b_{ga4} \cos(4 \Theta_{ag}) - \frac{1}{12} a_{ga12} \sin(12 \Theta_{ag}) \\
 & \left. + \frac{1}{12} b_{ga12} \cos(12 \Theta_{ag}) - \frac{1}{20} a_{ga20} \sin(20 \Theta_{ag}) + \frac{1}{20} b_{ga20} \cos(20 \Theta_{ag}) \right) \\
 & Ig \cos(wg \ ts)
 \end{aligned}$$

>  $F_{wgb} := wbsg \cdot igb$

$$\begin{aligned}
 F_{wgb} := & - \left( -\frac{1}{8} b_{gb4} - \frac{1}{24} b_{gb12} - \frac{1}{40} b_{gb20} + \frac{1}{8} a_{gb4} \sin\left(\frac{8\pi}{Pg}\right) - \frac{1}{8} b_{gb4} \cos\left(\frac{8\pi}{Pg}\right) \right. \\
 & + \frac{1}{24} a_{gb12} \sin\left(\frac{24\pi}{Pg}\right) - \frac{1}{24} b_{gb12} \cos\left(\frac{24\pi}{Pg}\right) + \frac{1}{40} a_{gb20} \sin\left(\frac{40\pi}{Pg}\right) - \frac{1}{40} b_{gb20} \cos\left(\frac{40\pi}{Pg}\right) \\
 & - \frac{1}{4} a_{gb4} \sin(4 \Theta_{ag}) + \frac{1}{4} b_{gb4} \cos(4 \Theta_{ag}) - \frac{1}{12} a_{gb12} \sin(12 \Theta_{ag}) \\
 & \left. + \frac{1}{12} b_{gb12} \cos(12 \Theta_{ag}) - \frac{1}{20} a_{gb20} \sin(20 \Theta_{ag}) + \frac{1}{20} b_{gb20} \cos(20 \Theta_{ag}) \right) \\
 & Ig \cos\left(wg \ ts + \frac{1}{3} \pi\right)
 \end{aligned}$$

>  $F_{wgc} := wcs g \cdot igc$

$$\begin{aligned}
 F_{wgc} := & - \left( -\frac{1}{8} b_{gc4} - \frac{1}{24} b_{gc12} - \frac{1}{40} b_{gc20} + \frac{1}{8} a_{gc4} \sin\left(\frac{8\pi}{Pg}\right) - \frac{1}{8} b_{gc4} \cos\left(\frac{8\pi}{Pg}\right) \right. \\
 & + \frac{1}{24} a_{gc12} \sin\left(\frac{24\pi}{Pg}\right) - \frac{1}{24} b_{gc12} \cos\left(\frac{24\pi}{Pg}\right) + \frac{1}{40} a_{gc20} \sin\left(\frac{40\pi}{Pg}\right) - \frac{1}{40} b_{gc20} \cos\left(\frac{40\pi}{Pg}\right) \\
 & - \frac{1}{4} a_{gc4} \sin(4 \Theta_{ag}) + \frac{1}{4} b_{gc4} \cos(4 \Theta_{ag}) - \frac{1}{12} a_{gc12} \sin(12 \Theta_{ag}) \\
 & \left. + \frac{1}{12} b_{gc12} \cos(12 \Theta_{ag}) - \frac{1}{20} a_{gc20} \sin(20 \Theta_{ag}) + \frac{1}{20} b_{gc20} \cos(20 \Theta_{ag}) \right) \\
 & Ig \sin\left(wg \ ts + \frac{1}{6} \pi\right)
 \end{aligned}$$

Figure F.8: Magnetomotive forces of each phase of grid winding.

>  $F_{wg3\phi} := F_{wga} + F_{wgb} + F_{wgc}$

$$\begin{aligned}
F_{wg3\phi} := & \left( -\frac{1}{8} b_{ga4} - \frac{1}{24} b_{ga12} - \frac{1}{40} b_{ga20} + \frac{1}{8} a_{ga4} \sin\left(\frac{8\pi}{P_g}\right) - \frac{1}{8} b_{ga4} \cos\left(\frac{8\pi}{P_g}\right) \right. \\
& + \frac{1}{24} a_{ga12} \sin\left(\frac{24\pi}{P_g}\right) - \frac{1}{24} b_{ga12} \cos\left(\frac{24\pi}{P_g}\right) + \frac{1}{40} a_{ga20} \sin\left(\frac{40\pi}{P_g}\right) - \frac{1}{40} b_{ga20} \cos\left(\frac{40\pi}{P_g}\right) \\
& - \frac{1}{4} a_{ga4} \sin(4 \text{ Theta}_{ag}) + \frac{1}{4} b_{ga4} \cos(4 \text{ Theta}_{ag}) - \frac{1}{12} a_{ga12} \sin(12 \text{ Theta}_{ag}) \\
& \left. + \frac{1}{12} b_{ga12} \cos(12 \text{ Theta}_{ag}) - \frac{1}{20} a_{ga20} \sin(20 \text{ Theta}_{ag}) + \frac{1}{20} b_{ga20} \cos(20 \text{ Theta}_{ag}) \right) \\
I_g \cos(wg \text{ ts}) - & \left( -\frac{1}{8} b_{gb4} - \frac{1}{24} b_{gb12} - \frac{1}{40} b_{gb20} + \frac{1}{8} a_{gb4} \sin\left(\frac{8\pi}{P_g}\right) - \frac{1}{8} b_{gb4} \cos\left(\frac{8\pi}{P_g}\right) \right. \\
& + \frac{1}{24} a_{gb12} \sin\left(\frac{24\pi}{P_g}\right) - \frac{1}{24} b_{gb12} \cos\left(\frac{24\pi}{P_g}\right) + \frac{1}{40} a_{gb20} \sin\left(\frac{40\pi}{P_g}\right) - \frac{1}{40} b_{gb20} \cos\left(\frac{40\pi}{P_g}\right) \\
& - \frac{1}{4} a_{gb4} \sin(4 \text{ Theta}_{ag}) + \frac{1}{4} b_{gb4} \cos(4 \text{ Theta}_{ag}) - \frac{1}{12} a_{gb12} \sin(12 \text{ Theta}_{ag}) \\
& \left. + \frac{1}{12} b_{gb12} \cos(12 \text{ Theta}_{ag}) - \frac{1}{20} a_{gb20} \sin(20 \text{ Theta}_{ag}) + \frac{1}{20} b_{gb20} \cos(20 \text{ Theta}_{ag}) \right) \\
I_g \cos\left(wg \text{ ts} + \frac{1}{3} \pi\right) - & \left( -\frac{1}{8} b_{gc4} - \frac{1}{24} b_{gc12} - \frac{1}{40} b_{gc20} + \frac{1}{8} a_{gc4} \sin\left(\frac{8\pi}{P_g}\right) \right. \\
& - \frac{1}{8} b_{gc4} \cos\left(\frac{8\pi}{P_g}\right) + \frac{1}{24} a_{gc12} \sin\left(\frac{24\pi}{P_g}\right) - \frac{1}{24} b_{gc12} \cos\left(\frac{24\pi}{P_g}\right) + \frac{1}{40} a_{gc20} \sin\left(\frac{40\pi}{P_g}\right) \\
& - \frac{1}{40} b_{gc20} \cos\left(\frac{40\pi}{P_g}\right) - \frac{1}{4} a_{gc4} \sin(4 \text{ Theta}_{ag}) + \frac{1}{4} b_{gc4} \cos(4 \text{ Theta}_{ag}) \\
& - \frac{1}{12} a_{gc12} \sin(12 \text{ Theta}_{ag}) + \frac{1}{12} b_{gc12} \cos(12 \text{ Theta}_{ag}) - \frac{1}{20} a_{gc20} \sin(20 \text{ Theta}_{ag}) \\
& \left. + \frac{1}{20} b_{gc20} \cos(20 \text{ Theta}_{ag}) \right) I_g \sin\left(wg \text{ ts} + \frac{1}{6} \pi\right)
\end{aligned}$$

Figure F.9: Total magnetomotive force of grid winding.

Similarly, the analytical solution of the contribution of each phase in (F.3) to the total MMF of the control winding is shown in Fig. F.10 considering balanced three-phase currents. The total contribution  $\mathbb{F}_c(\theta_{ag}, ts) = Fwc3\phi$  is depicted in Fig. F.10. The analytical calculations have also been obtained from Maple  $\text{\textcircled{R}}$ .

$$\begin{aligned}
 &> Fwca := wasc \cdot ica \\
 Fwca := &\left( -\frac{1}{4} b_{ca2} - \frac{1}{12} b_{ca6} - \frac{1}{20} b_{ca10} + \frac{1}{4} a_{ca2} \sin\left(\frac{4\pi}{Pc}\right) - \frac{1}{4} b_{ca2} \cos\left(\frac{4\pi}{Pc}\right) \right. \\
 &+ \frac{1}{12} a_{ca6} \sin\left(\frac{12\pi}{Pc}\right) - \frac{1}{12} b_{ca6} \cos\left(\frac{12\pi}{Pc}\right) + \frac{1}{20} a_{ca10} \sin\left(\frac{20\pi}{Pc}\right) - \frac{1}{20} b_{ca10} \cos\left(\frac{20\pi}{Pc}\right) \\
 &- \frac{1}{2} a_{ca2} \sin(2 \text{Theta}_{ag}) + \frac{1}{2} b_{ca2} \cos(2 \text{Theta}_{ag}) - \frac{1}{6} a_{ca6} \sin(6 \text{Theta}_{ag}) \\
 &+ \left. \frac{1}{6} b_{ca6} \cos(6 \text{Theta}_{ag}) - \frac{1}{10} a_{ca10} \sin(10 \text{Theta}_{ag}) + \frac{1}{10} b_{ca10} \cos(10 \text{Theta}_{ag}) \right) Ic \cos( \\
 &-ts \text{wc} + \text{Alpha}_c) \\
 &- \\
 &> Fweb := wbsc \cdot icb \\
 Fweb := &\left( -\frac{1}{4} b_{cb2} - \frac{1}{12} b_{cb6} - \frac{1}{20} b_{cb10} + \frac{1}{4} a_{cb2} \sin\left(\frac{4\pi}{Pc}\right) - \frac{1}{4} b_{cb2} \cos\left(\frac{4\pi}{Pc}\right) \right. \\
 &+ \frac{1}{12} a_{cb6} \sin\left(\frac{12\pi}{Pc}\right) - \frac{1}{12} b_{cb6} \cos\left(\frac{12\pi}{Pc}\right) + \frac{1}{20} a_{cb10} \sin\left(\frac{20\pi}{Pc}\right) - \frac{1}{20} b_{cb10} \cos\left(\frac{20\pi}{Pc}\right) \\
 &- \frac{1}{2} a_{cb2} \sin(2 \text{Theta}_{ag}) + \frac{1}{2} b_{cb2} \cos(2 \text{Theta}_{ag}) - \frac{1}{6} a_{cb6} \sin(6 \text{Theta}_{ag}) \\
 &+ \left. \frac{1}{6} b_{cb6} \cos(6 \text{Theta}_{ag}) - \frac{1}{10} a_{cb10} \sin(10 \text{Theta}_{ag}) + \frac{1}{10} b_{cb10} \cos(10 \text{Theta}_{ag}) \right) Ic \sin\left( \right. \\
 &- \text{wc} \text{ts} + \text{Alpha}_c + \left. \frac{1}{6} \pi \right) \\
 &- \\
 &> Fwcc := wesc \cdot icc \\
 Fwcc := &\left( -\frac{1}{4} b_{cc2} - \frac{1}{12} b_{cc6} - \frac{1}{20} b_{cc10} + \frac{1}{4} a_{cc2} \sin\left(\frac{4\pi}{Pc}\right) - \frac{1}{4} b_{cc2} \cos\left(\frac{4\pi}{Pc}\right) \right. \\
 &+ \frac{1}{12} a_{cc6} \sin\left(\frac{12\pi}{Pc}\right) - \frac{1}{12} b_{cc6} \cos\left(\frac{12\pi}{Pc}\right) + \frac{1}{20} a_{cc10} \sin\left(\frac{20\pi}{Pc}\right) - \frac{1}{20} b_{cc10} \cos\left(\frac{20\pi}{Pc}\right) \\
 &- \frac{1}{2} a_{cc2} \sin(2 \text{Theta}_{ag}) + \frac{1}{2} b_{cc2} \cos(2 \text{Theta}_{ag}) - \frac{1}{6} a_{cc6} \sin(6 \text{Theta}_{ag}) \\
 &+ \left. \frac{1}{6} b_{cc6} \cos(6 \text{Theta}_{ag}) - \frac{1}{10} a_{cc10} \sin(10 \text{Theta}_{ag}) + \frac{1}{10} b_{cc10} \cos(10 \text{Theta}_{ag}) \right) Ic \cos\left( \right. \\
 &- \text{wc} \text{ts} + \text{Alpha}_c + \left. \frac{1}{3} \pi \right)
 \end{aligned}$$

Figure F.10: Magnetomotive forces of each phase of control winding.

>  $F_{wc3\phi} := F_{wca} + F_{wcb} + F_{wcc}$

$$\begin{aligned}
F_{wc3\phi} := & \left( -\frac{1}{4} b_{ca2} - \frac{1}{12} b_{cab} - \frac{1}{20} b_{ca10} + \frac{1}{4} a_{ca2} \sin\left(\frac{4\pi}{P_c}\right) - \frac{1}{4} b_{ca2} \cos\left(\frac{4\pi}{P_c}\right) \right. \\
& + \frac{1}{12} a_{cab} \sin\left(\frac{12\pi}{P_c}\right) - \frac{1}{12} b_{cab} \cos\left(\frac{12\pi}{P_c}\right) + \frac{1}{20} a_{ca10} \sin\left(\frac{20\pi}{P_c}\right) - \frac{1}{20} b_{ca10} \cos\left(\frac{20\pi}{P_c}\right) \\
& - \frac{1}{2} a_{ca2} \sin(2 \text{ Theta}_{ag}) + \frac{1}{2} b_{ca2} \cos(2 \text{ Theta}_{ag}) - \frac{1}{6} a_{cab} \sin(6 \text{ Theta}_{ag}) \\
& \left. + \frac{1}{6} b_{cab} \cos(6 \text{ Theta}_{ag}) - \frac{1}{10} a_{ca10} \sin(10 \text{ Theta}_{ag}) + \frac{1}{10} b_{ca10} \cos(10 \text{ Theta}_{ag}) \right) I_c \cos(-ts \text{ wc} + \text{ Alpha}_c) \\
& - \left( -\frac{1}{4} b_{cb2} - \frac{1}{12} b_{cb6} - \frac{1}{20} b_{cb10} + \frac{1}{4} a_{cb2} \sin\left(\frac{4\pi}{P_c}\right) \right. \\
& - \frac{1}{4} b_{cb2} \cos\left(\frac{4\pi}{P_c}\right) + \frac{1}{12} a_{cb6} \sin\left(\frac{12\pi}{P_c}\right) - \frac{1}{12} b_{cb6} \cos\left(\frac{12\pi}{P_c}\right) + \frac{1}{20} a_{cb10} \sin\left(\frac{20\pi}{P_c}\right) \\
& - \frac{1}{20} b_{cb10} \cos\left(\frac{20\pi}{P_c}\right) - \frac{1}{2} a_{cb2} \sin(2 \text{ Theta}_{ag}) + \frac{1}{2} b_{cb2} \cos(2 \text{ Theta}_{ag}) \\
& - \frac{1}{6} a_{cb6} \sin(6 \text{ Theta}_{ag}) + \frac{1}{6} b_{cb6} \cos(6 \text{ Theta}_{ag}) - \frac{1}{10} a_{cb10} \sin(10 \text{ Theta}_{ag}) \\
& \left. + \frac{1}{10} b_{cb10} \cos(10 \text{ Theta}_{ag}) \right) I_c \sin(-\text{wc} \text{ ts} + \text{ Alpha}_c + \frac{1}{6} \pi) - \left( -\frac{1}{4} b_{cc2} - \frac{1}{12} b_{cc6} \right. \\
& - \frac{1}{20} b_{cc10} + \frac{1}{4} a_{cc2} \sin\left(\frac{4\pi}{P_c}\right) - \frac{1}{4} b_{cc2} \cos\left(\frac{4\pi}{P_c}\right) + \frac{1}{12} a_{cc6} \sin\left(\frac{12\pi}{P_c}\right) \\
& - \frac{1}{12} b_{cc6} \cos\left(\frac{12\pi}{P_c}\right) + \frac{1}{20} a_{cc10} \sin\left(\frac{20\pi}{P_c}\right) - \frac{1}{20} b_{cc10} \cos\left(\frac{20\pi}{P_c}\right) - \frac{1}{2} a_{cc2} \sin(2 \text{ Theta}_{ag}) \\
& \left. + \frac{1}{2} b_{cc2} \cos(2 \text{ Theta}_{ag}) - \frac{1}{6} a_{cc6} \sin(6 \text{ Theta}_{ag}) + \frac{1}{6} b_{cc6} \cos(6 \text{ Theta}_{ag}) \right) \\
& - \frac{1}{10} a_{cc10} \sin(10 \text{ Theta}_{ag}) + \frac{1}{10} b_{cc10} \cos(10 \text{ Theta}_{ag}) \Big) I_c \cos\left(-\text{wc} \text{ ts} + \text{ Alpha}_c + \frac{1}{3} \pi\right)
\end{aligned}$$

Figure F.11: Total magnetomotive force of control winding.

# Appendix G

## Semi-Analytical Model Spreadsheet in Mathcad ®

### G.1 Global Sizing and Optimization Model by using the Semi-Analytical Model

# Brushless Doubly-Fed Reluctance Machine (BDFRM)

## Pre-Design Parameters (fixed):

$P_g := 8$	Grid winding number of poles
$P_c := 4$	Control winding number of poles
$P_r := \frac{P_g + P_c}{2} = 6.00000000$	Rotor number of poles
$N_{slr} := 66$	Rotor number of slots.
$N_{sl} := 48$	Stator number of slots.

## Input parameters definition:

$D_{condWc} := 0.91186mm$	wire diameter control
$D_{condWg} := 0.91186mm$	wire diameter grid
$Des := 235mm$	stator external diameter
$Dis := 144.23944878269637mm$	Stator Internal diameter
$D_{shf} := 65mm$	rotor internal diameter
$gap := 0.5mm$	air gap length
$L_{stkef} := 69mm$	Effective machine axial length
$N_{phc} := 312$	actual number of turns grid winding
$N_{phg} := 448$	actual number of turns control winding
$slop := 1.6mm$	slot opening in stator
$SlotRotorAngleDeg := 120^\circ$	FBAngle arc angle of the rotor Flux barrier
$SlrWidth := 2.727272727272548mm$	Rotor slot width
$thh := 2.0mm$	tooth head length
$thn := 2.0mm$	tooth neck length
$ykw := 14.495515845373408mm$	yoke length
$ytr := 2.8268379550890437$	Yoke width to stator teeth width ratio
$ltw := 0.8mm$	Parameters that define the ducted rotor geometry near the air gap.

## Setting simulation parameters (machine excitation):

$I_{phc} := 3.232430931633097A$	$I_{phg}$ and $I_{phc}$ have been previously defined, but these values may be changed here to test different conditions and excitation.
$I_{phg} := 3.0729859439218177A$	
$f_g := 50Hz$	Grid winding frequency
$f_c := 50Hz$	Control winding frequency
$\phi_{torque} := 90^\circ$	Torque is proportional to $\sin(\phi_{torque})$ . When it is $90^\circ$ it is the Max torque / Amps condition
$\phi_{torque} < 0$ --- motoring	
$\phi_{torque} > 0$ --- generating	



alpha := 0.0038

tsta := 130

copper resistivity as a function of the temperature  
considered temperature in stator windings

### Iron Losses input parameters

fop := fg·s = 50.00000000

ftest := 60

kh := 0.0171

αh := 1.6353

kf := 0.0059

ke := 0.0031

Kwirel := 1.1

## Time and position vectors definition in mathcad to plot graphs:

tf :=  $\frac{1}{fg} \cdot 2 = 0.04000000$  s

final time used depending on fg

Δt :=  $1 \times 10^{-6}$  s      t := 0, Δt.. tf

time vector

μ0 :=  $4 \cdot \pi \cdot 10^{-7} \frac{\text{H}}{\text{m}}$

vacuum permeability

θ := 0°, 1° .. 360°

angle vectors to plot curves

θag := θ

θag0 := 0°

mechanical rotor position at t=0s

rho :=  $0.017 \cdot 10^{-6} = 1.70000000 \times 10^{-8}$

copper resistivity

$$\rho_{\text{iron}} := 7.65 \frac{\text{kg} \div 1000}{\text{cm}^3} = 7.65000000 \times 10^3 \frac{\text{kg}}{\text{m}^3 \cdot 3.00000000}$$

$$\rho_{\text{copper}} := 8.96 \frac{\text{kg} \div 1000}{\text{cm}^3} = 8.96000000 \times 10^3 \frac{\text{kg}}{\text{m}^3 \cdot 3.00000000}$$

## Definitions to make the equivalence with the FEA model:

θrm0<sub>FEM</sub> := 0°

Initial rotor position in FEA model reference

θrm0 := θrm0<sub>FEM</sub> = 0.00000000.°

Rotor initial position in the Semi-Analytical model

γ<sub>1</sub> := Pr·θrm0 = 0.00000000.°

Angle proportional to rotor initial position found in the derivation of the analytical model [5]

αc := φtorque - γ<sub>1</sub> = 90.00000000.°

Phase difference between grid and control windings current to get defined φtorque

*Current Phasors for the equivalent electric circuit:*

$$\Psi_{Iga} := \frac{I_{phg}}{\sqrt{2}} \cdot e^{-0 \cdot i} = 2.17292920 \text{ A}$$

$$\Psi_{Ica} := \frac{I_{phc}}{\sqrt{2}} \cdot e^{-\alpha c \cdot i} = -2.28567383i \text{ A}$$

$$\overline{\Psi_{Iga}} = 2.17292920 \text{ A}$$

$$\overline{\Psi_{Ica}} = 2.28567383i \text{ A}$$

### Internal Parameters:

$$I_{phgrms} := I_{phg} \div \sqrt{2} = 2.17292920 \text{ A}$$

Grid winding rms current

$$I_{phcrms} := I_{phc} \div \sqrt{2} = 2.28567383 \text{ A}$$

Control winding rms current

$$p_g := \frac{P_g}{2} = 4.00000000$$

Grid winding number of pole pairs

$$p_c := \frac{P_c}{2} = 2.00000000$$

Control winding number of pole pairs

### Frequencies:

$$\omega_g := 2 \cdot \pi \cdot f_g = 314.15926536 \frac{1}{s}$$

Grid Winding angular frequency

$$\omega_c := 2 \cdot \pi \cdot f_c = 314.15926536 \frac{1}{s}$$

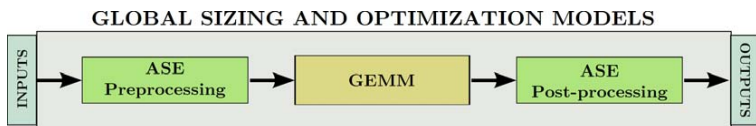
Control winding angular frequency

$$\omega_{rm} := \frac{(\omega_c + \omega_g)}{Pr} = 1.00000000 \times 10^3 \cdot \text{rpm}$$

Rotor mechanical speed for this frequency combination according to machine theory of torque production

# GLOBAL SIZING AND OPTIMIZATION MODEL (GSOM):

The figure below shows the data flow in the GSOM, defining the relationship between the additional sizing equations (ASE) and the Global Electromagnetic Models (GEMM)



These sub-blocks are discussed in the sequence.

This Mathcad file implements the additional sizing equations (valid for both the Semi-analytical Model (SAM) and the Multi-Static Reluctance Network model (MSRN)).

Concerning the GEMM, this spreadsheet implements the analytical / semi-analytical equations of the SAM.

# Preprocessing Additional Sizing Equations

## 1- Geometrical parameters defining machine topology

Fig 1 shows the dimensions associated to the stator.

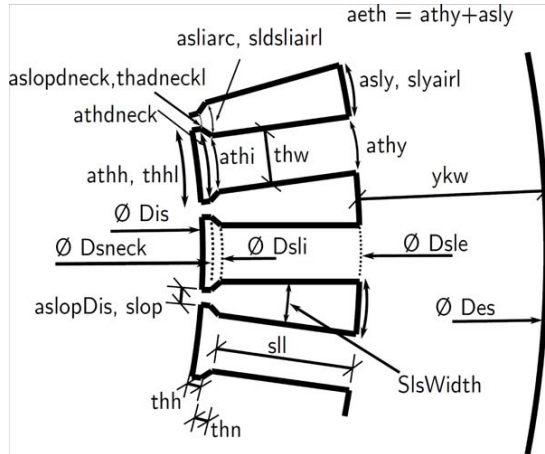


Fig 1 - Parameter definitions associated to the stator.

$$D_{gap} := Dis = 144.23944878 \cdot \text{mm}$$

Air gap diameter is defined according to Dis

$$\tau r_{pitch} := \frac{(\pi \cdot Dis)}{Pr} = 75.52359878 \cdot \text{mm}$$

Rotor pole pitch

**The following parameters are calculated as a function of the inputs:**

$$Dsle := 2 \cdot \left( \frac{Des}{2} - ykw \right) = 0.20600897 \text{ m} \quad \text{slot external diameter}$$

$$Dsli := 2 \cdot \left( \frac{Dis}{2} + thh + thn \right) = 0.15223945 \text{ m} \quad \text{slot internal diameter}$$

$$Dsneck := Dis + 2 \cdot thh = 148.23944878 \cdot \text{mm} \quad \text{stator tooth neck region diameter}$$

$$thw := \frac{ykw}{ytr} = 5.12781987 \cdot \text{mm} \quad \text{stator tooth width.}$$

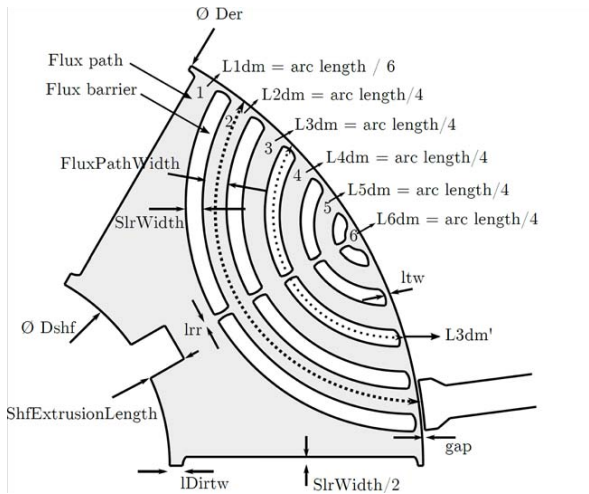
$$sll := \frac{Dsle}{2} - \frac{Dsli}{2} = 0.02688476 \text{ m} \quad \text{slot length}$$

$$thhl := \pi \cdot \frac{Dis}{Nsl} - slop = 7.84044985 \times 10^{-3} \text{ m} \quad \text{stator tooth head length}$$

$$\alpha_{thh} := \frac{thhl}{Dis} \cdot 2 = 0.10871436 \quad \text{stator tooth head angle}$$

$\alpha_{thy} := 2 \cdot \text{asin}\left(\frac{thw}{Dsle}\right) = 2.85262129^\circ$	tooth angle in yoke region
$\alpha_{sly} := \frac{(2\pi - Nsl \cdot \alpha_{thy})}{Nsl} = 4.64737871^\circ$	slot angle in yoke region
$slyairl := \alpha_{sly} \cdot \frac{Dsle}{2} = 8.35490591 \cdot \text{mm}$	air region length in slot yoke region
$\alpha_{eth} := \alpha_{thy} + \alpha_{sly} = 7.50000000^\circ$	angle between teeth
$\alpha_{thi} := 2 \cdot \text{asin}\left(\frac{thw}{Dsli}\right) = 3.86047140^\circ$	tooth angle in the internal (Dsli) region
$\alpha_{sliarc} := \frac{(2\pi - Nsl \cdot \alpha_{thi})}{Nsl} = 3.63952860^\circ$	slot angle in the internal (Dsli) region
$sldsliairl := \alpha_{sliarc} \cdot \frac{Dsli}{2} = 4.83525865 \cdot \text{mm}$	slot Dsli air length
$\alpha_{thdneck} := 2 \cdot \text{asin}\left[\frac{\left[\frac{Dis}{2} \cdot \sin\left(\frac{\alpha_{thh}}{2}\right)\right]}{\left(\frac{Dis}{2} + thh\right)}\right] = 6.06063904^\circ$	
$\alpha_{slopdneck} := \frac{(2 \cdot \pi - Nsl \cdot \alpha_{thdneck})}{Nsl} = 1.43936096^\circ$	
$thadneckl := \alpha_{slopdneck} \cdot \frac{Dsneck}{2} = 1.86200517 \cdot \text{mm}$	tooth air middle head neck length
$\alpha_{slopDis} := \frac{(2\pi - Nsl \cdot \alpha_{thh})}{Nsl} = 1.27112587^\circ$	angle in slop region
$\tau_{th} := \frac{2 \cdot \pi}{Nsl} \cdot \frac{Dgap}{2} = 9.44044985 \cdot \text{mm}$	tooth pitch including slot opening

Fig. 2 shows the parameters associated to the ducted rotor.



**Rotor parameters:**

$Der := Dis - 2 \cdot gap = 143.23944878 \cdot mm$  Rotor external diameter

$r_{radius} := \frac{Der}{2} = 71.61972439 \cdot mm$  rotor radius in air gap region

$\lambda_r := 2 \cdot \frac{\pi}{Pr} = 60.00000000 \cdot ^\circ$  rotor pole arc angle

$AlphaFirstPointSlEnd := \arcsin\left(\frac{\frac{SlrWidth}{2}}{r_{radius}}\right) = 1.09097501 \cdot ^\circ$

$alphaSlr := 2 \cdot AlphaFirstPointSlEnd = 2.18195003 \cdot ^\circ$  angle of rotor slot

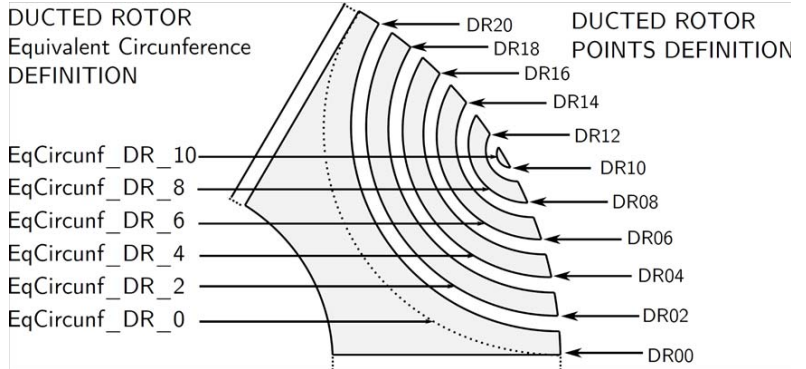
$Nslr\_pole := \frac{Nslr}{Pr} = 11.00000000$  number of slots per rotor pole

$alphaFluxPath := \frac{(2 \cdot \pi \div Pr - alphaSlr \cdot Nslr\_pole)}{Nslr\_pole} = 3.27259543 \cdot ^\circ$  Equivalent angle of the flux path in air gap region

$rgap := \frac{Dis}{2} = 72.11972439 \cdot mm$  air gap radius

**Calculation of the parameters associated to the ducted rotor**

The intermediary parameters calculated in the sequence are necessary to obtain the Lxdm and Sxdm parameters defined in Fig. 2. DRPoints\_X and DRPoints\_Y refers to the points used to draw the rotor slots.



$$\text{AlphaLastPointSIEnd} := 2 \cdot \frac{\pi}{Pr} - \text{AlphaFirstPointSIEnd} = 58.90902499 \cdot ^\circ$$

Calculate angles and points around the rotor ducted:

$$\text{DRPoints\_X\_00} := r_{\text{radius}} \cdot \cos(\text{AlphaFirstPointSIEnd}) = 71.60674143 \cdot \text{mm}$$

$$\text{DRPoints\_Y\_00} := r_{\text{radius}} \cdot \sin(\text{AlphaFirstPointSIEnd}) = 1.36363636 \cdot \text{mm}$$

$$\text{ThetaRotorPoints\_00} := \text{atan}[\text{DRPoints\_Y\_00} \div (\text{DRPoints\_X\_00})] = 1.09097501 \cdot ^\circ$$

$$\text{ThetaRotorPoints\_01} := \text{AlphaFirstPointSIEnd} + \text{alphaFluxPath} = 4.36357044 \cdot ^\circ$$

$$\text{DRPoints\_X\_01} := r_{\text{radius}} \cdot \cos(\text{ThetaRotorPoints\_01}) = 71.41212243 \cdot \text{mm}$$

$$\text{DRPoints\_Y\_01} := r_{\text{radius}} \cdot \sin(\text{ThetaRotorPoints\_01}) = 5.44919180 \cdot \text{mm}$$

$$\text{ThetaRotorPoints\_02} := \text{ThetaRotorPoints\_01} + \text{alphaSlr} = 6.54552047 \cdot ^\circ$$

$$\text{DRPoints\_X\_02} := r_{\text{radius}} \cdot \cos(\text{ThetaRotorPoints\_02}) = 71.15287868 \cdot \text{mm}$$

$$\text{DRPoints\_Y\_02} := r_{\text{radius}} \cdot \sin(\text{ThetaRotorPoints\_02}) = 8.16411523 \cdot \text{mm}$$

$$\text{ThetaRotorPoints\_03} := \text{ThetaRotorPoints\_02} + \text{alphaFluxPath} = 9.81811589 \cdot ^\circ$$

$$\text{DRPoints\_X\_03} := r_{\text{radius}} \cdot \cos(\text{ThetaRotorPoints\_03}) = 70.57078420 \cdot \text{mm}$$

$$\text{DRPoints\_Y\_03} := r_{\text{radius}} \cdot \sin(\text{ThetaRotorPoints\_03}) = 12.21267124 \cdot \text{mm}$$

$$\text{ThetaRotorPoints\_04} := \text{ThetaRotorPoints\_03} + \text{alphaSlr} = 12.0006592 \cdot ^\circ$$

$$\text{DRPoints\_X\_04} := r_{\text{radius}} \cdot \cos(\text{ThetaRotorPoints\_04}) = 70.05464445 \cdot \text{mm}$$

$$\text{DRPoints\_Y\_04} := r_{\text{radius}} \cdot \sin(\text{ThetaRotorPoints\_04}) = 14.89065860 \cdot \text{mm}$$

$$\text{ThetaRotorPoints\_05} := \text{ThetaRotorPoints\_04} + \text{alphaFluxPath} = 15.27266135 \cdot ^\circ$$

$$\text{DRPoints\_X\_05} := r_{\text{radius}} \cdot \cos(\text{ThetaRotorPoints\_05}) = 69.09034602 \cdot \text{mm}$$

$$\text{DRPoints\_Y\_05} := r_{\text{radius}} \cdot \sin(\text{ThetaRotorPoints\_05}) = 18.86555084 \cdot \text{mm}$$

ThetaRotorPoints\_06 := ThetaRotorPoints\_05 + alphaSlr = 17.45461138.°  
DRPoints\_X\_06 := rradius\*cos(ThetaRotorPoints\_06) = 68.32198450-mm  
DRPoints\_Y\_06 := rradius\*sin(ThetaRotorPoints\_06) = 21.48234986-mm

ThetaRotorPoints\_07 := ThetaRotorPoints\_06 + alphaFluxPath = 20.72720680.°  
DRPoints\_X\_07 := rradius\*cos(ThetaRotorPoints\_07) = 66.98421497-mm  
DRPoints\_Y\_07 := rradius\*sin(ThetaRotorPoints\_07) = 25.34758109-mm

ThetaRotorPoints\_08 := ThetaRotorPoints\_07 + alphaSlr = 22.90915683.°  
DRPoints\_X\_08 := rradius\*cos(ThetaRotorPoints\_08) = 65.97059009-mm  
DRPoints\_Y\_08 := rradius\*sin(ThetaRotorPoints\_08) = 27.87949363-mm

ThetaRotorPoints\_09 := ThetaRotorPoints\_08 + alphaFluxPath = 26.18175226.°  
DRPoints\_X\_09 := rradius\*cos(ThetaRotorPoints\_09) = 64.27146449-mm  
DRPoints\_Y\_09 := rradius\*sin(ThetaRotorPoints\_09) = 31.60005972-mm

ThetaRotorPoints\_10 := ThetaRotorPoints\_09 + alphaSlr = 28.36370229.°  
DRPoints\_X\_10 := rradius\*cos(ThetaRotorPoints\_10) = 63.02175579-mm  
DRPoints\_Y\_10 := rradius\*sin(ThetaRotorPoints\_10) = 34.02415640-mm

ThetaRotorPoints\_11 := ThetaRotorPoints\_10 + alphaFluxPath = 31.63629771.°  
DRPoints\_X\_11 := rradius\*cos(ThetaRotorPoints\_11) = 60.97666168-mm  
DRPoints\_Y\_11 := rradius\*sin(ThetaRotorPoints\_11) = 37.56636331-mm

ThetaRotorPoints\_12 := ThetaRotorPoints\_11 + alphaSlr = 33.81824774.°  
DRPoints\_X\_12 := rradius\*cos(ThetaRotorPoints\_12) = 59.50218672-mm  
DRPoints\_Y\_12 := rradius\*sin(ThetaRotorPoints\_12) = 39.86069113-mm

ThetaRotorPoints\_13 := ThetaRotorPoints\_12 + alphaFluxPath = 37.09084317.°  
DRPoints\_X\_13 := rradius\*cos(ThetaRotorPoints\_13) = 57.12964478-mm  
DRPoints\_Y\_13 := rradius\*sin(ThetaRotorPoints\_13) = 43.19246010-mm

ThetaRotorPoints\_14 := ThetaRotorPoints\_13 + alphaSlr = 39.27279320.°  
DRPoints\_X\_14 := rradius\*cos(ThetaRotorPoints\_14) = 55.44375663-mm  
DRPoints\_Y\_14 := rradius\*sin(ThetaRotorPoints\_14) = 45.33624127-mm

ThetaRotorPoints\_15 := ThetaRotorPoints\_14 + alphaFluxPath = 42.54538862.°  
DRPoints\_X\_15 := rradius\*cos(ThetaRotorPoints\_15) = 52.76525296-mm  
DRPoints\_Y\_15 := rradius\*sin(ThetaRotorPoints\_15) = 48.42739929-mm

$\text{ThetaRotorPoints}_{16} := \text{ThetaRotorPoints}_{15} + \alpha\text{Slr} = 44.72733865^\circ$   
 $\text{DRPoints}_{X_{16}} := r\text{radius} \cdot \cos(\text{ThetaRotorPoints}_{16}) = 50.88321929\text{-mm}$   
 $\text{DRPoints}_{Y_{16}} := r\text{radius} \cdot \sin(\text{ThetaRotorPoints}_{16}) = 50.40121939\text{-mm}$

$\text{ThetaRotorPoints}_{17} := \text{ThetaRotorPoints}_{16} + \alpha\text{FluxPath} = 47.99993408^\circ$   
 $\text{DRPoints}_{X_{17}} := r\text{radius} \cdot \cos(\text{ThetaRotorPoints}_{17}) = 47.92301085\text{-mm}$   
 $\text{DRPoints}_{Y_{17}} := r\text{radius} \cdot \sin(\text{ThetaRotorPoints}_{17}) = 53.22377244\text{-mm}$

$\text{ThetaRotorPoints}_{18} := \text{ThetaRotorPoints}_{17} + \alpha\text{Slr} = 50.18188411^\circ$   
 $\text{DRPoints}_{X_{18}} := r\text{radius} \cdot \cos(\text{ThetaRotorPoints}_{18}) = 45.86187564\text{-mm}$   
 $\text{DRPoints}_{Y_{18}} := r\text{radius} \cdot \sin(\text{ThetaRotorPoints}_{18}) = 55.00975626\text{-mm}$

$\text{ThetaRotorPoints}_{19} := \text{ThetaRotorPoints}_{18} + \alpha\text{FluxPath} = 53.45447953^\circ$   
 $\text{DRPoints}_{X_{19}} := r\text{radius} \cdot \cos(\text{ThetaRotorPoints}_{19}) = 42.64677053\text{-mm}$   
 $\text{DRPoints}_{Y_{19}} := r\text{radius} \cdot \sin(\text{ThetaRotorPoints}_{19}) = 57.53814288\text{-mm}$

$\text{ThetaRotorPoints}_{20} := \text{ThetaRotorPoints}_{19} + \alpha\text{Slr} = 55.63642956^\circ$   
 $\text{DRPoints}_{X_{20}} := r\text{radius} \cdot \cos(\text{ThetaRotorPoints}_{20}) = 40.42519975\text{-mm}$   
 $\text{DRPoints}_{Y_{20}} := r\text{radius} \cdot \sin(\text{ThetaRotorPoints}_{20}) = 59.12011627\text{-mm}$

$\text{ThetaRotorPoints}_{21} := \text{ThetaRotorPoints}_{20} + \alpha\text{FluxPath} = 58.90902499^\circ$   
 $\text{DRPoints}_{X_{21}} := r\text{radius} \cdot \cos(\text{ThetaRotorPoints}_{21}) = 36.98431445\text{-mm}$   
 $\text{DRPoints}_{Y_{21}} := r\text{radius} \cdot \sin(\text{ThetaRotorPoints}_{21}) = 61.33143898\text{-mm}$

$\text{ThetaRotorPoints}_{22} := \text{ThetaRotorPoints}_{21} + \alpha\text{Slr} = 61.09097501^\circ$   
 $\text{DRPoints}_{X_{22}} := r\text{radius} \cdot \cos(\text{ThetaRotorPoints}_{22}) = 34.62242698\text{-mm}$   
 $\text{DRPoints}_{Y_{22}} := r\text{radius} \cdot \sin(\text{ThetaRotorPoints}_{22}) = 62.69507534\text{-mm}$

$\text{ThetaRotorPoints}_{23} := \text{ThetaRotorPoints}_{22} + \alpha\text{FluxPath} = 64.36357044^\circ$   
 $\text{DRPoints}_{X_{23}} := r\text{radius} \cdot \cos(\text{ThetaRotorPoints}_{23}) = 30.98692269\text{-mm}$   
 $\text{DRPoints}_{Y_{23}} := r\text{radius} \cdot \sin(\text{ThetaRotorPoints}_{23}) = 64.56930807\text{-mm}$

Calculate distance between points and radius of equivalent circumference:

$$\text{DistBtwPoints}_{DR0} := \sqrt{(\text{DRPoints}_{X_{21}} - \text{DRPoints}_{X_{00}})^2 + (\text{DRPoints}_{Y_{21}} - \text{DRPoints}_{Y_{00}})^2}$$

$$\text{DistBtwPoints}_{DR0} = 69.24485396\text{-mm}$$

$$\text{RadiusEqCircunf}_{DR0} := \frac{(\text{DistBtwPoints}_{DR0} \div 2)}{\sin(\text{SlotRotorAngleDeg} \div 2)} = 39.97853507\text{-mm}$$

$$\text{DistBtwPoints}_{DR1} := \sqrt{(\text{DRPoints}_{X_{20}} - \text{DRPoints}_{X_{01}})^2 + (\text{DRPoints}_{Y_{20}} - \text{DRPoints}_{Y_{01}})^2}$$



$$\text{DistBtwPoints\_DR1} = 61.97384537 \cdot \text{mm}$$

$$\text{RadiusEqCircunf\_DR\_1} := \frac{(\text{DistBtwPoints\_DR1} \div 2)}{\sin(\text{SlotRotorAngleDeg} \div 2)} = 35.78061631 \cdot \text{mm}$$

$$\text{DistBtwPoints\_DR2} := \sqrt{(\text{DRPoints\_X\_19} - \text{DRPoints\_X\_02})^2 + (\text{DRPoints\_Y\_19} - \text{DRPoints\_Y\_02})^2}$$

$$\text{DistBtwPoints\_DR2} = 57.01221631 \cdot \text{mm}$$

$$\text{RadiusEqCircunf\_DR\_2} := \frac{(\text{DistBtwPoints\_DR2} \div 2)}{\sin(\text{SlotRotorAngleDeg} \div 2)} = 32.91601843 \cdot \text{mm}$$

$$\text{DistBtwPoints\_DR3} := \sqrt{(\text{DRPoints\_X\_18} - \text{DRPoints\_X\_03})^2 + (\text{DRPoints\_Y\_18} - \text{DRPoints\_Y\_03})^2}$$

$$\text{DistBtwPoints\_DR3} = 49.41781712 \cdot \text{mm}$$

$$\text{RadiusEqCircunf\_DR\_3} := \frac{(\text{DistBtwPoints\_DR3} \div 2)}{\sin(\text{SlotRotorAngleDeg} \div 2)} = 28.53139002 \cdot \text{mm}$$

$$\text{DistBtwPoints\_DR4} := \sqrt{(\text{DRPoints\_X\_17} - \text{DRPoints\_X\_04})^2 + (\text{DRPoints\_Y\_17} - \text{DRPoints\_Y\_04})^2}$$

$$\text{DistBtwPoints\_DR4} = 44.26326720 \cdot \text{mm}$$

$$\text{RadiusEqCircunf\_DR\_4} := \frac{(\text{DistBtwPoints\_DR4} \div 2)}{\sin(\text{SlotRotorAngleDeg} \div 2)} = 25.55540923 \cdot \text{mm}$$

$$\text{DistBtwPoints\_DR5} := \sqrt{(\text{DRPoints\_X\_16} - \text{DRPoints\_X\_05})^2 + (\text{DRPoints\_Y\_16} - \text{DRPoints\_Y\_05})^2}$$

$$\text{DistBtwPoints\_DR5} = 36.41425345 \cdot \text{mm}$$

$$\text{RadiusEqCircunf\_DR\_5} := \frac{(\text{DistBtwPoints\_DR5} \div 2)}{\sin(\text{SlotRotorAngleDeg} \div 2)} = 21.02377903 \cdot \text{mm}$$

$$\text{DistBtwPoints\_DR6} := \sqrt{(\text{DRPoints\_X\_15} - \text{DRPoints\_X\_06})^2 + (\text{DRPoints\_Y\_15} - \text{DRPoints\_Y\_06})^2}$$

$$\text{DistBtwPoints\_DR6} = 31.11346308 \cdot \text{mm}$$

$$\text{RadiusEqCircunf\_DR\_6} := \frac{(\text{DistBtwPoints\_DR6} \div 2)}{\sin(\text{SlotRotorAngleDeg} \div 2)} = 17.96336629 \cdot \text{mm}$$

$$\text{DistBtwPoints\_DR7} := \sqrt{(\text{DRPoints\_X\_14} - \text{DRPoints\_X\_07})^2 + (\text{DRPoints\_Y\_14} - \text{DRPoints\_Y\_07})^2}$$

$$\text{DistBtwPoints\_DR7} = 23.08091667 \cdot \text{mm}$$

$$\text{RadiusEqCircunf\_DR\_7} := \frac{(\text{DistBtwPoints\_DR7} \div 2)}{\sin(\text{SlotRotorAngleDeg} \div 2)} = 13.32577345 \cdot \text{mm}$$

$$\text{DistBtwPoints\_DR8} := \sqrt{(\text{DRPoints\_X\_13} - \text{DRPoints\_X\_08})^2 + (\text{DRPoints\_Y\_13} - \text{DRPoints\_Y\_08})^2}$$

$$\text{DistBtwPoints\_DR8} = 17.68189063 \cdot \text{mm}$$

$$\text{RadiusEqCircunf\_DR\_8} := \frac{(\text{DistBtwPoints\_DR8} \div 2)}{\sin(\text{SlotRotorAngleDeg} \div 2)} = 10.20864431 \cdot \text{mm}$$

$$\text{DistBtwPoints\_DR9} := \sqrt{(\text{DRPoints\_X\_12} - \text{DRPoints\_X\_09})^2 + (\text{DRPoints\_Y\_12} - \text{DRPoints\_Y\_09})^2}$$

$$\text{DistBtwPoints\_DR9} = 9.53855554 \cdot \text{mm}$$

$$\text{RadiusEqCircunf\_DR\_9} := \frac{(\text{DistBtwPoints\_DR9} \div 2)}{\sin(\text{SlotRotorAngleDeg} \div 2)} = 5.50708761 \cdot \text{mm}$$

$$\text{DistBtwPoints\_DR10} := \sqrt{(\text{DRPoints\_X\_11} - \text{DRPoints\_X\_10})^2 + (\text{DRPoints\_Y\_11} - \text{DRPoints\_Y\_10})^2}$$

$$\text{DistBtwPoints\_DR10} = 4.09018823 \cdot \text{mm}$$

$$\text{RadiusEqCircunf\_DR\_10} := \frac{(\text{DistBtwPoints\_DR10} \div 2)}{\sin(\text{SlotRotorAngleDeg} \div 2)} = 2.36147128 \cdot \text{mm}$$

**Calculate length and area of each flux path:**

$$\text{L1dm} := \frac{(\text{RadiusEqCircunf\_DR\_0} + \text{RadiusEqCircunf\_DR\_1})}{2} \cdot \text{SlotRotorAngleDeg} = 79.33479781 \cdot \text{mm}$$

$$\text{S1dm} := \sqrt{(\text{DRPoints\_X\_01} - \text{DRPoints\_X\_00})^2 + (\text{DRPoints\_Y\_01} - \text{DRPoints\_Y\_00})^2} \cdot \text{Lstkef}$$

$$\text{S1dm} = 282.22298812 \cdot \text{mm}^2$$

$$\text{L2dm} := \frac{(\text{RadiusEqCircunf\_DR\_2} + \text{RadiusEqCircunf\_DR\_3})}{2} \cdot \text{SlotRotorAngleDeg} = 64.34757565 \cdot \text{mm}$$

$$\text{S2dm} := \sqrt{(\text{DRPoints\_X\_03} - \text{DRPoints\_X\_02})^2 + (\text{DRPoints\_Y\_03} - \text{DRPoints\_Y\_02})^2} \cdot \text{Lstkef}$$

$$\text{S2dm} = 282.22298812 \cdot \text{mm}^2$$

$$\text{L3dm} := \frac{(\text{RadiusEqCircunf\_DR\_4} + \text{RadiusEqCircunf\_DR\_5})}{2} \cdot \text{SlotRotorAngleDeg} = 48.77761189 \cdot \text{mm}$$

$$\text{S3dm} := \sqrt{(\text{DRPoints\_X\_05} - \text{DRPoints\_X\_04})^2 + (\text{DRPoints\_Y\_05} - \text{DRPoints\_Y\_04})^2} \cdot \text{Lstkef}$$

$$\text{S3dm} = 282.22298812 \cdot \text{mm}^2$$

$$\text{L4dm} := \frac{(\text{RadiusEqCircunf\_DR\_6} + \text{RadiusEqCircunf\_DR\_7})}{2} \cdot \text{SlotRotorAngleDeg} = 32.76591052 \cdot \text{mm}$$

$$\text{S4dm} := \sqrt{(\text{DRPoints\_X\_07} - \text{DRPoints\_X\_06})^2 + (\text{DRPoints\_Y\_07} - \text{DRPoints\_Y\_06})^2} \cdot \text{Lstkef}$$

$$\text{S4dm} = 282.22298812 \cdot \text{mm}^2$$

$$L5dm := \frac{(\text{RadiusEqCircunf\_DR\_8} + \text{RadiusEqCircunf\_DR\_9})}{2} \cdot \text{SlotRotorAngleDeg} = 16.45747598 \cdot \text{mm}$$

$$S5dm := \sqrt{(\text{DRPoints\_X\_09} - \text{DRPoints\_X\_08})^2 + (\text{DRPoints\_Y\_09} - \text{DRPoints\_Y\_08})^2} \cdot \text{Lstkef}$$

$$S5dm = 282.22298812 \cdot \text{mm}^2$$

$$L6dm := (\text{RadiusEqCircunf\_DR\_10}) \cdot \text{SlotRotorAngleDeg} = 4.94585388 \cdot \text{mm}$$

$$S6dm := \frac{\sqrt{(\text{DRPoints\_X\_11} - \text{DRPoints\_X\_10})^2 + (\text{DRPoints\_Y\_11} - \text{DRPoints\_Y\_10})^2}}{2} \cdot \text{Lstkef}$$

$$S6dm = 141.11149406 \cdot \text{mm}^2$$

## **2- Electrical parameters**

### **Winding Parameters Calculation:**

$$\text{Nslg} := \frac{\text{Nphg}}{\text{Nsl} \div (3 \cdot 2)} = 56.00000000 \quad \text{number of turns per slot}$$

$$\text{Nslc} := \frac{\text{Nphc}}{[\text{Nsl} \div (3 \cdot 2)]} = 39.00000000 \quad \text{number of turns per slot}$$

$$\text{ng} := \frac{\text{Nphg}}{\text{Pg}} = 56.00000000 \quad \text{number of turns per pole (primary)}$$

$$\text{nc} := \frac{\text{Nphc}}{\text{Pc}} = 78.00000000 \quad \text{number of turns per pole (secondary)}$$

$$\text{Nslcoilside\_g} := \frac{\text{Nsl}}{3 \cdot \text{Pg}} = 2.00000000 \quad \text{number of slots per coil side grid}$$

$$\text{Nslcoilside\_c} := \frac{\text{Nsl}}{3 \cdot \text{Pc}} = 4.00000000 \quad \text{number of slots per coil side control}$$

$$\text{SlotAngle} := 2 \cdot \frac{\pi}{\text{Nsl}} = 7.50000000 \cdot ^\circ \quad \text{slot angle}$$

$$\text{SlotPitch} := \frac{(\pi \cdot \text{Dis})}{\text{Nsl}} = 9.44044985 \cdot \text{mm} \quad \text{slot pitch}$$

$$\phi_{\text{phg}} := \text{Nslcoilside\_g} \cdot 2 \cdot \text{SlotAngle} = 30.00000000 \cdot ^\circ \quad \text{angle of phase a of grid winding in relation to the reference}$$

$$\phi_{\text{phc}} := \text{Nslcoilside\_c} \cdot 2 \cdot \text{SlotAngle} = 60.00000000 \cdot ^\circ$$

$$\phi_{\text{phge}} := \phi_{\text{phg}} \cdot \frac{\text{Pg}}{2} = 120.00000000 \cdot ^\circ \quad \text{electrical angle is always } 120^\circ \text{ when the reference is } 0^\circ \text{ over the x axis}$$

$$\phi_{\text{phce}} := \phi_{\text{phc}} \cdot \frac{\text{Pc}}{2} = 120.00000000 \cdot ^\circ$$

### **Phase winding resistances**

unit\_corr := m·Ω

temperature correction for copper resistivity

$$\text{rhot} := \text{rho} \cdot [1 + \text{alpha} \cdot (\text{tsta} - 20)] \cdot \text{unit\_corr} = 2.4106000 \times 10^{-8} \frac{\text{kg} \cdot \text{m}^{3.00000000}}{\text{s}^{3.00000000} \cdot \text{A}^{2.00000000}}$$

Calculation of required copper area to satisfy current density requirement:

$$\text{ScondWg} := \pi \cdot \left( \frac{\text{DcondWg}}{2} \right)^2 = 0.65304967 \cdot \text{mm}^2 \quad \text{conductor area}$$

Calculation of coil length:

$$\text{csl} := 2 \cdot \text{Lstkef} = 138.00000000 \cdot \text{mm} \quad \text{coil side length}$$

$$\text{cheadWg} := 2 \cdot \left[ \frac{(\text{Des} \div 2 + \text{Dsle} \div 2)}{2} \cdot \left( 2 \cdot \frac{\pi}{\text{Pg}} \right) \right] = 173.18381688 \cdot \text{mm} \quad \text{coil yoke length}$$

$$\text{tclWg} := \text{csl} + \text{cheadWg} = 311.18381688 \cdot \text{mm} \quad \text{total coil length for Wg}$$

$$\text{Rg} := \text{rhot} \cdot \frac{\left( \text{Kwirel} \cdot \text{tclWg} \cdot \frac{\text{Pg}}{2} \cdot \text{Nslcoilside\_g} \cdot \text{Nslg} \right)}{\text{ScondWg}} = 5.66065443 \Omega \quad \text{grid winding phase resistance}$$

$$\text{ScondWc} := \pi \cdot \left( \frac{\text{DcondWc}}{2} \right)^2 = 0.65304967 \cdot \text{mm}^2 \quad \text{conductor area}$$

Calculation of coil length:

$$\text{cheadWc} := 2 \cdot \left[ \frac{(\text{Des} \div 2 + \text{Dsle} \div 2)}{2} \cdot \left( 2 \cdot \frac{\pi}{\text{Pc}} \right) \right] = 346.36763375 \cdot \text{mm} \quad \text{coil yoke length}$$

$$\text{tclWc} := \text{csl} + \text{cheadWc} = 484.36763375 \cdot \text{mm} \quad \text{total coil length for Wc}$$

$$\text{Rc} := \text{rhot} \cdot \frac{\left( \text{Kwirel} \cdot \text{tclWc} \cdot \frac{\text{Pc}}{2} \cdot \text{Nslcoilside\_c} \cdot \text{Nslc} \right)}{\text{ScondWc}} = 6.13622583 \Omega \quad \text{Control winding phase resistance}$$

### Calculation of winding filling factor:

Calculation of slot available area:

$$\text{Sslot} := \left[ \frac{\left[ \left( \frac{\text{Dsle}}{2} \right)^2 - \left( \frac{\text{Dsl}}{2} \right)^2 \right]}{\text{Nsl}} \right] \cdot \pi - \text{thw} \cdot \text{sll} = 177.32736308 \cdot \text{mm}^2$$

Calculation of the area occupied by conductors in the slot

$$\text{wapsl\_g} := \text{ScondWg} \cdot \text{Nslg} = 36.57078130 \cdot \text{mm}^2$$

$$\text{wapsl\_c} := \text{ScondWc} \cdot \text{Nslc} = 25.46893698 \cdot \text{mm}^2$$

$$\text{wapsl} := \text{wapsl\_g} + \text{wapsl\_c} = 62.03971828 \cdot \text{mm}^2$$

Calculation of winding filling factor:

$$wff := \frac{wapsl}{Sslot} = 0.34985981$$

winding filling factor. It should be usually less than 0.4

## Windings Factors Calculation [7]:

### **Grid winding:**

$$\tau_{pg} := \frac{\pi \cdot Dis}{2 \cdot pg} = 56.64269908 \cdot \text{mm} \quad \text{pole pitch}$$

$$\gamma_{pg} := \tau_{pg} = 56.64269908 \cdot \text{mm} \quad \text{coil pitch, usually } \gamma_{pg}/\tau_{pg} > 2/3. \\ \text{No short-pitching considered}$$

$$qg := \frac{Nsl}{2 \cdot pg \cdot 3} = 2.00000000 \quad \text{average number of slots per pole per phase}$$

$$\alpha_{seg} := \frac{(2 \cdot pg \cdot \pi)}{Nsl} = 30.00000000 \cdot ^\circ \quad \text{angle between the center lines of adjacents slots}$$

$$K_{pg} := \sin\left(\frac{\gamma_{pg}}{\tau_{pg}} \cdot \frac{\pi}{2}\right) = 1.00000000 \quad \text{pitch factor}$$

$$K_{dg} := \frac{\sin\left(\frac{\pi}{6}\right)}{qg \cdot \sin\left(\frac{\pi}{6 \cdot qg}\right)} = 0.96592583 \quad \text{distribution factor}$$

$$K_{wg} := K_{pg} \cdot K_{dg} = 0.96592583 \quad \text{winding factor grid winding}$$

### **Control winding:**

$$\tau_{pc} := \frac{\pi \cdot Dis}{2 \cdot pc} = 113.28539816 \cdot \text{mm} \quad \text{pole pitch}$$

$$\gamma_{pc} := \tau_{pc} = 113.28539816 \cdot \text{mm} \quad \text{coil pitch, usually } \gamma_{pc}/\tau_{pc} > 2/3 \text{ No short-pitching considered}$$

$$qc := \frac{Nsl}{2 \cdot pc \cdot 3} = 4.00000000 \quad \text{average number of slots per pole per phase}$$

$$\alpha_{sec} := \frac{(2 \cdot pc \cdot \pi)}{Nsl} = 15.00000000 \cdot ^\circ \quad \text{angle between the center lines of adjacents slots}$$

$$K_{pc} := \sin\left(\frac{\gamma_{pc}}{\tau_{pc}} \cdot \frac{\pi}{2}\right) = 1.00000000 \quad \text{pitch factor}$$

$$K_{dc} := \frac{\sin\left(\frac{\pi}{6}\right)}{qc \cdot \sin\left(\frac{\pi}{6 \cdot qc}\right)} = 0.95766220 \quad \text{distribution factor}$$

$$K_{wc} := K_{pc} \cdot K_{dc} = 0.95766220 \quad \text{winding factor control winding}$$

### 3- Specific electric loading

#### Actual specific electric loading grid winding [3.1]

$$\lambda_{selg} := \frac{3 \cdot (N_{phg} \cdot K_{wgc})}{\pi \cdot r_{gap}} \cdot (I_{phg} \div \sqrt{2}) = 1.24504398 \times 10^4 \frac{A}{m}$$

Actual specific electric loading control winding

$$\lambda_{selc} := \frac{3 \cdot (N_{phc} \cdot K_{wcc})}{\pi \cdot r_{gap}} \cdot (I_{phc} \div \sqrt{2}) = 9.04270823 \times 10^3 \frac{A}{m}$$

Total specific electric loading at rated current

$$\lambda_{sel\_total} := \lambda_{selg} + \lambda_{selc} = 2.14931480 \times 10^4 \frac{A}{m}$$

Total estimated specific electrical loading of the machine

### 4- Duct ratio

#### Calculation of the Duct Ratio [8]

$$\tau_{rpole} := \frac{2 \cdot \pi}{Pr} \cdot \frac{Der}{2} = 75.00000000 \cdot mm$$

$$\text{DuctRatio} := \frac{N_{slr} \cdot SlrWidth}{Pr \cdot (\tau_{rpole})} = 0.40000000$$

$$\lambda_{ratioL\tau\_actual} := \frac{L_{stkef}}{\tau_{rpitch}} = 0.91362172$$

Ratio axial length / rotor pole pitch [1]

actual L/τ ratio. Values should be between 0.6 < λ < 3.0

### 5- Carter's Factor

The Carter's factor is calculated according to Ref [1], pag 161, and it assumes that both stator and rotor have open slots.

Carter's coefficient for the stator:

$$\tau_{ths} := \tau_{th} = 9.44044985 \cdot mm$$

stator tooth pitch including slot opening

$$\kappa_s := \frac{2}{\pi} \left[ \operatorname{atan} \left( \frac{\text{slop}}{2 \cdot \text{gap}} \right) - \frac{2 \cdot \text{gap}}{\text{slop}} \ln \left[ 1 + \left( \frac{\text{slop}}{2 \cdot \text{gap}} \right)^2 \right] \right] = 0.39177380$$

$$K_{cs} := \frac{\tau_{ths}}{\tau_{ths} - \text{slop} \cdot \kappa_s} = 1.07112159$$

Carter's coefficient for rotor:

$$\tau_{thr} := 2 \cdot \frac{\pi}{N_{slr}} \cdot \frac{D_{gap}}{2} = 6.86578171 \cdot mm$$

rotor tooth pitch including slot opening

$$\kappa_r := \frac{2}{\pi} \left[ \operatorname{atan} \left( \frac{\operatorname{SlrWidth}}{2 \cdot \operatorname{gap}} \right) - \frac{2 \cdot \operatorname{gap}}{\operatorname{SlrWidth}} \ln \left[ \sqrt{1 + \left( \frac{\operatorname{SlrWidth}}{2 \cdot \operatorname{gap}} \right)^2} \right] \right] = 0.52734263$$

$$K_{cr} := \frac{\tau_{thr}}{\tau_{thr} - \operatorname{SlrWidth} \cdot \kappa_r} = 1.26498156$$

Total carter's coefficient:

$$K_{cTotal} := K_{cs} \cdot K_{cr} = 1.35494906$$

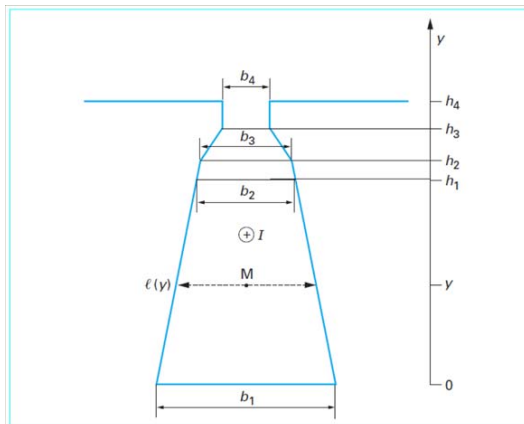
$$\boxed{\operatorname{gap}_{ef} := \operatorname{gap} \cdot K_{cTotal} = 0.67747453 \cdot \operatorname{mm}}$$

## **6- Leakage inductance**

### **Calculation of Leakage inductance [9]:**

Methodology adapted from [9] to calculate leakage inductances

From the drawing below and using the following definitions:



$h_4$  and  $h_8$  height occupied by each winding,  $x_1$  width in slot near yoke,  $x_2$  width in the beginning of Wg,  $x_3$  width at Dsl in slot,  $x_4 = \operatorname{slop}$   
This calculation assumes that Wc is near the yoke and Wg is near the airgap

$$h_c := \frac{\operatorname{wapsl}_c}{\operatorname{wapsl}} \cdot \operatorname{sll} = 11.03690138 \cdot \operatorname{mm}$$

equivalent length occupied by winding c

$$h_g := \frac{\operatorname{wapsl}_g}{\operatorname{wapsl}} \cdot \operatorname{sll} = 15.84785839 \cdot \operatorname{mm}$$

equivalent length occupied by winding g

$x1 := \text{slyairl} = 8.35490591 \cdot \text{mm}$	length at yoke
$Dx2 := \left( \frac{Dslc}{2} - hc \right) \cdot 2 = 183.93516556 \cdot \text{mm}$	Diameter in middle slot in the begining of Wg
$\alpha_{thDx2} := 2 \cdot \text{asin} \left( \frac{thw}{Dx2} \right) = 3.19504437 \cdot ^\circ$	tooth angle in the Dx2 slot region
$\alpha_{sliarDx2} := \frac{(2\pi - Nsl \cdot \alpha_{thDx2})}{Nsl} = 4.30495563 \cdot ^\circ$	slot angle in x2
$x2 := \alpha_{sliarDx2} \cdot \frac{Dx2}{2} = 6.91004410 \cdot \text{mm}$	slot Dx2 air length
$x3 := \text{sldsliairl} = 4.83525865 \cdot \text{mm}$	slot Dsli air length
$x4 := \text{slop} = 1.60000000 \cdot \text{mm}$	slot opening
$a_{\text{paralel}} := 1$	nr of paralel path in a winding
$Nc_{\text{induct}} := Nslc = 39.00000000$	$kLlc := 1$
$Ng_{\text{induct}} := Nslg = 56.00000000$	$kLlg := 1$

**Leakage inductance in slot:**

$$Llsc := \mu_0 \cdot Nc_{\text{induct}}^2 \cdot Lstkef \cdot \left[ \frac{(2 \cdot hc)}{3 \cdot (x1 + x2)} + \frac{2 \cdot hg}{x2 + x3} + \frac{thn}{x3 - x4} \cdot \ln \left( \frac{x3}{x4} \right) + \frac{thh}{x4} + \frac{gapef}{\tau th} \right]$$

$Llsc = 0.68394929 \cdot \text{mH}$  coil inductance in slot due to Wc

$$Lslg := \mu_0 \cdot Ng_{\text{induct}}^2 \cdot Lstkef \cdot \left[ \frac{(2 \cdot hg)}{3 \cdot (x2 + x3)} + \frac{thn}{x3 - x4} \cdot \ln \left( \frac{x3}{x4} \right) + \frac{thh}{x4} + \frac{gapef}{\tau th} \right]$$

$Lslg = 0.78990711 \cdot \text{mH}$  coil inductance in slot due to Wg

**Leakage inductance due to differential flux [A. Foggia]**

$$\tau_{wg\text{demi}} := \frac{2 \cdot \pi}{Pg} \cdot \frac{Dg_{\text{gap}}}{2} = 56.64269908 \cdot \text{mm} \quad \text{half winding pitch}$$

$$\tau_{wc\text{demi}} := \frac{2 \cdot \pi}{Pc} \cdot \frac{Dg_{\text{gap}}}{2} = 113.28539816 \cdot \text{mm} \quad \text{half winding pitch}$$

$$Ll_{dc} := 0.0025 \cdot \mu_0 \cdot Nc_{\text{induct}}^2 \cdot Lstkef \cdot \frac{\tau_{wg\text{demi}}^2}{\pi^2 \cdot gapef \cdot \tau th}$$

$Ll_{dc} = 0.06703331 \cdot \text{mH}$  differential inductance due to control winding

$$Ll_{dg} := 0.0025 \cdot \mu_0 \cdot Ng_{\text{induct}}^2 \cdot Lstkef \cdot \frac{\tau_{wg\text{demi}}^2}{\pi^2 \cdot gapef \cdot \tau th}$$

$Ll_{dg} = 0.03455234 \cdot \text{mH}$  differential inductance due to grid winding



### Leakage due to zig zag inductance

$$Llzc := \mu_0 \cdot Nc_{\text{induct}}^2 \cdot Lstkef \cdot \frac{(\tau_{\text{th}} - \text{slop})^2}{8 \cdot g_{\text{apef}} \cdot \tau_{\text{th}}}$$

$$Llzc = 0.15845082 \cdot \text{mH}$$

leakage due to zig zag flux in control winding

$$Llzg := \mu_0 \cdot Ng_{\text{induct}}^2 \cdot Lstkef \cdot \frac{(\tau_{\text{th}} - \text{slop})^2}{8 \cdot g_{\text{apef}} \cdot \tau_{\text{th}}}$$

$$Llzg = 0.32669412 \cdot \text{mH}$$

leakage due to zig zag flux in grid winding

### Total Leakage inductance

In the total leakage inductance, the overhang leakage flux is not considered. This flux is not considered in 2D FEA and that's why is not calculated here

$$Llcs_{\text{lot}} := (Llslc) \cdot \frac{Nsl}{3} = 10.94318859 \cdot \text{mH}$$

$$Llc := \frac{Nsl}{3} \cdot (Llslc + Lldc + Llzc) \cdot kLlc = 14.55093456 \cdot \text{mH}$$

$$Llg := \frac{Nsl}{3} \cdot (Llslg + Lldg + Llzg) \cdot kLlg = 18.41845726 \cdot \text{mH}$$

### Mass and volume calculation

$$Lstk := Lstkef = 69.00000000 \cdot \text{mm}$$

Machine outer volume:

$$\text{VolMachine}_L := \pi \left( \frac{\text{Des}}{2} \right)^2 \cdot Lstkef = 2.99277934 \text{ L}$$

Rotor Volume

$$\text{Vol}_{\text{rotor}} := \pi \left( \frac{\text{Dgap}}{2} \right)^2 \cdot Lstkef = 1.12747541 \text{ L} \quad \text{rotor volume according to parameters defined previously}$$

$$\text{VolumeTooth} := Lstk \cdot \left[ \frac{\left[ \left[ \left( \frac{\text{Dsle}}{2} \right)^2 - \left( \frac{\text{Dis}}{2} \right)^2 \right] \pi \right]}{Nsl} - \text{Sslot} - \text{slop} \cdot \text{thh} - \frac{(\text{sldslairl} + \text{thadneckl})}{2} \cdot \text{thh} \right]$$

$$\text{VolumeTooth} = 0.01150726 \text{ L}$$

$$\text{VolumeYoke1}_{\text{Pr}} := Lstk \cdot \left[ \frac{\left[ \left[ \left( \frac{\text{Des}}{2} \right)^2 - \left( \frac{\text{Dsle}}{2} \right)^2 \right] \pi \right]}{\text{Pr}} \right] = 0.11547788 \text{ L}$$

$$\text{VolumeFP1} := L1dm \cdot S1dm = 0.02239010 \text{ L}$$

$$\text{VolumeFP2} := L2dm \cdot S2dm = 0.01816037 \text{ L}$$

$$\text{VolumeFP3} := L3dm \cdot S3dm = 0.01376616 \text{ L}$$

$$\text{VolumeFP4} := L4\text{dm} \cdot S4\text{dm} = 9.24729317 \times 10^{-3} \text{ L}$$

$$\text{VolumeFP5} := L5\text{dm} \cdot S5\text{dm} = 4.64467805 \times 10^{-3} \text{ L}$$

$$\text{VolumeFP6} := L6\text{dm} \cdot S6\text{dm} = 6.97916830 \times 10^{-4} \text{ L}$$

$$\text{VolumeIronRotor} := (\text{VolumeFP1} + \text{VolumeFP2} + \text{VolumeFP3} + \text{VolumeFP4} + \text{VolumeFP5} + \text{VolumeFP6}) \cdot F$$

$$\text{VolumeIronRotor} = 0.41343912 \text{ L}$$

$$\text{VolumeIronStator} := \text{VolumeTooth} \cdot N\text{sl} + \text{VolumeYoke1\_Pr} \cdot Pr = 1.24521596 \text{ L}$$

$$\text{VolumeIronTotal} := \text{VolumeIronRotor} + \text{VolumeIronStator}$$

$$\text{VolumeCopperWg3}\phi := 3 \cdot \text{tclWg} \cdot \frac{Pg}{2} \cdot N\text{slcoilside\_g} \cdot N\text{slg} \cdot S\text{condWg} = 0.27312565 \text{ L}$$

$$\text{VolumeCopperWc3}\phi := 3 \cdot \text{tclWc} \cdot \frac{Pc}{2} \cdot N\text{slcoilside\_c} \cdot N\text{slc} \cdot S\text{condWc} = 0.29607189 \text{ L}$$

$$\text{VolumeCopperTotal} := \text{VolumeCopperWg3}\phi + \text{VolumeCopperWc3}\phi = 0.56919754 \text{ L}$$

$$\text{MassCopper} := \text{VolumeCopperTotal} \cdot \rho_{\text{copper}} = 5.10000993 \text{ kg}$$

$$\text{MassIron} := (\text{VolumeIronTotal}) \cdot \rho_{\text{iron}} = 12.68871136 \text{ kg}$$

$$\text{MassTotal} := \text{MassCopper} + \text{MassIron} = 17.78872129 \text{ kg}$$

$$\text{MassTooth} := \text{VolumeTooth} \cdot \rho_{\text{iron}} = 0.08803057 \text{ kg}$$

$$\text{MassYoke1\_Pr} := \text{VolumeYoke1\_Pr} \cdot \rho_{\text{iron}} = 0.88340581 \text{ kg}$$

$$\text{MassFP1} := \text{VolumeFP1} \cdot \rho_{\text{iron}} = 0.17128429 \text{ kg}$$

$$\text{MassFP2} := \text{VolumeFP2} \cdot \rho_{\text{iron}} = 0.13892679 \text{ kg}$$

$$\text{MassFP3} := \text{VolumeFP3} \cdot \rho_{\text{iron}} = 0.10531115 \text{ kg}$$

$$\text{MassFP4} := \text{VolumeFP4} \cdot \rho_{\text{iron}} = 0.07074179 \text{ kg}$$

$$\text{MassFP5} := \text{VolumeFP5} \cdot \rho_{\text{iron}} = 0.03553179 \text{ kg}$$

$$\text{MassFP6} := \text{VolumeFP6} \cdot \rho_{\text{iron}} = 5.33906375 \times 10^{-3} \text{ kg}$$

## Semi-Analytical Model: Sub-model 1: Equivalent Electric Circuit to determine phase voltages

### Flux Linkage and Inductance Calculation:

$$I_{g\_ind} := I_{phg} = 3.07298594 \text{ A}$$

currents used in each winding to inductance calculation

$$I_{c\_ind} := I_{phc} = 3.23243093 \text{ A}$$

$$\text{Ragmean} := \text{rgap} = 72.11972439 \cdot \text{mm}$$

mean airgap radius

$$\text{Lstkef} = 69.00000000 \cdot \text{mm}$$

machine length

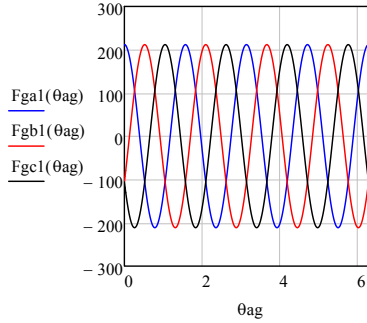
**Spatial MMF distribution (single phase):**

Grid Windings:

$$F_{ga1}(\theta_{ag}) := \frac{4}{\pi} \cdot \frac{N_{phg} \cdot K_{wg}}{P_g} \cdot I_{g\_ind} \cdot \cos\left(\frac{P_g}{2} \cdot \theta_{ag}\right)$$

$$F_{gb1}(\theta_{ag}) := \frac{4}{\pi} \cdot \frac{N_{phg} \cdot K_{wg}}{P_g} \cdot I_{g\_ind} \cdot \cos\left(\frac{P_g}{2} \cdot \theta_{ag} - 2 \cdot \frac{\pi}{3}\right)$$

$$F_{gc1}(\theta_{ag}) := \frac{4}{\pi} \cdot \frac{N_{phg} \cdot K_{wg}}{P_g} \cdot I_{g\_ind} \cdot \cos\left(\frac{P_g}{2} \cdot \theta_{ag} + 2 \cdot \frac{\pi}{3}\right)$$



Control Windings:

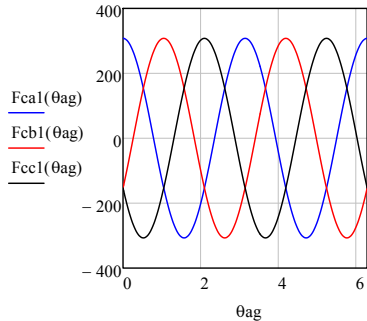
$\alpha_{temp} := 0^\circ$

angles which defines the position between grid and control a phase.  
 $0^\circ$  means that phase axis are coincidents

$$F_{ca1}(\theta_{ag}) := \frac{4}{\pi} \cdot \frac{N_{phc} \cdot K_{wc}}{P_c} \cdot I_{c\_ind} \cdot \cos\left(\frac{P_c}{2} \cdot \theta_{ag} - \alpha_{temp} \cdot \frac{P_c}{2}\right)$$

$$F_{cb1}(\theta_{ag}) := \frac{4}{\pi} \cdot \frac{N_{phc} \cdot K_{wc}}{P_c} \cdot I_{c\_ind} \cdot \cos\left(\frac{P_c}{2} \cdot \theta_{ag} - 2 \cdot \frac{\pi}{3} - \alpha_{temp} \cdot \frac{P_c}{2}\right)$$

$$F_{cc1}(\theta_{ag}) := \frac{4}{\pi} \cdot \frac{N_{phc} \cdot K_{wc}}{P_c} \cdot I_{c\_ind} \cdot \cos\left(\frac{P_c}{2} \cdot \theta_{ag} + 2 \cdot \frac{\pi}{3} - \alpha_{temp} \cdot \frac{P_c}{2}\right)$$



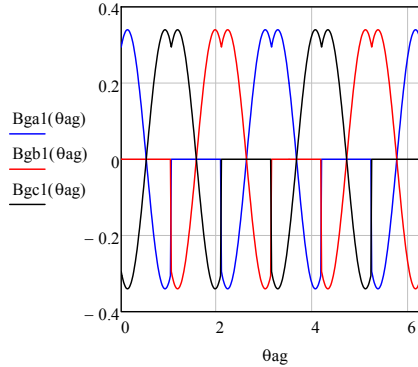
**Calculation of airgap flux density in air gap considering an ideal airgap**

Using the procedure described by Knight et al 2013 [3],  $B := \frac{\mu_0}{2g} \cdot (\text{FMM}(\theta_{\text{ag}1}) - \text{FMM}(\theta_{\text{ag}2}))$  ■

$$B_{\text{ga}1}(\theta_{\text{ag}}) := \frac{\mu_0}{2 \cdot \text{gap}_{\text{ef}}} \cdot (\text{Fga}1(\theta_{\text{ag}}) - \text{Fga}1(\theta_{\text{ag}} + \lambda r - 2 \cdot \text{mod}(\text{mod}(\theta_{\text{ag}} - \theta_{\text{ag}0}, \lambda r) + \lambda r, \lambda r)))$$

$$B_{\text{gb}1}(\theta_{\text{ag}}) := \frac{\mu_0}{2 \cdot \text{gap}_{\text{ef}}} \cdot (\text{Fgb}1(\theta_{\text{ag}}) - \text{Fgb}1(\theta_{\text{ag}} + \lambda r - 2 \cdot \text{mod}(\text{mod}(\theta_{\text{ag}} - \theta_{\text{ag}0}, \lambda r) + \lambda r, \lambda r)))$$

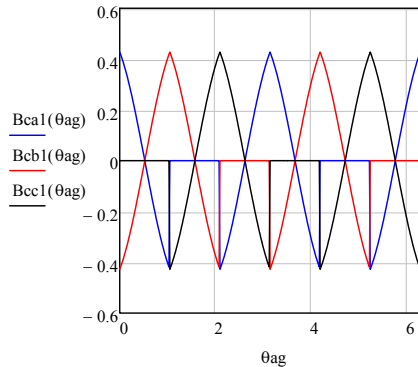
$$B_{\text{gc}1}(\theta_{\text{ag}}) := \frac{\mu_0}{2 \cdot \text{gap}_{\text{ef}}} \cdot (\text{Fgc}1(\theta_{\text{ag}}) - \text{Fgc}1(\theta_{\text{ag}} + \lambda r - 2 \cdot \text{mod}(\text{mod}(\theta_{\text{ag}} - \theta_{\text{ag}0}, \lambda r) + \lambda r, \lambda r)))$$



$$B_{\text{ca}1}(\theta_{\text{ag}}) := \frac{\mu_0}{2 \cdot \text{gap}_{\text{ef}}} \cdot (\text{Fca}1(\theta_{\text{ag}}) - \text{Fca}1(\theta_{\text{ag}} + \lambda r - 2 \cdot \text{mod}(\text{mod}(\theta_{\text{ag}} - \theta_{\text{ag}0}, \lambda r) + \lambda r, \lambda r)))$$

$$B_{\text{cb}1}(\theta_{\text{ag}}) := \frac{\mu_0}{2 \cdot \text{gap}_{\text{ef}}} \cdot (\text{Fcb}1(\theta_{\text{ag}}) - \text{Fcb}1(\theta_{\text{ag}} + \lambda r - 2 \cdot \text{mod}(\text{mod}(\theta_{\text{ag}} - \theta_{\text{ag}0}, \lambda r) + \lambda r, \lambda r)))$$

$$B_{\text{cc}1}(\theta_{\text{ag}}) := \frac{\mu_0}{2 \cdot \text{gap}_{\text{ef}}} \cdot (\text{Fcc}1(\theta_{\text{ag}}) - \text{Fcc}1(\theta_{\text{ag}} + \lambda r - 2 \cdot \text{mod}(\text{mod}(\theta_{\text{ag}} - \theta_{\text{ag}0}, \lambda r) + \lambda r, \lambda r)))$$



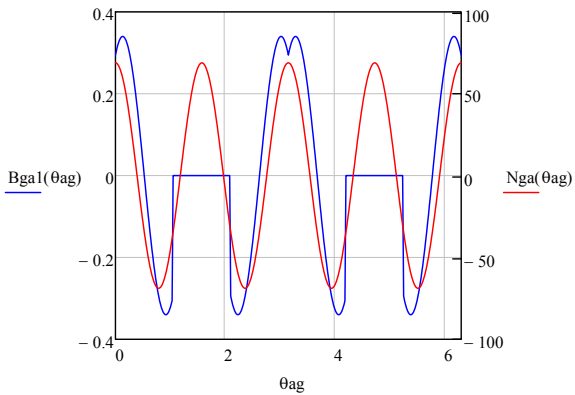
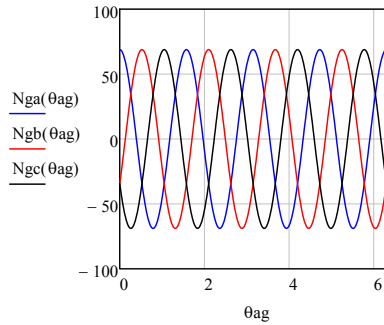
**Winding functions:**

Using the theory of winding functions to calculate inductances. See ref [5] for details

$$N_{ga}(\theta_{ag}) := \frac{F_{ga1}(\theta_{ag})}{I_{g\_ind}}$$

$$N_{gb}(\theta_{ag}) := \frac{F_{gb1}(\theta_{ag})}{I_{g\_ind}}$$

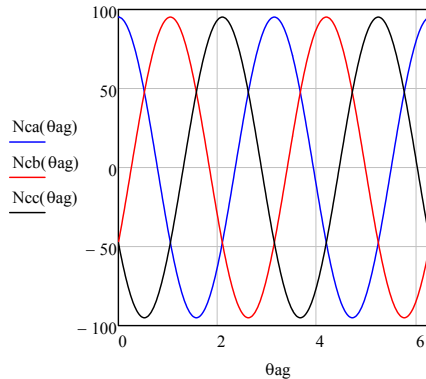
$$N_{gc}(\theta_{ag}) := \frac{F_{gc1}(\theta_{ag})}{I_{g\_ind}}$$



$$N_{ca}(\theta_{ag}) := \frac{F_{ca1}(\theta_{ag})}{I_{c\_ind}}$$

$$N_{cb}(\theta_{ag}) := \frac{F_{cb1}(\theta_{ag})}{I_{c\_ind}}$$

$$N_{cc}(\theta_{ag}) := \frac{F_{cc1}(\theta_{ag})}{I_{c\_ind}}$$



## The use of the winding function theory to calculate inductances:

$$\lambda_{ij} = rl \int_0^{2\pi} B_i(\theta, \theta_{rm}) N_j(\theta, \theta_{rm}) d\theta$$

winding function theory [5]

### Self flux linkage grid winding:

$$\lambda_{gaga} := \text{Ragmean} \cdot \text{Lstkef} \cdot \int_0^{2\pi} \text{Nga}(\theta_{ag}) \cdot \text{Bga1}(\theta_{ag}) d\theta_{ag} = 0.25503574 \text{ Wb}$$

$$\lambda_{ggbg} := \text{Ragmean} \cdot \text{Lstkef} \cdot \int_0^{2\pi} \text{Ngb}(\theta_{ag}) \cdot \text{Bgb1}(\theta_{ag}) d\theta_{ag} = 0.25504446 \text{ Wb}$$

$$\lambda_{gcgc} := \text{Ragmean} \cdot \text{Lstkef} \cdot \int_0^{2\pi} \text{Ngc}(\theta_{ag}) \cdot \text{Bgc1}(\theta_{ag}) d\theta_{ag} = 0.25503790 \text{ Wb}$$

$$L_{gaga} := \frac{\lambda_{gaga}}{I_{g\_ind}} = 82.99281087 \cdot \text{mH}$$

$$L_{ggbg} := \frac{\lambda_{ggbg}}{I_{g\_ind}} = 82.99564690 \cdot \text{mH}$$

$$L_{gcgc} := \frac{\lambda_{gcgc}}{I_{g\_ind}} = 82.99351216 \cdot \text{mH}$$

### Mutual flux linkage between grid winding phases:

Phase a:

$$\lambda_{gagb} := \text{Ragmean} \cdot \text{Lstkef} \cdot \int_0^{2\pi} \text{Nga}(\theta_{ag}) \cdot \text{Bgb1}(\theta_{ag}) d\theta_{ag} = -0.12752349 \text{ Wb}$$

$$\lambda_{gagc} := \text{Ragmean} \cdot \text{Lstkef} \cdot \int_0^{2 \cdot \pi} \text{Nga}(\theta_{ag}) \cdot \text{Bgb1}(\theta_{ag}) \, d\theta_{ag} = -0.12752349 \text{ Wb}$$

*Phase b:*

$$\lambda_{gbga} := \text{Ragmean} \cdot \text{Lstkef} \cdot \int_0^{2 \cdot \pi} \text{Ngb}(\theta_{ag}) \cdot \text{Bga1}(\theta_{ag}) \, d\theta_{ag} = -0.12751787 \text{ Wb}$$

$$\lambda_{gbgc} := \text{Ragmean} \cdot \text{Lstkef} \cdot \int_0^{2 \cdot \pi} \text{Ngb}(\theta_{ag}) \cdot \text{Bgc1}(\theta_{ag}) \, d\theta_{ag} = -0.12752611 \text{ Wb}$$

*Phase c:*

$$\lambda_{gcga} := \text{Ragmean} \cdot \text{Lstkef} \cdot \int_0^{2 \cdot \pi} \text{Ngc}(\theta_{ag}) \cdot \text{Bga1}(\theta_{ag}) \, d\theta_{ag} = -0.12751787 \text{ Wb}$$

$$\lambda_{gcgb} := \text{Ragmean} \cdot \text{Lstkef} \cdot \int_0^{2 \cdot \pi} \text{Ngc}(\theta_{ag}) \cdot \text{Bgb1}(\theta_{ag}) \, d\theta_{ag} = -0.12752460 \text{ Wb}$$

$$L_{gagb} := \frac{\lambda_{gagb}}{I_{g\_ind}} = -41.49823442 \cdot \text{mH}$$

$$L_{gagc} := \frac{\lambda_{gagc}}{I_{g\_ind}} = -41.49908795 \cdot \text{mH}$$

$$L_{gbga} := \frac{\lambda_{gbga}}{I_{g\_ind}} = -41.49640544 \cdot \text{mH}$$

$$L_{gbgc} := \frac{\lambda_{gbgc}}{I_{g\_ind}} = -41.49908795 \cdot \text{mH}$$

$$L_{gcga} := \frac{\lambda_{gcga}}{I_{g\_ind}} = -41.49640544 \cdot \text{mH}$$

$$L_{gcgb} := \frac{\lambda_{gcgb}}{I_{g\_ind}} = -41.49859444 \cdot \text{mH}$$

$$L_{gagb_{\text{teorique}}} := \frac{-1}{2} \cdot \frac{(L_{gaga} + L_{gbgb} + L_{gcgc})}{3} = -41.49699499 \cdot \text{mH}$$

## Self flux linkage control winding:

$$\lambda_{caca} := \text{Ragmean} \cdot \text{Lstkef} \cdot \int_0^{2 \cdot \pi} \text{Nca}(\theta_{ag}) \cdot \text{Bca1}(\theta_{ag}) \, d\theta_{ag} = 0.24864160 \text{ Wb}$$

$$\lambda_{cbcb} := \text{Ragmean} \cdot \text{Lstkef} \cdot \int_0^{2 \cdot \pi} \text{Ncb}(\theta_{ag}) \cdot \text{Bcb1}(\theta_{ag}) \, d\theta_{ag} = 0.24864156 \text{ Wb}$$

$$\lambda_{cccc} := \text{Ragmean} \cdot \text{Lstkef} \cdot \int_0^{2 \cdot \pi} \text{Ncc}(\theta_{ag}) \cdot \text{Bcc1}(\theta_{ag}) \, d\theta_{ag} = 0.24864343 \text{ Wb}$$

$$L_{caca} := \frac{\lambda_{caca}}{I_{c\_ind}} = 76.92093068 \cdot \text{mH}$$

$$L_{cbcb} := \frac{\lambda_{cbcb}}{I_{c\_ind}} = 76.92091990 \cdot \text{mH}$$

$$L_{cccc} := \frac{\lambda_{cccc}}{I_{c\_ind}} = 76.92149808 \cdot \text{mH}$$

## Mutual flux linkage between control winding phases:

*Phase a:*

$$\lambda_{cacb} := \text{Ragmean} \cdot \text{Lstkef} \cdot \int_0^{2 \cdot \pi} \text{Nca}(\theta_{ag}) \cdot \text{Bcb1}(\theta_{ag}) \, d\theta_{ag} = -0.12431549 \text{ Wb}$$

$$\lambda_{cacc} := \text{Ragmean} \cdot \text{Lstkef} \cdot \int_0^{2 \cdot \pi} \text{Nca}(\theta_{ag}) \cdot \text{Bcb1}(\theta_{ag}) \, d\theta_{ag} = -0.12431549 \text{ Wb}$$

*Phase b:*

$$\lambda_{cbca} := \text{Ragmean} \cdot \text{Lstkef} \cdot \int_0^{2 \cdot \pi} \text{Ncb}(\theta_{ag}) \cdot \text{Bca1}(\theta_{ag}) \, d\theta_{ag} = -0.12432080 \text{ Wb}$$

$$\lambda_{cbcc} := \text{Ragmean} \cdot \text{Lstkef} \cdot \int_0^{2 \cdot \pi} \text{Ncb}(\theta_{ag}) \cdot \text{Bcc1}(\theta_{ag}) \, d\theta_{ag} = -0.12432009 \text{ Wb}$$

*Phase c:*

$$\lambda_{ccca} := \text{Ragmean} \cdot \text{Lstkef} \cdot \int_0^{2 \cdot \pi} \text{Ncc}(\theta_{ag}) \cdot \text{Bca1}(\theta_{ag}) \, d\theta_{ag} = -0.12432080 \text{ Wb}$$

$$\lambda_{cccb} := \text{Ragmean} \cdot \text{Lstkef} \cdot \int_0^{2 \cdot \pi} \text{Ncc}(\theta_{ag}) \cdot \text{Bcb1}(\theta_{ag}) \, d\theta_{ag} = -0.12432009 \text{ Wb}$$

$$L_{cacb} := \frac{\lambda_{cacb}}{I_{c\_ind}} = -38.45882354 \cdot \text{mH}$$

$$L_{cacc} := \frac{\lambda_{cacc}}{I_{c\_ind}} = -38.46024539 \cdot \text{mH}$$

$$L_{cbca} := \frac{\lambda_{cbca}}{I_{c\_ind}} = -38.46046534 \cdot \text{mH}$$

$$L_{cbcc} := \frac{\lambda_{cbcc}}{I_{c\_ind}} = -38.46024539 \cdot \text{mH}$$

$$L_{ccca} := \frac{\lambda_{ccca}}{I_{c\_ind}} = -38.46046534 \cdot \text{mH}$$

$$L_{cccb} := \frac{\lambda_{cccb}}{I_{c\_ind}} = -38.46024539 \cdot \text{mH}$$



$$L_{cacb_{\text{teorique}}} := \frac{-1}{2} \cdot \frac{(L_{caca} + L_{cbcb} + L_{cccc})}{3} = -38.46055811 \cdot \text{mH}$$

## Mutual flux linkage between phases of DIFFERENT winding:

### **Grid Winding:**

*Phase a, grid:*

$$\lambda_{gaca} := \text{Ragmean} \cdot \text{Lstkef} \cdot \int_0^{2 \cdot \pi} \text{Nga}(\theta_{ag}) \cdot \text{Bca1}(\theta_{ag}) \, d\theta_{ag} = 0.25388075 \, \text{Wb}$$

$$\lambda_{gacb} := \text{Ragmean} \cdot \text{Lstkef} \cdot \int_0^{2 \cdot \pi} \text{Nga}(\theta_{ag}) \cdot \text{Bcb1}(\theta_{ag}) \, d\theta_{ag} = -0.12693201 \, \text{Wb}$$

$$\lambda_{gacc} := \text{Ragmean} \cdot \text{Lstkef} \cdot \int_0^{2 \cdot \pi} \text{Nga}(\theta_{ag}) \cdot \text{Bcc1}(\theta_{ag}) \, d\theta_{ag} = -0.12693201 \, \text{Wb}$$

$$L_{gaca} := \frac{\lambda_{gaca}}{I_{c\_ind}} = 78.54174009 \cdot \text{mH}$$

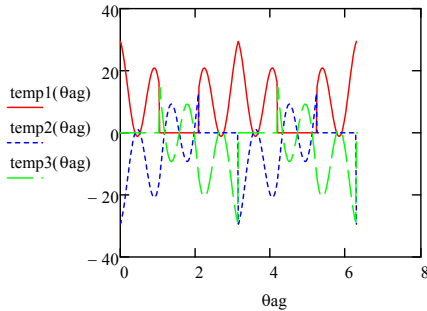
$$L_{gacb} := \frac{\lambda_{gacb}}{I_{c\_ind}} = -39.26828256 \cdot \text{mH}$$

$$L_{gacc} := \frac{\lambda_{gacc}}{I_{c\_ind}} = -39.26828256 \cdot \text{mH}$$

Verifying waveforms:

$$\text{temp1}(\theta_{ag}) := \text{Nga}(\theta_{ag}) \cdot \text{Bca1}(\theta_{ag}) \quad \text{temp2}(\theta_{ag}) := \text{Nga}(\theta_{ag}) \cdot \text{Bcb1}(\theta_{ag})$$

$$\text{temp3}(\theta_{ag}) := \text{Nga}(\theta_{ag}) \cdot \text{Bcc1}(\theta_{ag})$$



*Phase b, grid:*

$$\lambda_{gbca} := \text{Ragmean} \cdot \text{Lstkef} \cdot \int_0^{2 \cdot \pi} \text{Ngb}(\theta_{ag}) \cdot \text{Bca1}(\theta_{ag}) \, d\theta_{ag} = -0.12694049 \, \text{Wb}$$

$$\lambda_{gbcb} := \text{Ragmean} \cdot \text{Lstkef} \cdot \int_0^{2 \cdot \pi} \text{Ngb}(\theta_{ag}) \cdot \text{Bcb1}(\theta_{ag}) \, d\theta_{ag} = -0.12694013 \, \text{Wb}$$

$$\lambda_{gbcc} := \text{Ragmean} \cdot \text{Lstkef} \cdot \int_0^{2 \cdot \pi} \text{Ngb}(\theta_{ag}) \cdot \text{Bcc1}(\theta_{ag}) \, d\theta_{ag} = 0.25387477 \text{ Wb}$$

$$L_{gbca} := \frac{\lambda_{gbca}}{I_{c\_ind}} = -39.27090641 \cdot \text{mH}$$

$$L_{gbcb} := \frac{\lambda_{gbcb}}{I_{c\_ind}} = -39.27079414 \cdot \text{mH}$$

$$L_{gbcc} := \frac{\lambda_{gbcc}}{I_{c\_ind}} = 78.53989117 \cdot \text{mH}$$

*Phase c, grid:*

$$\lambda_{gccca} := \text{Ragmean} \cdot \text{Lstkef} \cdot \int_0^{2 \cdot \pi} \text{Ngc}(\theta_{ag}) \cdot \text{Bca1}(\theta_{ag}) \, d\theta_{ag} = -0.12694049 \text{ Wb}$$

$$\lambda_{gccb} := \text{Ragmean} \cdot \text{Lstkef} \cdot \int_0^{2 \cdot \pi} \text{Ngc}(\theta_{ag}) \cdot \text{Bcb1}(\theta_{ag}) \, d\theta_{ag} = 0.25387477 \text{ Wb}$$

$$\lambda_{gccc} := \text{Ragmean} \cdot \text{Lstkef} \cdot \int_0^{2 \cdot \pi} \text{Ngc}(\theta_{ag}) \cdot \text{Bcc1}(\theta_{ag}) \, d\theta_{ag} = -0.12694023 \text{ Wb}$$

$$L_{gccca} := \frac{\lambda_{gccca}}{I_{c\_ind}} = -39.27090641 \cdot \text{mH}$$

$$L_{gccb} := \frac{\lambda_{gccb}}{I_{c\_ind}} = 78.53989117 \cdot \text{mH}$$

$$L_{gccc} := \frac{\lambda_{gccc}}{I_{c\_ind}} = -39.27082655 \cdot \text{mH}$$

## **Control Winding:**

*Phase a, control*

$$\lambda_{caga} := \text{Ragmean} \cdot \text{Lstkef} \cdot \int_0^{2 \cdot \pi} \text{Nca}(\theta_{ag}) \cdot \text{Bga1}(\theta_{ag}) \, d\theta_{ag} = 0.24135775 \text{ Wb}$$

$$\lambda_{cagb} := \text{Ragmean} \cdot \text{Lstkef} \cdot \int_0^{2 \cdot \pi} \text{Nca}(\theta_{ag}) \cdot \text{Bgb1}(\theta_{ag}) \, d\theta_{ag} = -0.12068512 \text{ Wb}$$

$$\lambda_{cagc} := \text{Ragmean} \cdot \text{Lstkef} \cdot \int_0^{2 \cdot \pi} \text{Nca}(\theta_{ag}) \cdot \text{Bgc1}(\theta_{ag}) \, d\theta_{ag} = -0.12068440 \text{ Wb}$$

$$L_{caga} := \frac{\lambda_{caga}}{I_{g\_ind}} = 78.54176863 \cdot \text{mH}$$

$$L_{cagb} := \frac{\lambda_{cagb}}{I_{g\_ind}} = -39.27291548 \cdot \text{mH}$$

$$L_{cagc} := \frac{\lambda_{cagc}}{I_{g\_ind}} = -39.27268192 \cdot \text{mH}$$

*Phase b, control:*

$$\lambda_{cbga} := \text{Ragmean-Lstkef} \cdot \int_0^{2 \cdot \pi} \text{Ncb}(\theta_{ag}) \cdot \text{Bga1}(\theta_{ag}) \, d\theta_{ag} = -0.12067888 \text{ Wb}$$

$$\lambda_{cbgb} := \text{Ragmean-Lstkef} \cdot \int_0^{2 \cdot \pi} \text{Ncb}(\theta_{ag}) \cdot \text{Bgb1}(\theta_{ag}) \, d\theta_{ag} = -0.12068040 \text{ Wb}$$

$$\lambda_{cbgc} := \text{Ragmean-Lstkef} \cdot \int_0^{2 \cdot \pi} \text{Ncb}(\theta_{ag}) \cdot \text{Bgc1}(\theta_{ag}) \, d\theta_{ag} = 0.24135745 \text{ Wb}$$

$$L_{cbga} := \frac{\lambda_{cbga}}{I_{g\_ind}} = -39.27088432 \text{ mH}$$

$$L_{cbgb} := \frac{\lambda_{cbgb}}{I_{g\_ind}} = -39.27137954 \text{ mH}$$

$$L_{cbgc} := \frac{\lambda_{cbgc}}{I_{g\_ind}} = 78.54167125 \text{ mH}$$

*Phase c, control:*

$$\lambda_{ccga} := \text{Ragmean-Lstkef} \cdot \int_0^{2 \cdot \pi} \text{Ncc}(\theta_{ag}) \cdot \text{Bga1}(\theta_{ag}) \, d\theta_{ag} = -0.12067888 \text{ Wb}$$

$$\lambda_{ccgb} := \text{Ragmean-Lstkef} \cdot \int_0^{2 \cdot \pi} \text{Ncc}(\theta_{ag}) \cdot \text{Bgb1}(\theta_{ag}) \, d\theta_{ag} = 0.24135745 \text{ Wb}$$

$$\lambda_{ccgc} := \text{Ragmean-Lstkef} \cdot \int_0^{2 \cdot \pi} \text{Ncc}(\theta_{ag}) \cdot \text{Bgc1}(\theta_{ag}) \, d\theta_{ag} = -0.12068012 \text{ Wb}$$

$$L_{ccga} := \frac{\lambda_{ccga}}{I_{g\_ind}} = -39.27088432 \text{ mH}$$

$$L_{ccgb} := \frac{\lambda_{ccgb}}{I_{g\_ind}} = 78.54167125 \text{ mH}$$

$$L_{ccgc} := \frac{\lambda_{ccgc}}{I_{g\_ind}} = -39.27128873 \text{ mH}$$

**Three phase current definition: grid winding**

$$i_{Ag}(t) := I_{phg} \cdot \cos(\omega g \cdot t)$$

$$i_{Bg}(t) := I_{phg} \cdot \cos\left(\omega g \cdot t - \frac{2}{3} \cdot \pi\right)$$

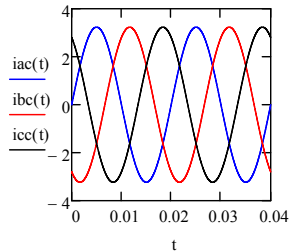
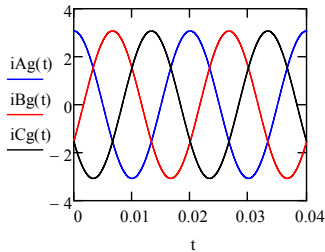
$$iCg(t) := Iphg \cdot \cos\left(\omega g \cdot t + \frac{2}{3} \cdot \pi\right)$$

### Three phase current definition: control winding

$$iac(t) := Iphc \cdot \cos(\omega c \cdot t - \alpha c)$$

$$ibc(t) := Iphc \cdot \cos\left(\omega c \cdot t - \frac{2}{3} \cdot \pi - \alpha c\right)$$

$$icc(t) := Iphc \cdot \cos\left(\omega c \cdot t + \frac{2}{3} \cdot \pi - \alpha c\right)$$



### RMS specific electric loading of a winding:

## Equivalent Electric Circuit

#### Inductance Definition:

$$Llg = 18.41845726 \cdot \text{mH}$$

$$Llc = 14.55093456 \cdot \text{mH}$$

$$Lgm := Lgaga = 82.99281087 \cdot \text{mH}$$

$$Lcm := Lcaca = 76.92093068 \cdot \text{mH}$$

$$Lcgmax := Lcaga = 78.54176863 \cdot \text{mH}$$

$$Lc := \frac{3}{2} \cdot Lcm + Llc = 129.93233058 \cdot \text{mH}$$

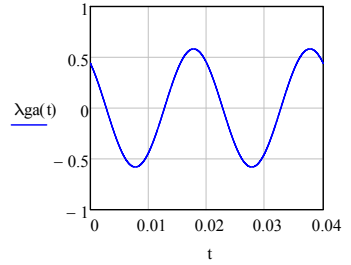
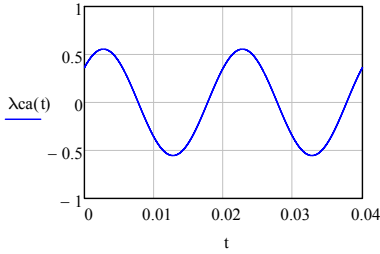
$$Lcg := \frac{3}{2} \cdot |Lcgmax| = 117.81265295 \cdot \text{mH}$$

$$Lg := \frac{3}{2} \cdot Lgm + Llg = 142.90767356 \cdot \text{mH}$$

#### Fluxes Calculation:

$$\lambda ga(t) := Lg \cdot Iphc \cdot \cos(\omega g \cdot t) + Lcg \cdot Iphc \cdot \cos(\omega g \cdot t + \gamma_1 + \alpha c)$$

$$\lambda ca(t) := Lc \cdot Iphc \cdot \cos(\omega c \cdot t - \alpha c) + Lcg \cdot Iphc \cdot \cos(\omega c \cdot t + \gamma_1)$$



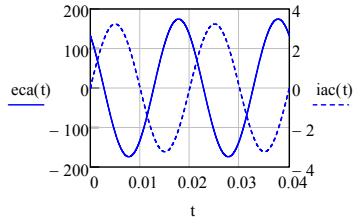
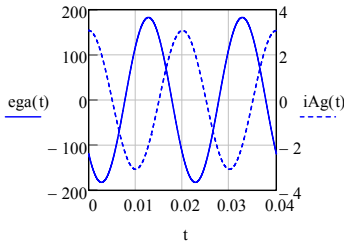
**Voltaçes:**

$$ega_{temp}(t) := \frac{d}{dt}(Lg \cdot Iphg \cdot \cos(\omega g \cdot t) + Lcg \cdot Iphc \cdot \cos(\omega g \cdot t + \gamma_1 + \alpha c))$$

$$ega(t) := -Iphg \cdot Lg \cdot \omega g \cdot \sin(t \cdot \omega g) - Iphc \cdot Lcg \cdot \omega g \cdot \sin(\alpha c + \gamma_1 + t \cdot \omega g)$$

$$eca_{temp}(t) := \frac{d}{dt}(Lc \cdot Iphc \cdot \cos(\omega c \cdot t - \alpha c) + Lcg \cdot Iphg \cdot \cos(\omega c \cdot t + \gamma_1))$$

$$eca(t) := -Iphg \cdot Lcg \cdot \omega c \cdot \sin(\gamma_1 + t \cdot \omega c) - Iphc \cdot Lc \cdot \omega c \cdot \sin(t \cdot \omega c - \alpha c)$$



## Steady state Equivalent Electric Circuit by using Inductances analytically calculated

Steady State:

*Voltage Phasors considering case (pr = p+q) [5]:*

$$\Psi Ega := i \cdot \omega g \cdot Lg \cdot \Psi Iga + i \cdot \omega g \cdot Lcg \cdot \Psi Ica \cdot e^{(2 \cdot \alpha c + \gamma_1) \cdot i} = (-84.59721471 + 97.55532900i) \text{ V}$$

$$\text{Mag} \Psi Ega := |\Psi Ega| = 129.12680184 \text{ V}$$

$$\text{Phase} \Psi Ega := \arg(\Psi Ega) = 130.93090168^\circ$$

$$\Psi Eca := i \cdot \omega c \cdot Lc \cdot \Psi Ica + i \cdot \omega c \cdot Lcg \cdot \Psi Iga \cdot e^{(\gamma_1) \cdot i} + 0.0000000001 \text{ V} = (93.29993844 + 80.42431755i) \text{ V}$$

$$\text{Mag} \Psi Eca := |\Psi Eca| = 123.17852640 \text{ V}$$

$$\text{Phase} \Psi Eca := \arg(\Psi Eca) = 40.76125749^\circ$$

**Including resistance effects**

$$\Psi V_{ca} := \Psi E_{ca} + \Psi I_{ca} \cdot R_c = (93.29993844 + 66.39890673i) \text{ V}$$

$$\text{Mag}\Psi V_{ca} := |\Psi V_{ca}| = 114.51503538 \text{ V}$$

Vca voltage phasor

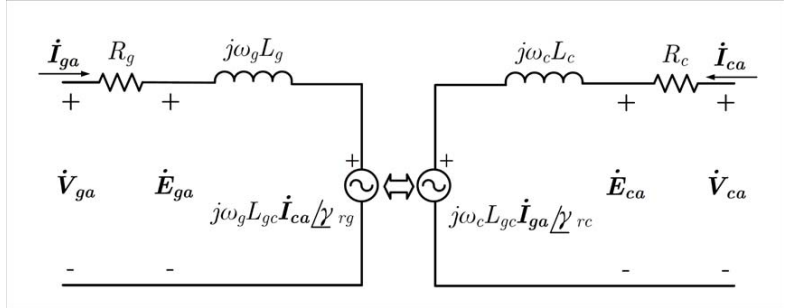
$$\text{Phase}\Psi V_{ca} := \arg(\Psi V_{ca}) = 35.43837401^\circ$$

$$\Psi V_{ga} := \Psi E_{ga} + \Psi I_{ga} \cdot R_g = (-72.29701341 + 97.55532900i) \text{ V}$$

Vga voltage phasor

$$\text{Mag}\Psi V_{ga} := |\Psi V_{ga}| = 121.42446362 \text{ V}$$

$$\text{Phase}\Psi V_{ga} := \arg(\Psi V_{ga}) = 126.54167385^\circ$$



BDFRM Equivalent Electric Circuit

## Semi-Analytical Model: Sub-model 2: power and torque calculations

### Internal Real Power (calculated by using voltage E)

$$P_{ga\_int} := \text{Re}(\Psi E_{ga} \cdot \overline{\Psi I_{ga}}) = -183.82375803 \text{ W}$$

$$P_{ca\_int} := \text{Re}(\Psi E_{ca} \cdot \overline{\Psi I_{ca}}) = -183.82375803 \text{ W}$$

$$P3\phi_{grid\_internal} := \text{Re}\left[3 \cdot (\Psi E_{ga} \cdot \overline{\Psi I_{ga}})\right] = -0.55147127 \text{ kW}$$

$$P3\phi_{grid\_internal2} := \frac{-3}{2} \cdot (\omega_g) \cdot L_{cg} \cdot I_{phc} \cdot I_{phg} \cdot \sin(\phi_{torque}) = -551.47127410 \text{ W}$$

$$P3\phi_{control\_internal} := \text{Re}\left[3 \cdot (\Psi E_{ca} \cdot \overline{\Psi I_{ca}})\right] = -0.55147127 \text{ kW}$$

$$P3\phi_{2control\_internal2} := \frac{-3}{2} \cdot (\omega_c) \cdot L_{cg} \cdot I_{phc} \cdot I_{phg} \cdot \sin(\phi_{torque}) = -551.47127410 \text{ W}$$

$$P3\phi_{total\_internal} := \text{Re}\left[3 \cdot (\Psi E_{ca} \cdot \overline{\Psi I_{ca}} + \Psi E_{ga} \cdot \overline{\Psi I_{ga}})\right] = -1.10294255 \text{ kW}$$

$$P3\phi_{total\_internal2} := \frac{-3}{2} \cdot (\omega_c + \omega_g) \cdot L_{cg} \cdot I_{phc} \cdot I_{phg} \cdot \sin(\phi_{torque}) = -1.10294255 \text{ kW}$$

### Terminal Real Power (calculated by using voltage V)

$$P_{ga\_ter} := \operatorname{Re}(\Psi V_{ga} \cdot \overline{\Psi I_{ga}}) = -157.09629147 \text{ W}$$

$$P_{ca\_ter} := \operatorname{Re}(\Psi V_{ca} \cdot \overline{\Psi I_{ca}}) = -151.76624356 \text{ W}$$

$$P_{3\phi\text{grid\_ter}} := \operatorname{Re} \left[ 3 \cdot (\Psi V_{ga} \cdot \overline{\Psi I_{ga}}) \right] = -471.28887442 \text{ W}$$

$$P_{3\phi\text{control\_ter}} := \operatorname{Re} \left[ 3 \cdot (\Psi V_{ca} \cdot \overline{\Psi I_{ca}}) \right] = -455.29873068 \text{ W}$$

$$P_{3\phi\text{total\_ter}} := \operatorname{Re} \left[ 3 \cdot (\Psi V_{ca} \cdot \overline{\Psi I_{ca}} + \Psi V_{ga} \cdot \overline{\Psi I_{ga}}) \right] = -926.58760510 \text{ W}$$

### **Electromagnetic Torque in steady-state**

$$\text{TorqueSS\_internal} := \frac{P_{3\phi\text{total\_internal}}}{\omega_{rm}} = -10.53232551 \text{ J}$$

$$\text{TorqueSS\_internal2} := \frac{-3}{2} \cdot \left( \frac{P_g}{2} + \frac{P_c}{2} \right) \cdot L_{cg} \cdot I_{phc} \cdot I_{phg} \cdot \sin(\phi_{\text{torque}}) = -10.53232551 \text{ J}$$

## **Semi-Analytical Model: Sub-model 3 - flux density calculation in several parts of the machine**

Calculation of MMF in airgap considering an ideal rotor:

**The peak fundamental MMF for each winding is:**

$$F_{ga1m} := \frac{4}{\pi} \cdot \frac{N_{phg} \cdot K_{wg}}{P_g} \cdot I_{phg} = 211.64231217 \text{ A} \quad \text{peak fundamental mmf grid w}$$

$$F_{g3\phi1m} := \frac{3}{2} \cdot F_{ga1m} = 317.46346825 \text{ A} \quad \text{equivalent mmf in three phase system gW}$$

$$F_{ca1m} := \frac{4}{\pi} \cdot \frac{N_{phc} \cdot K_{wc}}{P_c} \cdot I_{phc} = 307.43005272 \text{ A} \quad \text{peak fundamental mmf control w}$$

$$F_{c3\phi1m} := \frac{3}{2} \cdot F_{ca1m} = 461.14507908 \text{ A} \quad \text{equivalent mmf in three phase system cW}$$

$$F_{g3\phi}(t, \theta_{ag}) := F_{g3\phi1m} \cdot \cos\left(\omega_g \cdot t - \frac{P_g}{2} \cdot \theta_{ag}\right)$$

$$F_{c3\phi}(t, \theta_{ag}) := F_{c3\phi1m} \cdot \cos\left(\omega_c \cdot t - \frac{P_c}{2} \cdot \theta_{ag} - \alpha_c\right)$$

$$I_{phg} = 3.07298594 \text{ A}$$

$$F_{3phT}(t, \theta_{ag}) := F_{g3\phi}(t, \theta_{ag}) + F_{c3\phi}(t, \theta_{ag})$$

$$I_{phc} = 3.23243093 \text{ A}$$

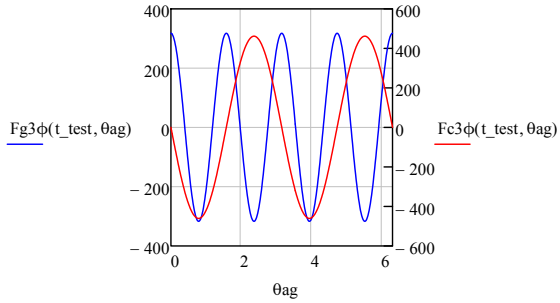
**Fixed time versus  $\theta$  around airgap: MMF grid and control**

$$F_{3phT}(0s, 0^\circ) = 317.46346825 \text{ A}$$

**t\_test := 0s**

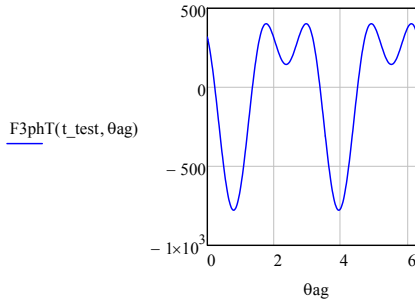
$$ttime(\theta\_test2) := \frac{\theta\_test2}{\omega_{rm}}$$

ttime(100°) = 0.01666667 s



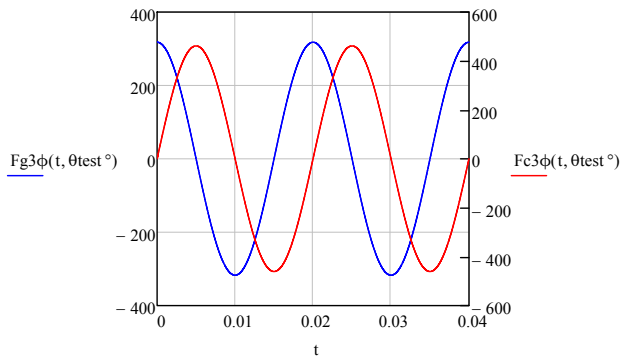
**Fixed time versus  $\theta$  around airgap: MMF total**

t\_test = 0.00000000



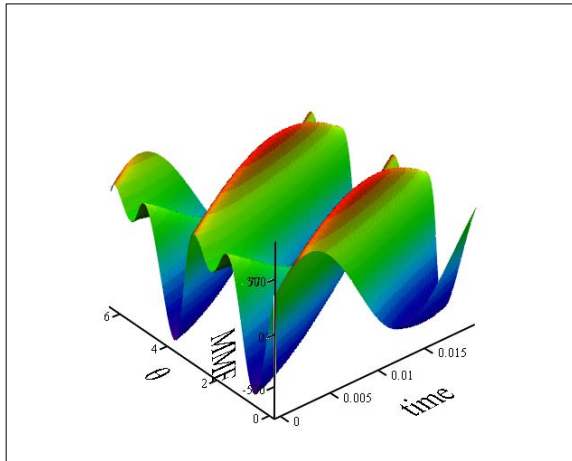
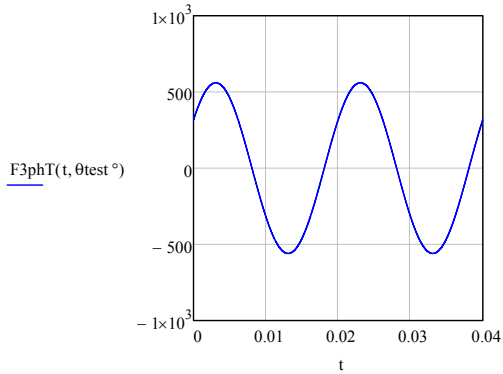
**Fixed theta versus time: MMF grid and control**

**θtest := 0°**





**Fixed theta versus time: MMF total**



F3phT

calculation: it considers that at time = 0s,  $\theta_{agec\_resp} = 0^\circ$

$$\theta_{agec\_resp}(t) := \omega_{rm} \cdot t + \theta_{ag0}$$

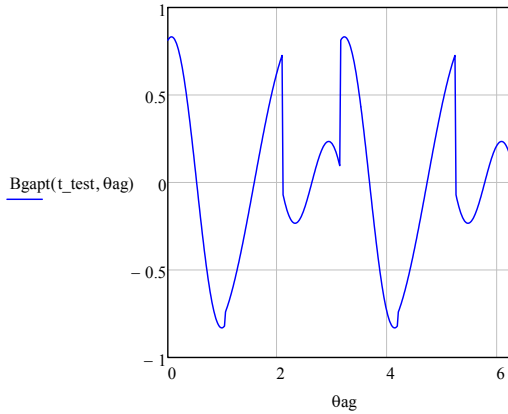
$$\theta_{agec\_resp}(t_{test}) = 0.00000000^\circ$$

$$\theta_{agDR}(\theta_{ag}, t) := 2 \cdot \text{mod}(\text{mod}(\theta_{ag} - \theta_{agec\_resp}(t), \lambda_r) + \lambda_r, \lambda_r)$$

$$B_{gapt}(t, \theta_{ag}) := \frac{\mu_0}{2 \cdot \text{gap}_{ef}} \cdot (F_{3phT}(t, \theta_{ag}) - F_{3phT}(t, \theta_{ag} + \lambda_r - \theta_{agDR}(\theta_{ag}, t)))$$

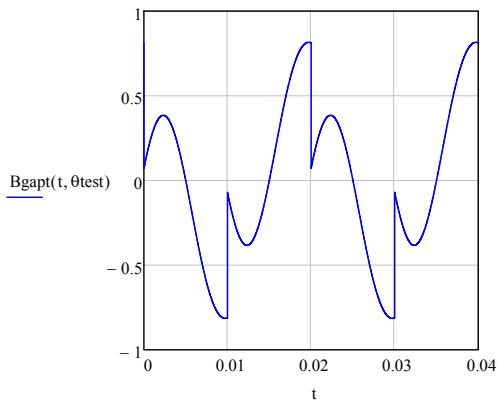
$$B_{ag}(t, \theta_{ag}) := B_{gapt}(t, \theta_{ag})$$

**Fixed time versus  $\theta$  around airgap: Flux Density**



**Fixed theta versus time: Flux Density**

$\theta_{test} = 0.00000000^\circ$



**Maximum induction in the stator teeth:**

Calculation of initial and final angles regarding the flux in each tooth

$$\alpha_{\phi th li} := -2 \cdot \frac{\pi}{N_{sl}} \div 2 = -3.75000000^\circ$$

$$\alpha_{\phi th lf} := 2 \cdot \frac{\pi}{N_{sl}} \div 2 = 3.75000000^\circ$$

$$\alpha_{th pitch} := 2 \cdot \frac{\pi}{N_{sl}} = 7.50000000^\circ$$

$$th\_area\_middle := thw \cdot L_{stkef} = 353.81957127 \cdot mm^2$$

## **Induction calculation in each tooth (24 out of 48 due to symmetry)**

thnr: indicates the stator tooth being calculated.

thnr := 1

$$\phi_{th01} := \frac{D_{gap}}{2} \cdot L_{stk} \cdot \int_{\alpha_{\phi_{th1i} + \alpha_{thpitch} \cdot (thnr-1)}}^{\alpha_{\phi_{th1f} + \alpha_{thpitch} \cdot (thnr-1)}} B_{gap}(t_{test}, \theta_{ag}) d\theta_{ag} = 3.06025378 \times 10^{-4} \text{ Wb}$$

$$B_{th01} := \frac{\phi_{th01}}{th\_area\_middle} = 0.86491931 \text{ T}$$

thnr := 2

$$\phi_{th02} := \frac{D_{gap}}{2} \cdot L_{stk} \cdot \int_{\alpha_{\phi_{th1i} + \alpha_{thpitch} \cdot (thnr-1)}}^{\alpha_{\phi_{th1f} + \alpha_{thpitch} \cdot (thnr-1)}} B_{gap}(t_{test}, \theta_{ag}) d\theta_{ag} = 5.24836804 \times 10^{-4} \text{ Wb}$$

$$B_{th02} := \frac{\phi_{th02}}{th\_area\_middle} = 1.48334588 \text{ T}$$

thnr := 3

$$\phi_{th03} := \frac{D_{gap}}{2} \cdot L_{stk} \cdot \int_{\alpha_{\phi_{th1i} + \alpha_{thpitch} \cdot (thnr-1)}}^{\alpha_{\phi_{th1f} + \alpha_{thpitch} \cdot (thnr-1)}} B_{gap}(t_{test}, \theta_{ag}) d\theta_{ag} = 4.23305442 \times 10^{-4} \text{ Wb}$$

$$B_{th03} := \frac{\phi_{th03}}{th\_area\_middle} = 1.19638787 \text{ T}$$

thnr := 4

$$\phi_{th04} := \frac{D_{gap}}{2} \cdot L_{stk} \cdot \int_{\alpha_{\phi_{th1i} + \alpha_{thpitch} \cdot (thnr-1)}}^{\alpha_{\phi_{th1f} + \alpha_{thpitch} \cdot (thnr-1)}} B_{gap}(t_{test}, \theta_{ag}) d\theta_{ag} = 2.36101622 \times 10^{-4} \text{ Wb}$$

$$B_{th04} := \frac{\phi_{th04}}{th\_area\_middle} = 0.66729384 \text{ T}$$

thnr := 5

$$\phi_{th05} := \frac{D_{gap}}{2} \cdot L_{stk} \cdot \int_{\alpha_{\phi_{th1i} + \alpha_{thpitch} \cdot (thnr-1)}}^{\alpha_{\phi_{th1f} + \alpha_{thpitch} \cdot (thnr-1)}} B_{gap}(t_{test}, \theta_{ag}) d\theta_{ag} = 0.00000000 \text{ Wb}$$

$$B_{th05} := \frac{\phi_{th05}}{th\_area\_middle} = 0.00000000 \text{ T}$$

thnr := 6

$$\phi_{th06} := \frac{D_{gap}}{2} \cdot L_{stk} \cdot \int_{\alpha_{\phi_{th1i} + \alpha_{thpitch} \cdot (thnr-1)}}^{\alpha_{\phi_{th1f} + \alpha_{thpitch} \cdot (thnr-1)}} B_{gap}(t_{test}, \theta_{ag}) d\theta_{ag} = -2.36101622 \times 10^{-4} \text{ Wb}$$

$$\text{Bth06} := \frac{\phi_{\text{th06}}}{\text{th\_area\_middle}} = -0.66729384 \text{ T}$$

$$\text{Bth04} = 0.66729384 \text{ T}$$

$$\underline{\text{thnr}} := 7$$

$$\phi_{\text{th07}} := \frac{\text{Dgap}}{2} \cdot \text{Lstkef} \cdot \int_{\alpha\phi_{\text{th1i}} + \alpha\text{thpitch} \cdot (\text{thnr} - 1)}^{\alpha\phi_{\text{th1f}} + \alpha\text{thpitch} \cdot (\text{thnr} - 1)} \text{Bgapt}(\underline{t}_{\text{test}}, \theta_{\text{ag}}) \, d\theta_{\text{ag}} = -4.23305442 \times 10^{-4} \text{ Wb}$$

$$\text{Bth07} := \frac{\phi_{\text{th07}}}{\text{th\_area\_middle}} = -1.19638787 \text{ T}$$

$$\text{Bth03} = 1.19638787 \text{ T}$$

$$\underline{\text{thnr}} := 8$$

$$\phi_{\text{th08}} := \frac{\text{Dgap}}{2} \cdot \text{Lstkef} \cdot \int_{\alpha\phi_{\text{th1i}} + \alpha\text{thpitch} \cdot (\text{thnr} - 1)}^{\alpha\phi_{\text{th1f}} + \alpha\text{thpitch} \cdot (\text{thnr} - 1)} \text{Bgapt}(\underline{t}_{\text{test}}, \theta_{\text{ag}}) \, d\theta_{\text{ag}} = -5.24836804 \times 10^{-4} \text{ Wb}$$

$$\text{Bth08} := \frac{\phi_{\text{th08}}}{\text{th\_area\_middle}} = -1.48334588 \text{ T}$$

$$\text{Bth02} = 1.48334588 \text{ T}$$

$$\underline{\text{thnr}} := 9$$

$$\phi_{\text{th09}} := \frac{\text{Dgap}}{2} \cdot \text{Lstkef} \cdot \int_{\alpha\phi_{\text{th1i}} + \alpha\text{thpitch} \cdot (\text{thnr} - 1)}^{\alpha\phi_{\text{th1f}} + \alpha\text{thpitch} \cdot (\text{thnr} - 1)} \text{Bgapt}(\underline{t}_{\text{test}}, \theta_{\text{ag}}) \, d\theta_{\text{ag}} = -5.00223939 \times 10^{-4} \text{ Wb}$$

$$\text{Bth09} := \frac{\phi_{\text{th09}}}{\text{th\_area\_middle}} = -1.41378256 \text{ T}$$

$$\text{Bth01} = 0.86491931 \text{ T}$$

$$\underline{\text{thnr}} := 10$$

$$\phi_{\text{th10}} := \frac{\text{Dgap}}{2} \cdot \text{Lstkef} \cdot \int_{\alpha\phi_{\text{th1i}} + \alpha\text{thpitch} \cdot (\text{thnr} - 1)}^{\alpha\phi_{\text{th1f}} + \alpha\text{thpitch} \cdot (\text{thnr} - 1)} \text{Bgapt}(\underline{t}_{\text{test}}, \theta_{\text{ag}}) \, d\theta_{\text{ag}} = -3.92862242 \times 10^{-4} \text{ Wb}$$

$$\text{Bth10} := \frac{\phi_{\text{th10}}}{\text{th\_area\_middle}} = -1.11034627 \text{ T}$$

$$\underline{\text{thnr}} := 11$$

$$\phi_{\text{th11}} := \frac{\text{Dgap}}{2} \cdot \text{Lstkef} \cdot \int_{\alpha\phi_{\text{th1i}} + \alpha\text{thpitch} \cdot (\text{thnr} - 1)}^{\alpha\phi_{\text{th1f}} + \alpha\text{thpitch} \cdot (\text{thnr} - 1)} \text{Bgapt}(\underline{t}_{\text{test}}, \theta_{\text{ag}}) \, d\theta_{\text{ag}} = -2.77795555 \times 10^{-4} \text{ Wb}$$

$$\text{Bth11} := \frac{\phi_{\text{th11}}}{\text{th\_area\_middle}} = -0.78513338 \text{ T}$$

$$\underline{\text{thnr}} := 12$$

$$\phi_{\text{th12}} := \frac{\text{Dgap}}{2} \cdot \text{Lstkef} \cdot \int_{\alpha\phi_{\text{th1i}} + \alpha\text{thpitch} \cdot (\text{thnr} - 1)}^{\alpha\phi_{\text{th1f}} + \alpha\text{thpitch} \cdot (\text{thnr} - 1)} \text{Bgapt}(\underline{t}_{\text{test}}, \theta_{\text{ag}}) \, d\theta_{\text{ag}} = -1.43797561 \times 10^{-4} \text{ Wb}$$

$$B_{th12} := \frac{\phi_{th12}}{th\_area\_middle} = -0.40641494 \text{ T}$$

$$\underline{thnr} := 13$$

$$\phi_{th13} := \frac{D_{gap}}{2} \cdot L_{stkef} \cdot \int_{\alpha\phi_{th1i} + \alpha thpitch \cdot (thnr-1)}^{\alpha\phi_{th1f} + \alpha thpitch \cdot (thnr-1)} B_{gap}(t\_test, \theta_{ag}) d\theta_{ag} = 0.00000000 \text{ Wb}$$

$$B_{th13} := \frac{\phi_{th13}}{th\_area\_middle} = 0.00000000 \text{ T}$$

$$\underline{thnr} := 14$$

$$\phi_{th14} := \frac{D_{gap}}{2} \cdot L_{stkef} \cdot \int_{\alpha\phi_{th1i} + \alpha thpitch \cdot (thnr-1)}^{\alpha\phi_{th1f} + \alpha thpitch \cdot (thnr-1)} B_{gap}(t\_test, \theta_{ag}) d\theta_{ag} = 1.43797561 \times 10^{-4} \text{ Wb}$$

$$B_{th14} := \frac{\phi_{th14}}{th\_area\_middle} = 0.40641494 \text{ T} \quad B_{th12} = -0.40641494 \text{ T}$$

$$\underline{thnr} := 15$$

$$\phi_{th15} := \frac{D_{gap}}{2} \cdot L_{stkef} \cdot \int_{\alpha\phi_{th1i} + \alpha thpitch \cdot (thnr-1)}^{\alpha\phi_{th1f} + \alpha thpitch \cdot (thnr-1)} B_{gap}(t\_test, \theta_{ag}) d\theta_{ag} = 2.77795555 \times 10^{-4} \text{ Wb}$$

$$B_{th15} := \frac{\phi_{th15}}{th\_area\_middle} = 0.78513338 \text{ T} \quad B_{th11} = -0.78513338 \text{ T}$$

$$\underline{thnr} := 16$$

$$\phi_{th16} := \frac{D_{gap}}{2} \cdot L_{stkef} \cdot \int_{\alpha\phi_{th1i} + \alpha thpitch \cdot (thnr-1)}^{\alpha\phi_{th1f} + \alpha thpitch \cdot (thnr-1)} B_{gap}(t\_test, \theta_{ag}) d\theta_{ag} = 3.92862242 \times 10^{-4} \text{ Wb}$$

$$B_{th16} := \frac{\phi_{th16}}{th\_area\_middle} = 1.11034627 \text{ T} \quad B_{th10} = -1.11034627 \text{ T}$$

$$\underline{thnr} := 17$$

$$\phi_{th17} := \frac{D_{gap}}{2} \cdot L_{stkef} \cdot \int_{\alpha\phi_{th1i} + \alpha thpitch \cdot (thnr-1)}^{\alpha\phi_{th1f} + \alpha thpitch \cdot (thnr-1)} B_{gap}(t\_test, \theta_{ag}) d\theta_{ag} = 1.94198560 \times 10^{-4} \text{ Wb}$$

$$B_{th17} := \frac{\phi_{th17}}{th\_area\_middle} = 0.54886325 \text{ T}$$

$$\underline{thnr} := 18$$

$$\phi_{th18} := \frac{D_{gap}}{2} \cdot L_{stkef} \cdot \int_{\alpha \phi_{th1i} + \alpha_{thpitch} \cdot (thnr-1)}^{\alpha \phi_{th1f} + \alpha_{thpitch} \cdot (thnr-1)} B_{gap}(t_{test}, \theta_{ag}) d\theta_{ag} = -1.31974562 \times 10^{-4} \text{ Wb}$$

$$B_{th18} := \frac{\phi_{th18}}{th\_area\_middle} = -0.37299961 \text{ T}$$

$$thnr := 19$$

$$\phi_{th19} := \frac{D_{gap}}{2} \cdot L_{stkef} \cdot \int_{\alpha \phi_{th1i} + \alpha_{thpitch} \cdot (thnr-1)}^{\alpha \phi_{th1f} + \alpha_{thpitch} \cdot (thnr-1)} B_{gap}(t_{test}, \theta_{ag}) d\theta_{ag} = -1.45509887 \times 10^{-4} \text{ Wb}$$

$$B_{th19} := \frac{\phi_{th19}}{th\_area\_middle} = -0.41125449 \text{ T}$$

$$thnr := 20$$

$$\phi_{th20} := \frac{D_{gap}}{2} \cdot L_{stkef} \cdot \int_{\alpha \phi_{th1i} + \alpha_{thpitch} \cdot (thnr-1)}^{\alpha \phi_{th1f} + \alpha_{thpitch} \cdot (thnr-1)} B_{gap}(t_{test}, \theta_{ag}) d\theta_{ag} = -9.23040612 \times 10^{-5} \text{ Wb}$$

$$B_{th20} := \frac{\phi_{th20}}{th\_area\_middle} = -0.26087890 \text{ T}$$

$$thnr := 21$$

$$\phi_{th21} := \frac{D_{gap}}{2} \cdot L_{stkef} \cdot \int_{\alpha \phi_{th1i} + \alpha_{thpitch} \cdot (thnr-1)}^{\alpha \phi_{th1f} + \alpha_{thpitch} \cdot (thnr-1)} B_{gap}(t_{test}, \theta_{ag}) d\theta_{ag} = 0.00000000 \text{ Wb}$$

$$B_{th21} := \frac{\phi_{th21}}{th\_area\_middle} = 0.00000000 \text{ T}$$

$$thnr := 22$$

$$\phi_{th22} := \frac{D_{gap}}{2} \cdot L_{stkef} \cdot \int_{\alpha \phi_{th1i} + \alpha_{thpitch} \cdot (thnr-1)}^{\alpha \phi_{th1f} + \alpha_{thpitch} \cdot (thnr-1)} B_{gap}(t_{test}, \theta_{ag}) d\theta_{ag} = 9.23040612 \times 10^{-5} \text{ Wb}$$

$$B_{th22} := \frac{\phi_{th22}}{th\_area\_middle} = 0.26087890 \text{ T}$$

$$thnr := 23$$

$$\phi_{th23} := \frac{D_{gap}}{2} \cdot L_{stkef} \cdot \int_{\alpha \phi_{th1i} + \alpha_{thpitch} \cdot (thnr-1)}^{\alpha \phi_{th1f} + \alpha_{thpitch} \cdot (thnr-1)} B_{gap}(t_{test}, \theta_{ag}) d\theta_{ag} = 1.45509887 \times 10^{-4} \text{ Wb}$$

$$B_{th23} := \frac{\phi_{th23}}{th\_area\_middle} = 0.41125449 \text{ T}$$

$$thnr := 24$$

$$\phi_{th24} := \frac{D_{gap}}{2} \cdot L_{stkef} \cdot \int_{\alpha_{\phi th1i} + \alpha_{\phi thpitch} \cdot (thnr-1)}^{\alpha_{\phi th1f} + \alpha_{\phi thpitch} \cdot (thnr-1)} B_{gap}(t_{test}, \theta_{ag}) d\theta_{ag} = 1.31974562 \times 10^{-4} \text{ Wb}$$

$$B_{th24} := \frac{\phi_{th24}}{th\_area\_middle} = 0.37299961 \text{ T}$$

### **Induction calculation in each part of stator yoke:**

The induction in stator yoke is calculated considering an equivalent pole number of Pr. The circulation of the flux in rotor/stator equivalent pole will be calculated accordingly.

$$\alpha_{rp} := 2 \cdot \frac{\pi}{Pr} = 60.00000000.^\circ \quad \text{rotor pole angle}$$

$$\alpha_{rp\_demi} := \frac{\alpha_{rp}}{2} = 30.00000000.^\circ \quad \text{demi rotor/stator equivalent pole number}$$

$$rp\_demi\_area := \frac{D_{gap}}{2} \cdot \alpha_{rp\_demi} \cdot L_{stkef} = 2.60556416 \times 10^3 \cdot \text{mm}^2$$

yoke area

$$yk\_area := ykw \cdot L_{stkef} = 1.00019059 \times 10^3 \cdot \text{mm}^2$$

Initial angles to define integration

$$\alpha_{rpi} := \theta_{agec\_resp}(t_{test}) = 0.00000000.^\circ$$

$$\alpha_{rpf} := \alpha_{rp\_demi} + \theta_{agec\_resp}(t_{test}) = 30.00000000.^\circ$$

### **Induction calculation - (only 6 out of 12 parts are done due to symmetry)**

$$r_{pnr} := 1$$

$$\phi_{rp01} := \frac{D_{gap}}{2} \cdot L_{stkef} \cdot \int_{\alpha_{rpi} + (r_{pnr}-1) \cdot \alpha_{rp\_demi}}^{\alpha_{rpf} + (r_{pnr}-1) \cdot \alpha_{rp\_demi}} B_{gap}(t_{test}, \theta_{ag}) d\theta_{ag} = 1.48371520 \times 10^{-3} \text{ Wb}$$

$$Byk01 := \frac{\phi_{rp01}}{yk\_area} = 1.48343246 \text{ T}$$

$$r_{pnr} := 3$$

$$\phi_{rp03} := \frac{D_{gap}}{2} \cdot L_{stkef} \cdot \int_{\alpha_{rpi} + (r_{pnr}-1) \cdot \alpha_{rp\_demi}}^{\alpha_{rpf} + (r_{pnr}-1) \cdot \alpha_{rp\_demi}} B_{gap}(t_{test}, \theta_{ag}) d\theta_{ag} = -1.06413721 \times 10^{-3} \text{ Wb}$$

$$Byk03 := \frac{\phi_{rp03}}{yk\_area} = -1.06393443 \text{ T}$$

$$r_{pnr} := 5$$

$$\phi_{rp05} := \frac{D_{gap}}{2} \cdot L_{stkef} \cdot \int_{\alpha_{rpi} + (r_{pnr}-1) \cdot \alpha_{rp\_demi}}^{\alpha_{rpf} + (r_{pnr}-1) \cdot \alpha_{rp\_demi}} B_{gap}(t_{test}, \theta_{ag}) d\theta_{ag} = -4.19577989 \times 10^{-4} \text{ Wb}$$

$$Byk05 := \frac{\phi_{rp05}}{yk\_area} = -0.41949804 \text{ T}$$

## Induction calculation in each flux path (FP) (11\*3 = 33 out of 66 due to symmetry)

The induction in the rotor flux path is calculated assuming the the flux that enters one flux path goes out entirely in the corresponding flux tube

$FPr\_area := S1dm = 2.82222988 \times 10^{-4} \text{ m}^2$  area corresponding to one flux path. All FB area are considered the same, only the length change

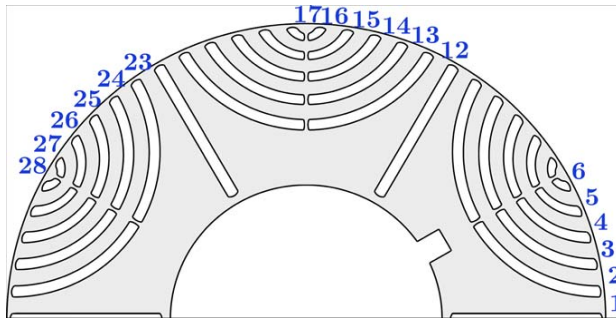
Initial angles to define integration

$\alpha FPstep := \alpha fluxPath + \alpha slr = 5.45454545^\circ$

$\alpha FPi := \theta_{agec\_resp}(t\_test) = 0.00000000^\circ$

$\alpha FPf := \alpha FPstep + \theta_{agec\_resp}(t\_test) = 5.45454545^\circ$

The figure below illustrates the flux paths being calculated.



## Induction calculation

Only 6 calculations are required for each rotor pole since a perfect flux guide is considered. It means that the flux entering at one side is going out the other side.

$FPrm1 := 1$

$$\phi FPr01 := \frac{D_{gap}}{2} \cdot L_{stkef} \cdot \int_{\alpha FPi + (FPrm1 - 1) \cdot \alpha FPstep}^{\alpha FPf + (FPrm1 - 1) \cdot \alpha FPstep} B_{gap}(t\_test, \theta_{ag}) d\theta_{ag} = 3.91719646 \times 10^{-4} \text{ Wb}$$

$$B\_FPr01 := \frac{\phi FPr01}{FPr\_area} = 1.38797923 \text{ T}$$

$FPrm2 := 2$

$$\phi FPr02 := \frac{D_{gap}}{2} \cdot L_{stkef} \cdot \int_{\alpha FPi + (FPrm2 - 1) \cdot \alpha FPstep}^{\alpha FPf + (FPrm2 - 1) \cdot \alpha FPstep} B_{gap}(t\_test, \theta_{ag}) d\theta_{ag} = 3.79468418 \times 10^{-4} \text{ Wb}$$

$$B\_FPr02 := \frac{\phi FPr02}{FPr\_area} = 1.34456949 \text{ T}$$



$$\begin{aligned} \underline{FPr}_{nr} &:= 3 \\ \phi_{FPr03} &:= \frac{D_{gap}}{2} \cdot L_{stkef} \cdot \int_{\alpha_{FPi}+(FPr-1) \cdot \alpha_{FPstep}}^{\alpha_{FPf}+(FPr-1) \cdot \alpha_{FPstep}} B_{gap}(t_{test}, \theta_{ag}) d\theta_{ag} = 3.27807856 \times 10^{-4} \text{ Wb} \\ B_{FPr03} &:= \frac{\phi_{FPr03}}{FPr\_area} = 1.16152075 \text{ T} \end{aligned}$$

$$\begin{aligned} \underline{FPr}_{nr} &:= 4 \\ \phi_{FPr04} &:= \frac{D_{gap}}{2} \cdot L_{stkef} \cdot \int_{\alpha_{FPi}+(FPr-1) \cdot \alpha_{FPstep}}^{\alpha_{FPf}+(FPr-1) \cdot \alpha_{FPstep}} B_{gap}(t_{test}, \theta_{ag}) d\theta_{ag} = 2.40900552 \times 10^{-4} \text{ Wb} \\ B_{FPr04} &:= \frac{\phi_{FPr04}}{FPr\_area} = 0.85358232 \text{ T} \end{aligned}$$

$$\begin{aligned} \underline{FPr}_{nr} &:= 5 \\ \phi_{FPr05} &:= \frac{D_{gap}}{2} \cdot L_{stkef} \cdot \int_{\alpha_{FPi}+(FPr-1) \cdot \alpha_{FPstep}}^{\alpha_{FPf}+(FPr-1) \cdot \alpha_{FPstep}} B_{gap}(t_{test}, \theta_{ag}) d\theta_{ag} = 1.27535232 \times 10^{-4} \text{ Wb} \\ B_{FPr05} &:= \frac{\phi_{FPr05}}{FPr\_area} = 0.45189527 \text{ T} \end{aligned}$$

$$\begin{aligned} \underline{FPr}_{nr} &:= 6 \\ \phi_{FPr06} &:= \frac{D_{gap}}{2} \cdot L_{stkef} \cdot \int_{\alpha_{FPi}+(FPr-1) \cdot \alpha_{FPstep}}^{\alpha_{FPf}+(FPr-1) \cdot \alpha_{FPstep} - \alpha_{FPstep} \div 2} B_{gap}(t_{test}, \theta_{ag}) d\theta_{ag} \\ B_{FPr06} &:= \frac{\phi_{FPr06}}{FPr\_area} = 0.05769725 \text{ T} \end{aligned}$$

Next rotor Pole

$$\begin{aligned} \underline{FPr}_{nr} &:= 12 \\ \phi_{FPr12} &:= \frac{D_{gap}}{2} \cdot L_{stkef} \cdot \int_{\alpha_{FPi}+(FPr-1) \cdot \alpha_{FPstep}}^{\alpha_{FPf}+(FPr-1) \cdot \alpha_{FPstep}} B_{gap}(t_{test}, \theta_{ag}) d\theta_{ag} = -3.29586138 \times 10^{-4} \text{ Wb} \\ B_{FPr12} &:= \frac{\phi_{FPr12}}{FPr\_area} = -1.16782173 \text{ T} \end{aligned}$$

$$\begin{aligned} \underline{FPr}_{nr} &:= 13 \\ \phi_{FPr13} &:= \frac{D_{gap}}{2} \cdot L_{stkef} \cdot \int_{\alpha_{FPi}+(FPr-1) \cdot \alpha_{FPstep}}^{\alpha_{FPf}+(FPr-1) \cdot \alpha_{FPstep}} B_{gap}(t_{test}, \theta_{ag}) d\theta_{ag} = -2.79213345 \times 10^{-4} \text{ Wb} \\ B_{FPr13} &:= \frac{\phi_{FPr13}}{FPr\_area} = -0.98933594 \text{ T} \end{aligned}$$

$$\begin{aligned} \underline{FPr}_{nr} &:= 14 \\ \phi_{FPr14} &:= \frac{D_{gap}}{2} \cdot L_{stkef} \cdot \int_{\alpha_{FPi}+(FPr-1) \cdot \alpha_{FPstep}}^{\alpha_{FPf}+(FPr-1) \cdot \alpha_{FPstep}} B_{gap}(t_{test}, \theta_{ag}) d\theta_{ag} = -2.18749054 \times 10^{-4} \text{ Wb} \end{aligned}$$

$$B\_FPr14 := \frac{\phi FPr14}{FPr\_area} = -0.77509297 \text{ T}$$

$$FPr_{14} := 15$$

$$\phi FPr15 := \frac{Dgap}{2} \cdot Lstkef \cdot \int_{\alpha FPi+(FPr-1) \cdot \alpha FPstep}^{\alpha FPf+(FPr-1) \cdot \alpha FPstep} Bgapt(t\_test, \theta ag) d\theta ag = -1.50378602 \times 10^{-4} \text{ Wb}$$

$$B\_FPr15 := \frac{\phi FPr15}{FPr\_area} = -0.53283612 \text{ T}$$

$$FPr_{15} := 16$$

$$\phi FPr16 := \frac{Dgap}{2} \cdot Lstkef \cdot \int_{\alpha FPi+(FPr-1) \cdot \alpha FPstep}^{\alpha FPf+(FPr-1) \cdot \alpha FPstep} Bgapt(t\_test, \theta ag) d\theta ag = -7.65730765 \times 10^{-5} \text{ Wb}$$

$$B\_FPr16 := \frac{\phi FPr16}{FPr\_area} = -0.27132119 \text{ T}$$

$$FPr_{16} := 17$$

$$\phi FPr17 := \frac{Dgap}{2} \cdot Lstkef \cdot \int_{\alpha FPi+(FPr-1) \cdot \alpha FPstep}^{\alpha FPf+(FPr-1) \cdot \alpha FPstep - \alpha FPstep \div 2} Bgapt(t\_test, \theta ag) d\theta ag$$

$$B\_FPr17 := \frac{\phi FPr17}{FPr\_area} = -0.03414673 \text{ T}$$

Next pole

$$FPr_{17} := 23$$

$$\phi FPr23 := \frac{Dgap}{2} \cdot Lstkef \cdot \int_{\alpha FPi+(FPr-1) \cdot \alpha FPstep}^{\alpha FPf+(FPr-1) \cdot \alpha FPstep} Bgapt(t\_test, \theta ag) d\theta ag = -6.21335081 \times 10^{-5} \text{ Wb}$$

$$B\_FPr23 := \frac{\phi FPr23}{FPr\_area} = -0.22015750 \text{ T}$$

$$FPr_{18} := 24$$

$$\phi FPr24 := \frac{Dgap}{2} \cdot Lstkef \cdot \int_{\alpha FPi+(FPr-1) \cdot \alpha FPstep}^{\alpha FPf+(FPr-1) \cdot \alpha FPstep} Bgapt(t\_test, \theta ag) d\theta ag = -1.00255073 \times 10^{-4} \text{ Wb}$$

$$B\_FPr24 := \frac{\phi FPr24}{FPr\_area} = -0.35523355 \text{ T}$$

$$FPr_{19} := 25$$

$$\phi FPr25 := \frac{Dgap}{2} \cdot Lstkef \cdot \int_{\alpha FPi+(FPr-1) \cdot \alpha FPstep}^{\alpha FPf+(FPr-1) \cdot \alpha FPstep} Bgapt(t\_test, \theta ag) d\theta ag = -1.09058802 \times 10^{-4} \text{ Wb}$$

$$B\_FPr25 := \frac{\phi FPr25}{FPr\_area} = -0.38642778 \text{ T}$$

$$FPr_{20} := 26$$

$$\phi_{FPr26} := \frac{D_{gap}}{2} \cdot L_{stkef} \cdot \int_{\alpha_{FPi+(FPmr-1) \cdot \alpha_{FPstep}}}^{\alpha_{FPf+(FPmr-1) \cdot \alpha_{FPstep}}} B_{gap}(t_{test}, \theta_{ag}) d\theta_{ag} = -9.05219497 \times 10^{-5} \text{ Wb}$$

$$B_{FPr26} := \frac{\phi_{FPr26}}{FPr\_area} = -0.32074620 \text{ T}$$

$$FPr_{mr} := 27$$

$$\phi_{FPr27} := \frac{D_{gap}}{2} \cdot L_{stkef} \cdot \int_{\alpha_{FPi+(FPmr-1) \cdot \alpha_{FPstep}}}^{\alpha_{FPf+(FPmr-1) \cdot \alpha_{FPstep}}} B_{gap}(t_{test}, \theta_{ag}) d\theta_{ag} = -5.09621557 \times 10^{-5} \text{ Wb}$$

$$B_{FPr27} := \frac{\phi_{FPr27}}{FPr\_area} = -0.18057408 \text{ T}$$

$$FPr_{mr} := 28$$

$$\phi_{FPr28} := \frac{D_{gap}}{2} \cdot L_{stkef} \cdot \int_{\alpha_{FPi+(FPmr-1) \cdot \alpha_{FPstep}}}^{\alpha_{FPf+(FPmr-1) \cdot \alpha_{FPstep}} - \alpha_{FPstep} \div 2} B_{gap}(t_{test}, \theta_{ag}) d\theta_{ag}$$

$$B_{FPr28} := \frac{\phi_{FPr28}}{FPr\_area} = -0.02355053 \text{ T}$$

## **Identification of maximum values in several parts of the machine**

$$B_{thmax} := |B_{th02}| = 1.48334588 \text{ T} \quad \text{Maximum induction in stator teeth}$$

$$B_{ykmax} := |B_{yk01}| = 1.48343246 \text{ T} \quad \text{Maximum value at stator yoke}$$

$$B_{FPrmaxFP1} := |B_{FPr01}| = 1.38797923 \text{ T} \quad \text{Maximum value at rotor flux path 1}$$

$$B_{FPrmaxFP2} := |B_{FPr02}| = 1.34456949 \text{ T} \quad \text{Maximum value at rotor flux path 2}$$

$$B_{FPrmaxFP3} := |B_{FPr03}| = 1.16152075 \text{ T} \quad \text{Maximum value at rotor flux path 3}$$

$$B_{FPrmaxFP4} := |B_{FPr04}| = 0.85358232 \text{ T} \quad \text{Maximum value at rotor flux path 4}$$

$$B_{FPrmaxFP5} := |B_{FPr05}| = 0.45189527 \text{ T} \quad \text{Maximum value at rotor flux path 5}$$

$$B_{FPrmaxFP6} := |B_{FPr06}| = 0.05769725 \text{ T} \quad \text{Maximum value at rotor flux path 6}$$

## **Post-processing Additional Sizing Equations: using the results from the Global Electromagnetic Model**

### **1- Losses calculation**

#### **Winding losses**

$$Loss_{Rc} := 3 \cdot R_c \cdot |\Psi_{Ica}|^2 = 96.17254342 \text{ W}$$

$$\text{LossRg} := 3 \cdot \text{Rg} \cdot \left| \Psi_{\text{Iga}}^2 \right| = 80.18239969 \text{ W}$$

$$\text{TotalWindingLosses} := \text{LossRc} + \text{LossRg} = 176.35494311 \text{ W}$$

### Estimating of iron losses

Removing unit to execute in Mathcad

$$\text{Bthmaxtemp} := \frac{\text{Bthmax}}{T} = 1.48334588$$

$$\text{Bykmaxtemp} := \frac{\text{Bykmax}}{T} = 1.48343246$$

$$\text{BFPmaxtempFP1} := \frac{\text{BFPmaxFP1}}{T} = 1.38797923$$

$$\text{BFPmaxtempFP2} := \frac{\text{BFPmaxFP2}}{T} = 1.34456949$$

$$\text{BFPmaxtempFP3} := \frac{\text{BFPmaxFP3}}{T} = 1.16152075$$

$$\text{BFPmaxtempFP4} := \frac{\text{BFPmaxFP4}}{T} = 0.85358232$$

$$\text{BFPmaxtempFP5} := \frac{\text{BFPmaxFP5}}{T} = 0.45189527$$

$$\text{BFPmaxtempFP6} := \frac{\text{BFPmaxFP6}}{T} = 0.05769725$$

#### **Loss calculated in J/kg at one stator tooth**

$$\text{W\_J\_Kg\_th} := \text{kh} \cdot \text{Bthmaxtemp}^{\text{oh}} + \frac{\text{fop}}{\text{frest}} \cdot \text{kf} \cdot \text{Bthmaxtemp}^2 + \sqrt{\frac{\text{fop}}{\text{frest}}} \cdot (\text{ke} \cdot \text{Bthmaxtemp}^{1.5}) = 0.04851657$$

#### **Loss calculated at stator teeth in Watts**

$$\text{LossIronToothTotal} := \text{Nsl} \cdot \text{fop} \cdot \text{MassTooth} \cdot (\text{W\_J\_Kg\_th}) \cdot \frac{\text{W}}{\text{kg}} = 10.25025826 \text{ W}$$

#### **Loss calculated in J/kg at one stator yoke**

$$\text{W\_J\_Kg\_yk} := \text{kh} \cdot \text{Bykmaxtemp}^{\text{oh}} + \frac{\text{fop}}{\text{frest}} \cdot \text{kf} \cdot \text{Bykmaxtemp}^2 + \sqrt{\frac{\text{fop}}{\text{frest}}} \cdot (\text{ke} \cdot \text{Bykmaxtemp}^{1.5})$$

#### **Loss calculated at stator teeth in Watts**

$$\text{LossIronYokeTotal} := \text{Pr} \cdot \text{fop} \cdot \text{MassYoke1\_Pr} \cdot (\text{W\_J\_Kg\_yk}) \cdot \frac{\text{W}}{\text{kg}} = 12.85922275 \text{ W}$$

#### **Loss calculated in J/kg at flux path 1**

$$\text{W\_J\_Kg\_fp1} := \text{kh} \cdot \text{BFPmaxtempFP1}^{\text{oh}} + \frac{\text{fop}}{\text{frest}} \cdot \text{kf} \cdot \text{BFPmaxtempFP1}^2 + \sqrt{\frac{\text{fop}}{\text{frest}}} \cdot (\text{ke} \cdot \text{BFPmaxtempFP1}^{1.5})$$

#### **Loss calculated at flux path 1 in Watts**

$$\text{LossIronFPTotal\_FP1} := \text{Pr} \cdot \text{fop} \cdot \text{MassFP1} \cdot (\text{W\_J\_Kg\_fp1}) \cdot \frac{\text{W}}{\text{kg}} = 2.22651406 \text{ W}$$

**Loss calculated in J/kg at flux path 2**

$$\text{W\_J\_Kg\_fp2} := \text{kh} \cdot \text{BFPmaxtempFP2}^{\text{oh}} + \frac{\text{fop}}{\text{ftest}} \cdot \text{kf} \cdot \text{BFPmaxtempFP2}^2 + \sqrt{\frac{\text{fop}}{\text{ftest}}} \cdot (\text{ke} \cdot \text{BFPmaxtempFP2}^{1.5})$$

**Loss calculated at flux path 2 in Watts**

$$\text{LossIronFPTotal\_FP2} := \text{Pr} \cdot \text{fop} \cdot \text{MassFP2} \cdot (\text{W\_J\_Kg\_fp2}) \cdot \frac{\text{W}}{\text{kg}} = 1.71093036 \text{ W}$$

**Loss calculated in J/kg at flux path 3**

$$\text{W\_J\_Kg\_fp3} := \text{kh} \cdot \text{BFPmaxtempFP3}^{\text{oh}} + \frac{\text{fop}}{\text{ftest}} \cdot \text{kf} \cdot \text{BFPmaxtempFP3}^2 + \sqrt{\frac{\text{fop}}{\text{ftest}}} \cdot (\text{ke} \cdot \text{BFPmaxtempFP3}^{1.5})$$

**Loss calculated at flux path 3 in Watts**

$$\text{LossIronFPTotal\_FP3} := \text{Pr} \cdot \text{fop} \cdot \text{MassFP3} \cdot (\text{W\_J\_Kg\_fp3}) \cdot \frac{\text{W}}{\text{kg}} = 1.01161469 \text{ W}$$

**Loss calculated in J/kg at flux path 4**

$$\text{W\_J\_Kg\_fp4} := \text{kh} \cdot \text{BFPmaxtempFP4}^{\text{oh}} + \frac{\text{fop}}{\text{ftest}} \cdot \text{kf} \cdot \text{BFPmaxtempFP4}^2 + \sqrt{\frac{\text{fop}}{\text{ftest}}} \cdot (\text{ke} \cdot \text{BFPmaxtempFP4}^{1.5})$$

**Loss calculated at flux path 4 in Watts**

$$\text{LossIronFPTotal\_FP4} := \text{Pr} \cdot \text{fop} \cdot \text{MassFP4} \cdot (\text{W\_J\_Kg\_fp4}) \cdot \frac{\text{W}}{\text{kg}} = 0.40351777 \text{ W}$$

**Loss calculated in J/kg at flux path 5**

$$\text{W\_J\_Kg\_fp5} := \text{kh} \cdot \text{BFPmaxtempFP5}^{\text{oh}} + \frac{\text{fop}}{\text{ftest}} \cdot \text{kf} \cdot \text{BFPmaxtempFP5}^2 + \sqrt{\frac{\text{fop}}{\text{ftest}}} \cdot (\text{ke} \cdot \text{BFPmaxtempFP5}^{1.5})$$

**Loss calculated at flux path 5 in Watts**

$$\text{LossIronFPTotal\_FP5} := \text{Pr} \cdot \text{fop} \cdot \text{MassFP5} \cdot (\text{W\_J\_Kg\_fp5}) \cdot \frac{\text{W}}{\text{kg}} = 0.06959600 \text{ W}$$

**Loss calculated in J/kg at flux path 6**

$$\text{W\_J\_Kg\_fp6} := \text{kh} \cdot \text{BFPmaxtempFP6}^{\text{oh}} + \frac{\text{fop}}{\text{ftest}} \cdot \text{kf} \cdot \text{BFPmaxtempFP6}^2 + \sqrt{\frac{\text{fop}}{\text{ftest}}} \cdot (\text{ke} \cdot \text{BFPmaxtempFP6}^{1.5})$$

**Loss calculated at flux path 6 in Watts**

$$\text{LossIronFPTotal\_FP6} := \text{Pr} \cdot \text{fop} \cdot \text{MassFP6} \cdot (\text{W\_J\_Kg\_fp6}) \cdot \frac{\text{W}}{\text{kg}} = 3.47082329 \times 10^{-4} \text{ W}$$

**Loss calculated at all rotor flux path in Watts**

$$\text{LossFP\_t} := \text{LossIronFPTotal\_FP1} + \text{LossIronFPTotal\_FP2} + \text{LossIronFPTotal\_FP3}$$

$$\text{LossIronFPTotal} := \text{LossFP\_t} + \text{LossIronFPTotal\_FP4} + \text{LossIronFPTotal\_FP5} + \text{LossIronFPTotal\_FP6}$$

$$\text{LossIronFPTotal} = 5.42251996 \text{ W}$$

$$\text{Loss\_wg} := 3 \cdot [(\Psi I_{ga})^2 \cdot R_g] = 80.18239969 \text{ W}$$

$$\text{Loss\_wc} := 3 \cdot [(\Psi I_{ca})^2 \cdot R_c] = 96.17254342 \text{ W}$$

$$\text{Loss\_windings} := \text{Loss\_wg} + \text{Loss\_wc} = 176.35494311 \text{ W}$$

$$\text{LossIronFPTotal} = 5.42251996 \text{ W}$$

$$\text{LossIronYokeTotal} = 12.85922275 \text{ W}$$

$$\text{LossIronToothTotal} = 10.25025826 \text{ W}$$

$$\text{Loss\_windings} = 176.35494311 \text{ W}$$

$$\text{LossIronTotal} := \text{LossIronFPTotal} + \text{LossIronYokeTotal} + \text{LossIronToothTotal} = 28.53200097 \text{ W}$$

$$\text{LossCopperIronTotal} := \text{Loss\_windings} + \text{LossIronTotal} = 204.88694408 \text{ W}$$

## **2- Machine Apparent Power**

### **Output power taking into account iron losses and efficiency calculation**

#### **Internal Power (calculated at voltage E)**

##### **Apparent Power**

$$S3\phi_{\text{grid\_internal}} := |3 \cdot \Psi E_{ga} \cdot \overline{\Psi I_{ga}}| = 841.75019444 \text{ W}$$

$$S3\phi_{\text{control\_internal}} := |3 \cdot \Psi E_{ca} \cdot \overline{\Psi I_{ca}}| = 844.63780319 \text{ W}$$

##### **Reactive Power**

$$Q3\phi_{\text{grid\_internal}} := \sqrt{S3\phi_{\text{grid\_internal}}^2 - P3\phi_{\text{grid\_internal}}^2} = 635.94246884 \text{ W}$$

$$Q3\phi_{\text{control\_internal}} := \sqrt{S3\phi_{\text{control\_internal}}^2 - P3\phi_{\text{control\_internal}}^2} = 639.75968333 \text{ W}$$

$$Q3\phi_{\text{total\_internal}} := Q3\phi_{\text{grid\_internal}} + Q3\phi_{\text{control\_internal}} = 1.27570215 \times 10^3 \text{ W}$$

##### **Total Apparent Power**

$$S3\phi_{\text{total\_internal}} := \sqrt{P3\phi_{\text{total\_internal}}^2 + Q3\phi_{\text{total\_internal}}^2} = 1.68638615 \times 10^3 \text{ W}$$

##### **Internal Power Factor (at voltage E)**

$$\text{PF}_{\text{gridSS\_internal}} := \frac{P3\phi_{\text{grid\_internal}}}{S3\phi_{\text{grid\_internal}}} = -0.65514838$$

$$PF_{\text{controlSS\_internal}} := \frac{P3\phi_{\text{control\_internal}}}{S3\phi_{\text{control\_internal}}} = -0.65290859$$

**Terminal Power (calculated at voltage V)**

**Apparent Power**

$$S3\phi_{\text{grid\_ter}} := \left| 3 \cdot \Psi V_{\text{ga}} \cdot \overline{\Psi I_{\text{ga}}} \right| = 791.54028756 \text{ W}$$

$$S3\phi_{\text{control\_ter}} := \left| 3 \cdot \Psi V_{\text{ca}} \cdot \overline{\Psi I_{\text{ca}}} \right| = 785.23205906 \text{ W}$$

**Reactive Power**

$$Q3\phi_{\text{grid\_ter}} := \sqrt{S3\phi_{\text{grid\_ter}}^2 - P3\phi_{\text{grid\_ter}}^2} = 635.94246884 \text{ W}$$

$$Q3\phi_{\text{control\_ter}} := \sqrt{S3\phi_{\text{control\_ter}}^2 - P3\phi_{\text{control\_ter}}^2} = 639.75968333 \text{ W}$$

$$Q3\phi_{\text{total\_ter}} := Q3\phi_{\text{grid\_ter}} + Q3\phi_{\text{control\_ter}} = 1.27570215 \times 10^3 \text{ W}$$

**Total Apparent Power**

$$S3\phi_{\text{total\_ter}} := \sqrt{P3\phi_{\text{total\_ter}}^2 + Q3\phi_{\text{total\_ter}}^2} = 1.57669926 \times 10^3 \text{ W}$$

**Power Factor**

$$PF_{\text{gridSS\_ter}} := \frac{P3\phi_{\text{grid\_ter}}}{S3\phi_{\text{grid\_ter}}} = -0.59540731$$

$$PF_{\text{controlSS\_ter}} := \frac{P3\phi_{\text{control\_ter}}}{S3\phi_{\text{control\_ter}}} = -0.57982698$$

### **3- Efficiency**

***If  $\Phi$ torque > 0, generating operation:***

$$\phi_{\text{torque}} = 90.00000000.^\circ$$

**OBS: if  $\phi$ torque does not satisfy >0 condition, neglect the following results because they will not be coherent.**

$$P3\phi_{\text{total\_internal}} = -1.10294255 \times 10^3 \text{ W}$$

$$\text{LossCopperIronTotal} = 204.88694408 \text{ W}$$

$$P3\phi_{\text{out\_generating}} := P3\phi_{\text{total\_internal}} + \text{LossCopperIronTotal} = -898.05560412 \text{ W}$$

$$\text{Efficiency\_generating} := \frac{P3\phi_{\text{out\_generating}}}{P3\phi_{\text{total\_internal}}} = 81.42360684. \%$$

$$\text{Torque\_density\_generating} := \frac{(P3\phi_{\text{out\_generating}} \div \omega_{\text{rm}})}{\text{VolMachine\_L}} = -2.86549670 \times 10^3 \text{ Pa} = \text{N.m/m}^3$$

***If  $\Phi$ torque < 0, motoring operation:***

$$\phi_{\text{torque}} = 90.00000000.^\circ$$

OBS: if  $\phi$ torque does not satisfy  $<0$  condition, neglect the following results because they will not be coherent.

$$P3\phi_{total\_internal} = -1.10294255 \times 10^3 \text{ W}$$

$$\text{LossCopperIronTotal} = 204.88694408 \text{ W}$$

$$P3\phi_{out\_motoring} := P3\phi_{total\_ter} - \text{LossCopperIronTotal} = -1.13147455 \times 10^3 \text{ W}$$

$$\text{Efficiency\_motoring} := \frac{P3\phi_{out\_motoring}}{P3\phi_{total\_ter}} = 122.11198844\%$$

$$\text{Torque\_density\_motoring} := \frac{(P3\phi_{out\_motoring} \div \omega_{rm})}{\text{VolMachine\_L}} = -3.61028490 \times 10^3 \text{ Pa} = \text{N.m/m}^3$$

## End of the GSOM model

#####

## From Chapter II Slot and Duct Numbers Selection (Knight et al., 2013):

As presented in chapter II (Section II.2.b.ii - Number of rotor slots), the number of stator slots and rotor ducts must be chosen in a way to avoid slotting harmonics with the same space order. The procedure below has been presented in [3] and it is used to determine this parameters in the BDFRM.

**Definition of the required parameters:**

$$P_r := 6$$

$$N_{sl} := 48$$

$$P_g := 8$$

$$P_c := 4$$

$$\text{ORIGIN} := 1$$

Mathcad internal parameters: redefine the first index in the vector

**Segmented rotor design:**

$$N_{sl\_multiple} := P_r = 6.00000000 \quad \text{The number of ducts must be a multiple of } P_r \text{ poles}$$

$$\text{MinDuctsNumber} := 9 \quad \text{Minimum number of ducts per rotor pole}$$

The slotting harmonics for a p-pole conventional machine are given by:



$$\begin{cases} h_{St} = p \left( 1 \pm m \frac{N_{Stat}}{p} \right) \\ h_R = p \left( 1 \pm n \frac{N_{Rot}}{p} \right) \end{cases} \quad (\text{Eq. 1})$$

where m and n are integers.

Since the BDFRM has two 3-phase windings with different pole numbers, there are more constraints on the design that must be taken into account simultaneously. The significant stator and rotor slotting harmonics are defined as having space orders:

$$\begin{cases} h_{Stg} = p_g \left( 1 \pm \frac{N_{Stat}}{p_g} \right) \\ h_{Sts} = p_s \left( 1 \pm \frac{N_{Stat}}{p_s} \right) \\ h_{Rg} = p_g \left( 1 \pm \frac{N_{Rot}}{p_g} \right) \\ h_{Rs} = p_s \left( 1 \pm \frac{N_{Rot}}{p_s} \right) \end{cases} \quad (\text{Eq. 2})$$

Defining the indexes for Mathcad spreadsheet:

$$\text{idrs1} := 1, 2 \dots 4$$

$$\text{idcs1} := 1, 2 \dots 2$$

$$\text{Slot\_Harm}_{\text{idrs1}, \text{idcs1}} :=$$

Nsl
$\text{Nslr}_{\text{multiple}} \cdot \text{MinDuctsNumber} + (\text{Nslr}_{\text{multiple}} \cdot 0)$
Nsl
$\text{Nslr}_{\text{multiple}} \cdot \text{MinDuctsNumber} + (\text{Nslr}_{\text{multiple}} \cdot 1)$
Nsl
$\text{Nslr}_{\text{multiple}} \cdot \text{MinDuctsNumber} + (\text{Nslr}_{\text{multiple}} \cdot 2)$
Nsl
$\text{Nslr}_{\text{multiple}} \cdot \text{MinDuctsNumber} + (\text{Nslr}_{\text{multiple}} \cdot 3)$

The slotting harmonics combination that will be analysed for Nsl (number of stator slots) and Nslr (number of rotor slots or ducts) are:

$$\text{Slot\_Harm} = \begin{pmatrix} \text{Nsl} & \text{Nslr} \\ 48.00000000 & 54.00000000 \\ 48.00000000 & 60.00000000 \\ 48.00000000 & 66.00000000 \\ 48.00000000 & 72.00000000 \end{pmatrix}$$

Each line of the matrix Slot\_Harm shown above, forming the stator/rotor possible slot combinations, are considered and the associated slotting harmonics calculated from (Eq. 2) are



$$\text{hstcP3}_{\text{idrs1}} := \text{Pc} \cdot \left( 1 + 3 \cdot \frac{\text{Slot\_Harm}_{\text{idrs1},1}}{\text{Pc}} \right)$$

$$\text{hRcP3}_{\text{idrs1}} := \text{Pc} \cdot \left( 1 + 3 \cdot \frac{\text{Slot\_Harm}_{\text{idrs1},2}}{\text{Pc}} \right)$$

$$\text{hstcN3}_{\text{idrs1}} := \text{Pc} \cdot \left( 1 - 3 \cdot \frac{\text{Slot\_Harm}_{\text{idrs1},1}}{\text{Pc}} \right)$$

$$\text{hRcN3}_{\text{idrs1}} := \text{Pc} \cdot \left( 1 - 3 \cdot \frac{\text{Slot\_Harm}_{\text{idrs1},2}}{\text{Pc}} \right)$$

$$\text{hstcP4}_{\text{idrs1}} := \text{Pc} \cdot \left( 1 + 4 \cdot \frac{\text{Slot\_Harm}_{\text{idrs1},1}}{\text{Pc}} \right)$$

$$\text{hRcP4}_{\text{idrs1}} := \text{Pc} \cdot \left( 1 + 4 \cdot \frac{\text{Slot\_Harm}_{\text{idrs1},2}}{\text{Pc}} \right)$$

$$\text{hstcN4}_{\text{idrs1}} := \text{Pc} \cdot \left( 1 - 4 \cdot \frac{\text{Slot\_Harm}_{\text{idrs1},1}}{\text{Pc}} \right)$$

$$\text{hRcN4}_{\text{idrs1}} := \text{Pc} \cdot \left( 1 - 4 \cdot \frac{\text{Slot\_Harm}_{\text{idrs1},2}}{\text{Pc}} \right)$$

$$\text{hstcP5}_{\text{idrs1}} := \text{Pc} \cdot \left( 1 + 5 \cdot \frac{\text{Slot\_Harm}_{\text{idrs1},1}}{\text{Pc}} \right)$$

$$\text{hRcP5}_{\text{idrs1}} := \text{Pc} \cdot \left( 1 + 5 \cdot \frac{\text{Slot\_Harm}_{\text{idrs1},2}}{\text{Pc}} \right)$$

$$\text{hstcN5}_{\text{idrs1}} := \text{Pc} \cdot \left( 1 - 5 \cdot \frac{\text{Slot\_Harm}_{\text{idrs1},1}}{\text{Pc}} \right)$$

$$\text{hRcN5}_{\text{idrs1}} := \text{Pc} \cdot \left( 1 - 5 \cdot \frac{\text{Slot\_Harm}_{\text{idrs1},2}}{\text{Pc}} \right)$$

The results for the positive (P) and negative (N) cases from equations in (Eq. 2) are depicted in the sequence.

Each line in the vectors below are associated to the lines of the matrix Slot\_Harm.

$$\text{Slot\_Harm} = \begin{pmatrix} 48.00000000 & 54.00000000 \\ 48.00000000 & 60.00000000 \\ 48.00000000 & 66.00000000 \\ 48.00000000 & 72.00000000 \end{pmatrix}$$

To identify the lower order matching harmonics, the results from stator and rotor for each combination must be analysed.

#### Harmonic Calculation Results:

##### STATOR

$$\text{hstgP1} = \begin{pmatrix} 56.00000 \\ 56.00000 \\ 56.00000 \\ 56.00000 \end{pmatrix} \quad \text{hstgN1} = \begin{pmatrix} -40.00000000 \\ -40.00000000 \\ -40.00000000 \\ -40.00000000 \end{pmatrix}$$

$$\text{hstgP2} = \begin{pmatrix} 104.0000 \\ 104.0000 \\ 104.0000 \\ 104.0000 \end{pmatrix} \quad \text{hstgN2} = \begin{pmatrix} -88.00000000 \\ -88.00000000 \\ -88.00000000 \\ -88.00000000 \end{pmatrix}$$

$$\text{hstgP3} = \begin{pmatrix} 152.000 \\ 152.000 \\ 152.000 \\ 152.000 \end{pmatrix} \quad \text{hstgN3} = \begin{pmatrix} -136.00000000 \\ -136.00000000 \\ -136.00000000 \\ -136.00000000 \end{pmatrix}$$

##### ROTOR

$$\text{hRgP1} = \begin{pmatrix} 62.00000 \\ 68.00000 \\ 74.00000 \\ 80.00000 \end{pmatrix} \quad \text{hRgN1} = \begin{pmatrix} -46.00000000 \\ -52.00000000 \\ -58.00000000 \\ -64.00000000 \end{pmatrix}$$

$$\text{hRgP2} = \begin{pmatrix} 116.0000 \\ 128.0000 \\ 140.0000 \\ 152.0000 \end{pmatrix} \quad \text{hRgN2} = \begin{pmatrix} -100.00000000 \\ -112.00000000 \\ -124.00000000 \\ -136.00000000 \end{pmatrix}$$

$$\text{hRgP3} = \begin{pmatrix} 170.0000 \\ 188.0000 \\ 206.0000 \\ 224.0000 \end{pmatrix} \quad \text{hRgN3} = \begin{pmatrix} -154.00000000 \\ -172.00000000 \\ -190.00000000 \\ -208.00000000 \end{pmatrix}$$

$$\begin{aligned}
\text{hstgP4} &= \begin{pmatrix} 200.000 \\ 200.000 \\ 200.000 \\ 200.000 \end{pmatrix} & \text{hstgN4} &= \begin{pmatrix} -184.00000000 \\ -184.00000000 \\ -184.00000000 \\ -184.00000000 \end{pmatrix} & \text{hRgP4} &= \begin{pmatrix} 224.0000 \\ 248.0000 \\ 272.0000 \\ 296.0000 \end{pmatrix} & \text{hRgN4} &= \begin{pmatrix} -208.00000000 \\ -232.00000000 \\ -256.00000000 \\ -280.00000000 \end{pmatrix} \\
\text{hstgP5} &= \begin{pmatrix} 248.0000 \\ 248.0000 \\ 248.0000 \\ 248.0000 \end{pmatrix} & \text{hstgN5} &= \begin{pmatrix} -232.00000000 \\ -232.00000000 \\ -232.00000000 \\ -232.00000000 \end{pmatrix} & \text{hRgP5} &= \begin{pmatrix} 278.0000 \\ 308.0000 \\ 338.0000 \\ 368.0000 \end{pmatrix} & \text{hRgN5} &= \begin{pmatrix} -262.00000000 \\ -292.00000000 \\ -322.00000000 \\ -352.00000000 \end{pmatrix} \\
\text{hstcP1} &= \begin{pmatrix} 52.00000 \\ 52.00000 \\ 52.00000 \\ 52.00000 \end{pmatrix} & \text{hstcN1} &= \begin{pmatrix} -44.00000000 \\ -44.00000000 \\ -44.00000000 \\ -44.00000000 \end{pmatrix} & \text{hRcP1} &= \begin{pmatrix} 58.00000 \\ 64.00000 \\ 70.00000 \\ 76.00000 \end{pmatrix} & \text{hRcN1} &= \begin{pmatrix} -50.00000000 \\ -56.00000000 \\ -62.00000000 \\ -68.00000000 \end{pmatrix} \\
\text{hstcP2} &= \begin{pmatrix} 100.0000 \\ 100.0000 \\ 100.0000 \\ 100.0000 \end{pmatrix} & \text{hstcN2} &= \begin{pmatrix} -92.00000000 \\ -92.00000000 \\ -92.00000000 \\ -92.00000000 \end{pmatrix} & \text{hRcP2} &= \begin{pmatrix} 112.0000 \\ 124.0000 \\ 136.0000 \\ 148.0000 \end{pmatrix} & \text{hRcN2} &= \begin{pmatrix} -104.00000000 \\ -116.00000000 \\ -128.00000000 \\ -140.00000000 \end{pmatrix} \\
\text{hstcP3} &= \begin{pmatrix} 148.0000 \\ 148.0000 \\ 148.0000 \\ 148.0000 \end{pmatrix} & \text{hstcN3} &= \begin{pmatrix} -140.00000000 \\ -140.00000000 \\ -140.00000000 \\ -140.00000000 \end{pmatrix} & \text{hRcP3} &= \begin{pmatrix} 166.0000 \\ 184.0000 \\ 202.0000 \\ 220.0000 \end{pmatrix} & \text{hRcN3} &= \begin{pmatrix} -158.00000000 \\ -176.00000000 \\ -194.00000000 \\ -212.00000000 \end{pmatrix} \\
\text{hstcP4} &= \begin{pmatrix} 196.0000 \\ 196.0000 \\ 196.0000 \\ 196.0000 \end{pmatrix} & \text{hstcN4} &= \begin{pmatrix} -188.00000000 \\ -188.00000000 \\ -188.00000000 \\ -188.00000000 \end{pmatrix} & \text{hRcP4} &= \begin{pmatrix} 220.0000 \\ 244.0000 \\ 268.0000 \\ 292.0000 \end{pmatrix} & \text{hRcN4} &= \begin{pmatrix} -212.00000000 \\ -236.00000000 \\ -260.00000000 \\ -284.00000000 \end{pmatrix} \\
\text{hstcP5} &= \begin{pmatrix} 244.0000 \\ 244.0000 \\ 244.0000 \\ 244.0000 \end{pmatrix} & \text{hstcN5} &= \begin{pmatrix} -236.00000000 \\ -236.00000000 \\ -236.00000000 \\ -236.00000000 \end{pmatrix} & \text{hRcP5} &= \begin{pmatrix} 274.0000 \\ 304.0000 \\ 334.0000 \\ 364.0000 \end{pmatrix} & \text{hRcN5} &= \begin{pmatrix} -266.00000000 \\ -296.00000000 \\ -326.00000000 \\ -356.00000000 \end{pmatrix}
\end{aligned}$$

The lower matching slotting harmonics considering the analysed combinations for the number of stator and rotor slots are summarized in Table I below.

Table I - Lower matching slotting harmonics considering some combinations for the number of stator and rotor slots.

$N_{sl}$	$N_{slr}$	Lower matching space order	
48	54	104	104
48	60	52	56
48	66	136	140
48	72	136	140

## References for the Mathcad file:

- [1] Pyrhönen, J., Jokinen, T., & Hrabovcova, V. (2008). Design of Electrical Machines (1st ed.). John Wiley & Sons, Ltd.
- [2] Boldea, I. (2006). Synchronous Generators - The Electric Generators Handbook (1st ed.). New York: CRC Press.
- [3] Knight, A. M., Betz, R. E., & Dorrell, D. G. (2013). Design and Analysis of Brushless Doubly Fed Reluctance Machines. IEEE Transactions on Industry Applications, 49(1), 50–58. doi:10.1109/TIA.2012.2229451
- [4] Boldea, I., & Nasar, S. A. (2002). The Induction Machine Handbook (1st ed.). Boca Raton: CRC Press.
- [5] Betz, R. E., & Jovanovic, M. G. (1998). Introduction to Brushless Doubly Fed Reluctance Machines. The Basic Equations. Aalborg, Denmark. Retrieved from <ftp://vcs2.newcastle.edu.au/Papers/BDFRM-Review.pdf>
- [6] Wurtz, F. (1996). Une Nouvelle Approche pour la Conception Sous Contraintes de Machines Électriques. INSTITUT NATIONAL POLYTECHNIQUE DE GRENOBLE.
- [7] Ong, C.-M. (1997). Dynamic Simulation of Electric Machinery. (P. Hall, Ed.) (1st ed., p. 688). New Jersey.
- [8] Dorrell, D. G., Knight, A. M., Song, W. K., & Betz, R. E. (2013). Saturation and Ducting Effects in a Brushless Doubly-Fed Reluctance Machine. IEEE Transactions on Magnetics, 49(7), 3933–3936. doi:10.1109/TMAG.2013.2251458
- [9] Foggia, A. (1999). Méthodes de calcul des inductances de fuites. Techniques de L'ingénieur Généralités Sur Les Machines Électriques Tourmantes, base docum(ref. article : d3440), 1–20. Retrieved from <http://www.techniques-ingenieur.fr/base-documentaire/energies-th4/generalites-sur-les-machines-electriques-tourmantes-42250210/methodes-de-calcul-des-inductances-de-fuites-d3440/>